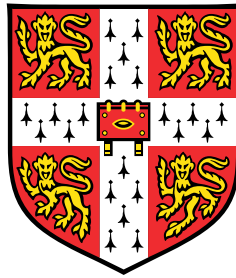


Activation processes in biology

A collection of problems



Samuel Bell

Supervisor: Prof. Eugene M. Terentjev

Department of Physics
University of Cambridge

This dissertation is submitted for the degree of
Doctor of Philosophy

Trinity College

March 2019

DECLARATION

This dissertation is the result of my own work and includes nothing which is the outcome of work done in collaboration, except as specified in the text. It is not substantially the same as any that I have submitted, or, is being concurrently submitted for a degree or diploma or other qualification at the University of Cambridge or any other University or similar institution except as declared in the Preface and specified in the text. I further state that no substantial part of my dissertation has already been submitted, or, is being concurrently submitted for any such degree, diploma or other qualification at the University of Cambridge or any other University or similar institution except as specified in the text. This dissertation does not exceed 60,000 words, including summary/abstract, tables, footnotes and appendices. Part of this work has been presented in the following publications:

1. S. Bell and E. M. Terentjev (2015). Unfolding of globular polymers by external force. *J. Chem. Phys.* 143:184902.
2. S. Bell and E. M. Terentjev (2016). Non-exponential kinetics of unfolding under a constant force. *J. Chem. Phys.* 145:185102.
3. S. Bell and E. M. Terentjev (2017). Focal adhesion kinase: the reversible mechanosensor. *Biophys. J.* 112:2439-2450.
4. S. Bell and E. M. Terentjev (2017). Kinetics of tethered ligands binding to surface receptors. *Macromolecules* 50:8810-8815.
5. S. Bell and E. M. Terentjev (2017). Specific binding of a polymer chain to a sequence of surface receptors. *Sci. Rep.* 7:17272.
6. T. Jakuszeit, O. A. Croze and S. Bell (2019). Diffusion of active particles in complex environments: Role of surface scattering. *Phys. Rev. E* 99:012610.
7. S. Bell, A.-L. Redmann, and E. M. Terentjev (2019). Universal kinetics of the onset of cell spreading on substrates of different stiffness. *Biophys. J.* 116:551-559.

Samuel Bell

ABSTRACT: ACTIVATION PROCESSES IN BIOLOGY

Many processes in physics and biology can be understood through the framework of escape from a metastable state, including (but not limited to) the rates of chemical reactions, the unfolding of proteins, the nucleation of bubbles, and the condensation of gases. To understand the kinetics of these processes, we have to be able to calculate the rate of escape. In this thesis, I solve several of such of escape problems, each addressing a specific physical or biological system. I first show how the forced unfolding of heteropolymers could be a process with non-exponential kinetics, developing ideas about the importance of unfolding pathways in determining kinetics of unfolding. Then, I consider forced unfolding when a molecule is attached to a yielding (viscoelastic) substrate, and a constant force is applied. I show that the rates of unfolding depend on both the elastic and viscous response of the substrate. This problem is related to the biological process of mechanosensing, when the unfolding ‘sensor’ protein exposes catalytic residues and generates a chemical signal to the cell. Related to this is the analysis of population-dynamics study of cells adhesion on substrates, which allows me to extract key characteristics and parameters of the adhesome complex. Then, I apply the ideas of escape from a metastable state to ask about the rates of a ligand at the end of a tethered polymer binding to a surface receptor, using a mean field approach to reduce the problem to one dimension. I show that there is a trade-off between the entropic cost of reaching to a receptor vs the volumetric cost of expanding the tether length. I then show that for a Gaussian chain with multiple ligands along its length, there exists a finite, non-zero optimal number of ligands to minimise the time taken for the end of the chain to bind to the surface. Finally, I consider the problem of microswimmers in an obstacle lattice, calculating their transport properties, and showing how we can use lattices to examine the underlying stochastic dynamics.

Samuel Bell

Dearest John, may you live forever in the winds over the peaks, and may my work remain unburdened by third-order asymptotic expansions.

ACKNOWLEDGEMENTS

I would first like to thank my supervisor, Eugene Terentjev, for his unwavering supply of good advice and support. I am in large part a physicist of his making, and there has been no greater pleasure during my study than sitting together with a piece of paper, working through ideas and calculations for hours at a time. I would also like to thank Theresa Jakuszeit for a very productive period of procrastination in 2018, where we worked on the material now presented in Chapter 6, and for making the office a fun place to work. I owe many contributions to my work from useful discussions held with Robyn Pritchard, Mark Warner, Pete Townsend and John Ellis, Ottavio Croze, Mike Cates, Heidi Welch and Shery Huang. Finally, I would like to thank the help provided with my understanding of mathematics by Preeyan Parmar and John Grenfell-Shaw, two of my closest friends.

On a personal note, I would like to thank my parents for their guidance through the sticky bits, and their extensive support during a difficult final year. It is too easy to get caught up in the small details, and they have tried to help me keep this in mind throughout. I could not have wished for a better pair in my corner. To my close friends, both those at Trinity and the Marshall Road gang, who have been there to provide light relief in the form of crosswords and hill runs, thank you. Finally, I would like to thank Chloe, who has made everything that much easier and better.

TABLE OF CONTENTS

Preface	1
1 Theoretical background	5
1.1 A history of fluctuations in physics	5
1.2 The Fokker-Planck equation	12
1.3 Interpretation of stochastic integrals	14
1.4 Overdamped dynamics	18
1.5 Escape from metastable state: Kramers theory	20
1.6 Mean first passage time	22
2 Unfolding of polymers under constant force	29
2.1 Polymer model	32
2.2 Homopolymer unfolding	36
2.3 Heteropolymer unfolding free energy curves	41
2.4 Rate constants	45
2.5 Ensemble average	49
3 Mechanosensing: unfolding on non-rigid substrates	55
3.1 Model of coupled viscoelastic elements	59
3.2 Fixed reaction path approach	63
3.3 Ornstein-Uhlenbeck approach	68
3.4 Mean field approach	74
4 The onset of cell spreading as a study in population kinetics	85
4.1 Experimental details	87
4.2 Long-time kinetics: a rate-limiting process	91
4.3 Short-time kinetics: a nucleation process	92
4.4 Kinetics of adhesome assembly	94

5	The binding of tethered ligands to surface receptors	101
5.1	Diffusion of a tethered ligand	103
5.2	Mean first passage time to target	106
5.3	Bridging across a gap	108
5.4	Optimising the reaction time	110
5.5	Multiple ligands on a tethered chain	112
5.6	Accelerated zipper binding	114
5.7	Drift of center of mass	118
6	Diffusion of microswimmers in obstacle lattices	125
6.1	Equations of motion and boundary conditions	126
6.2	Diffusion of an active Lorentz gas	129
6.3	Run-and-tumble model	132
6.4	High-density geometrical effects	143
6.5	How should we model active particles?	146
7	Conclusions and outlook	149
	References	155

PREFACE

The second law of thermodynamics is considered so fundamental that it has transcended the field of physics, and entered into popular culture. It fascinates us; it is our oblivion. The Universe is marching towards a heat death, as its stores of ‘useful’ energy are slowly degraded – a future where time itself may cease to have any meaning.

Life exists as a parasite, its own existence dependent on accelerating the Universe’s decay (of course, the total entropy generated by life on Earth will be but an infinitesimal portion of that contained in a single black hole, which acts as an ‘entropic sink’). But what a wondrous parasite it is! Living organisms have ‘learnt’ to harness entropy production and self-replicate, adapt and flourish. Evolution has made this struggle diverse, across the micron scale to the kilometre scale (the largest organisms in the world, aspen clonal colonies, are many square kilometres and can be 100,000 years old!). However, common threads run across all organisms. One particular thread, relevant for this thesis, is that all organisms have microscopic structure – they are composed of one, ten, or ten trillion cells, each of which are approximately the same order of magnitude in size (10-100 μm). Prokaryotes, simpler organisms without a nucleus, are smaller at around 1 μm .

I was extremely fortunate to learn my undergraduate cell biology from a converted engineer, Murray Stewart. He tried to invoke physical principles when talking about cellular processes, and one notion in particular has stuck with me. Prokaryotes, such as bacteria, have a simple internal structure, without any of the membraned sub-compartments of eukaryotic cells. As such, they are less able to direct molecules around the cell to where they are required, and need to rely on simple diffusion for absorbed nutrients and ions to spread throughout the cell. If we take a response time of 1s for a cell to respond to an influx of ions (perhaps a chemical gradient), then, using the diffusion coefficient of water $D = 3 \times 10^{-12}\text{m}^2\text{s}^{-1}$, we get that the largest size of the cell can be $\sqrt{2 \times 3 \times 10^{-12}}\text{m} \approx 2.5\mu\text{m}$. This was the first example I saw that thermal motion was an important driving force in cellular processes and, looking back, it probably helped shape my interest in physics towards its application in biological systems.

Even the larger eukaryotic cells are well-placed to make use of thermal motion. Protein conformational changes often involve the making or breaking of weak links such as hydrogen bonds, where the activation energy is of the order of $10k_B T$. These bonds are such that they will be broken by thermal fluctuations with the help of a destabilising force. One good example of this is in forced protein unfolding, either in the muscles, where titin acts as a force buffer, or in cell-surface adhesion via focal contacts. Here, the cell cytoskeleton will exert forces on the substrate through membrane-bound protein complexes, and these may undergo conformational changes as a result. Fluctuations, both in the substrate, and in the cell, may play a crucial role in the rate of these conformational changes. This means that we must consider a two-dimensional stochastic process – a formidable theoretical problem. The general case is impossible to solve completely, and so we must dream up approximations to try and calculate the reaction time. In fact, it is possible to make multiple seemingly sensible choices and end up with vastly different results, as I will show. The art is in finding a choice that gives qualitatively correct results – not an easy task for coupled stochastic variables.

Once we understand the kinetics of a singular molecular process, one goal of cell biophysicists must be to coarse-grain. We are interested in the behaviour of cells and tissues – on the properties and pathologies of cell collectives such as ourselves. In the context of cell adhesion, we must try and understand how molecular processes translate upwards. This is an area where physics can play a crucial role – biology creates more and more data every year, and to make sense of it we must look for sensible simplifications of behaviour, and new ways of interpreting data. In this thesis, I show that cell populations can offer insight into more than macroscopic behaviours. Of course, there is a limit to what you can infer, but it is interesting in and of itself to see clean population kinetics – it is a truth often related from biologists to physicists that each cell has its own distinct character. While this is no doubt true of some cell characteristics, in the context of cell adhesion, we find beautiful examples of nucleation kinetics. In my mind, such discoveries are why statistical physics is such a vital tool for understanding the behaviour of biological systems. There is important information to be had everywhere, as long as you know how to look.

Protein unfolding is far from the only activated process in the cell, and in Chapter 5 I consider entropic barriers, rather than enthalpic barriers. A ligand tethered to the end of a chain must reach a receptor on the surface some distance away – this is a problem seen in the thrombin receptor and in cell-cell adhesion. Such problems offer intriguing avenues for theoretical work, because they offer multi-dimensional problems in non-trivial geometries. For a surface-based receptor, the tether itself offers another

entropic constraint (a non-absorbing Gaussian chain suffers an entropic repulsion from a hard wall), which modifies the scaling relations in the reaction time. I then extend this to a problem of self-assembly: that of multiple ligands binding in turn to a surface.

In the final chapter of this thesis, I move sideways, and focus on the problem of microswimmers in obstacle lattices. These are really interesting model systems – the hydrodynamics of their surface interactions means that their trajectories break time-reversal symmetry. These surface interactions allow them to traverse lattices much more efficiently than a classical reflection would. This may have been selected for – faster organisms can reach food sources faster, and out-compete slower species. The beauty of these model systems is that with careful experimentation, we may be able to explore some fundamental ideas surrounding non-equilibrium physics. The final chapter of this thesis provides a basis for exploring the basic stochastic dynamics driving the motion of microswimmers.

CHAPTER 1

THEORETICAL BACKGROUND

Before we begin, it is necessary to outline the current state of our understanding. To understand activation processes, one has to understand the underlying thermal fluctuations, how they are modelled, and the limitations of those models. Once I have outlined this historical development of fluctuations and thermal motion, I move on to how the effects of these fluctuations on a single particle can be shifted to an ensemble level, replacing well-defined particle positions and velocities with a probability density in phase space. This probability density obeys a partial differential equation, and I demonstrate how we can derive these partial differential equations. I discuss the limitations and choices made when we model stochastic processes, and then show how the partial differential equations were first used to calculate the escape rates from a metastable state. Then, I show how the calculation of the escape rate can be framed in the context of a first passage time, and introduce the machinery used to calculate mean first passage times.

1.1 A history of fluctuations in physics

In 1828, Robert Brown published “A brief account of microscopical observations made in the months of June, July and August 1827, on the particles contained in the pollen of plants; and on the general existence of active molecules in organic and inorganic bodies” in a privately circulated pamphlet. In this work, he describes the existence of small active molecules, initially isolated from pollen grains, of diameters “ $\frac{1}{15000}$ th - $\frac{1}{20000}$ th of an inch” (0.8-1.3 μm) [1]. These active molecules were different from the “animalcules” (such as bacteria), whose free motion in fluids is, amusingly, now a major topic in the modern field of active matter. Brown observed that these active molecules not only moved within the fluid, but underwent small shape changes. He was satisfied that these motions were not due to fluid flow, but belonged to the particles themselves. To check the extent of

these active molecules, he first checked different parts of the same plant: squeezing the leaves, and then suspending the material, he found the same thing. His real contribution lies in ruling out a vital force – he extended his investigation from alive plants, to those dead “not less than a century”, and then finally on to inorganic materials. All exhibited these small motions, which came to be known as Brownian motion.

It is not clear that Brown should really be attributed the discovery of Brownian motion: in 1784, Jan Ingen-Housz published a paper in *Journal de Physique* discussing the problem of evaporation of liquid droplets in microscopy, and his proposed solution of placing a glass coverslip over liquid droplets [2]. In it, he makes the following observation:

As long as the droplet lasts, the entire liquid and consequently everything that is kept within it is kept in motion by the evaporation [of the droplet], and this motion can give the impression that *some of the corpuscles are living, even if they have not the slightest life in them*. To see clearly how one can deceive one’s mind on this if one is not careful, one only has to place a drop of alcohol in the focal point of a microscope and introduce a little finely ground charcoal therein, and one will see these corpuscles in a *confused, continuous and violent motion*, as if they were animalcules which move rapidly around.

While Ingen-Housz did observe a type of Brownian motion in inanimate matter, he attributes this to flow of fluid. Brown ruled out this possibility by “reducing the drop of water containing the particles to microscopic minuteness, and prolonging its existence by immersing it in a transparent fluid of inferior specific gravity, with which it is not miscible, and in which evaporation is extremely slow”. Brown added small amounts of water to almond oil, managing to isolate individual active molecules within small droplets, ruling out the influence of other particles, and observed undiminished activity.

Brown was systematically studied these active particles for a large range of organic and inorganic materials, finding active molecules in all materials he studied, but he did not understand the mechanism for their motion, appearing to attribute it to the molecules themselves. It was not until 1877 that Joseph Delsaux attributed the motion to the discrete nature of the surrounding fluid [3], and then not until 1888 that Gouy demonstrated the first experimental proof, by eliminating as many confounding variables as possible, and finding that the activity of particles was smaller when the fluid viscosity was higher [4]. Gouy writes

I do not believe after careful observation that it can be doubted that this is due to accidental currents, vibrations, or temperature differences, but is instead down to a natural phenomenon, occurring at a constant temperature,

and due to the constitution of liquids. ... The Brownian motion thus shows us something that, while certainly not the exact movements of molecules, is something very close, and provides us with direct and visible proof about the accuracy of the current assumptions of the nature of heat. If we adopt these views, the phenomenon – whose study is far from complete – takes on first-rate importance in molecular physics.

Gouy would prove to be correct. In 1905, as part of his *annus mirabilis*, Einstein published his work on the theory of Brownian motion, connecting the movements of microscopic bodies to the molecular-kinetic theory of heat [5]. Einstein first showed that the molecular-kinetic theory of heat should give rise to an osmotic pressure for macroscopic particles, identical to that of smaller, solute molecules. In particular, for n suspended particles in a volume V^* , enclosed by a semi-permeable membrane, and forming part of a total volume V , the osmotic pressure Π is given by

$$\Pi = \frac{RT}{V^*} \frac{n}{N_A}, \quad (1.1)$$

where R is the molar gas constant, N_A is Avogadro's number and T is the temperature. This is just the ideal gas law, with the particles moving according to the equipartition theorem. Einstein then imposed a force K acting on the particles, exerted everywhere in the direction of the x -axis. The number of suspended particles per unit volume, ν , would be a function of x such that the free energy is minimal with respect to small displacements in the positions of the suspended particles δx :

$$\delta F = \delta E - T\delta S = 0. \quad (1.2)$$

The change in energy is given by

$$\delta E = - \int d^3x K \nu \delta x, \quad (1.3)$$

and the change in entropy by

$$\delta S = \int d^3x R \frac{\nu}{N_A} \frac{\partial \delta x}{\partial x} = - \frac{R}{N} \int d^3x \delta x \frac{\partial \nu}{\partial x}, \quad (1.4)$$

and so the condition of thermodynamic equilibrium is

$$-K\nu + \frac{RT}{N_A} \frac{\partial \nu}{\partial x}. \quad (1.5)$$

This condition could be allied to the steady-state diffusive flux condition, where the drift caused by the force K is balanced by diffusion. For spherical particles with a radius a there will be a drift flux of

$$\frac{K\nu}{6\pi\eta a} \quad (1.6)$$

particles through unit area perpendicular to the x -axis per unit time, where η is the viscosity of the fluid, and $6\pi\eta a$ is the Stokes drag on a sphere in viscous flow. The diffusive flux for a system with constant diffusion coefficient D is

$$-D\frac{\partial\nu}{\partial x} \quad (1.7)$$

particles through unit area perpendicular to the x -axis per unit time, and so the flux balance equation will read

$$\frac{K\nu}{6\pi\eta a} - D\frac{\partial\nu}{\partial x} = 0 \quad (1.8)$$

Eqs. (1.5) and (1.8) can be used to find the diffusion coefficient:

$$D = \frac{RT}{N_A} \frac{1}{6\pi\eta a}. \quad (1.9)$$

This is called the Einstein-Stokes relation, and tells us particles will diffuse slower when there is greater dissipation as they move in the system. Einstein goes on to show that the density of suspended particles will indeed follow a diffusion equation as a result of molecular collisions, and that the mean square displacement of suspended particles is a linear function of time! Interestingly, at that time, Einstein proposed the measurement of diffusion coefficients as an accurate measure of Avagadro's number, which was still not precisely known.

As one might imagine, this paper sent a shockwave through the world of statistical physics. There followed a flurry of experimental activity looking to verify Einstein's findings, and it is in an early note to experimentalists from Einstein in 1907 that we first see a discussion about the root mean square velocity [6], and the ghost of the modern treatment of stochastic processes. Einstein writes that

The molecular theory of heat allows the calculation of the mean value of the instantaneous velocity a particle possesses at the absolute temperature T , since the kinetic energy of the particle's center-of-gravity motion is independent of the size and nature of the particle and of the nature of its environment, e.g., of the liquid in which the particle is suspended; this kinetic energy is equal to that of a monoatomic gas molecule.

As such, by equipartition, Einstein noted that the root mean square velocity for particles of mass m was given by

$$\frac{m}{2}\langle v^2 \rangle = \frac{3}{2}k_B T. \quad (1.10)$$

For normal colloidal particles, this velocity is massive (Einstein calculates a speed of 8.6cm/sec for colloidal platinum particles observed by Svedberg) [6]. Einstein explains that this velocity is not seen in practice. In particular, if one knew nothing about the molecular theory of heat, the velocity will evolve according to

$$m \frac{\partial v}{\partial t} = -6\pi\eta a v, \quad (1.11)$$

where again, η is the viscosity of the surrounding fluid, and a is the particle radius. Thus the velocity imparted to the particle will quickly dissipate, with characteristic time $\tau_v = m/6\pi\eta a v$. However, the analysis must be modified to take into account the molecular theory of heat. As Einstein notes,

we must assume now as well that, due to friction, the particle loses almost all its initial motion during the very short time d . But we also must assume that during this time the particle receives new impulses by a process that is the reverse of internal friction, so that it retains a velocity that on the average equals $\sqrt{v^2}$. But since we must imagine that the direction and magnitude of these impulses are (almost) independent of the initial direction of motion and velocity of the particle, we must conclude that the velocity and direction of motion had changed drastically, and in a completely irregular manner, already in the extraordinarily short time τ_v .

In fact, this was also known to Smoluchowski, who published a paper independently of Einstein in 1906, on his treatment of Brownian motion in relation to the molecular theory of heat [7]. Smoluchowski started by arguing that Brownian motion was a result of infinitesimal collisions from random directions with the surrounding fluid molecules. Smoluchowski showed, by considering the effect of these collisions on the velocity, you could derive the mean square displacement, finding an expression similar to Einstein's that differed only by a numerical factor.

Einstein and Smoluchowski had changed the landscape of statistical physics, by moving the discussion away from measurements of Brownian motion trajectories, to measurements of stochastic displacements. It was this understanding that laws could only be described upon ensemble averaging that allowed mathematical progress to be made. The next real theoretical development came in 1908, with Langevin's paper "On

the theory of Brownian motion” [8]. Langevin wanted to unite Einstein’s result with Smoluchowski’s, and succeeded, but also stumbled across another way of deriving a diffusion coefficient directly. Crucially, he writes a full equation for the stochastic force balance:

$$m \frac{\partial^2 x}{\partial t^2} = -6\pi\eta a \frac{\partial x}{\partial t} + \xi. \quad (1.12)$$

This expression, known as the Langevin equation, is familiar to all physicists working in stochastic processes today, and underpins the field. On the mysterious force ξ , Langevin writes (from translation [9]):

About the complementary force ξ , we know that it is indifferently positive and negative and that its magnitude is such that it maintains the agitation of the particle, which the viscous resistance would stop without it.

Langevin multiplied his equation through by the particle position x ,

$$\begin{aligned} mx \frac{\partial^2 x}{\partial t^2} &= -6\pi\eta ax \frac{\partial x}{\partial t} + \xi x \\ \implies \frac{m}{2} \frac{\partial^2 x^2}{\partial t^2} - m \left(\frac{\partial x}{\partial t} \right)^2 &= -3\pi\eta a \frac{\partial x^2}{\partial t} + \xi x, \end{aligned} \quad (1.13)$$

where the chain rule has been applied to simplify the partial derivatives. Then, Langevin asks what happens if we consider a large number of particles. He asserts, by the irregularity of ξ , that the average value of the quantity ξx is zero, and by acknowledging that

$$m \left\langle \left(\frac{\partial x}{\partial t} \right)^2 \right\rangle = m \langle v^2 \rangle = k_B T \quad (1.14)$$

by equipartition, he recovers that

$$\frac{m}{2} \left\langle \frac{\partial^2 x^2}{\partial t^2} \right\rangle + 3\pi\eta a \left\langle \frac{\partial x^2}{\partial t} \right\rangle = k_B T, \quad (1.15)$$

and so the mean square displacement $\langle x^2 \rangle$ evolves according to the solution:

$$\frac{\partial \langle x^2 \rangle}{\partial t} = \frac{k_B T}{3\pi\eta a} + C e^{-t/\tau_v}, \quad (1.16)$$

where $\tau_v = m/6\pi\eta a$ is Einstein's velocity relaxation time. For times $t \gg \tau_v$, we get the diffusive relation

$$\langle (x(t) - x(0))^2 \rangle = \frac{k_B T}{3\pi\eta a} t = 2Dt \quad (1.17)$$

$$\implies D = \frac{k_B T}{6\pi\eta a}. \quad (1.18)$$

Thus, Langevin recovered the diffusion coefficient of Einstein. In doing so, he introduced the concept of the stochastic force ξ , and much of what has followed has been variations on this theme. By 1917, Ornstein had shown that the Langevin equation was consistent with statistical mechanics [10, 11]. It became accepted that a Gaussian white noise term was an appropriate approximation when the velocity relaxation time was very short compared to experimental timescales. How though, to deal with short times, with few collisions? One proposed solution was to re-write the Langevin equation, allowing the friction coefficient to have a memory kernel:

$$\dot{x}(t) = v(t) \quad (1.19)$$

$$m\dot{v}(t) = f(x) - \int_0^t \gamma(t-t')v(t')dt' + \xi(t), \quad (1.20)$$

with the problem then shifting to how best to model the dissipation kernel $\gamma(t-t')$. However, we now also have the problem of the random force. The reason for this is easiest seen conceptually: the source of dissipation is collisions with surrounding molecules, but these collisions are also the source of the fluctuating random force $\xi(t)$. Therefore, it is perhaps reasonable to expect some kind of relationship between the relaxation kernel and the random force. While I will not relate the development of this theory in detail (for this, see Kubo's excellent review [12], one of the first to notice this was Nyquist in 1928 [13], in the context of thermal agitation in conductors. The fluctuation-dissipation relation as we know it now relates the correlation function of the noise to the friction kernel via the equipartition theorem:

$$\langle \xi(t)\xi(t') \rangle = mk_B T \gamma(t-t'). \quad (1.21)$$

The fluctuation-dissipation relation theorem, and the generalised Langevin equation, are very useful when we want to find correlation functions. This maybe be in an experimental context: for example, the intermediate structure factor in spin-echo measurements [14, 15] is related to a velocity correlation function, and modelling this it is useful to appeal to the generalised Langevin equation [16]. However, in many applications,

we seek instead the probability distribution of an ensemble of systems, and its evolution in time.

1.2 The Fokker-Planck equation

The probability distribution and diffusion equation were first discussed in Einstein's original paper [5], but was developed in greater detail by Fokker [17], Planck [18] and Smoluchowski [19]. The derivation presented here is given by Wang and Uhlenbeck in their review [20], but I have chosen to reproduce it here, because it shows some interesting aspects of stochastic processes, and their physical relevance. One starts with what is called the evolution equation [or equivalently, the Chapman-Kolmogorov equation if one is interested in conditional probabilities respecting the initial condition, $W(x, t|x_0, t_0)$]:

$$W(x, t + \Delta t) = \int dy P(x, t + \Delta t|y, t)W(y, t). \quad (1.22)$$

We want to get to a differential equation, by taking the limit to small Δt , where we will expect that the difference $|x - y|$ will also be small. As such, we can expand in this difference $\Delta x = x - y$:

$$\begin{aligned} W(x, t + \Delta t) &= \int d(\Delta x) P(x, t + \Delta t|x - \Delta x, t)W(x - \Delta x, t) \\ &= \int d(\Delta x) P(x - \Delta x + \Delta x, t + \Delta t|x - \Delta x, t)W(x - \Delta x, t) \\ &= \int d(\Delta x) \sum_{n=0}^{\infty} \frac{(-\Delta x)^n}{n!} \frac{\partial^n}{\partial x^n} P(x + \Delta x, t + \Delta t|x, t)W(x, t) \\ &= W(x, t) + \int d(\Delta x) \sum_{n=1}^{\infty} \frac{(-\Delta x)^n}{n!} \frac{\partial^n}{\partial x^n} P(x + \Delta x, t + \Delta t|x, t)W(x, t). \end{aligned} \quad (1.23)$$

This is often called the Kramers-Moyal expansion. Taking the sum and differential operator outside of the integral, we can define the Kramers-Moyal coefficients of the stochastic process as the limit of the moments as $\Delta t \rightarrow 0$ (including the $n!$ term for neatness):

$$M^{(n)}(x) = \lim_{\Delta t \rightarrow 0} \frac{1}{\Delta t} \int d(\Delta x) \frac{(\Delta x)^n}{n!} P(x + \Delta x, t + \Delta t|x, t). \quad (1.24)$$

Now, we can write that

$$\begin{aligned} \frac{\partial W}{\partial t} &= \lim_{\Delta t \rightarrow 0} \frac{W(x, t + \Delta t) - W(x, t)}{\Delta t} = \sum_{n=1}^{\infty} (-1)^n \frac{\partial^n}{\partial x^n} (M^{(n)}(x)W(x, t)) \\ &= \mathcal{L}_{KM}W, \end{aligned} \quad (1.25)$$

where \mathcal{L}_{KM} is the Kramers-Moyal operator. This is the partial differential equation governing the probability density of the stochastic process $x(t)$, and also the propagator $P(x, t|x_0, t_0)$ (taking the initial condition to be $\delta(x - x_0)$). The beauty of this is that the quantities $M^{(n)}(x)$ can be calculated directly from the underlying Langevin equation(s). Let us examine this for a simple example of constant damping without a potential:

$$\dot{x} = v \quad (1.26)$$

$$m\dot{v} = -\gamma v + \xi(t), \quad (1.27)$$

where $\xi(t)$ is a usual Gaussian noise process, obeying the moments

$$\langle \xi(t) \rangle = 0 \quad (1.28)$$

$$\langle \xi(t_1)\xi(t_2) \rangle = 2k_B T \gamma \delta(t_1 - t_2). \quad (1.29)$$

The moments of the process are calculated by integrating the Langevin equation. For the velocity, we can write that

$$v(t + \Delta t) = v(t) - \frac{\gamma}{m} \int_t^{t+\Delta t} v(t') dt' + \frac{1}{m} \int_t^{t+\Delta t} \xi(t') dt'. \quad (1.30)$$

From this, it is fairly clear (using $\langle \xi \rangle = 0$) that the first moment of the velocity is given by

$$\langle v(t + \Delta t) - v(t) \rangle = -\frac{\gamma}{m} v \Delta t, \quad (1.31)$$

and so the first Kramers-Moyal coefficient in the velocity is given by

$$M^{(1)}(v) = \lim_{\Delta t \rightarrow 0} \langle v(t + \Delta t) - v(t) \rangle = -\frac{\gamma}{m} v. \quad (1.32)$$

The first moment in the position is given by

$$\langle x(t + \Delta t) - x(t) \rangle = a_1(x, \Delta t) = v \Delta t, \quad (1.33)$$

and so $M^{(1)}(x) = v$. The second moment of the particle position is also easy to write down:

$$\langle (x(\Delta t) - x(0))^2 \rangle = v^2 (\Delta t)^2. \quad (1.34)$$

Since only terms in the moments of linear order in Δt contribute to the Kramers-Moyal coefficients, $M^{(n)}(x) = 0$ for all values of $n \geq 2$. All that is left is to calculate the higher order Kramers-Moyal coefficients in the velocity.

The second moment in the velocity can be written as

$$\langle (v(t) - v(0))^2 \rangle = \left[\frac{\gamma}{m} \int_0^{\Delta t} v(t') dt' \right]^2 + \frac{1}{m^2} \int_0^{\Delta t} \int_0^{\Delta t} \langle \xi(t') \xi(t'') \rangle dt' dt'', \quad (1.35)$$

where we have used the property $\langle \xi(t') \rangle = 0$ to evaluate a cross-term integral as zero. It is clear that the first integral will contribute to the moment as $\mathcal{O}(\Delta t^2)$, and so we are left with

$$\langle (v(t) - v(0))^2 \rangle = \frac{\Gamma}{m^2} \int_0^{\Delta t} \int_0^{\Delta t} \delta(t' - t'') dt' dt'' = \frac{2k_B T \gamma}{m^2} \Delta t. \quad (1.36)$$

Therefore, the second Kramers-Moyal coefficient in the velocity is given by

$$M^{(2)}(v) = \frac{k_B T \gamma}{m^2}. \quad (1.37)$$

There are some arguments that simplify this process: first, all terms not arising from the stochastic force will contribute at higher than first order. Secondly, all odd moments vanish for the Gaussian stochastic force, so all odd Kramers-Moyal coefficients are zero. All that is left is to evaluate the higher order moments for the stochastic force, using Wick's relation for moments of a Gaussian:

$$\langle \xi(t_1) \xi(t_2) \dots \xi(t_{2n}) \rangle = \sum_{\text{permutations}} \langle \xi(t_1) \xi(t_2) \rangle \dots \langle \xi(t_{2n-1}) \xi(t_{2n}) \rangle. \quad (1.38)$$

As seen in Eq. (1.36), each correlation function contributes a factor of Δt , so the $2n^{\text{th}}$ moment is of the order $\mathcal{O}(\Delta t^n)$, and the Kramers-Moyal coefficient is zero. In fact, the Pawula theorem states that a Kramers-Moyal expansion must terminate at the first or second term, or not at all. If it terminates at the second term (as is the case with a Gaussian stochastic force), the resulting differential equation for the probability density $W(x, v, t)$ is the classical Fokker-Planck equation of a free Brownian particle:

$$\frac{\partial W}{\partial t} + \frac{\partial(vW)}{\partial x} = \frac{\gamma}{m} \frac{\partial}{\partial v} \left(vW + \frac{k_B T}{m} \frac{\partial W}{\partial v} \right). \quad (1.39)$$

1.3 Interpretation of stochastic integrals

The calculation above is simple if your noise is not coordinate-dependent. This is not always the case. Consider the Langevin equation

$$\dot{q} = F(q) + G(q)\xi(t), \quad (1.40)$$

where $\xi(t)$ is a normalised Gaussian white noise source, with zero mean and unit variance. This type of coordinate-dependent fluctuation is called multiplicative noise, and leads to a dilemma in the derivation of the Fokker-Planck equation. Following our simple Langevin equation, we can create an integral equation

$$q(\Delta t) = q(0) + \int_0^{\Delta t} F(q(t'))dt' + \int_0^{\Delta t} G(q(t'))\xi(t')dt'. \quad (1.41)$$

The problem is that the second term on the RHS is not an integral in the typical sense. The function $\xi(t)$ is neither continuous, nor differentiable, and so we have to define what we mean by integration. There are two common interpretations of stochastic processes in this way: one based on the Ito calculus, the other - on the Stratonovich assumption. To illustrate this, we will cover the derivation of the Fokker-Planck equation once more, carefully showing where the two interpretations differ. If we assume that Δt is small, then we can expand the continuous functions $F(q(t'))$ and $G(q(t'))$ at $t = 0$:

$$\begin{aligned} q(\Delta t) - q(0) = & \int_0^{\Delta t} (F(q(0)) + F'(q(0))(q(t') - q(0)) + \dots)dt' \\ & + \int_0^{\Delta t} \xi(t')(G(q(0)) + G'(q(0))(q(t') - q(0)) + \dots)dt' \end{aligned} \quad (1.42)$$

The point of this expansion is that you can iterate by substituting for $q(t') - q(0)$, recovering that

$$\begin{aligned} q(\Delta t) - q(0) = & F(q(0)) \int_0^{\Delta t} dt' \\ & + F'(q(0)) \int_0^{\Delta t} \int_0^{t'} [F(q(t'')) + G(q(t''))\xi(t'')]dt'' dt' \\ & + G(q(0)) \int_0^{\Delta t} \xi(t')dt' \\ & + G'(q(0)) \int_0^{\Delta t} \int_0^{t'} [F(q(t'')) + G(q(t''))\xi(t'')] \xi(t')dt'' dt' \\ & + \dots \end{aligned} \quad (1.43)$$

The higher order terms in the expansion are all irrelevant for calculation of Kramers-Moyal coefficients, because they contribute terms of $\mathcal{O}(\Delta t^2)$ or higher. We will show this once we have considered the terms above. It will be useful to define the function:

$$\omega(\tau) = \int_0^{\tau} \xi(t)dt, \quad (1.44)$$

which has the following properties: $\langle \omega(\tau) \rangle = 0$ and $\langle \omega(\tau_1)\omega(\tau_2) \rangle = \min[\tau_1, \tau_2]$. These properties are derived in Risken [21]. Using this notation we can rewrite our expansion

$$\begin{aligned}
q(\Delta t) - q(0) &= F(q(0))\Delta t + F'(q(0))F(q(0))\frac{\Delta t^2}{2} \\
&\quad + F'(q(0))G(q(0))\omega(\Delta t) \\
&\quad + G(q(0))\omega(\Delta t) + G'(q(0))F(q(0))\omega(\Delta t) \\
&\quad + G'(q(0))G(q(0))\int_0^{\Delta t}\omega(t')\xi(t')dt'.
\end{aligned} \tag{1.45}$$

Now, performing the average, using that $\langle \omega(\Delta t) \rangle = 0$ and dropping terms of $\mathcal{O}(\Delta t^2)$, we obtain

$$\langle q(\Delta t) - q(0) \rangle = F(q(0))\Delta t + G(q(0))G'(q(0))\left\langle \int_0^{\Delta t}\omega(t')\xi(t')dt' \right\rangle \tag{1.46}$$

It is the treatment of this stochastic integral that is different for the Ito and Stratonovich representations (and other versions of this analysis). In the Ito calculus, the integral is defined as a sum of small steps according to the scheme

$$\int_0^\tau \omega(t')\xi(t')dt' = \lim_{N \rightarrow \infty} \sum_i^{N-1} \omega(t_i)[\omega(t_{i+1}) - \omega(t_i)], \tag{1.47}$$

where $t_i = i\tau/N$. The expression $\omega(t_{i+1}) - \omega(t_i) = \xi(t_i)(t_{i+1} - t_i)$ is the part of the integrand associated with the noise term ξ , and the multiplying factor $\omega(t')$ is sampled at the beginning of each interval $\{t_i, t_{i+1}\}$. We can use the properties of $\omega(t)$ to simplify this expression:

$$\begin{aligned}
\left\langle \int_0^{\Delta t} \omega(t')\xi(t')dt' \right\rangle_I &= \lim_{N \rightarrow \infty} \sum_i^{N-1} (\langle \omega(t_i)\omega(t_{i+1}) \rangle - \langle \omega(t_i)\omega(t_i) \rangle) \\
&= \min[t_{i+1}, t_i] - \min[t_i, t_i] = 0
\end{aligned} \tag{1.48}$$

By contrast, the Stratonovich integral samples the function $\omega(t')$ in the middle of the interval $\{t_i, t_{i+1}\}$:

$$\int_0^\tau \omega(t')\xi(t')dt' = \lim_{N \rightarrow \infty} \sum_i^{N-1} \omega\left(\frac{t_i + t_{i+1}}{2}\right) [\omega(t_{i+1}) - \omega(t_i)]. \tag{1.49}$$

This leads to a different average value for the integral:

$$\begin{aligned}
\left\langle \int_0^{\Delta t} \omega(t') \xi(t') dt' \right\rangle_S &= \frac{1}{2} \lim_{N \rightarrow \infty} \sum_{i=0}^{N-1} (\langle \omega(t_{i+1}) \omega(t_{i+1}) \rangle + \langle \omega(t_i) \omega(t_{i+1}) \rangle \\
&\quad - \langle \omega(t_{i+1}) \omega(t_i) \rangle - \langle \omega(t_i) \omega(t_i) \rangle) \\
&= \frac{1}{2} \lim_{N \rightarrow \infty} \sum_{i=0}^{N-1} (t_{i+1} + t_i - t_i - t_i) = \frac{1}{2} \lim_{N \rightarrow \infty} \sum_{i=0}^{N-1} (t_{i+1} - t_i) \\
&= \frac{\Delta t}{2}
\end{aligned} \tag{1.50}$$

As such, the moments for the Ito and Stratonovich Fokker-Planck equations are different:

$$M_I^{(1)}(q) = \lim_{\Delta t \rightarrow 0} \frac{1}{\Delta t} \langle q(\Delta t) - q(0) \rangle_I = F(q) \tag{1.51}$$

$$M_S^{(1)}(q) = \lim_{\Delta t \rightarrow 0} \frac{1}{\Delta t} \langle q(\Delta t) - q(0) \rangle_S = F(q) + \frac{1}{2} G(q) G'(q). \tag{1.52}$$

The second moment is the same for the Ito and Stratonovich interpretations: $M^{(2)}(q) = \frac{1}{2} G^2(q)$, but this is a general feature in Fokker-Planck equations. Where a noise term appears in a variable's Langevin equation, then the first Kramers-Moyal coefficient will differ by a term due to the gradient of the noise field (for constant coefficient noise sources, there will be no difference between the Ito and Stratonovich Fokker-Planck equations). These equations can be generalised to multiple dimensions:

$$\dot{q}_\alpha = F_\alpha(\mathbf{q}(t)) + G_\alpha^i(\mathbf{q}(t)) \xi_i(t). \tag{1.53}$$

For multiple dimensions, the Fokker-Planck equation in the Stratonovich interpretation takes the form

$$\begin{aligned}
\frac{\partial P(\mathbf{q}, t)}{\partial t} &= \left\{ -\frac{\partial}{\partial q_\alpha} \left(F_\alpha(\mathbf{q}) + \frac{1}{2} G_\beta^i(\mathbf{q}) \frac{\partial G_\alpha^k(\mathbf{q})}{\partial q_\beta} \delta_{ik} \right) + \frac{1}{2} \frac{\partial^2}{\partial q_\alpha \partial q_\beta} G_\alpha^i(\mathbf{q}) G_\beta^k(\mathbf{q}) \delta_{ik} \right\} P(\mathbf{q}, t) \\
&= \mathcal{L}_{FP}^S(\mathbf{q}) P(\mathbf{q}, t),
\end{aligned} \tag{1.54}$$

while the Ito Fokker-Planck equation is

$$\begin{aligned}
\frac{\partial P(\mathbf{q}, t)}{\partial t} &= \left\{ -\frac{\partial}{\partial q_\alpha} F_\alpha(\mathbf{q}) + \frac{1}{2} \frac{\partial^2}{\partial q_\alpha \partial q_\beta} G_\alpha^i(\mathbf{q}) G_\beta^k(\mathbf{q}) \delta_{ik} \right\} P(\mathbf{q}, t) \\
&= \mathcal{L}_{FP}^I(\mathbf{q}) P(\mathbf{q}, t).
\end{aligned} \tag{1.55}$$

Physics has typically taken the Stratonovich interpretation as the Fokker-Planck equation. There are good practical reasons for doing this: the Stratonovich interpretation works if the stochastic process is the limiting case $\tau \rightarrow 0$ of coloured noise, $\langle \xi(t)\xi(t') \rangle = \exp[-|t - t'|/\tau]$. This is a good physical interpretation, as in reality, no collisions are instantaneous. In fact, the seminal Wong-Zakai theorem [22] shows that if the Wiener white-noise stochastic process $\xi(t)$ is the approximation of a sequence of n independent but continuous processes (which is certainly the case with Brownian motion, when each collision event is an act of momentum transfer, with fast subsequent decay), then the Langevin equation (1.40) is taking a different form:

$$\dot{q} = \left[F(q) + \frac{1}{2}G(q)\frac{\partial G(q)}{\partial q} \right] + G(q)\xi(t), \quad (1.56)$$

which leads to the Stratonovich form of the Fokker-Planck equation following the classical Itoh stochastic calculus. So the resolution of the ‘Itoh-Stratonovich dilemma’ is in the interpretation of the underlying physics, which leads to the Langevin stochastic differential equation. It is not a matter of choice. The Itoh calculus is the mathematically correct way of working with such equations. So, if the underlying physics is such that (1.40) with the true Wiener noise $\xi(t)$ is valid, then the Itoh Fokker-Planck equation (1.55) follows; this is thought to often be the case in financial statistics. But the Brownian motion, and many other thermal-fluctuation driven processes, follow the Wong-Zakai theorem and result in the modified Langevin equation (1.56), as long as there is a reason for multiplicative factor in the noise. Then the Stratonovich Fokker-Planck equation (1.54) follows.

In practical cases, it makes sense that we should try and test how good the Stratonovich interpretation is before we try and make predictions arising from it. At the end of this thesis, in Chapter 6, I propose a simple experimental test for the dynamics of microswimmers, using a spatially varying diffusion coefficient.

1.4 Overdamped dynamics

Let us write the dynamics of particles subject to thermal motion and an external potential in the notation of generalised coordinates:

$$\dot{\mathbf{x}} = \mathbf{v} \quad (1.57)$$

$$\dot{\mathbf{v}} = -\frac{1}{m}\nabla V(\mathbf{x}) - \frac{\gamma}{m}\mathbf{v} + \frac{1}{m}\sqrt{2k_B T\gamma}\boldsymbol{\xi}(t). \quad (1.58)$$

We can use the results above to produce a Fokker-Planck equation:

$$\frac{\partial f}{\partial t} + \nabla_{\mathbf{x}} \cdot (\mathbf{v}f) = \frac{1}{m} \nabla_{\mathbf{v}} \cdot ([\nabla V(\mathbf{x}) + \gamma \mathbf{v}] f) + \frac{k_B T \gamma}{m^2} \nabla_{\mathbf{v}}^2 f \quad (1.59)$$

However, at a cellular and molecular level, the velocity relaxation timescale m/γ is often very small compared to experimental timescales. We can see this by considering the Reynolds number, a dimensionless variable considering the balance of kinetic vs. dissipative forces:

$$\text{Re} = \frac{\text{K.E}}{f_{\text{res}} a} \propto \frac{\rho a^3 v^2}{\gamma v a} = \frac{\rho a v}{\eta}, \quad (1.60)$$

where a is the size of the particle, v is its characteristic velocity, and γ is the coefficient of dissipative friction, which for a sphere in viscous flow is given by $\gamma = 6\pi\eta a$. On a length scale of cells ($1 - 10 \mu\text{m}$), the speed must be $v \sim 0.1 - 1 \text{ m/s}$ to reach $Re = 1$. For all realistic speeds, at the cell (and even more so, on the subcellular level of proteins) the Reynolds number is vanishingly small, and no momentum transfer could be taking place.

In the case of low Reynolds flows, fluctuations in the velocity distribution decay away very fast, since the velocity relaxation time, m/γ , is very small compared to experimental timescales, and there is no observable ballistic part of the particle trajectories. In this case, it is possible to integrate out the fast variable of velocity, and reduce the Fokker-Planck to an equation purely in position x . We call this equation the Smoluchowski equation, as it was discussed by Smoluchowski in his 1916 paper [19].

It is possible to derive the Smoluchowski equation by assuming that the velocity is always in its equilibrium Maxwell distribution, and then averaging over this distribution in the limit of small velocity relaxation time. Such a derivation typically relies on an appropriate non-dimensionalisation of the Fokker-Planck equation, which is usually potential-dependent and therefore not easily applicable to more complex situations. Here, I consider an approach taken directly from the solution to the underlying stochastic differential equations. Starting with the full Langevin equation that includes the inertial effects:

$$\dot{v} = -\frac{1}{m} \nabla V(x) - \frac{\gamma}{m} v + \frac{1}{m} \sqrt{2k_B T \gamma} \xi(t) \quad (1.61)$$

We can write the formal solution to Eq. (1.61) as

$$v(t) = v(0)e^{-t/\tau_v} - \frac{1}{m} \int_0^t dt' \nabla V(x(t')) e^{-(t-t')/\tau_v} + \frac{\sqrt{2k_B T \gamma}}{m} \int_0^t dt' e^{-(t-t')/\tau_v} \xi(t'), \quad (1.62)$$

where $\tau_v = m/\gamma$ is the velocity relaxation time, as usual. This solution is deceptively simple, but riddled with hidden mathematical complications. The final term on the

right hand side is a stochastic integral, and since the function $\xi(t)$ is neither continuous, nor differentiable, its exact meaning is a little unclear (see the earlier discussion of Itoh-Stratonovich issues). Here, we need only that

$$\lim_{\tau_v \rightarrow 0} \left(\frac{1}{\tau_v} e^{-(t-t')/\tau_v} \right) = \delta(t-t'), \quad (1.63)$$

i.e. there is no memory in the velocity, and the instantaneous velocity of the particle has contributions only from the present moment. In this limit, we can write the velocity as

$$\begin{aligned} v(t) &= -\frac{1}{\gamma} \int_0^t dt' \nabla V(x(t')) \delta(t-t') + \sqrt{\frac{2k_B T}{\gamma}} \int_0^t dt' \xi(t') \delta(t-t') \\ &= -\frac{1}{\gamma} \nabla V(x) + \sqrt{\frac{2k_B T}{\gamma}} \xi(t). \end{aligned} \quad (1.64)$$

Then, we substitute this in (1.57) and obtain the stochastic differential equation for x :

$$\dot{x} = -\frac{1}{\gamma} \nabla V(x) + \sqrt{\frac{2k_B T}{\gamma}} \xi(t). \quad (1.65)$$

This is the familiar overdamped Langevin equation, and from this we can use the equation derived earlier to directly write down the equation for its probability density (with the velocity averaged out):

$$\frac{\partial w}{\partial t} = \frac{k_B T}{\gamma} \frac{\partial^2 w}{\partial x^2} - \frac{1}{\gamma} \frac{\partial}{\partial x} (-\nabla V(x) w(x, t)) = D \frac{\partial}{\partial x} \left(\frac{\nabla V(x)}{k_B T} w + \frac{\partial w(x, t)}{\partial x} \right) \quad (1.66)$$

We can see that is is valid in the limit $\tau_v \rightarrow 0$. The Smoluchowski equation is often written as

$$\frac{\partial w}{\partial t} = -\frac{\partial J}{\partial x}, \quad \text{with} \quad J = -D e^{-\beta V(x)} \frac{\partial}{\partial x} \left(e^{\beta V(x)} w(x, t) \right) \quad (1.67)$$

being the probability flux. Here, and throughout the thesis, $\beta = 1/k_B T$ is the inverse temperature.

1.5 Escape from metastable state: Kramers theory

We have now formed a theoretical framework for understanding thermally driven motion, either looking at the individual particles (Langevin equation), or the distribution of an ensemble of thermally driven particles (Fokker-Planck/Smoluchowski equation). Now, we use this formulation to describe the rate of escape from a metastable state, as illustrated in

Fig. 1.1. Here, we will look at the high-friction limit, where the dynamics is overdamped. Additionally, we consider only a high-temperature classical limit, where we can neglect quantum effects. Quantum mechanical treatment of the escape problem is a fascinating and beautiful topic, but outside the scope of this work.

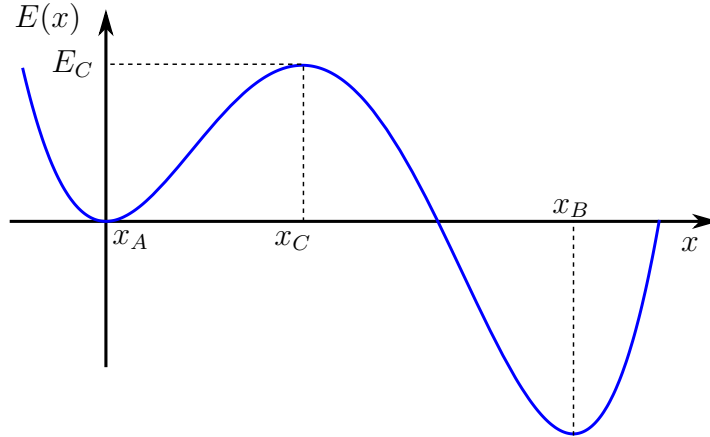


Fig. 1.1 A schematic showing two potential minima, state A and state B , separated by an energy barrier of size E_c , positioned at the state $x = x_c$. Kramers calculated the steady-state non-equilibrium rate of transition from state A to state B .

The seminal approach to the escape problem was described by Kramers in [23]. Also important in this context is the work of Brinkman [24], who added the analysis of detailed balance between the states in a two-well potential. On a basic level, consider the constant-flux idea in equilibrium, and we know the form of the flux:

$$J(x, t) = -D \frac{\partial P(x, t)}{\partial x} + \frac{f(x)}{\gamma} P(x, t) = -D e^{-\beta E(x)} \frac{\partial}{\partial x} \left[e^{\beta E(x)} P(x, t) \right]. \quad (1.68)$$

At constant J , we can integrate this, and use the fact that the potential energy in the state B is large and negative (so $e^{\beta E(B)} \rightarrow 0$):

$$\int_A^B J e^{\beta E(s)} ds = -D \left[e^{\beta E(x)} P(x) \right]_A^B = D e^{\beta E(A)} P(A). \quad (1.69)$$

I.e. the particles are absorbed at the boundary B . Then, we may write the (constant) flux over the barrier as

$$J = \frac{D e^{\beta E(A)} P(A)}{\int_A^B e^{\beta E(s)} ds}. \quad (1.70)$$

The denominator will be dominated by the largest values of the energy, at the barrier top C . To demonstrate this, and make use of approximation, we can expand the energy around the barrier: $E(x) \approx E_C - \frac{1}{2} \omega_C (x - x_C)^2$, with ω_C the curvature around the barrier

top, and make the approximation that the barrier height E_C is much greater than the thermal energy $k_B T$. In this limit, we may write that

$$\int_A^B e^{\beta E(s)} ds = \int_{-\infty}^{\infty} e^{\beta[E_C - \omega_C(x-x_0)^2/2]} = \sqrt{\frac{2\pi k_B T}{\omega_C}} e^{\beta E_C} \quad (1.71)$$

The rate constant $k = J/N_A$, where N_A is the number of particles in well A :

$$N_A \approx \int_{\text{near } A} ds P(A) e^{-\beta \omega_A(x-x_0)^2/2} = P(A) \sqrt{\frac{2\pi k_B T}{\omega_A}} e^{-\beta E_A} \quad (1.72)$$

where ω_A is the curvature of the potential energy around the metastable minimum. Now we can write the rate constant k as

$$k = \frac{J}{N_A} = \frac{\sqrt{\omega_A \omega_C}}{2\pi\gamma} e^{-\beta \Delta E}, \quad (1.73)$$

where $\Delta E = E_C - E_A$ is the height of the barrier separating the two wells. Depending on the precise geometry of the confining potentials, the rate constant pre-factor may be modified (for instance, the quadratic expansion of energy would not be valid for a cusp-shaped potential), but there always is this common suppression of the rate due to the height of the energy barrier (c.f. the Arrhenius law of thermal activation in chemical reactions). Such rates are important in problems of protein folding and unfolding, and often measured single-molecule atomic force microscopy. This is a useful approach when the energy barriers are large. If we wish to be more accurate with our calculation of reaction rate constants, especially when the $\beta \Delta E \gg 1$ limit is not strong, we must turn to more sophisticated machinery; with many situations are described very well by Gardiner [25].

1.6 Mean first passage time

Suppose we have a region of space that is bounded by walls. Some of these walls, the surface Ω , allow confined particles to exit the region, and some of them reflect particles back into the confined region. A sensible question to ask might be: how long does it take particles to exit our region of space? In the case of particles subject to thermal motion, this question only makes sense statistically: what is the probability that a particle starting at a position x' at $t = 0$ exits the region at some later time t ? We can

certainly find out what the probability is that the particle still remains in the region is:

$$Q(t) = \int_V dx P(x, t|x', 0). \quad (1.74)$$

The transition probability $P(x, t|x', t')$ is found by solving the underlying Fokker-Planck equation, subject to some specific boundary conditions: where the boundary is hard, a zero flux boundary condition is implemented $(\partial P/\partial \mathbf{n}) = 0$ for the vector normal to the reflecting surface, \mathbf{n} . For any boundary where the particle may escape, we must implement the absorbing boundary condition $P(x, t|x', t')_{\Omega} = 0$.

It is interesting to spend a moment understanding the physical meaning of the absorbing boundary condition. What it means is that any particle that reaches the boundary is no longer considered part of the probability distribution. One of the consequences is that the probability density is no longer normalised: the total ‘number of particles’ is depleting, and at $t \rightarrow \infty$ we may expect none to remain in the box. The transition probability $P(x, t|x', t')$ can be interpreted a sum over weighted paths. When we calculate the survival probability $Q(t)$ for particles that have not exited our confined region, we must sum over those paths that have not exited the region at any earlier time. At any time t , we can write that the Chapman-Kolmogorov equation for the probability of being at a point x within the region as

$$P(x, t|x', 0) = \int_V P(x, t|x'', t'')P(x'', t''|x', 0) dx'' + \int P(x, t|\Omega, t'')P(\Omega, t''|x', 0) d\Omega, \quad (1.75)$$

where the second integral (when adequately normalised) is over the paths that have touched the absorbing surface Ω . Observing the absorbing boundary condition means the second integral is strictly zero (or appropriately modified in the cases when the type of the ‘exit condition’ is not a simple unconditional exit, e.g. [26]).

Suppose we have the survival probability $Q(t)$, defined in (1.74). This is a monotonically decreasing function from one (at $t = 0$) to zero (at $t \rightarrow \infty$). What is the probability that a particle starting at x' will leave the region V between the times t and $t + \delta t$? The difference $Q(t) - Q(t + dt)$ is essentially the probability of particles to have escaped in this interval of time, which we can write as $f(t)dt$ defining the probability distribution of escape times:

$$f(t|x', 0) = -\frac{\partial Q(t|x', 0)}{\partial t}. \quad (1.76)$$

Then the average time of particles to escape, or the Mean First Passage Time, is simply

$$\langle t(x') \rangle = \int_0^{\infty} t f(t|x', 0) dt = \int_0^{\infty} Q(t|x', 0) dt = \int_0^{\infty} \int_V P(x, t|x', 0) dx dt, \quad (1.77)$$

where the second relation obtained via integration by parts. Naturally, the MFPT remains a function of the initial position x' .

We now wish to derive a differential equation that would allow finding the MFPT $\langle t(x') \rangle$, in a 1D diffusion process along the axis x . It is immediately clear that, to achieve this, we need differential operators that act on x' , that is, on the initial position of the stochastic process determined by $P(x, t|x', 0)$. If we write the Chapman-Kolmogorov equation, and take the time derivative, then:

$$\begin{aligned} P(x, \dot{t}|x', 0) &= \int \dot{P}(x, t|x'', t'') P(x'', t''|x', 0) dx'' \\ &= \int \mathcal{L}(x) P(x, t|x'', t'') P(x'', t''|x', 0) dx'' \end{aligned} \quad (1.78)$$

where $\mathcal{L}(x)$ is the Fokker-Planck (or Smoluchowski) operator

$$\mathcal{L}(x) = D \frac{\partial}{\partial x} \left[e^{-\beta V(x)} \frac{\partial}{\partial x} e^{\beta V(x)} \right]. \quad (1.79)$$

If, on the other hand, we take the time-derivative over the time t'' , the left-hand side will be zero (as it does not depend on this time). On the other hand, t'' appears twice under the Chapman-Kolmogorov integral:

$$\begin{aligned} 0 &= \int \frac{\partial}{\partial t''} P(x, t|x'', t'') P(x'', t''|x', 0) dx'' + \int P(x, t|x'', t'') \frac{\partial}{\partial t''} P(x'', t''|x', 0) dx'' \\ &= \int \left[\frac{\partial}{\partial t''} P(x, t|x'', t'') P(x'', t''|x', 0) + P(x, t|x'', t'') \mathcal{L}(x'') P(x'', t''|x', 0) \right] dx''. \end{aligned} \quad (1.80)$$

By renaming the variables and integrating by parts, one defines the so-called ‘backward’ or adjoint Fokker-Planck operator:

$$\begin{aligned} 0 &= \int \left[\frac{\partial}{\partial t''} P(x, t|x'', t'') P(x'', t''|x', 0) - \mathcal{L}^\dagger(x'') P(x, t|x'', t'') P(x'', t''|x', 0) \right] dx'' \\ &= \int \left[\frac{\partial}{\partial t''} P(x, t|x'', t'') + \mathcal{L}^\dagger(x'') P(x, t|x'', t'') \right] P(x'', t''|x', 0) dx'', \end{aligned} \quad (1.81)$$

where

$$\mathcal{L}^\dagger(x) = D \frac{\partial}{\partial x} \left[e^{\beta V(x)} \frac{\partial}{\partial x} e^{-\beta V(x)} \right] = D \left(-\frac{\nabla V(x)}{k_B T} \frac{\partial}{\partial x} + \frac{\partial^2}{\partial x^2} \right). \quad (1.82)$$

The backward Fokker-Planck equation can then be written down:

$$\frac{\partial P(x, t|x', t')}{\partial t'} = -\mathcal{L}^\dagger(x') P(x, t|x', t'). \quad (1.83)$$

The details of this derivation, and the discussion of the adjoint Fokker-Planck operator are found in textbooks [27, 28, 25]. Now we have the ability to derive the equation for MFPT. Start with applying the adjoint operator:

$$\begin{aligned}\mathcal{L}^\dagger(x')\langle t(x')\rangle &= \int_0^\infty \int_V \mathcal{L}^\dagger(x')P(x, t|x', t') dx dt = - \int_0^\infty \int_V \frac{\partial}{\partial t'} P(x, t|x', t') dx dt \\ &= \int_0^\infty \int_V \frac{\partial}{\partial t} P(x, t-t'|x', 0) dx dt = \int_0^\infty dt \frac{\partial}{\partial t} \int_V P(x, t|x', 0) dx \\ &= \int_0^\infty dt \frac{\partial}{\partial t} Q(t) = - \int_0^\infty f(t|x', 0) dt = -1\end{aligned}\quad (1.84)$$

This finally gives

$$D \frac{\partial}{\partial x} \left[e^{\beta V(x)} \frac{\partial}{\partial x} \left(e^{-\beta V(x)} \langle t(x') \rangle \right) \right] = -1. \quad (1.85)$$

Integrating this equation twice gives the solution that respects the required boundary conditions:

$$\langle t(x') \rangle = \frac{1}{D} \int_{x'}^L e^{\beta V(x)} \left(\int_B^x e^{-\beta V(y)} dy \right), \quad (1.86)$$

where the upper limit L is the position of the absorbing boundary, where $P(x=L)=0$, and the lower limit B is the position of any reflecting boundary which confines the away-motion of the particle along x (in many cases, in a confining potential $V(x)$, that limit is $B=-\infty$). Of course, the initial position x' remains the argument of MFPT.

The utility of the mean first passage time could be shown if we approximate the survival probability as a generic decaying function: $Q(t|x', 0) \approx e^{-t/T(x')}$. The assumption has to be that the probability of reacting (or ‘escaping’ at the absorbing point) is time-independent, with some rate constant k :

$$Q(t + \Delta t|x', 0) = (1 - k\Delta t)Q(t|x', 0) \quad (1.87)$$

Then, we can write this as

$$\frac{\partial Q}{\partial t} = -kQ, \quad (1.88)$$

and so the survival probability is indeed an exponential, and importantly, the rate constant k is the reciprocal of the mean first passage time $T(x')$:

$$T(x') = \int_0^\infty dt Q(t|x', 0) = \int_0^\infty dt e^{-kt} = \frac{1}{k}, \quad (1.89)$$

This is not true for all Markov processes, especially at short times: then we must care about the details of the process. A good example is that of transitions between two states in a finite state Markov chain such as a chemical reaction. Starting with the

chemical kinetic equations of transition $[1] \rightarrow [2] \rightarrow [3]$:

$$\frac{\partial N_1}{\partial t} = -k_1 N_1(t) \quad (1.90)$$

$$\frac{\partial N_2}{\partial t} = k_1 N_1(t) - k_2 N_2(t) \quad (1.91)$$

$$\frac{\partial N_3}{\partial t} = k_2 N_2(t) \quad (1.92)$$

This can be solved explicitly, but we are not too interested in this at the moment. Instead, we can write the short-time decay from the first state as $N_1(t) = 1 - k_1 t$. Then, the next equations become, consecutively:

$$\frac{\partial N_2}{\partial t} = k_1 t \implies N_2(\Delta t) = \frac{1}{2} k_1 t^2 \quad (1.93)$$

$$\frac{\partial N_3}{\partial t} = k_2 \times \frac{1}{2} k_1 t^2 \implies N_3(t) = \frac{1}{6} k_1 k_2 t^3 \quad (1.94)$$

This kind of simple power law expands to more complicated reaction networks too, not just those in a line. It is possible to show that the first passage density f_{ij} between from a state i to a state j in a reaction network (this need not be linear) is given by

$$f_{ij}(t) = \left(\frac{k_{iq_1} k_{q_1 q_2} \dots k_{q_m j}}{u_{ij}} \right) \frac{t^m}{m!}, \quad (1.95)$$

where $m + 1$ is the length of the minimum connector between the two states, $i \rightarrow q_1 \rightarrow q_2 \rightarrow \dots \rightarrow q_m \rightarrow j$. The factor u_{ij} is the probability of absorption in state j (this is 1 if j is the only absorbing state, but can be less than one if there are multiple states) [29]. These power-law kinetics at short times then give some information about the underlying structure of the reaction network. The long time dynamics of this reaction from i to j are dominated by the smallest rate constant k_{\min} the system must pass through – this is a bottleneck. At long times the survival probability is again exponential:

$$Q(t) \propto e^{-k_{\min} t}. \quad (1.96)$$

To calculate the mean first passage time is not an easy task (if it was, Kramers would have done it), and we must often resort to approximations of the effective potential, using the generic solution (1.86), as in various studies used to refine the Kramers method [26, 30], or in problems of diffusion in periodic potential [31, 32], or in the specific geometry of the escape window (the narrow escape problem [33, 34]).

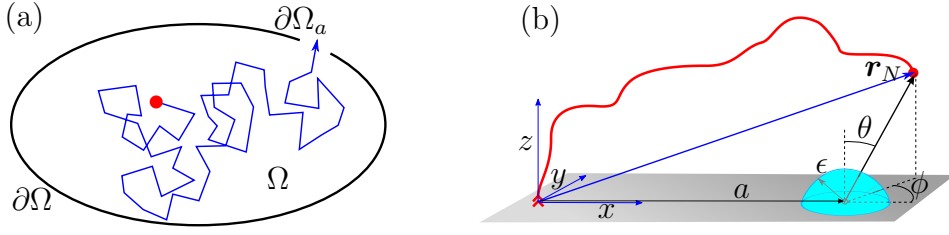


Fig. 1.2 Two narrow escape problems. In (a), a Brownian particle is confined within a domain Ω , with reflecting boundaries $\partial\Omega$. There is a small absorbing window in this boundary, $\partial\Omega_a$, through which the particle can escape. The narrow escape problem seeks to find the time at which the particle first exits the region Ω [33]. In b), a ligand has a soft restraint due to a surface tether, and must hit a small receptor of size ϵ some distance a from the tethering point. This process has an entropic barrier associated with stretching the chain [35].

Narrow escape problems

One problem of first passage times is a generic problem of the escape of a Brownian region from a confining region Ω through a small hole $\partial\Omega_a$ in its boundary $\partial\Omega$ (see Fig. 1.2). This amounts to solving the Smoluchowski equation

$$\frac{\partial p(\mathbf{x}, t)}{\partial t} = -\frac{1}{\gamma} \nabla \cdot (p(\mathbf{x}, t) \mathbf{f}(\mathbf{x})) D \nabla^2 p(\mathbf{x}, t) = \mathcal{L} p(\mathbf{x}, t), \quad (1.97)$$

with mixed Dirichlet-Neumann boundary conditions:

$$p(\mathbf{x}, t) = 0, \text{ for } \mathbf{x} \in \partial\Omega_a \quad (1.98)$$

$$D \frac{\partial p(\mathbf{x}, t)}{\partial \mathbf{n}} - \frac{p(\mathbf{x}, t)}{\gamma} \mathbf{f}(\mathbf{x}) \cdot \mathbf{n}(\mathbf{x}) = 0, \text{ for } \mathbf{x} \in \partial\Omega, \quad (1.99)$$

where \mathbf{n} is the normal to the surface, and \mathcal{L} is the Fokker-Planck operator for the Smoluchowski equation. The escape time can be estimated asymptotically in powers of the small parameter

$$\epsilon = \frac{|\partial\Omega_a|}{|\partial\Omega|} \ll 1. \quad (1.100)$$

The probability density can be written as an eigenfunction expansion:

$$p(\mathbf{x}, t | \mathbf{y}, 0) = \sum_{i=0}^{\infty} a_i \psi_{i,\epsilon}(\mathbf{x}) \psi_{i,\epsilon}(\mathbf{y}) e^{-\lambda_i(\epsilon)t}, \quad (1.101)$$

where $\psi_{i,\epsilon}(\mathbf{x})$ are the eigenfunctions corresponding to eigenvalues $\lambda_i(\epsilon)$ of the Fokker-Planck operator in Eq. (1.97), and \mathbf{y} is the initial position.

Since the eigenvalues $\lambda_i(\epsilon)$ are positive and increasing with the eigenmode index i , so for times longer than $t \gg 1/\lambda_1(\epsilon)$ the probability distribution is dominated by the ‘ground state’ (for the big volume of work on ‘ground state dominance’ in polymer physics, see [36, 37]):

$$p(\mathbf{x}, t) \approx \alpha_0 \psi_{0,\epsilon}(\mathbf{x}) \psi_{0,\epsilon}(\mathbf{y}) e^{-\lambda_0(\epsilon)t}. \quad (1.102)$$

Then, the survival probability

$$Q(t) = \int d\mathbf{x} p(\mathbf{x}, t) \approx e^{-\lambda_0(\epsilon)t}, \text{ for } t \gg \frac{1}{\lambda_1(\epsilon)}, \quad (1.103)$$

from which it is clear that the mean first passage time $T = 1/\lambda_0(\epsilon)$. Solving for this eigenvalue depends on the dimensionality d of the problem, and the geometry of the confining volume. When the boundary of the domain is regular, the MFPT takes the form of

$$T \approx \begin{cases} \frac{L^2}{\pi D} \ln \frac{1}{\epsilon} + \mathcal{O}(1) & \text{for } d = 2 \\ \frac{L^3}{4aD} = \frac{L^2}{4\epsilon D} & \text{for } d = 3. \end{cases} \quad (1.104)$$

Here, L represents the characteristic size of the confining volume of the domain, D is the free space diffusion coefficient, and $a = \epsilon L$ is the characteristic size of the absorbing window. These results highlight the mathematical complexity of narrow escape problems, such that only asymptotic results are possible, even for free diffusion. In this thesis, I approximate the mean hitting time of the end of a tethered polymer chain to a surface receptor. With no hard confining boundaries (only the soft quadratic free energy of the Gaussian chain), and a potential to move in, this problem is far more mathematically challenging to tackle using the narrow escape approach, and so instead I develop new mean field ideas to make progress.

UNFOLDING OF POLYMERS UNDER CONSTANT FORCE

The start of the study into escape from metastable states was with a simple problem of unfolding polymers under constant force.

Self-assembly and controlled unfolding of biological macromolecules is a fundamental process in cell biology, and is crucial to life itself. It has proven to be a rich area of research, and while there has been much progress and understanding achieved, there is still much left to discover. Part of the reason for this is the unique set of interactions for each protein sequence, and the resulting complexity of the phase space, as well as the many mechanisms for denaturation, including temperature, pH, force and enzymatic action.

The response of biomolecules to mechanical forces has been a popular area of study within biophysics [38]. The sensitivity of experimental tools like optical tweezers and atomic force microscopy (AFM), and their ability to work in a ‘wet’ environment, have made them ideal for probing biology with mechanical forces at a molecular level. They have been used extensively to characterise the unfolding kinetics of a range of biomolecules [39, 40]. As well as working with DNA, many experiments have focused on compact globular protein structures, such as the Ig domain, an important subdomain of several proteins, including titin [41–43].

AFM experiments can be performed in the position-clamp mode, where the force is measured by the cantilever [42], or in the force-clamp mode, where a constant force is applied and the resulting extension measured. In force-clamp experiments, biomolecules typically show all-or-nothing transitions between folded and unfolded states [44, 45], meaning that denaturation occurs abruptly and completely once a critical force is reached in the case of force-ramp, or a characteristic time is reached if a constant force is applied.

Theoreticians working to interpret AFM pulling experiments have originally focused on the position-clamp mode. Many papers have shown that using models of semi-flexible

polymer chains accounts well for the shape of force-extension curves [46–49]. Applying a force (or impose deformation) to a polymer globule is a different problem. Halperin and Zhulina first demonstrated that globular homopolymers being extended in this way will undergo a first order phase transition from a weakly extended globular state to an extended state [50]. Later, simple models were able to account for internal properties of the globule: either the bending rigidity or specific bonding between its units (replicating the protein morphology) [51]. There has been previous theoretical work on the force-clamp mode for poor solvents [52, 53]. Polotsky et al. used self-consistent field modelling and verified an ‘all-or-nothing’ transition in this regime. However, although their numerical results extend across a wide range of parameters, the analytical work presented in these papers only remains valid in the vicinity of the Θ -point, i.e. for weakly confined polymer globules. Our main interest here is to understand the ‘strongly confined’ globules such as folded proteins, or just chains precipitated in poor solvent.

A lot of the work in protein dynamics focus around energy landscapes [54], which are useful for computation using dynamics simulations. In practice, it would be impossible to accurately determine a complete energy landscape through single-molecule experiments; efforts to determine landscapes have thus far focussed on how the landscape varies over the extension of the molecule. One approach, employed by Szabo et al., is only interested in the potential well the native state resides in, and calculates the rate constant for biomolecules’ extension using classical Kramers’ theory [55, 56]. This says nothing about the final state energy, which will change with applied force and the quality of solvent, and will only be appropriate when refolding can be neglected. However, it does offer easy calculation and is useful under generalisation to several unfolding paths [57].

These models exist to determine key features of the energy landscape from experimental data, but they do not seek to predict the behaviour of a polymer under mechanical loading. A perfect starting point in this problem is the theory of a self-attracting semiflexible homopolymer. Although the lack of specific interactions that are present in proteins means that the native state will not be as stable as for heteropolymer proteins, as we move away from the ground state, we can merely average over the heterogeneity introduced by a protein’s primary structure, and approach a homopolymer. In the limit of large deformations, when the polymers are highly stretched and self interactions are minimal, one would expect the two models to behave almost identically.

There have been several computational studies of the self-attracting homopolymer on 2 and 3 dimensional lattices, with the 2-dimensional case showing different phase transition behaviour than for the 3-dimensional case [58, 59]. These are able to account

for topology of the globule as well, and offer an insight into the ruggedness of energy landscapes.

The first part of this chapter aims to construct an energy landscape for a collapsed homopolymer in poor solvent using a Flory mean-field theory. Taking cues from the theoretical work on the position-clamp mode [50], I allow the polymer to have a globular section and an extended section. In the first section, I calculate the Gibbs free energy for a compact globule in poor solvent, accounting for the monomer-solvent interactions at the globule's surface. In the next section, I do the same for an extended chain, accounting for the entropy of stretching. Then, I consider these energies together, and analyse the phase behaviour of the polymer under tension. I show the existence of an 'all-or-nothing' transition, and calculate the transition force. I also calculate the energy barriers separating the globule state from the extended state.

Having treated the equilibrium behaviour of globular polymers under tension, I then move on to study kinetic aspects of polymer unfolding. Initially, the kinetics of transitions were studied using a two-state system, with a potential barrier modified by the introduction of force [60]. When the final state is much lower in energy than the initial state, such a reaction is essentially irreversible, and the survival probability of the initial state decays exponentially with time. This is the regime of the original Kramers problem of escape over the barrier [23].

Recent analysis of ubiquitin unfolding data from single-molecule pulling experiments has found this simple model fails at describing the experimental data [61, 62]. Strongly non-exponential kinetics have been also found in other biological systems, such as ligand binding in myoglobin, and are usually attributed to random variations in molecule conformations [61]. These ensemble variations may have an additional time-dependence. As such, some early work thought of the protein free energy landscape as a collection of native globular states (of similar but not identical energies) and extended unfolded states, separated by a single energy barrier, in a globally connected energy landscape [63, 64]. This idea of heterogeneity can also be modeled using disorder theory [65]. The variation of unfolding rate in the ensemble of molecules can be described by introducing a stochastic internal parameter, which could follow a chosen pattern of static or dynamic disorder.

When the rate of change of internal parameter is much slower than the unfolding rate, we can regard it as fixed for each molecule, and consider the regime of static, or quenched, disorder. In this limit, Kuo et al. [66] introduced a Gaussian variation in the barrier height to be surmounted by individual molecules. However, Lannon et al. [62] subsequently found this model to be a poorer fit to the data than a stretched exponential distribution.

When the internal parameter can no longer be regarded as fixed on the time-scale of unfolding, one enters the regime of dynamical disorder [65]. Recent work by Hyeon et al. [67] have looked at the role of dynamical disorder in the unfolding kinetics of macromolecules, and other work has had some success at fitting ubiquitin unfolding data using a generalised Langevin equation with fractional Gaussian noise [68]. These approaches are still relatively new, and have yet to be fleshed into a physical model where parameters are obtained from physical quantities.

In the second part of this chapter I take inspiration from earlier work by Geissler and Shakhnovich [69]. They studied the mechanical response of random copolymers in equilibrium (a problem in static disorder). In attempting to adapt their analysis to look at the unfolding kinetics, I found that a much simpler model is already showing non-exponential kinetic features. Even the introduction of only a single inhomogeneous residue into an otherwise homogeneous polymer chain can lead to a significant change in the unfolding kinetics. Although the position of this residue could be fully prescribed by the sequence, its exposure to solvent has to be treated as a random variable. This variable affects the unfolding rate constant, making the ensemble-average phenomena highly non-exponential. This could provide a crude but effective model for hydrophobic cores of biomolecules.

2.1 Polymer model

We consider a model polymer consisting of a single type of hydrophobic monomer, with just one additional ‘core’ monomer, which we take to be much harder to remove from the bulk of a polymer globule than all the others. This could be a toy model for the hydrophobic core of a protein, or a particular sequence of residues that binds to its matching counterpart stronger than others. We shall assume that the position M of this particular monomer in the polymer sequence ($1 \dots N$) is known, and remains fixed. The reason why we only consider one such ‘locked’ monomer, and not several (as would be the case in a real folded protein), is simply because the qualitative features emerging due to the presence of such an internal ‘lock’ are clear already in the singlet case – while the calculations are kept simpler and transparent.

Given poor solvent conditions, we expect that the unstretched polymer is folded in equilibrium, and will form a compact globule. Following earlier works, we model the free energy of the globule as the sum of favourable monomer-monomer pair interactions in the bulk, and unfavourable monomer-solvent interactions at the surface. To minimise the free energy, the core monomer will always be buried deep within the bulk of the globule,

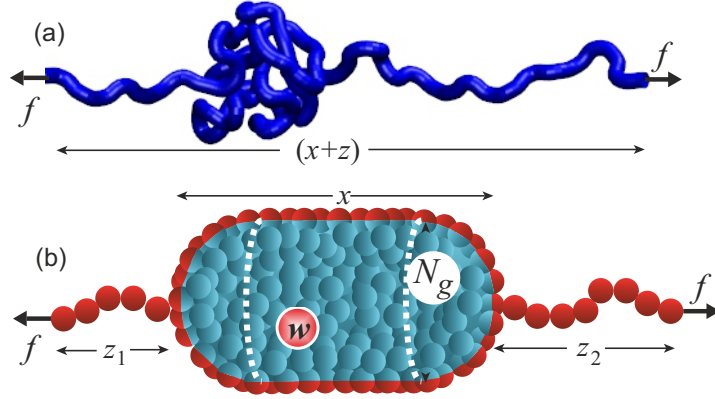


Fig. 2.1 Spherocylinder model of the globular polymer in poor solvent, being stretched by an application of force f to its two ends. (a) A tube representation of a chain in Brownian dynamics simulation; (b) a scheme illustrating the force-induced asymmetry of the remaining globule with N_g monomers, one of which has a stronger binding energy in the globule, $-(u + w)$. Chain can be removed from both ends when the polymer is unravelling.

and provide no contribution to the surface energy. The free energy of the globule can be written as a function of the number of monomers in the globule N_g , the force-induced extension of the globule x , the bulk energy of the monomers, $-u$, and the additional binding energy of the ‘lock’ monomer w , such that the total energy of this residue in the bulk of the globule is $-(u + w)$. This gives the free energy of the globule:

$$F_g(N_g, x) = -N_g u - w + \frac{A(x)u}{b^2} \frac{1}{2} = -N_g u - w + \left(\frac{2N_g b}{3x} + \sqrt{\frac{\pi N_g x}{b}} \right) u, \quad (2.1)$$

where $A(x)$ is the surface area of the deformed globule, and b is the monomer size. Following an earlier work [70], for efficient analytical treatment we take the shape of the globule to be a spherocylinder (see Fig. 2.1), with a constant volume $N_g b^3$. In Eq. (2.1) we assume that any monomers on the surface are half-solvated, with the binding energy $-u/2$, and that a completely solvated monomer in the exposed chain segments has the potential energy level of zero. The term $-w$ may or may not be present in F_g , depending on whether the w -monomer is still inside, or has been removed from the globule into the stretched-out segments.

The surface energy $A(x)$ has an inflection point, which indicates an instability in the globule past certain extensions (see [70] for a detailed discussion). In the force-clamp regime, this manifests in the globule’s inability to supply restoring forces beyond a certain critical value of its extension, x_{crit} . For a given applied force f , the minimum size of the

globule to provide an equal and opposite restoring force is given by:

$$N_g(\text{stab}) = N - N_s = \frac{2}{3\pi^2} \left(\frac{16fb}{3u} \right)^3, \quad (2.2)$$

Globules below this size cannot sustain the applied force in equilibrium. For compactness of later expressions, we define the amount of chain that must be removed to reach this threshold of stability, N_s . We posit that once a globule has been reduced below its smallest stable size, it will rapidly unfold and extend to a chain state, with little regard for features of the globule. This issue will become important later, when we start calculating the rate at which a globule transforms into an extended chain.

Since we have chosen to measure the potential energy of fully solvated monomers as zero (in the poor solvent, this leads to the negative potential energy of monomers inside the globule, Eq. (2.1)), the remaining free energy of the expanded chain with contour length $L = b(N - N_g)$ is entirely dependent on the chain's properties. A general form for this free energy in terms of the chain's end-to-end extension, z , was derived by Blundell [49], and here we reduce the full expression to the flexible chain limit, where the persistence length l_p is small – of the order of the monomer size, $l_p \approx b \ll L$:

$$F_{ch}(z) = \frac{2k_B T L}{\pi b (1 - (z/L)^2)} - \frac{2k_B T L}{\pi b}. \quad (2.3)$$

The constant term is added to fix the energy of the chain at zero extension: $F_{ch}(0) = 0$. This expression is valid across the different regimes of stretching as the chain is being pulled. For small deformations, Eq. (2.3) reduces to the entropic spring expression, $F_{ch}(z) \approx (2k_B T / \pi L b) z^2$. In the limit of large stretching, $z \rightarrow L$, the expression shows the well-discussed divergence for an inextensible chain, known as the Marko-Siggia or Fixman-Kovacs limit [46, 47].

In the force-clamp mode of a typical AFM stretching experiment, we need to work with the Gibbs free energy,

$$G(f) = F[x_{eq}(f)] - f x_{eq}(f), \quad (2.4)$$

where $x_{eq}(f)$ comes from the condition of mechanical equilibrium. To calculate the Gibbs free energy of the whole system, we must add the contributions from any globular part with N_g monomers, $G_1(f)$, any chain parts, $G_2(f)$ with a total of $N_c = N - N_g$ monomers,

and whether or not the w -monomer is solvated (i.e. extracted from the globule):

$$G(f, N, N_g) = G_1(f, N_g) + G_2(f, N - N_g) - (w), \quad (2.5)$$

To find an expression for the Gibbs free energy of the remaining globule, G_1 , we need to use Eq. (2.1) in (2.4). In order to obtain a simple and compact form of the equilibrium extension $x_{eq}(f)$, we need to make the assumption that the globule only suffers a small deformation when a force is applied; this will be the case when the solvent is sufficiently poor. Then the deformation is linear with applied force,

$$x_{eq}(f) = \sqrt[3]{\frac{6}{\pi} N_g b^3} + \frac{16b^2}{9\pi u} f, \quad (2.6)$$

where the first term is the diameter of spherical globule.

For the pulled-out chain segment, we need to impose the condition of mechanical equilibrium as well, finding the tensile force

$$f = -\frac{\partial F_{ch}(z)}{\partial z} = -\frac{4k_B T}{\pi l_p} \left(\frac{z}{L} \right) \frac{1}{\left(1 - (z/L)^2\right)^2}, \quad (2.7)$$

and inverting it to obtain the equilibrium extension $z_{eq}(f)$ to be then used in Eqs. (2.3) and (2.4). Since all expressions depend strictly on the ratio (z/L) , we can infer that the total extension in response to an applied force is proportional to the contour length L of the exposed chain. As a consequence, the (negative) Gibbs free energy of the chain, $G_2(f)$, is proportional to the contour length of the chain, $L = N_c b$, where the number of solvated monomers is $N_c = N - N_g$. As a result, we can separate the effective chemical potential factor: $G_2(f) = \mu(f) N_c$. In the limit of large extension, when $(L - z)/L \ll 1$, this chemical potential takes the form [70]:

$$\mu(f) \approx \frac{2k_B T}{\pi} \left(\frac{1}{1 - \xi^2} - 1 \right) - fb\xi. \quad (2.8)$$

Here the dimensionless parameter ξ is a measure of the fractional extension of the chain relative to its contour length:

$$\xi = \frac{z_{eq}}{L} = 1 - \frac{1}{\sqrt{1 + \pi fb/k_B T}}. \quad (2.9)$$

2.2 Homopolymer unfolding

Before we consider the heteropolymer detailed above, I want to highlight the existence of a first order phase transition in the case where $w = 0$, i.e. when the chain is a homopolymer.

To calculate the Gibbs free energy of the polymer, we assume that in equilibrium the polymer can be completely compact, or completely extended, or consist of a single, smaller globule with $N_g = N - N_c$ and a stretched-out tail of N_c monomers, as in Fig. 2.1. The full Gibbs free energy can then be written as

$$G(f, N) = G_1(f, N - N_c) + G_2(f, N_c). \quad (2.10)$$

The construction of G is illustrated in Fig. 2.2, which shows the existence of two metastable states: when the polymer is fully globular ($N_c = 0$), and when the polymer is fully extended ($N_c = N$).

Figure 2.3 shows the variation of the full Gibbs free energy G with the chain conformation characterised by N_c , which plays the role of ‘reaction coordinate’ in our problem, for several values of applied tension f . We see first that the free energy curves are disjoint. For each force f , there is a range of globule sizes that will not sustain a restoring force of its magnitude,

$$f_{\text{crit}} = \frac{3u}{16b} \left(\frac{3\pi^2 N_g}{2} \right)^{1/3}, \quad (2.11)$$

determined by inverting Eq. (2.2); the boundary of this region is marked by the dashed line in Fig. 2.3. The right-most states on this plot (marked with the cross) correspond to the fully unfolded chain. Since no globule can exist beyond the critical force, there are no physical states with a defined Gibbs free energy $G(N_c < N)$ in this region: the only state (whether stable or metastable) is when $N_c = N$.

We also see the existence of a first order (discontinuous) phase transition at a force f_* . At this point, the two equilibrium states of equal depth are separated by an energy barrier ΔG . It is not until the force reaches a much higher value f_2 that the globule loses its metastability and the chain can only exist in the fully extended state with $N_c = N$ (these end values for each curve are marked by a cross in the figure). It is clear from Fig. 2.3 that there is no intermediate minimum between the globular state, and the stretched chain.

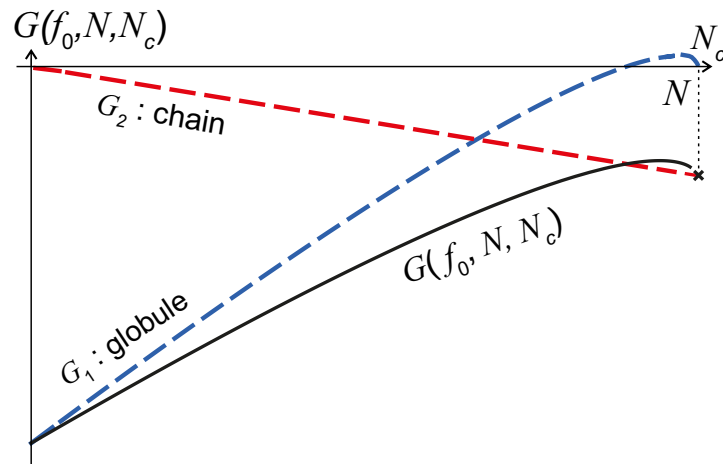


Fig. 2.2 Gibbs free energy curve for a polymer of total length N , subject to a particular tension force, f_0 , as a function of varying numbers of monomers in the stretched-out chain, N_c . The final free energy is a sum of the Gibbs energies of the chain, $G_2(N_c)$, and of the remaining globule with $N - N_c$ monomers, G_1 .

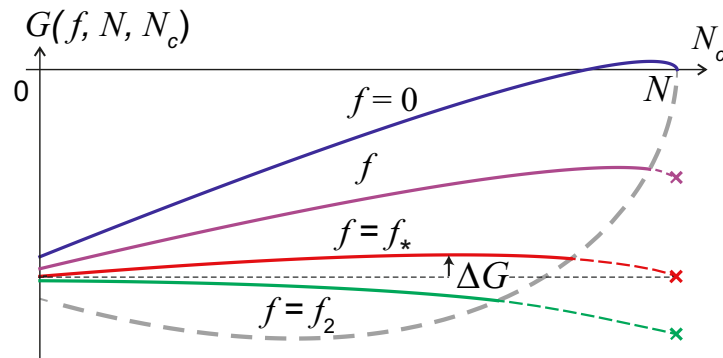


Fig. 2.3 Gibbs free energy curves against the number of monomers within the polymer that are in an extended phase. The different curves are for different constant forces, $0 < f < f_* < f_2$. ΔG is the energy barrier separating the two states $N_c = 0$ and $N_c = N$ when they are of equal energy. The thick grey dashed line indicates the boundary of critical force, past which there are no equilibrium solutions except the fully extended phase.

To find the force at the equilibrium thermodynamic phase transition, f_* , we equate the Gibbs energies of the globule and the chain, $G_1(f, N) = G_2(f, N)$:

$$-Nu + \left(\frac{2Nb}{3x(f_*, N)} + \sqrt{\frac{\pi Nx(f_*, N)}{b}} \right) u - f_* x(f_*, N) = N\mu(f_*) \quad (2.12)$$

Inserting Eq. (2.6) for $x_{\text{eq}}(f)$ again, we find, to leading order terms in N ,

$$\mu(f_*) = -u \left(1 - \frac{3}{2} \left(\frac{4\pi}{3} \right)^{1/3} N^{-1/3} \right) - \frac{4}{3} \left(\frac{3}{4\pi} \right)^{1/3} fbN^{-2/3}. \quad (2.13)$$

For sufficiently large u , we can find an approximate expression for f_* :

$$\frac{f_* b}{k_B T} \approx \frac{1 + 3a_*}{2\pi(1 - a_*)^2} + \frac{u_*}{1 - a_*} + \frac{\sqrt{2(3a_* - 1 + 2\pi(1 - a_*)u_*)}}{\pi(1 - a_*)^2}, \quad (2.14)$$

where the dimensionless shorthand parameters u_* and a_* are identified as

$$\begin{aligned} u_* &= \frac{u}{k_B T} \left(1 - \frac{3}{2} \left(\frac{4\pi}{3} \right)^{1/3} N^{-1/3} \right), \\ a_* &= \frac{4}{3} \left(\frac{3}{4\pi} \right)^{1/3} N^{-2/3}. \end{aligned} \quad (2.15)$$

For large $N \gg 1$ (as expected to be the case in most polymers), in the leading order:

$$f_* \approx \frac{u}{b} + \sqrt{\frac{8}{\pi} \frac{\sqrt{uk_B T}}{b}}. \quad (2.16)$$

There is an important difference with the earlier work of Polotsky *et al.* [52, 53], who have only considered weak globules and small forces (to Taylor-expand their expressions) and effectively remained in the quadratic region $G_{\text{eq}} \sim -f^2$ in Fig. 2.4. Therefore, in order to have any transition at all, they had to consider a very low binding enthalpy u (i.e. the solvent close to the Θ -point). Although our results look qualitatively similar in plots, the algebraic differences in allowing for large tension forces and strongly compacted globules are significant.

We are also able to find the position of the free energy maximum (the barrier), G^* , in Fig. 2.3:

$$0 = \frac{\partial G}{\partial N_c} = u + \mu(f) - \left(\frac{4\pi}{3} \right)^{1/3} u(N - N_c)^{-1/3} + \frac{4}{9} \left(\frac{3}{4\pi} \right)^{1/3} fb(N - N_c)^{-2/3}. \quad (2.17)$$

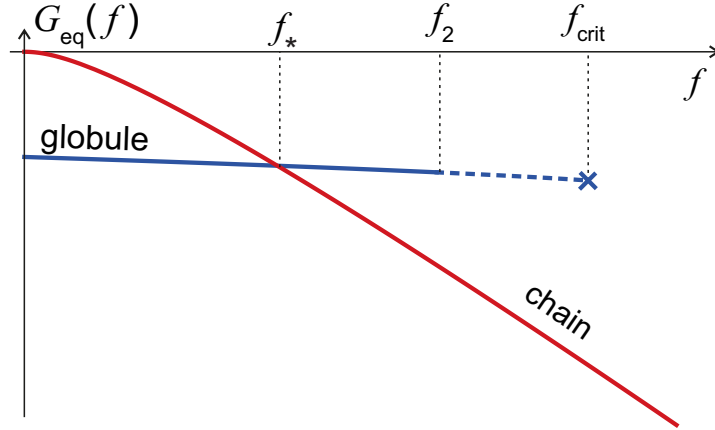


Fig. 2.4 Schematic phase diagram indicating the point at which the phase transition occurs (f_*), the force at which the globular phase is no longer metastable (f_2), and the critical force of the globule (f_{crit}).

These terms have clear physical meaning. The first term is the (positive) energy change when a monomer is taken from the bulk of a globule, and the second is the (negative) energy change when a monomer is added to the chain allowing it to be stretched less. The third term is the (negative) leading-order term due to contraction of the surface of the globule when a monomer is removed. This is force-independent; the first order correction due to the application of a force is identically zero. The final term is the increase in mechanical work on the system due to the globule shrinking against an applied force when a monomer is removed.

The point at which the globule completely loses its metastability, $f = f_2$, is reached when the barrier G^* reaches the boundary $N_c = 0$. This gives a condition for f_2 , when we let $N_c \rightarrow 0$ in Eq. (2.17) and find:

$$\mu(f_2) = -u \left(1 - \left(\frac{4\pi}{3} \right)^{1/3} N^{-1/3} \right) - \frac{4}{9} \left(\frac{3}{4\pi} \right)^{1/3} f b N^{-2/3}. \quad (2.18)$$

In a way identical to Eq. (2.14), we can find an approximate expression for f_2 for sufficiently large u :

$$\frac{f_2 b}{k_B T} \approx \frac{1 + 3a_2}{2\pi(1 - a_2)^2} + \frac{u_2}{1 - a_2} + \frac{\sqrt{2(3a_2 - 1 + 2\pi(1 - a_2)u_2)}}{\pi(1 - a_2)^2}, \quad (2.19)$$

where the dimensionless shorthand parameters u_2 and a_2 are identified as

$$u_2 = \frac{u}{k_B T} \left(1 - \left(\frac{4\pi}{3} \right)^{1/3} N^{-1/3} \right), \quad a_2 = \frac{4}{9} \left(\frac{3}{4\pi} \right)^{1/3} N^{-2/3}. \quad (2.20)$$

For large N , in the leading order we find $f_2 \approx f_*$ in Eq. (2.16). However, from comparing Eqs. (2.15) and (2.20), we see that $u_2 \geq u_*$, and so it is clear from Eqs. (2.14) and (2.19) that $f_2 \geq f_*$, with equality holding only at $N \rightarrow \infty$.

More generally, and noting that $N_g = N - N_c$, we can find an expression for the number of monomers in the globule at the free energy maximum, N_g^* , by solving the effective quadratic in Eq. (2.17), to find

$$N_g^* \approx \frac{\pi}{6} \left(\frac{u}{\Delta\epsilon} \right)^3 \left(1 + \sqrt{1 - \frac{4fb}{3\pi u^2} \Delta\epsilon} \right)^3, \quad (2.21)$$

where $\Delta\epsilon = \mu(f) + u$ is the (positive) net change in the energy per monomer between the globule and the expanded state (which reflects the fact that the solvent remains poor even though the monomers were forced into the expanded configuration). The position of the free energy barrier is plotted in Fig. 2.5, where we see that it becomes equal to N at $f = f_2$, that is, at $f \geq f_2$ even the full globule is ‘past the barrier’ and is absolutely unstable.

We can use this expression for N_g^* to find the energy barriers, both from the globular state, and from the fully expanded state of the chain. The barrier height from the globular state for a polymer of N monomers: $\Delta G_g = G^* - G_1(N)$, is found to be

$$\Delta G_g(f) = (N - N_g^*)\Delta\epsilon - \frac{3}{2} \left(\frac{4\pi}{3} \right)^{1/3} (N^{2/3} - (N_g^*)^{2/3})u + \frac{4}{3} \left(\frac{3}{4\pi} \right)^{1/3} (N^{1/3} - (N_g^*)^{1/3})fb, \quad (2.22)$$

and the barrier height from the extended chain state for a polymer of N monomers, $\Delta G_c = G^* - G_2(N)$, is

$$\Delta G_c(f) = -N_g^*\Delta\epsilon + \frac{3}{2} \left(\frac{4\pi}{3} \right)^{1/3} (N_g^*)^{2/3}u - \frac{4}{3} \left(\frac{3}{4\pi} \right)^{1/3} (N_g^*)^{1/3}fb. \quad (2.23)$$

By equating the Eqs. (2.22) and (2.23), we can recover the condition for the thermodynamic transition, f_* , found in Eq. (2.13), which is a reassuring check, since when the energy barriers from the globule state and from the chain state are equal, the two states themselves are equal in energy. This is illustrated in Fig. 2.5. From Eq. (2.21) we can also see that $\Delta G_g(f_2) = 0$ for $N_g^* = N$ (see Fig. 2.5), again confirming the point at which the globular state is no longer metastable.

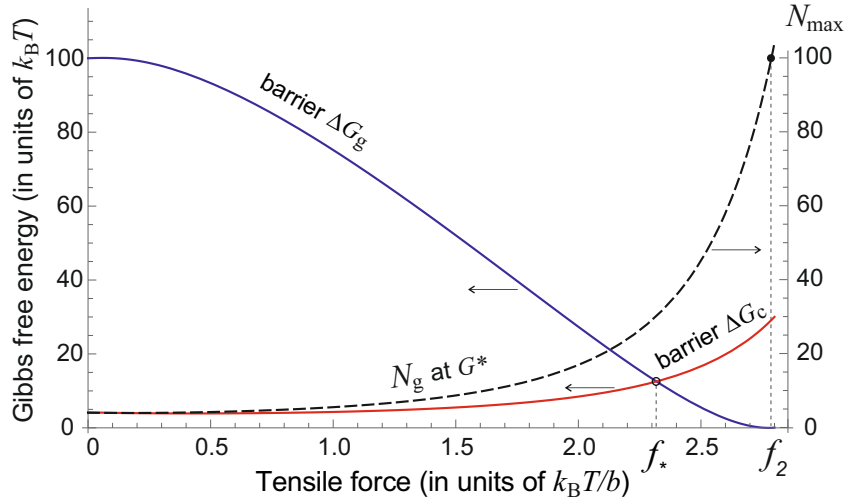


Fig. 2.5 The energy barriers for a polymer, with $N = 100$, $u = 2k_B T$. The crossing of the curves for $\Delta G_g(f)$ and $\Delta G_c(f)$ marks the point of thermodynamic transition between the two states, at f_* . The dashed curve corresponds to the axis on the right, and gives the size of the globule at the free energy barrier, N_g^* .

Another interesting and subtle feature of Fig. 2.5 is that the free energy barrier $\Delta G_c(0)$ remains non-zero even at $f \rightarrow 0$. Equally, the free energy barrier position $N_g^* \neq 0$ at $f \rightarrow 0$. This means that if we prepare a chain in a fully expanded (coil) state (with $N_c = N$) and then rapidly quench the temperature, or otherwise make the solvent poor – there will nevertheless remain a free energy barrier to nucleate a globular state. The same effect can be seen in Fig. 2.3, where the zero force curve has a region with positive energy near $N_c \rightarrow N$. This is an effect similar to the barrier arising in the classical nucleation theory [71]. This barrier height will be further enhanced by the high curvature in small globules, if bending energy is taken into account.

2.3 Heteropolymer unfolding free energy curves

Having considered the equilibrium behaviour of a globular polymer under a constant tension, I now move on to the case of a simple heteropolymer with a super-hydrophobic w -monomer, $w > 0$. To compare the results and predictions here to experimental data, a set of realistic model parameters will need to be chosen. For these, we will follow the directly related experiments by Fernandez and Brujic [44, 61, 66, 62], where ubiquitin or Ig-like I27 domains of titin were unfolded at constant force. Hence, I will take a polymer chain with $N = 100$ residues, as a value close to the above proteins. Since the minimal force these authors were using was ~ 90 pN, and I have earlier obtained the theoretical value for the critical unfolding force f^* in this regime (see Eq. (2.16)), quite a reasonable

value of the globule ‘hydrophobic strength’ $u = 5k_B T$ has to be chosen (assuming the characteristic size of an amino acid residue is $b \sim 0.3$ nm); at this strength of globule the critical force for a homopolymer would be $f^* \approx 4.48(k_B T/b) = 59.7$ pN, acceptably slightly below what was used in experiment.

The impact of this heterogeneity can be seen by considering the extended chain’s Gibbs free energy

$$G_2(f) = \mu(f)N_c \quad (2.24)$$

where the chemical potential $\mu(f)$ is as in Eq. (2.8). Note that the free energy is merely a function of the extended chain’s length. This additive form of the free energy of the extended portion of the polymer has an important consequence. We can in principle divide any chain of N_c monomers into two separate segments linked in series (see Fig. 2.1), and the Gibbs free energy will be the same, regardless of how we distribute the N_c monomers between the two parts. This means that monomers can be pulled out of the globule from either end of the chain, forming two tails of length z_1 and $z_2 = z - z_1$, without any additional free energy penalty. This means that the ‘lock’, positioned at $M < N/2$ from one end of the chain, could be exposed to the solvent for any N_c in the range $M \leq N_c \leq N$. Let us denote which monomer it is to leave the globule as N_w (meaning that the exposed chain segments have the total of $N_c = N_w$ monomers when the ‘lock’ is pulled out). The exposure of the w -monomer will manifest itself as a discontinuous jump in the free energy profile $G(N_c, N_w)$ at $N_c = N_w$. There are three qualitatively different situations, depending on the value of N_w , illustrated in Figures 2.7, 2.8 and 2.9, which sketch the dependence of $G(N_c)$ for a fixed value of applied force f (the dashed region on these plots represents the unstable globule, with $N_g \leq N - N_s$, see Eq. 2.2). The three regimes, which will be discussed in more detail in the next sections, are:

1. The lock could be exposed before the free energy barrier ($N_w \leq N_c^*$), as in Fig. 2.8. This results in a simple two-state kinetics with an enhanced barrier.
2. The lock could be exposed past the barrier, in the stable region of the free energy curve ($N_c^* < N_w < N_s$), as in Fig. 2.9. In this case, we have a meta-stable intermediate state, and a resulting three-state kinetics.
3. The lock is exposed in the unstable region ($N_w > N_s$), as in Fig. 2.7. This means that the system effectively does not see the free energy jump and the globule unfolds as if there was no w -monomer.

The value of N_w (the total length of the pulled-out chain for which the w -monomer gets exposed) is a random variable. The randomness arises purely because there is a choice

in how to distribute the pulled-out segments z_1 and z_2 (see Fig. 2.1) before the ‘locked’ monomer is at the surface. We derive the probability to have the w -monomer pulled out, given its sequential position $M < N/2$ along a chain of N monomers: $P(N_w|N, M)$. Let us assume that each time a monomer is pulled from the globule, we have an equal probability $p = 1/2$ of it being pulled from the left or the right. $P(N_w|N, M)$ is therefore similar to the binomial distribution, with the difference in that we could remove the w -monomer by approaching from the left or the right, equivalently. To remove the w -monomer at N_w from the shorter end, we must first remove $M - 1$ ordinary monomers in a total of $N_w - 1$ exposure events. Let us call the probability of that P_S ; this is given by the binomial expression $P_S = 2^{-(N_w-1)} \binom{N_w-1}{M-1}$. In the same way, to remove the w -monomer from the longer end, we must remove $N - M$ ordinary monomers first, with probability $P_L = 2^{-(N_w-1)} \binom{N_w-1}{N-M}$. The total probability is then given by the sum $\frac{1}{2}(P_S + P_L)$, which takes the form:

$$P(N_w|N, M) = \frac{1}{2^{N_w}} \left[\binom{N_w - 1}{M - 1} + \binom{N_w - 1}{N - M} \right]. \quad (2.25)$$

Figure 2.6 gives the shape of this distribution for various positions of the w -monomer in the chain sequence. $P(N_w|N, M) = 0$ for $N_w < M$: one cannot remove the w -monomer without first removing a certain number of ordinary monomers. It is normalised, as expected for a probability distribution: $\sum_{N_w} P(N_w|N, M) = 1$.

We will shortly determine how the position of the jump N_w determines the rate constant of the transition to the unfolded state. Let us split the population according to each unfolding trajectory, defined by the value of N_w . These sub-populations will decay according to their specific rate constant $k(N_w)$, and the number of folded polymers $n(N_w)$ will vary according to the simple exponential rate law:

$$\dot{n}(N_w, t) = -k(N_w)n(N_w, t). \quad (2.26)$$

However, in experiment, we cannot distinguish between different sub-populations. Instead, we track how the total population evolves over time. To calculate this, we have to weight each sub-population by its fraction, i.e. average $\langle n(N_w) \rangle$. The fraction of the population in the sub-population $n(N_w)$ is given by $P(N_w)$. Accordingly, the rate equation for the entire population takes the form:

$$\langle \dot{n}(t, M) \rangle = n_0 \sum_{N_w=1}^N P(N_w|N, M) e^{-k(N_w)t}. \quad (2.27)$$

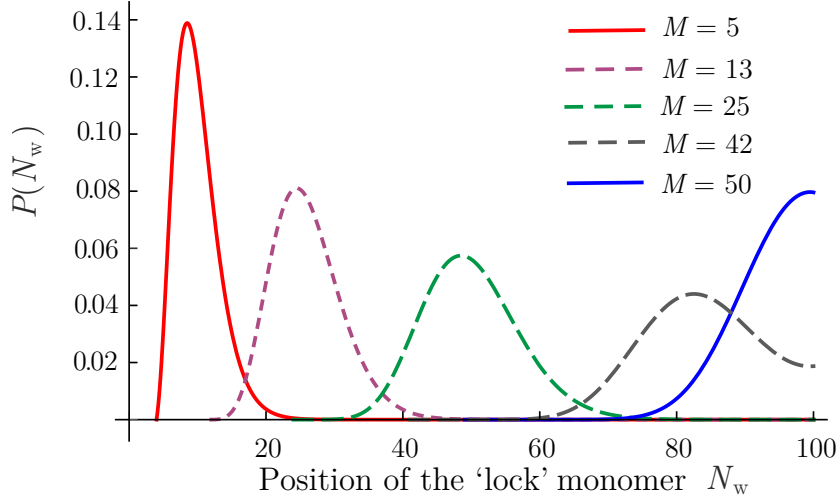


Fig. 2.6 The likelihood of the jump occurring at N_w is given by $P(N_w)$. The distribution $P(N_w)$ is plotted here for $N = 100$ and several values of the w-monomer's position, M , in the sequence along the chain.

In order to efficiently evaluate the ensemble-averaged population kinetics for the chains unfolding by the pulling force, we need to make an approximation for the probability distribution of the random variable N_w . This discrete distribution was given by the Eq. (2.25) and plotted (for $N = 100$) in Fig. 2.6. It is clear that, although the binomial expressions involved are skewed, even at these moderate chain lengths the Central Limit Theorem holds, and we can approximate the distribution as a Gaussian with good accuracy. The conversion from a strict binomial distribution of a random variable X with $N_w - 1$ 'attempts' corresponds to replacing it with a continuous Gaussian [72] with the mean $y = (N_w - 1)/2$ and variance $\sigma^2 = (N_w - 1)/4$. For the binomial probability P_S contributing to the first term in Eq. (2.25), the variable is $X = M - 1$; for the distribution P_L in the second term of Eq. (2.25), the variable $X = N - M$. Put together, these two expressions (Gaussian in the variable X) produce the final continuous probability density of our actual random variable N_w :

$$P(N_w) = \sqrt{\frac{1}{\pi y}} \left(e^{-\frac{(M-1-y)^2}{y}} + e^{-\frac{(N-M-y)^2}{y}} \right), \quad (2.28)$$

where the shorthand $y = (N_w - 1)/2$ is employed. This approximate expression turns out to be indistinguishable from the exact curves in Fig. 2.6, plotted for $N = 100$. The compact analytical expression in Eq. (2.28) can now be used to calculate the observed

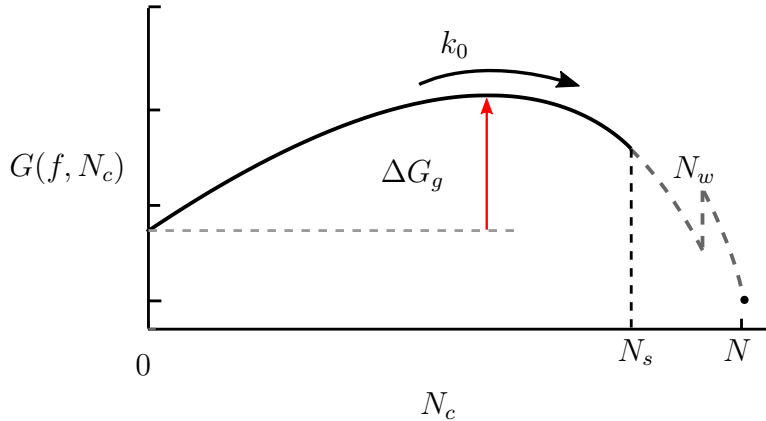


Fig. 2.7 This is the Gibbs free energy curve versus the number of monomers in the chain N_c , for the case where the w -monomer is exposed once the globule is already unstable to force, $N_w > N_s$. Here, there will be no contribution to the opening rate from the exposure of the w -monomer.

population kinetics, which replaces Eq. (2.27):

$$\langle n(t) \rangle = \int_0^{\frac{N-1}{2}} dy P(y) e^{-k(y)t}. \quad (2.29)$$

2.4 Rate constants

The equilibrium rate constants $k(N_w)$ could be found using a Kramers-like method, first explored by Brinkman for the case of two-well potential [24]. The expression for the rate constant is given by a steady-state limit of the Ornstein-Uhlenbeck theory for the mean first passage time [25], when the ensemble distribution in the initial potential well had enough time to equilibrate before the average transition occurs:

$$k = \frac{k_B T}{\gamma} \frac{1}{\int_{\text{well}} e^{-\beta G(N_c)} dN_c \int_{\text{barrier}} e^{\beta G(N_c)} dN_c}, \quad (2.30)$$

where γ is the frictional coefficient for the effective energy landscape characterised by the reaction coordinate N_c ; as usual $\beta = 1/k_B T$. We use the same approach here to calculate the rate constants for the three separate cases identified above.

2.4.1 Jump in the unstable region

We start with this region ($N_w > N_s$), as illustrated in Fig 2.7, in spite of it appearing the last on the list, because the transition rate obtained in this regime is unaffected by

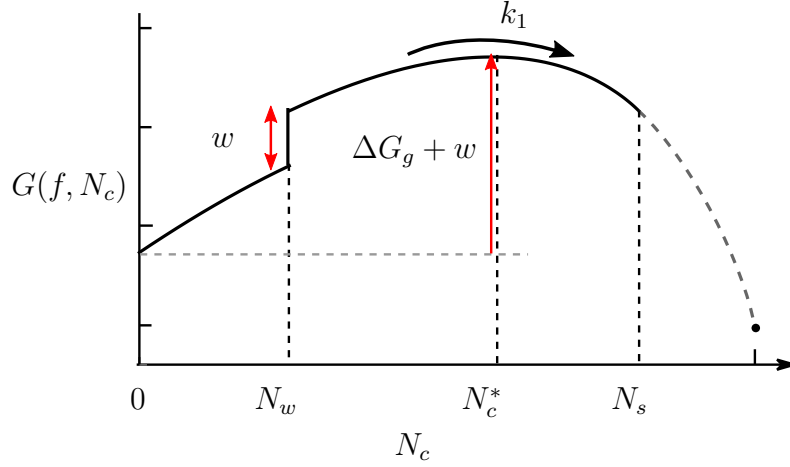


Fig. 2.8 This is the Gibbs free energy curve versus the number of monomers in the chain N_c , for the case where the w -monomer is exposed before the homopolymer curve maximum, $N_w < N_c^*$. This will increase the height of the energy barrier from ΔG_g to $\Delta G_g + w$, but does not substantially change the calculation of the rate constant k_1 .

the ‘lock’ and forms the reference for all other cases. When the jump in the free energy happens in this unstable region, we are reduced to the homopolymer problem [70], since the extraction of the w -monomer has no effect on the process (the remaining globule loses its stability before the ‘lock’ is forced out). The forward rate constant is given by

$$k_0 = \frac{\alpha}{\gamma} \sqrt{\frac{\omega}{2\pi k_B T}} \kappa_\alpha e^{-\beta \Delta G_G}, \quad (2.31)$$

where ΔG_G is the energy barrier at N_c^* , see Fig. 2.7 for illustration. ω is the curvature of the barrier, and $\alpha = (\partial G / \partial N_c)|_{N_c=0}$ is the slope of the native potential well (which is treated as approximately triangular). The pre-factor κ_α is determined by the geometry of the well, and we define it for the convenience of later expressions:

$$\kappa_\alpha(N_c^*) = \left[1 - \exp\left(-\frac{\alpha N_c^*}{2k_B T}\right) \right]^{-1}. \quad (2.32)$$

Note that the rate k_0 is not a function of our random variable N_w .

2.4.2 Jump before the barrier

In most cases, when $N_w < N_c^*$, the fixed jump in the free energy has only a minor effect of slightly distorting the pre-exponential factor in the basic homopolymer expression of Eq. (2.31) due to the distortion of the native well, see Fig. 2.8. However, the effective height of the barrier is increased by the magnitude of this jump. To estimate the resulting

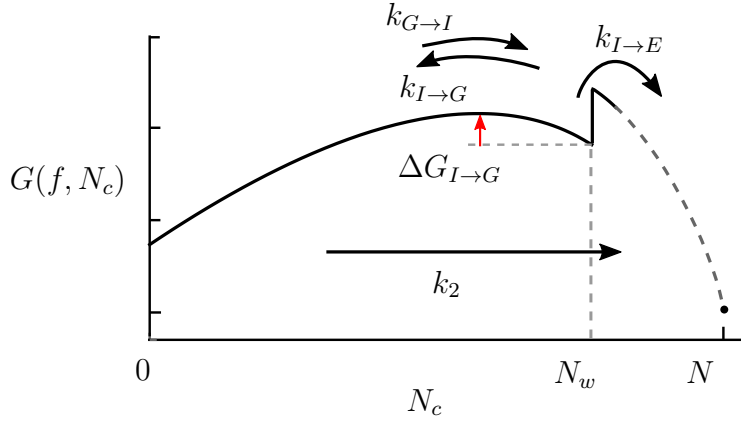


Fig. 2.9 This is the Gibbs free energy curve versus the number of monomers in the chain N_c , for the case where the w -monomer is exposed after the homopolymer curve maximum, but before the globule loses stability, $N_c^* < N_w < N_s$. Here, the energy barrier from exposure of the w -monomer creates a new meta-stable state, and to calculate the rate of transition over the barrier, k_2 , we have to use three state kinetics.

rate constant k_1 we can split the integral over the barrier (having approximated the potential as harmonic) into two pieces,

$$\int_{-\infty}^{\infty} e^{\beta G} dN_c = \int_{-\infty}^{N_w} e^{\beta(G+w)} dN_c + \int_{N_w}^{\infty} e^{\beta G} dN_c.$$

This leads to a modified form of Eq. (2.31):

$$k_1(N_w) = f_w(N_w) \cdot k_0 e^{-\beta w}, \quad \text{with} \quad (2.33)$$

$$f_w = \frac{2}{(1 - e^{-\beta w}) \operatorname{erf}\left(\sqrt{\frac{\omega}{2k_B T}}(N_c^* - N_w)\right) + (1 + e^{-\beta w})}.$$

Naturally, the rate constant k_1 reduces to k_0 when $w = 0$, that is, when there is no ‘locked’ w -monomer present in the polymer globule. In the special case when $N_w = N_c^*$, the exposure happens at the top of the barrier and the rate constant simplifies to:

$$k_1(N_c^*) = \frac{2k_0}{1 + e^{\beta w}}. \quad (2.34)$$

2.4.3 Intermediate state kinetics

When the jump occurs in the region $N_c^* < N_w < N_s$, we have three (meta-)stable states and two free energy barriers between them, see Fig. 2.9. With three-state kinetics, one has to make approximations to find an analytic expression for the rate constant. We

choose to follow the steady-state approximation [73], where the intermediate state is assumed to be in equilibrium with the native state, and transitions to the extended state are assumed to be permanent (no refolding). In this approximation, the rate constant is expressed as

$$k_2 = \frac{k_{G \rightarrow I} k_{I \rightarrow E}}{k_{I \rightarrow G} + k_{I \rightarrow E}} \quad (2.35)$$

where G , I , and E refer to the globular (native), the intermediate, and the extended states, respectively.

$$k_{G \rightarrow I} = k_0, \quad (2.36)$$

$$k_{I \rightarrow G} = \frac{\alpha'}{\gamma} \sqrt{\frac{\omega}{2\pi k_B T}} \kappa_{\alpha'} e^{-\beta \Delta G_{I \rightarrow G}} \quad (2.37)$$

where α' is the reverse gradient of the intermediate well, and $\Delta G_{I \rightarrow G} = G(f, N_c^*) - G(f, N_w)$ is free energy barrier for the transition from the intermediate state back to the native globular state, see Fig. 2.9 for illustration. The pre-factor $\kappa_{\alpha'}$ is given by the same form as Eq. (2.32), but with the arguments α' and $(N_w - N_c^*)$. Finally, the rate constant of escape into the fully extended state is:

$$k_{I \rightarrow E} = \frac{\alpha'^2}{k_B T \gamma} \kappa_{\alpha'}^{(1)} \kappa_{\alpha'}^{(2)} e^{-\beta w}. \quad (2.38)$$

α' appears twice in the expression for $k_{I \rightarrow E}$, and so is the pre-factor $\kappa_{\alpha'}$: once with the argument $(N_w - N_c^*)$ from the Kramers integral over the triangular well of the intermediate state, and again with the argument $(N_s - N_w)$ from the integral over the $I \rightarrow E$ barrier, which is also triangular with the same slope α' .

The full expression for the rate k_2 in the three-state regime can be simplified into a form:

$$k_2(N_w) = \frac{k_0}{\sqrt{\frac{\omega}{8\pi k_B T}} (N_s - N_w) e^{\beta w} e^{-\frac{1}{2}\beta\omega(N_w - N_c^*)^2} + 1} \quad (2.39)$$

We can plot the rate constants derived above for a range of w and f , as illustrated in Fig. 2.10. For values of N_w close to N_c^* , the expression for k_2 deviates from its expected value where it needs to join the end-point of k_1 : here the approximations made by Brinkman (that of a high barrier) break down. However, we expect that the value of k_1 itself is actually valid at any value of N_w within the region $0 \leq N_w \leq N_c^*$. Therefore, we get a good idea of the true profile of $k(N_w)$ in spite of approximations.

For small $N_w \ll N_c^*$, the rate constant k_1 differs from the homopolymer rate of escape k_0 only by the Arrhenius factor for the jump, $\exp(-\beta w)$. For $N_w > N_s$, the rate is just

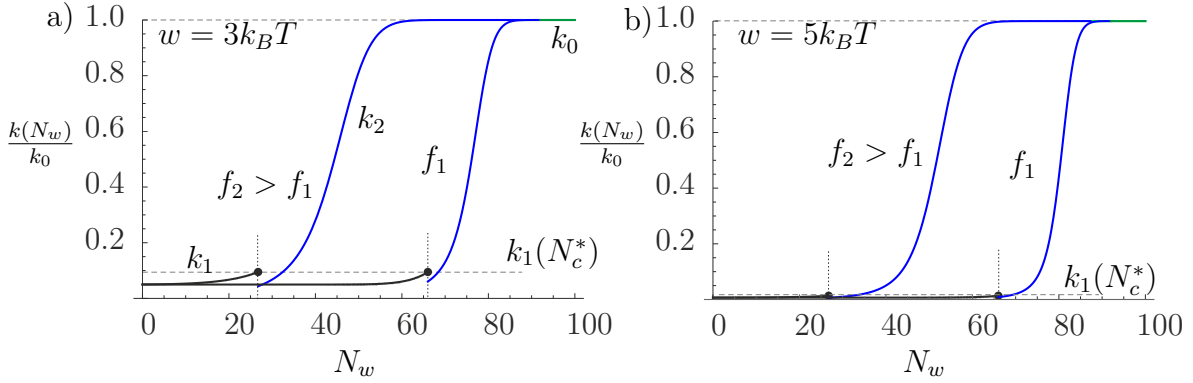


Fig. 2.10 Plots of the rate constants $k(N_w)/k_0$ for $N = 100$, $u = 5k_B T$ for two values of pulling force: $f_1 = 4.8k_B T/b$ (only slightly above the critical force f^*), and $f_2 = 5.3k_B T/b$. Two values of the ‘lock’ energy w are shown in the plots. The segments k_1 (at low N_w) terminate at the points when $N_w = N_c^*(f)$, Eq. (2.34), labelled by \bullet . The segments in the three-state regime, $k_2(N_w)$, reach the value k_0 (1 in the scaled plots) when $N_w = N_s(f)$.

a constant k_0 . Because of these constant values of rates, the average $\langle n(t, M) \rangle$, given by Eq. (2.27), will retain a simple exponential time dependence in certain ranges of ‘lock’ monomer positions M .

2.5 Ensemble average

We are now in a position to evaluate the integral in Eq. (2.29), and plot the resulting average population dynamics against time. In a typical AFM experiment [45, 61, 62] a constant force is applied to a folded protein, and a time of a sharp unfolding transition is recorded. After many repeats, a distribution of rupture times is obtained with great accuracy. The cumulant of this distribution represents the relative population of chains unfolded up to time t . With a single rate of unfolding, one expects this population to grow as $(1 - e^{-k_0 t})$. To represent the same population in our analysis, we plot $1 - \langle n(t) \rangle$ in Fig. 2.11. In the plot we use constant force slightly above the critical value f^* , and the fixed added strength of the ‘lock’ that is equal to the hydrophobic strength of the main monomers. In this representation it is difficult to distinguish exponential from non-exponential kinetics: all curves show qualitatively the same cumulative effect of an increasing fraction of unfolded chains as time passes under a constant force. It is, however, remarkable that for all the same parameters of the chain, the mere position of the ‘locked’ monomer along the sequence has such a strong effect on the apparent rate of unfolding.

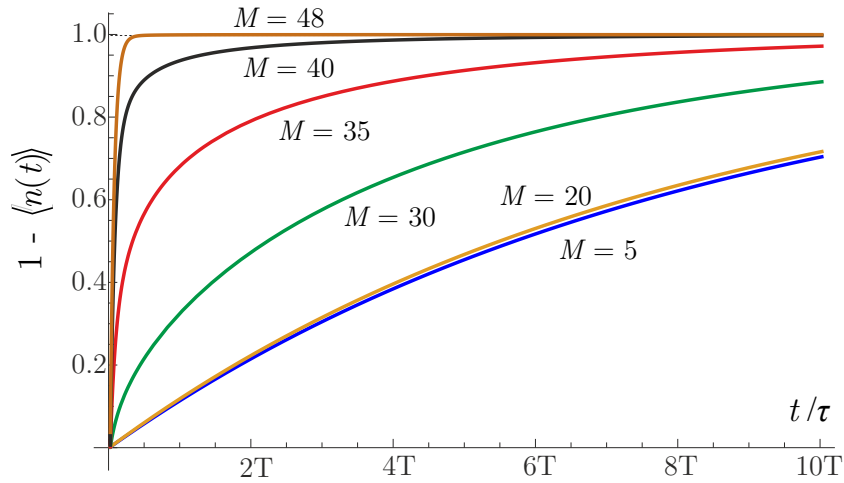


Fig. 2.11 We plot the cumulant $1 - \langle n(t) \rangle$ as an illustration of a typical experimental trace. We have the same force for each of the curves, and strength of w -monomer ($fb = 4.8k_B T$, $u = 5k_B T$, $w = 5k_B T$ for $N = 100$), but vary the position of the w -monomer, M . The linear non-dimensional time axis is measured in units of 10^{12} , which we shorthand as $T = \text{'tera'}$.

Note that the time axis in Fig. 2.11 and subsequent plots is scaled by a dimensional constant $\tau = \gamma/k_B T$, evident in the original definition of all rates, Eq. (2.30). This time scale is an inverse of a diffusion constant of fluctuations in the reaction coordinate N_c . To relate it to a more familiar diffusion constant D of a single residue (monomer), we have to use the length scale of our monomer: $\tau = b^2/D$. Taking $D \sim 6 \cdot 10^{-10} \text{m}^2/\text{s}$ for an average amino acid in water (which is almost certainly an overestimate in this case), we obtain $\tau \sim 1.5 \cdot 10^{-10} \text{s}$. This means that the real time scale in Fig. 2.11 and subsequent plots is measured in minutes. It is a bit longer than in experiments we quoted [45, 61, 62], but our aim was not to reproduce the experimental results quantitatively: we built a minimal model with a single ‘lock’ to illustrate the point, with both u and w magnitudes chosen somewhat arbitrarily. It is very easy to change these parameters slightly and achieve a much better agreement with measured time scales, but we believe this is not necessary or particularly beneficial.

To what extent does the ‘lock’ affect the kinetics? To distinguish the exponential relaxation, we first plot $\langle n(t) \rangle$ for different lock positions, M , on a logarithmic scale in Fig. 2.12. As in Fig. 2.11, for a range of w -monomer positions near the end of the chain, there is a very little change in the slow single-exponential relaxation. The deviation from single exponential kinetics (showing as a straight line in this logarithmic plot) is increasingly evident for values of M closer to the middle of the chain. Initially, the decay is fast, and follows a simple exponential law, as those globules that transition with the

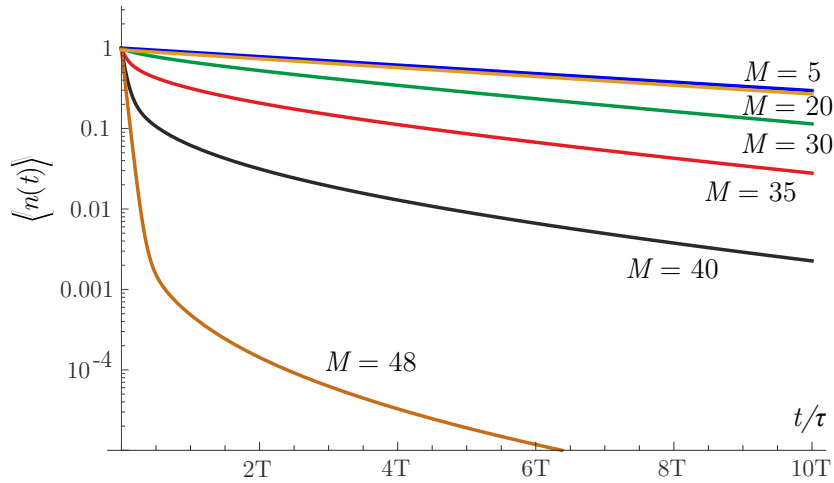


Fig. 2.12 The plot $\langle n(t) \rangle$ on a logarithmic scale, where $\langle n(t) \rangle$ is the same as in Fig 2.11, for $fb = 4.8k_B T$, $u = 5k_B T$, $w = 5k_B T$ and $N = 100$. For the core located at $M \approx 20$ or less, we have an approximately single exponential decay. For the intermediate core positions, there is a transition from faster decay to the single exponential at longer times (leading to a long tail). Note that as the core gets close to the middle of the chain the slower (sub-exponential) relaxation becomes increasingly apparent.

fast rate k_0 unfold first. It is difficult to discern this regime in the log-linear plot in Fig. 2.12, because we concentrate on the long-time effects. At much longer times, there is a gradual crossover to a different simple-exponential decay with the rate constant $k_0 e^{-\beta w}$, much smaller for significant w . As M gets larger, the time this crossover occurs increases – whereas for small M we mostly see the slow exponential rate.

For small M , the deviation from single exponential kinetics will not be observed in experiment. This is easy to understand: the probability of exposure, $P(N_w)$, is relatively sharply peaked, so for small M , almost all the probability mass will lie in the two opposite regions where the rate constant is independent of N_w . Thus, the ensemble average $\langle n(t) \rangle$ remains a single exponential, with only a small extra contribution from other rate constants. Non-exponential effects are most prominent when M lies close to the middle of the chain where the rate constant undergoes the rapid change, cf. Fig. 2.10.

We examine the effect of varying the ‘lock’ strength w in Fig. 2.13, comparing a mid-range position $M = 30$ and near the middle position $M = 42$. As the ‘locked’ monomer becomes increasingly hydrophobic, the rate of slow decay $k_0 e^{-\beta w}$ will obviously decrease, and so the folded molecule is more stable for larger w . It is apparent that, at short times of folded population decay, all curves follow the fast simple-exponential relaxation k_0 that is independent of the ‘lock’ strength w . The position of the crossover to

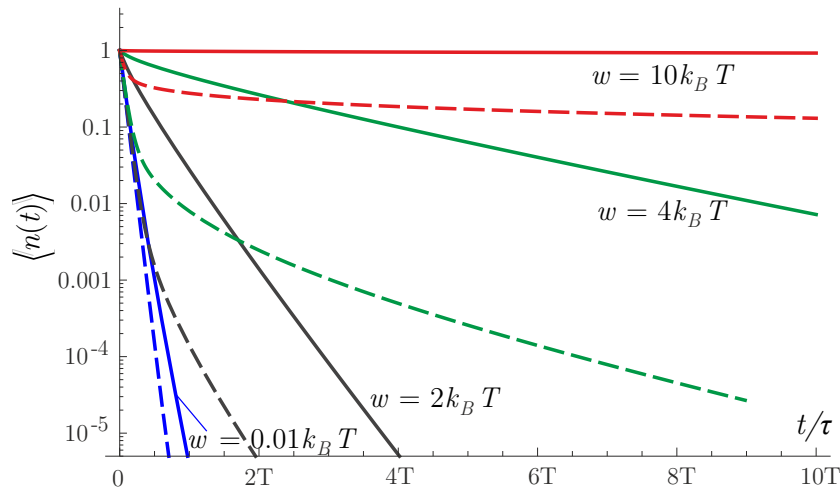


Fig. 2.13 The plot $\langle n(t) \rangle$ on a logarithmic scale, for $N = 100$, $fb = 4.8k_B T$, $u = 5k_B T$ and varying core strengths, w , listed in the plot. Solid lines are for a mid-range $M = 30$, the matching dashed lines are for $M = 42$, close to the middle of the chain. A stronger core (larger w) leads to a very long tail in the distribution, even for the same position M .

the slow simple-exponential relaxation with the rate constant $k_0 e^{-\beta w}$ occurs at different times depending on the ‘lock’ position M .

Not all cores will influence the unfolding kinetics, and we have demonstrated that much depends on the position of such a ‘lock’ along the chain. When the core is close to the terminus of a polymer, it will unfold on average after a much longer time than those where the core is in the middle of the polymer’s sequence. However, the globules with cores close to the middle of their sequence exhibit a pronounced non-exponential dynamics (on average) upon the application of constant force. Unsurprisingly, stronger locks stabilise the molecule more than weak locks.

What if there are multiple cores within the heteropolymer? The probability distribution now has multiple degrees of freedom: the exposures of the different cores. The probability will be sharply peaked around the point \mathbf{M} , which is now a vector containing the sequence positions of the different cores. There may be small breakage events into smaller globules (but each larger than the critical size), each protecting a strongly bound region, before the chain fully extends. These might manifest as short-lived intermediate plateaus on experimental traces.

It is possible to verify these predictions experimentally, using synthetic polymers. Construction of heteropolymers with controlled placement of more hydro-phobic monomers would allow a precise test of the predictions of non-exponential kinetics. The advantage of these constructed biomolecules would be the simplicity of inter-monomer interactions compared to the complexity of biological proteins.

In reality, biomolecules have a whole range of varied local and non-local interactions that help stabilise their specific structure. Experimental work that shows distinctly non-exponential kinetics of unfolding has been mostly done on ubiquitin protein [61, 66, 62]. The structure of ubiquitin has been resolved in 1987 [74], where the authors clearly identify the residues that form the hydrophobic core, which is created by bonding the α -helical segment (residues 23-34) with the β -sheet segment. By examining the sequence and the folded structure, Fig. 2.14, we conclude that the main hydrophobic bond is formed between Ala28 and Leu43, out of the total sequence of 76 residues. Since force is applied at the N- and C-termini of the protein, we say that the intermediate chain segment (28-43) between these two residues is only exposed to the force upon the breaking of this bond. Therefore, we introduce an effective chain length of $N = 61$, with a lock at $M = 28$ and $N - M = 33$. This is close to the middle of the effective chain, which agrees with the non-exponential kinetics prediction.

It would be irresponsible to suggest that this analysis offers the final word in non-exponential kinetics of ubiquitin unfolding. Proteins are very complicated structures, with several levels of organisation above simple primary sequence. Where interactions of the core residues are much stronger than all other interactions in the molecule, there may be some justification in taking other interactions within the protein as approximately equal in strength, as in my model. However, generally, the level of non-local interactions in a protein's structure does not allow its partition into a series of smaller units. In reality, force propagation along a protein's backbone under applied force is not linear, and not all interactions within a protein will propagate stress through them [75]. Then, as the molecule unfolds, the distribution of applied force through the molecule will change. Molecular dynamics simulations of ubiquitin unfolding under applied force show that dynamic disorder within ubiquitin, i.e. conformational fluctuations leading to changes in unfolding barriers, could explain non-exponential kinetics in the fast mechanical unfolding of ubiquitin [76], though it should be noted that fast unfolding is achieved through extremely high unfolding forces (500-1000

N), well past the usual forces applied in force-clamp AFM experiments [44].

Nevertheless, the concept of multiplicity of unfolding pathways is not controversial [77], and I believe there is utility in coarse-grained descriptions of proteins in this way. In particular, if one is able to consider a graph of the protein, through which force propagates, with stochastic breaking of individual links within the propagation backbone, then it might be possible to identify certain types of network structures that lead to more stable structures under loading. One simple model could look like so: consider a collection of springs between two plates, with a constant pulling force applied to the plates. These

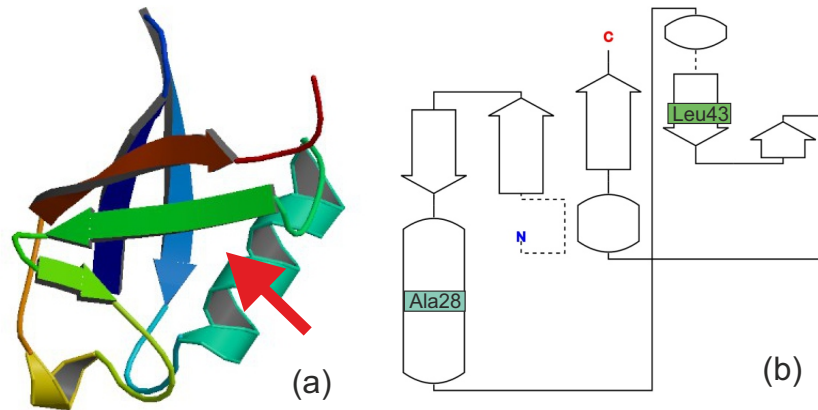


Fig. 2.14 The structure of ubiquitin: (a) the PDB 1ubq rendering, the arrow pointing at the strongest hydrophobic bond between Ala28 and Leu43; (b) the corresponding sequence annotation with the labelled hydrophobic residues.

springs could have different breaking energies, and different spring constants. Force applied will now be spread across these springs, which will break, according to the same principles as discussed here. As each springs break, the force will re-distribute across the remaining springs, and each will have a force increased. This linkage of the bonds will lead to non-exponential kinetics as well, as many other effects such a random variation of sequence. It would be most interesting to look at this from the more general perspective of graph theory and network connectivity, where the theoretical tools for characterisation of networks is more developed.

In this chapter I have looked at the simplest possible scenario, and found that the introduction of even a single specifically-placed inhomogeneity to an otherwise homopolymer chain already produces non-exponential kinetics when chains are unfolded under constant force. The inhomogeneity leads to a statistical randomness in the way the chain unfolds and results in stretching of the decay curve, with a long tail decay after an initial fast exponential decay (corresponding to the situations when a significant portion of the chain can be pulled out of the globule before the ‘lock’ is affected). While this is very much a toy model, such behaviour mimics quite well the behaviour of biological macromolecules in AFM pulling experiments, and highlights that where multiple unfolding pathways exist, one may find non-exponential kinetics without either static or dynamic disorder.

CHAPTER 3

MECHANOSENSING: UNFOLDING ON NON-RIGID SUBSTRATES

One interesting topic to which we can apply the ideas of forced unfolding is cell mechanosensation – the transduction of mechanical stimuli from the environment across the cell membrane. Mechanosensors are the protein complexes that produce responses to mechanical inputs [78, 79]. There are two distinct types of mechanosensing: reacting to an external force, or sensing the viscoelastic properties of the cell environment. Here, I refer to the first as mechanosensitivity of the 1st kind, and the latter as mechanosensitivity of the 2nd kind.

Mechanosensitive ion channels (MSC), such as alamethicin [80], are an example of mechanosensors of the 1st kind. MSCs exist in all cells and provide a non-specific response to stress in a bilayer membrane [81, 82]. Traditionally, MSC operation is understood as a two-state model. These two-state systems (open/closed, or bonded/released) with the energy barrier between the states depending on applied force, are common in biophysics [83, 84]. Rates of transition in these systems are often calculated using the ‘Bell formula’ [60], which has them increasing exponentially with the force. This is just the classical result of Kramers and Smoluchowski [23, 85], but the application of this formula is problematic in the limit of small barriers.

A mechanosensor of the 2nd kind has a different challenge: to actively measure the response coefficient (stiffness in this case, or matrix viscosity in the case of bacterial flagellar motion). On macroscopic scales (in engineering or rheometry) this is done with two separate measurements: of force (stress) and of position (strain), or we could contrast two separate points of force application. One could also use inertial effects, such as impact or oscillation, to measure the stiffness or elastic constant of the element. None of these options are available on a molecular scale because of a very high resistance, and of a short-distance cutoff of elasticity. The single sensor complex cannot measure

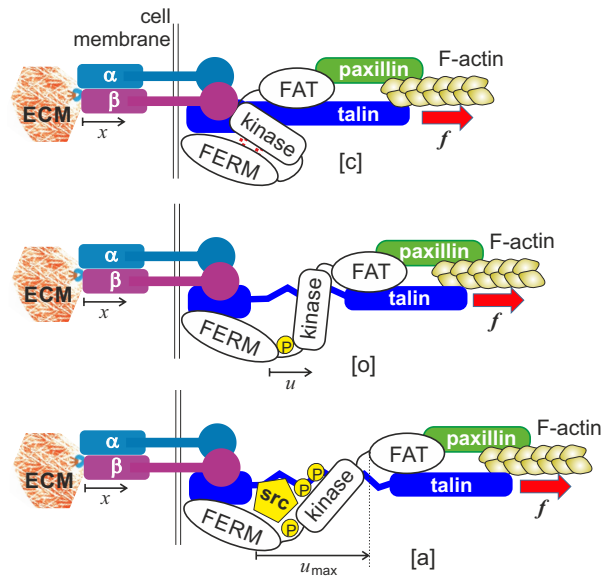


Fig. 3.1 The assumed chain of force transduction from the F-actin of the cytoskeleton, through the activated β integrin binding to ligands of the deformable ECM. The FERM domain of FAK is associated with the cell membrane, near the integrin-talin head assembly, while the FAT domain is associated with actin through its binding to paxillin [90]. The pulling force is transmitted through this chain to the FERM-kinase physical bond. In the closed state [c] the kinase domain is inactive and the whole FAK protein is in its native low-energy state. Once the physical bond holding the FERM domain and the kinase together is broken, the protein adopts the open conformation [o]. In the open state, first the Tyr397 site spontaneously phosphorylates, which in turn allows binding of Src and further phosphorylation of the kinase - turning it into the active state [a], see [91–93].

relative displacements in the substrate, and the overdamped dynamics prevents any role of inertia. Cells must come up with novel ways of measurement.

Mechanosensing at focal adhesions

To probe the mechanical modulus of a medium, a force has to be applied to it, either as a local point source, or as distributed stress. In focal adhesions the source of this force is the actin-myosin activity of the cytoskeleton. Therefore, we need to trace the series of connected devices, from the point of force origin (F-actin) to the point of its application to the ECM. Figure 3.1 illustrates this force chain, which has been reproduced in a large number of important publications in this field [86–90]. There are several key players that we should consider: integrins, focal adhesion kinase, talin, paxillin, and the cytoskeleton. How do these components each contribute to the function of the complex?

The integrin family of transmembrane proteins link the extracellular matrix (ECM) to the intracellular actin cytoskeleton via a variety of protein-tyrosine kinases, one of which is FAK [94]. Integrins are aggregated in focal adhesions, and they mediate the cell interaction with ECM [78]. Activation of integrins is required for adhesion to the substrate; active integrins acquire ligand affinity and bind to the proteins of the ECM. It is well established that integrin activation and clustering leads to FAK activation and the subsequent signalling chain of mechanosensing and cytoskeletal remodelling, e.g. see the review by Parsons [95]. There is a large body of literature on integrins, with definitive reviews by Hynes [96, 97] explicitly stating that integrins are the mechanosensors. It has recently been demonstrated [98, 99] that the integrin bond with fibronectin has catch-bond characteristics, and therefore could have a graded response to force and stiffness.

However, activated integrins possess no further catalytic activity, and so cannot act as a mechanosensor on their own. A good summary by Giancotti [100], while talking about integrin signalling, in fact shows schemes where FAK is the nearest to cytoskeletal actin filaments. The important work by Guan et al. [101, 102] establishes a clear correlation chain of extracellular fibronectin – transmembrane integrins – intracellular FAK, but offers no reason to assume that integrin is the sensing device on this chain. There is a clear indication that phosphorylation of FAK is a key step in the mechanosensing process [79]. Indeed, Schaller et al. [103] state that FAK phosphorylation is the initial step of signalling, and show evidence that crosslinking integrins and ECM (i.e. making the ‘substrate’ stiffer) leads to an enhanced FAK phosphorylation, while conversely, a damage to integrin is connected with a reduced activation of FAK.

This lack of clarity on the link between integrin engagement and FAK activation during mechanosensing arises from the lack of detailed knowledge at a molecular/physical level of how FAK is activated. One possibility, explored by U. Schwartz [104, 105], is that clusters of activated integrins always activate FAK and generate the mechanosensing signal that leads to the increasing F-actin pulling force. As some of the integrins are broken off their ECM attachment, the associated FAK signal reduces, regulating the further force increase – and that is the action of the focal adhesion mechanosensor complex. More recently, these same ideas have incorporated newly-discovered catch-bond characteristics of the the integrin-ECM links [98]. In both cases, the mechanosensing response is an emergent property – you need a collection of coupled mechanosensors of the 1st kind to generate a stiffness sensing response. I think this work is elegant, and important, but ask the question: are there any other possible mechanisms?

The application of tension in mechanosensing at focal adhesions is now well established [90]. A key role in this system is played by talin. There are many papers investigating the correlation of talin (as well as paxillin) with β -integrin and FAK; recent studies clearly show that talin is capable of high stretching by a tensile force [106, 107], implying a function similar to that of titin in muscle cells: acting as an extension-limiter. It is also now clear that the immobile domain at the N-terminal of talin is associated with integrin, and also closely associated with the FERM domain of FAK [106, 107], while the C-terminal of talin is associated with paxillin, which in turn may associate (perhaps via vinculin) with the focal adhesion targeting (FAT) domain (C-terminal) of FAK. Both talin and paxillin also bind to cytoskeletal F-actin. These actin filaments exert a pulling force on the C-terminal of talin, making it play a role of a scaffold for other proteins to arrange around. More importantly, this allows the pulling force to be transmitted from the cytoskeleton to the ECM, via the force chain sketched in Fig. 3.1. This could be used to effect the conformational change in FAK required for its activation. In this model, integrin is merely the bridging element from FAK to the ECM, with the FERM domain localized near the cell membrane and N-terminal of talin. At the opposite end, the FAT domain can be pulled away by the cytoskeletal force transmitted through paxillin/talin. This model is supported by the recent computational analysis [108] showing that the closed and the open states of FAK are reversibly reached by increasing and decreasing of pulling force.

Here, using this idea of FAK conformational change under applied force, I demonstrate that sensing of stiffness may be a distinct single-molecule response, and develop a theoretical model of reversible mechanosensor of the 2nd kind. The underlying physics of this model is applicable to a wide variety of protein complexes, but here I concentrate on the focal adhesion kinase, because FAK occupies a central point in mechanosensing pathways of focal adhesions [109]. I posit that the activation of FAK is dependent on cytoskeletal tension and ECM stiffness, and the integrin (along with other members of the force chain in Fig. 3.1) is playing a role of force transducer. Of course, without the activated integrin there would be no force transduction to ECM, and no mechanosensing. I do not consider the role of clustering. This is clearly an area of further work in this field, since clustering is definitely an important aspect of the process on stiff substrates: allostery of integrins (and associated FAK) must have a role in the signalling process, as it has in chemotaxis [110, 111]. This chapter focuses on the physical model of an individual FAK sensor operation.

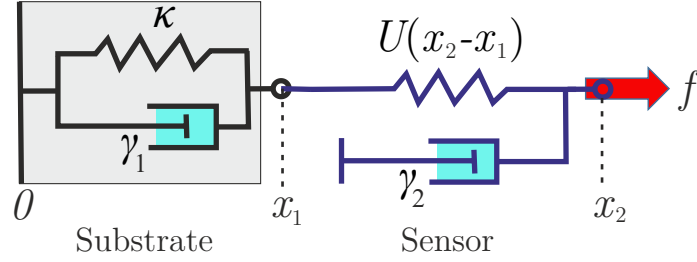


Fig. 3.2 A scheme of the 2-spring model used to produce equations (3.1). The viscoelastic substrate is characterized by its elastic stiffness and stress-relaxation time given by γ_1/κ . The conformational change of FAK is described by a potential $U(u)$, see Fig. 3.3, and the associated relaxation time determined by the damping constant γ_2 .

3.1 Model of coupled viscoelastic elements

At its heart, the problem of a bond unfolding under duress can be captured with two stochastic differential equations. The variables under consideration relate to the position of the substrate, x_1 , and the point of force application, x_2 , and the viscoelastic system is shown in Fig. 3.2. Therefore, the difference in these is effectively the separation of the bond. These variables are subject to separate thermal noise sources, if they are spatially separated: by a flexible linker in the case of single-molecule spectroscopy, and by the cell membrane in the case of cell adhesion. Regarding the bond as harmonic, and the substrate response as viscoelastic, we can write down our system:

$$\begin{aligned}\gamma_1 \dot{x}_1(t) &= -\kappa x_1(t) - \frac{\partial U[x_2(t) - x_1(t)]}{\partial x_1} + \sqrt{2k_B T \gamma_1} \xi_1(t) \\ \gamma_2 \dot{x}_2(t) &= -\frac{\partial U[x_2(t) - x_1(t)]}{\partial x_2} + f + \sqrt{2k_B T \gamma_2} \xi_2(t)\end{aligned}\quad (3.1)$$

where κ and γ_1 are the elastic and viscous response coefficients of the substrate, γ_2 is the strength of dissipation around the bond, f is the force applied to the complex, and $U(x_2 - x_1)$ is the free energy of the bond, where the bond separation $u = x_2 - x_1$. The thermal noise terms, $\xi_{1,2}(t)$, are independent normalised Gaussian noise processes.

At this point, it is important to note how the friction across the bond is implemented in the Langevin equations. The dissipation in the bond is not connected to the cell membrane, which in the language of Fig. 3.2 is at position x_1 - friction is assumed due to absolute motion of the bond, \dot{x}_2 , rather than relative to the substrate, $\dot{u} = \dot{x}_2 - \dot{x}_1$. For instance, in the case of an AFM pulling experiment, where a protein may be attached to a yielding substrate (perhaps a hydrogel), the friction resisting the absolute motion

at x_2 is a very reasonable assumption, due to the physical separation of the unfolding molecule and the substrate. The case of mechanosensing at focal adhesions is a little more nuanced. At the cell membrane, one might suspect that its motion will create a relative reference state for the sensor, and then the friction γ_2 responding to this relative motion. However, the cell membrane is not a rigid wall: it is permeable to fluids, and its transverse rigidity is negligible. So, motion in the cell membrane will not be directly translated to the sensor's environment, and we are free to consider the component of friction coming from the sensor's absolute motion. The alternative, if we were to consider a purely relative friction, i.e. the sensor represented by another Voigt model pair of elements, Fig. 3.2, would lead to the pair of equations

$$\begin{aligned}\gamma_1 \dot{x}_1(t) &= -\kappa x_1(t) + f + \sqrt{2k_B T \gamma_1} \xi_1(t) \\ \gamma_2 \dot{u}(t) &= -\frac{\partial U[u(t)]}{\partial u} + f + \sqrt{2k_B T \gamma_2} \xi_2(t),\end{aligned}\quad (3.2)$$

that is, a pair of completely independent processes with no possibility for mechanosensitivity in the bond.

For many biomolecules, there are crucial bonds that have to be overcome before the structure unfolds. Under tension, a molecule will then stretch out until we reach the limit of the molecule's length. Then the free energy will rapidly increase. If we apply a force, this will bias the free energy in favour of extended configurations. Such a profile, and the effect of applied force, is sketched out in Fig. 3.3.

The important bond's effect is encapsulated in a steep well, which has a length $u = u_m$. Beyond this, the potential is flat, as the polymer unfolds. We treat the rise in free energy due to the entropic stretching as negligible compared to the bond energy in this problem. Then, at $u = u_{\max}$, we have reached the inextensible limit of the polymer/protein. In this toy reaction profile, $U(u > u_{\max}) = \infty$.

In what follows, I show several ways to approach this problem. First, I show how we can choose a reaction pathway, and calculate the rate from this. I discuss the results, and show the limitations of this approach. Then, I ask about the mean first passage time to the end of the bond's influence, u_m . First, I consider special cases in which we can solve the system (3.1) analytically. Then, I show how we can use a different reduction of variables, by considering the mean weight at a fixed distance from the line of first passage, and then using the distance from the line of first passage as our variable.

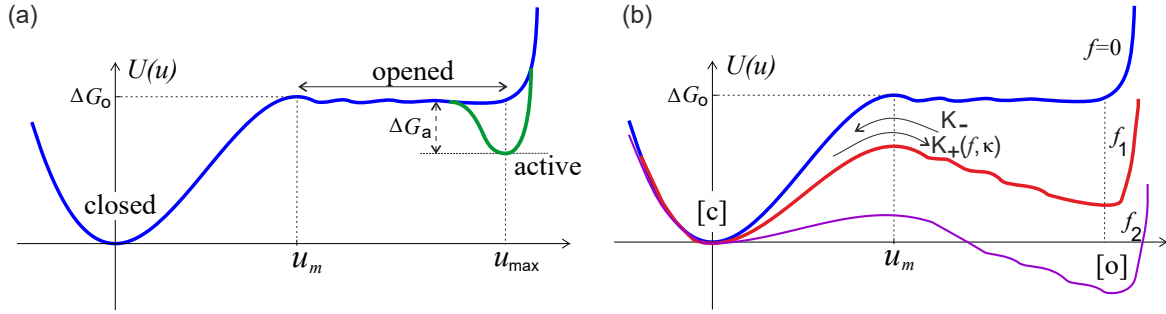


Fig. 3.3 Schematic potential energy of different FAK conformations. (a) The force-free molecule has its native folded state [c]. The binding free energy ΔG_o has to be overcome to separate the kinase from the FERM domain, after which there is a range of conformations of roughly the same energy is achieved by further separating these two domains in the open state [o]. At full separation (distance u_{\max}) the Src binding and kinase phosphorylation lead to the active state [a] of the protein, with the free energy gain ΔG_a . (b) When a pulling force is applied to this system ($f_2 > f_1 > 0$) the potential energy profile distorts, so that both [o] and [a] states shift down in energy by the same amount of $-f \cdot u_{\max}$.

3.1.1 Estimates of material parameters

We shall find that the model predictions are very sensitive to values of several key parameters so a careful discussion of their estimates is required.

We start with the strength of the bond holding the FERM and kinase domain in the closed (inhibited) state, labeled as ΔG_o in Fig. 3.3. The MD simulation study [108] estimated the energy barrier for FAK opening as $\Delta G_o \approx 28.5k_B T$, which is 17 kcal/mol at room temperature. This value seems too high, and the authors of [108] also comment on that. It is known that interdomain hydrophobic interaction in such proteins is usually low-affinity. For instance, a measurement in a different multi-domain protein gives a value for this bonding energy is 7 kcal/mol, or $\sim 11k_B T$ [112]. However, this is close to an energy of just 1-2 hydrophobic contacts, and there is more affinity between FERM and kinase domains observed in [108]. In the end, we select an intermediate value between the two limits mentioned above: $\Delta G_o \approx 17k_B T$, or 10 kcal/mol.

We take the position of the barrier from the computational study: $u_m = 0.9$ nm [108], which is a reasonable value for the protein domain structure. This determines the value of critical force at which the native minimum disappears, and the closed state [c] becomes completely unstable, $f_c = 2\Delta G_o/u_m \approx 150$ pN. This is a very high force that is likely to unfold most proteins, and is also unlikely to be generated by a single actin filament of a cell cytoskeleton. For comparison, studies investigating the force required to disrupt the fibronectin-integrin-cytoskeleton linkage, report the value of only 1–2 pN [113, 114];

this is probably too low (an underestimate), since a single myosin motor exerts ~ 3 pN of force [115, 116]. So we should explore the effect of pulling forces in the range of single to tens of pN.

We now look at substrate stiffness. For reference, the elastic modulus of a typical collagen-rich mammalian tendon is 1.2 GPa [117], of a collagen/elastin ligament: 1.1 Mpa [118], and of an aorta wall: 0.8 MPa [119]. Synthetic rubber has a modulus around 100 kPa [120]. Epithelial and glial tissues have a much lower modulus: 100 Pa-1 kPa [121, 122]. If a half-space occupied by an elastic medium (e.g. gel substrate or glass plate) with the Young modulus Y , and a point force f is applied along the surface (modeling the pulling of the integrin-ECM junction, Fig. 3.1), the response coefficient (spring constant) that we have called the stiffness is given by $\kappa = (4/3)\pi Y\xi$, where ξ is a short-distance elastic cutoff: a length scale analogous to the mesh size of a densely packed (non-filamentous) substrate. This is a classical relation going as far back as Lord Kelvin [123]. In the work of Janmey et. al [124] on comparative cell response on soft substrates, the weakest meaningful substrate had $Y = 540$ Pa. For a more typical weak gel with $Y = 10$ kPa, and a characteristic network mesh size $\xi = 10$ nm, we obtain $\kappa = 4.2 \cdot 10^{-4}$ N/m. On a stiff mineral glass with $Y = 10$ GPa, we must take the characteristic size to be a ‘cage’ size (slightly above the size of a monomer), $\xi = 1$ nm, which gives $\kappa = 42$ N/m. A typical stiff plastic has a value about 10 times smaller. So a large spectrum of stiffnesses κ could be explored by living cells.

Finally, we need estimates of the damping constants. The simulation study [108] determined a very reasonable value for the internal diffusion constant of the FAK complex: $D = k_B T / \gamma_2 \approx 6 \cdot 10^{-12} \text{m}^2 \text{s}^{-1}$. At room temperature, this gives the damping constant: $\gamma_2 = 7 \cdot 10^{-10} \text{kg s}^{-1}$. Then, the overall scale (‘bare magnitude’) of the opening rate derived below, Eq. (3.56), is approximately $(2\Delta G_o / u_m^2 \gamma_2) \approx 1.6 \cdot 10^8 \text{s}^{-1}$, which means a time scale of ca. 6 ns. This ‘bare’ time scale is compatible with available data and simulations on full and partial protein unfolding [125]; naturally, at given bonding energy and low pulling force the actual rate of FAK opening/activation would be much lower: the plots below suggest tens of microseconds to milliseconds range.

To estimate the damping constant of the viscoelastic substrate, we need the characteristic time of its internal relaxation, which is the ratio $\gamma_1 / \kappa = \tau_1$ in our notation. It is important to note here that the local time of relaxation of thermal fluctuations must not be confused with the macroscopic stress relaxation time, which can sometimes be very long in rubbers and gels. To estimate this, I use a study conducted using both AFM and a classical rheometer on a variety of polyacrylamide gels [126]. They found a reasonably constant value of $\tau_1 = 2 \times 10^{-4} \text{s}$ across gels from 300 Pa-10 kPa. Therefore, we

take $\gamma_1 = \tau_1 \kappa$. As such, the ratio between the damping coefficients, γ_2/γ_1 , takes a wide range of values, from 0.2 for soft substrates, to 10^{-4} for stiffer substrates.

3.2 Fixed reaction path approach

The first attempt to solve this problem considered a fixed reaction path approach. This begins by noticing that the problem naturally reduces to a 2-dimensional Smoluchowski equation for the variables $x(t) = x_1$ for the substrate, and $u(t)$ for the FAK conformations, with the corresponding diffusion constants $D_i = k_B T / \gamma_i$, and the Cartesian components of diffusion current:

$$J_i = -\frac{k_B T}{\gamma_i} e^{-V_{\text{eff}}/k_B T} \nabla_i \left(e^{V_{\text{eff}}/k_B T} P \right), \quad (3.3)$$

where the index $i = 1, 2$ refers to the spatial coordinates, $P(x_1, x_2; t)$ is the probability distribution of the process, and

$$V_{\text{eff}}(x_1, x_2) = \frac{1}{2} \kappa x_1^2 - f x_2 + U(x_2 - x_1) = \frac{1}{2} \kappa x^2 - f x + U(u) - f u \quad (3.4)$$

represents the effective potential landscape over which the substrate and the mechanosensor complex move, subject to thermal excitation and the external constant force f . This landscape is illustrated in Fig. 3.4.

The effective Kramers problem of escape over the barrier has been solved many times over the years [23, 24, 85, 83, 127]. The multi-dimensional Kramers escape problem, with the potential profile not dissimilar to that in Fig. 3.4 was also solved several times [128, 129]. Unlike previous approaches, here I do not allow unphysical solutions by mistreating the case of very low/vanishing barrier. In the case when the effective potential barrier is not high enough to permit the classical Kramers approach of steepest descent integrals, one of several good general methods is via Laplace transformation of the Smoluchowski equation [25, 85]. The compact answer for the mean time of first passage from the closed state [c] to the top of the barrier of height ΔG a distance Δu away is:

$$\tau_+ = \frac{\Delta u^2}{D} \left[\left(\frac{k_B T}{\Delta G} \right)^2 \left(e^{\Delta G/k_B T} - 1 \right) - \frac{k_B T}{\Delta G} \right]. \quad (3.5)$$

There are many complexities regarding choosing an optimal path across the potential landscape $V_{\text{eff}}(x, u)$, some of which are discussed in [128, 129], but we are aiming for the quickest way to a qualitatively meaningful answer. As such, let us assume that the reaction path consists of two ‘legs’: from the origin down to the minimum of the

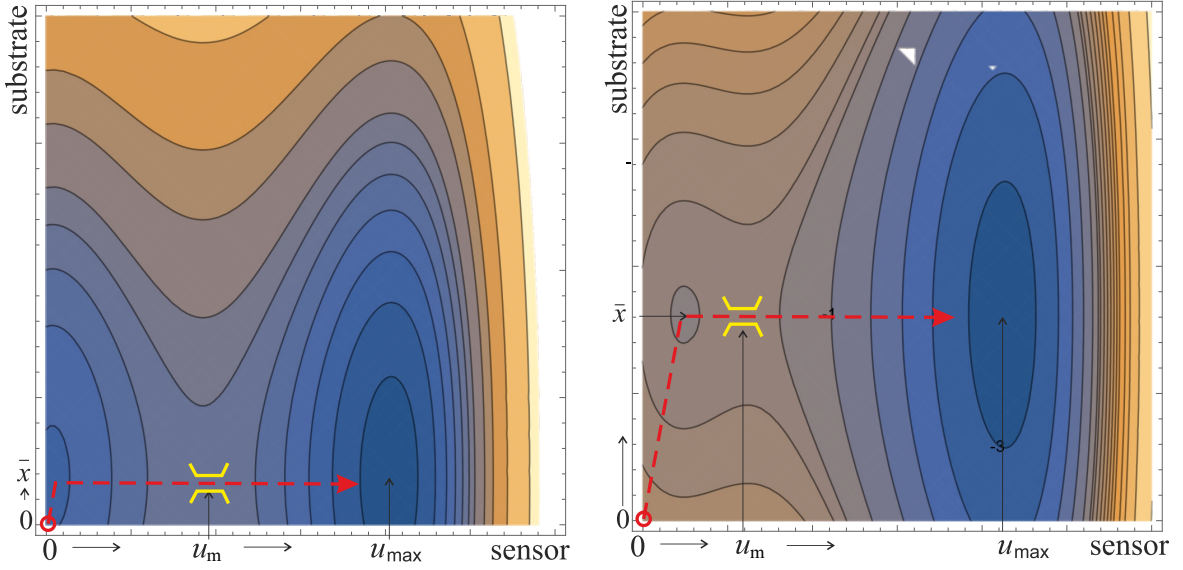


Fig. 3.4 The 2D contour plot of the effective potential $V_{\text{eff}}(x, u)$ at low pulling force [left] and at high pulling force [right]. The position of substrate anchoring has moved from $x = 0$ to $\bar{x} = f/\kappa$, and the depth of the energy well of the [o] state has lowered to $\Delta G_o - fu_{\text{max}}$. The dashed line shows the path of the system evolution that leads to crossing the barrier towards the open state.

potential, which is shifted to $\bar{x} = f/\kappa$ due to the substrate deformation, and then from this minimum straight over the saddle (barrier) into the open state of FAK conformation. The average time along the first leg is given by Eq. (3.5) with the distance $\Delta u = \bar{x}$ and the negative elastic energy in this minimum, $E = -f^2/2\kappa$, with the diffusion constant determined by the damping constant of the substrate:

$$\tau_{\text{drift}} = \frac{2\gamma_1}{\kappa} + \frac{4\gamma_1 k_B T}{f^2} \left(e^{-f^2/2\kappa k_B T} - 1 \right). \quad (3.6)$$

Here the ratio γ_1/κ is the characteristic time of fluctuation relaxation in the viscoelastic substrate [130], which will play a significant role in our results. Naturally, $\tau_{\text{drift}} = 0$ when there is no pulling force and the effective potential minimum is at $(x = 0, u = 0)$.

In the region between the minimum of V_{eff} and the potential barrier, a number of earlier papers [131, 127, 129] have used the effective cubic potential to model this portion of $U(u)$. In this case, when the pulling force is applied, the barrier height is reducing as: $E = \Delta G_o (1 - 2fu_m/3\Delta G_o)^{3/2}$. The distance between the minimum [c] and the maximum at the top of the barrier is reducing as well: $\Delta u = u_m (1 - 2fu_m/3\Delta G_o)^{1/2}$.

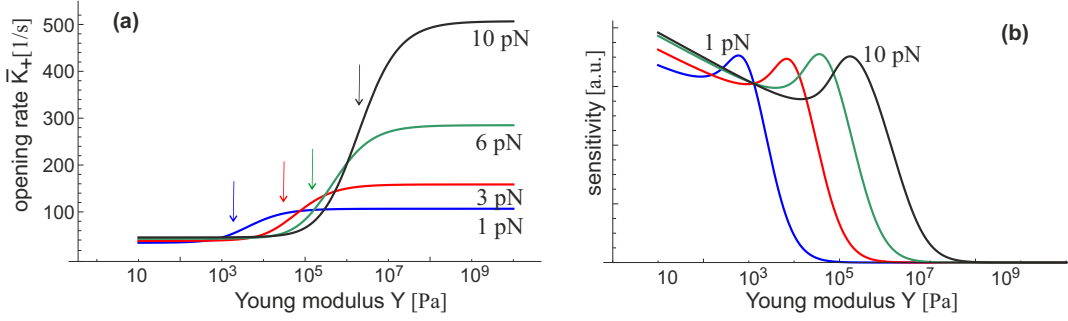


Fig. 3.5 (a) The rate constant of the $[c] \rightarrow [o]$ transition $K_+(f, \kappa)$ plotted against the substrate stiffness (on logarithmic scale) for several values of pulling force f . The arrows point at the inflection point on each curve, i.e. the region of maximum sensitivity. (b) The plot of ‘sensitivity’ dK_+/dY for the same parameters, illustrating the maximum sensitivity range at each level of pulling force. In this figure, $\tau_1 = 0.01s$.

Substituting these values into Eq. (3.5), we find the mean passage time over the barrier:

$$\tau_{\text{open}} = -\frac{\gamma_2 u_m^2}{\Delta G_o \left(1 - \frac{2fu_m}{3\Delta G_o}\right)^{1/2}} + \frac{\gamma_2 k_B T u_m^2}{\Delta G_o^2 \left(1 - \frac{2fu_m}{3\Delta G_o}\right)^2} \left(e^{\Delta G_o \left(1 - \frac{2fu_m}{3\Delta G_o}\right)^{3/2} / k_B T} - 1 \right). \quad (3.7)$$

In the limit of high barrier $\Delta G_o \gg k_B T$, and small pulling force, this expression becomes proportional to $e^{-(\Delta G_o - fu_m)/k_B T}$, i.e. recovers the ‘Bell formula’ that people use widely. When the force increases towards the limit $f_c = 3\Delta G_o/2u_m$, this time τ_{open} reduces dramatically: there is no barrier left to overcome, and the minimum of V_{eff} shifts to coincide with the entrance to the $[o]$ state.

The overall rate constant of the $[c] \rightarrow [o]$ transition, K_+ , is then determined as the inverse of the total time:

$$K_+ = \frac{1}{\tau_{\text{drift}} + \tau_{\text{open}}}. \quad (3.8)$$

Figure 3.5 presents the rate of FAK opening for several values of pulling force, as a function of substrate stiffness. The rate of FAK activation has a characteristic (generic) form of any sensor, in that it undergoes a continuous change between the ‘off’ and ‘on’ states. The latter is a state of high rate of FAK opening and the subsequent phosphorylation that occurs on stiffer substrates. The force applied to the complex determines its response for a given substrate: the substrate could be ‘too soft’, meaning that FAK does not activate at all – and also ‘too stiff’, where the rate of activation reaches a plateau and no longer responds to further stiffening. Between these two limits, there is a range of maximum sensitivity where the rate of activation directly reflects the change of substrate stiffness. Note, that due to the logarithmic scale, this range is actually as

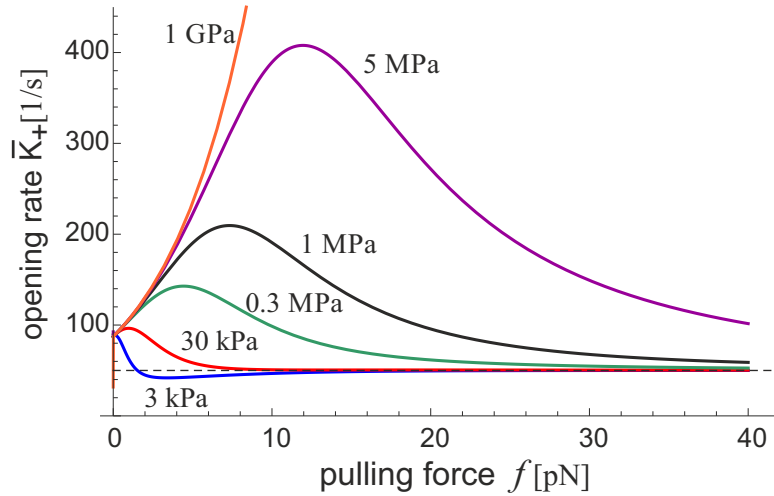


Fig. 3.6 The rate constant of FAK opening $K_+(f, \kappa)$ is plotted as a function of the cytoskeletal pulling force f , for several values of substrate stiffness labelled on the plot. The dashed line marks the rate $K_{\text{sub}} = 1/2\tau_1$ for the opening without any barrier. The homeostatic peaks of activation rate $K_+(f)$, for each given substrate stiffness, roughly correspond to the peak of sensitivity in Fig. 3.5(b) at the same level of force. This suggests that the cell self-adjusts the sensor to keep it at the optimal sensitivity on each substrate. In this figure, $\tau_1 = 0.01\text{s}$

much as one order of magnitude in stiffness – quite broad, and we suspect more than enough to precisely sense local variations in stiffness. Figure 3.5(b) highlights this by presenting the ‘sensitivity’ directly as the value of the derivative $dK_+/d\kappa$. We see that cells with a higher pulling force (i.e. with high actin-myosin activity and more developed stress fibers) are sensitive to the substrates in the more stiff range. In contrast, cells that exert a low pulling force (i.e. no stress fibers, lower actin-myosin activity) are mostly sensitive to soft substrates. This is in good agreement with broad observations about the cell mechanosensitivity of the 2nd kind, and their response to substrate stiffness.

The dependence of the sensor on the force applied by the cytoskeleton is illustrated in Fig. 3.6. We see a rapid increase in the rate that FAK opens (and its subsequent phosphorylation) on stiffer substrates. For the complex to actively probe the substrate stiffness (mechanosensitivity of the 2nd kind), we posit that the cell remodels itself in response to FAK activation, increasing the pulling force. This further increases the level of FAK activation in a positive feedback manner, until a maximum rate is reached. Any increase in force beyond this point decreases the rate of FAK opening. This would act as a mechanism for negative feedback, which settles the cell tension in homeostasis at the peak of the corresponding curves in Fig. 3.6. The stiffer the substrate, the higher the rate of FAK activation and, accordingly, the more α -SMA stress fibres one would find

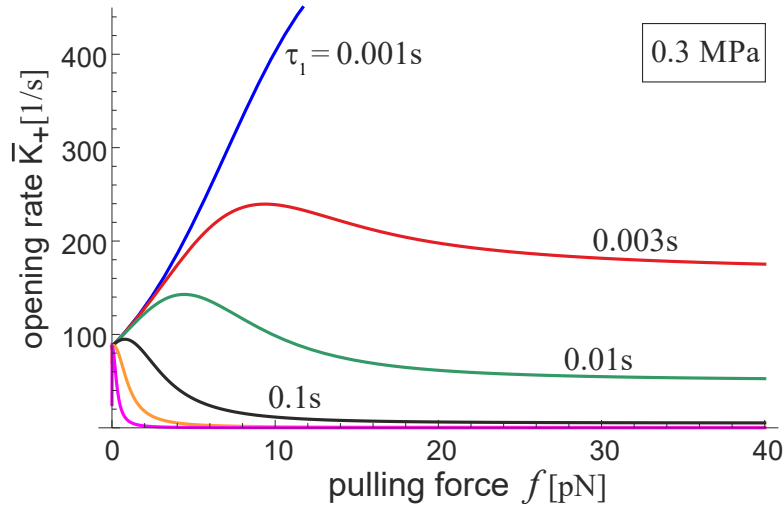


Fig. 3.7 The rate of the $[c] \rightarrow [o]$ transition $K_+(f, \kappa)$ plotted against the pulling force f (in the biologically relevant range of small forces) for a set of values τ_1 labelled on the plot representing the change in stress-relaxation characteristics of the substrate (the last two curves are for $\tau_1 = 1\text{s}$ and 10s , respectively).

in this adjusted cell (leading to morphological changes such as fibroblast-myofibroblast transition, or the fibrosis of smooth muscle cells). On soft substrates with sufficiently small Young's modulus there is no positive force that gives a maximum in the opening rate. Thus, any pulling force on the FAK-integrin-ECM chain has the effect of further lowering the activation of FAK relative to the tension-free state, and so the cell does not develop any additional tension in the cytoskeleton. This is consistent with the observation that cells do not develop focal adhesions on soft gels. The strong effect of substrate viscoelasticity on the absolute value of rate of FAK activation K_+ is shown in Fig. 3.7, for an example of a typical rubber with the Young modulus of $\sim 300\text{ MPa}$. A range of τ_1 is tested, and here these results predict that material with a longer relaxation time has a reduced response at any pulling force. This is essentially analogous to the substrate appearing 'softer'.

The fixed reaction path approach gives very nice biological behaviour – a built-in mechanism for homeostatic response, and a sensor whose sensitivity adapts according to the applied force. However, on closer reflection, it became less clear how we could explain the peaked response of the sensor to applied force. The mechanism for it in the fixed reaction path is that the system must wait until the substrate is in equilibrium to transition, which effectively caps the rate at the substrate relaxation rate. However, there is no a priori reason to assume this – there will always be an applied force across the bond as the substrate is equilibrating (although perhaps not the full force f), and

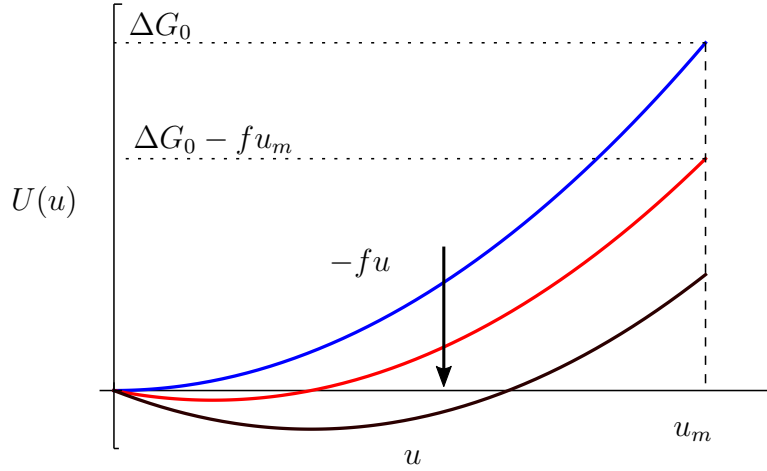


Fig. 3.8 Harmonic potential modelling a bond under force. Once the bond length $u = x_2 - x_1$ reaches a critical value, u_m , it will snap open irreversibly (the potential drops to $U = -\infty$ past the barrier). Increasing the force applied to the bond lowers the barrier height and moves the minimum at f/μ closer to the barrier position.

this may well destabilise the bond enough to transition before the substrate reaches mechanical equilibrium. To examine this, we can strip the problem back, removing the complexity of the potential, and looking for limiting cases.

3.3 Ornstein-Uhlenbeck approach

Instead of considering the whole free energy profile of our extending biomolecule, we can ask about the mean first passage time to the end of the harmonic section of potential, so that we may consider the potential $U(x_2 - x_1) = \mu(x_2 - x_1)^2/2$ as in Fig. 3.8. We can write out the system in Eqs. (3.1) in a standard vector form, for $\mathbf{x}(t) = (x_1(t), x_2(t))$, and stochastic force $\boldsymbol{\xi}(t) = (\xi_1(t), \xi_2(t))$:

$$\dot{\mathbf{x}} = -M(\mathbf{x}(t) - \bar{\mathbf{x}}) + \sigma\boldsymbol{\xi}(t), \quad (3.9)$$

where the quantities M , $\bar{\mathbf{x}}$, and σ are defined as:

$$M = \begin{pmatrix} (\kappa + \mu)/\gamma_1 & -\mu/\gamma_1 \\ -\mu/\gamma_2 & \mu/\gamma_2 \end{pmatrix}, \quad \bar{\mathbf{x}} = M^{-1} \begin{pmatrix} 0 \\ f/\gamma_2 \end{pmatrix}, \quad \sigma = \begin{pmatrix} \sqrt{2k_B T/\gamma_1} & 0 \\ 0 & \sqrt{2k_B T/\gamma_2} \end{pmatrix}. \quad (3.10)$$

Physically, the matrix M is the coefficient of restoring force, and the matrix σ gives the strength of thermal fluctuations in the system. The vector $\bar{\mathbf{x}}$ gives the equilibrium position of the system in phase space in the absence of thermal fluctuations. Equation (3.9) is the

standard form of a two-dimensional Ornstein-Uhlenbeck process. In general, the matrix M is not diagonal. The stochastic force matrix σ need not be diagonal either, but in the set-up of our problem in (x_1, x_2) variables, it is.

To solve this equation we diagonalise M , and finding its eigenvectors, \mathbf{e}_i , and corresponding eigenvalues, λ_i . These give the normal modes and their characteristic relaxation times. Then, we can use a result in the literature to give us information about the first passage time to the barrier, when $x_2 - x_1 = u_m$. Once we have found the eigenvalues, we can diagonalise M by using the matrix whose columns are the eigenvectors,

$$R = \begin{pmatrix} \mathbf{e}_1 & \mathbf{e}_2 \end{pmatrix}. \quad (3.11)$$

Then, left multiplying by the inverse of R , and insertion of the identity matrix:

$$\frac{\partial}{\partial t} R^{-1} \mathbf{x} = -R^{-1} M R (R^{-1} \mathbf{x} - R^{-1} \bar{\mathbf{x}}) + (R^{-1} \sigma) \boldsymbol{\xi}(t) \quad (3.12)$$

gives a system of equations diagonal in the new variables $\mathbf{x}' = R^{-1} \mathbf{x}$:

$$\dot{\mathbf{x}}' = -\text{diag} M (\mathbf{x}' - \bar{\mathbf{x}}') + \sigma' \boldsymbol{\xi}(t), \quad (3.13)$$

where $\bar{\mathbf{x}}' = R^{-1} \bar{\mathbf{x}}$, and $\text{diag} M_{ij} = \lambda_i \delta_{ij}$. Note that the stochastic matrix $\sigma' = R^{-1} \sigma$ is not diagonal, and so the stochastic forces affecting the two natural variables are no longer independent sources of noise.

Now, since we have expressed the process in its natural variables, we can treat each one as a separate Ornstein-Uhlenbeck process, and write the solution for each of the natural variables x'_i as

$$x'_i(t) = x'_i(0) e^{-\lambda_i t} + \bar{x}'_i (1 - e^{-\lambda_i t}) + \sigma'_{ij} \int_0^t e^{-\lambda_i(t-s)} \xi_j(s) ds \quad (3.14)$$

From this equation, we can calculate the mean and expectation of the variables \mathbf{x}' , but this is only of limited use in our problem. The main issue for finding first passage times is that the separation $x_2 - x_1$ is a function of both x'_1 and x'_2 . Hence, when we look for the approach to the line of first passage, we have to consider a 2D first passage process. It is only in certain cases that we can address the problem analytically, where the 2D problem naturally simplifies to one dimension.

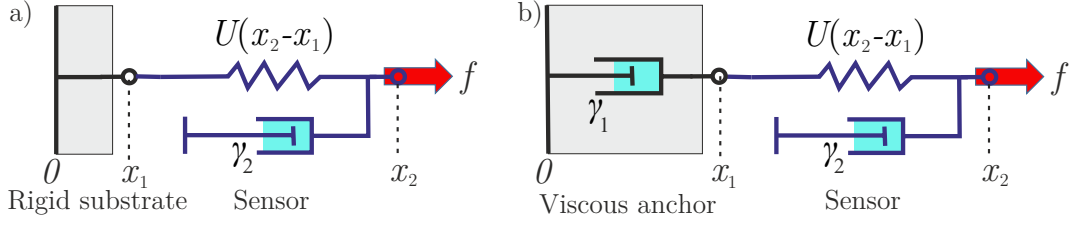


Fig. 3.9 Schematics showing the two limiting cases in which the two-dimensional problem reduces naturally to a single variable: the bond separation u . Schematic a) shows the rigid substrate case, where $\kappa \rightarrow \infty$, and b) shows the viscous anchor case, where $\kappa \rightarrow 0$.

3.3.1 Two limiting cases

It turns out that there are two different cases where the problem reduces easily to one variable: the case of $\kappa \rightarrow \infty$, when the substrate is completely rigid, and x_1 becomes fixed, and the case that $\kappa = 0$, when the anchoring substrate has no elastic modulus. In these cases, we can quickly arrive at expressions for time to u_m .

The mean first passage time for this is a known formula, derived in one paper by Ricciardi and Sato [132]. This paper takes a one-dimensional Ornstein-Uhlenbeck process written in a standard form,

$$\dot{x}(t) = -Mx(t) + \sigma\xi(t), \quad (3.15)$$

starting at $x(0)$, and reaching a final value $S > x(0)$. Then, the MFPT is given by

$$\tau = \phi(S) - \phi(x(0)), \quad (3.16)$$

where the function $\phi(z)$ is the infinite series

$$\phi(z) = \frac{1}{2M} \sum_{n=1}^{\infty} \frac{\Gamma(n/2)}{n!} \left(\frac{z\sqrt{M}}{\sigma} \right)^n. \quad (3.17)$$

In the case that $0 < S < x(0)$, then one should take the problem with $S \rightarrow -S$ and $x(0) \rightarrow -x(0)$. This careful treatment of signs is necessary as the initial conditions explored are force-dependent, and so depending on the value of the force we may have to use different expressions.

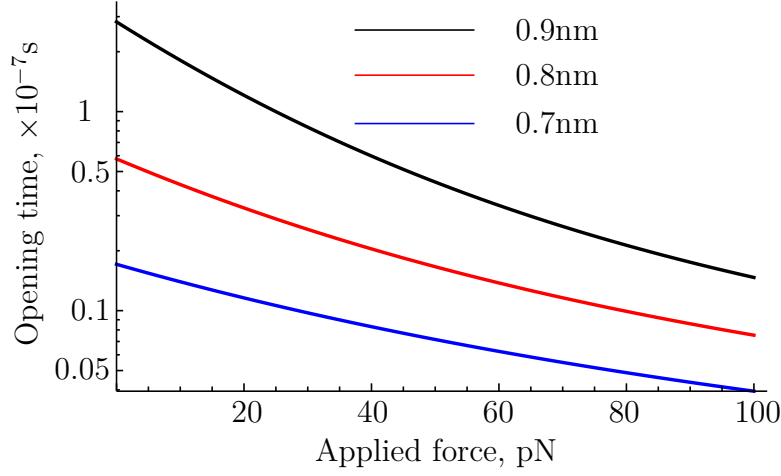


Fig. 3.10 The MFPT plotted against applied force on a rigid substrate. The critical bond separation u_m is different for the two curves: $u_m = 0.9\text{nm}$ for the black curve, $u_m = 0.8\text{nm}$ for the red curve, and $u_m = 0.7\text{nm}$ for the blue curve, with the same energy barrier height. A smaller u_m implies a steeper quadratic well, as $\mu = 2\Delta G/u_m^2$. The plot shows that higher stiffness results in a smaller unbinding time.

A rigid substrate

In this case of a rigid substrate, the set of equations reduces to simply the dynamical equation for x_2 , and so the equation determining the separation, u , is

$$\dot{u} = -\frac{\mu}{\gamma_2} \left(u - \frac{f}{\mu} \right) + \sqrt{\frac{2k_B T}{\gamma_2}} \xi(t) \quad (3.18)$$

We are seeking the MFPT from $u_0 = 0$ to the final bond length $S = u_m > 0$. To put Eq. (3.18) into the Ricciardi-Sato form, we shift the variable u : $\tilde{u} = u - f/\mu$. Then, we can use the Ricciardi-Sato formula, starting at $\tilde{u}(0) = -f/\mu$, and finishing at $\tilde{S} = u_m - f/\mu$. The function $\phi_{\text{rigid}}(z)$ has the form:

$$\phi_{\text{rigid}}(z) = \frac{\gamma_2}{2\mu} \sum_{n=1}^{\infty} \frac{\Gamma(n/2)}{n!} \left(z \sqrt{\frac{\mu}{2k_B T}} \right)^n \quad (3.19)$$

Then, the MFPT is

$$\tau_{\text{rigid}} = \phi_{\text{rigid}}(u_m - f/\mu) - \phi_{\text{rigid}}(-f/\mu). \quad (3.20)$$

This result holds while there is still a stable minimum in the potential. This will be true for forces less than the critical force $f_c = \mu u_m$, where the minimum will coincide with the barrier position u_m . Figure 3.10 shows that the MFPT decreases as a function of applied

force. For a fixed barrier height, stiffer bonds will be easier to break, as the barrier is closer to the minimum.

A viscous anchor

When the substrate has no elastic response, and is instead only a viscous anchor, we can set $\kappa = 0$ in Eq. (3.9). The restoring matrix M then has a particularly simple form:

$$M = \mu \begin{pmatrix} 1/\gamma_1 & -1/\gamma_1 \\ -1/\gamma_2 & 1/\gamma_2 \end{pmatrix}. \quad (3.21)$$

The eigenvectors reduce to a simple form as well, and then we can write the matrix R as

$$R = \begin{pmatrix} 1 & -\gamma_2/\gamma_1 \\ 1 & 1 \end{pmatrix} \quad (3.22)$$

The inverse of the matrix gives the natural variables

$$\mathbf{x}' = R^{-1}\mathbf{x} = \frac{\gamma_1}{\gamma_1 + \gamma_2} \begin{pmatrix} 1 & \gamma_2/\gamma_1 \\ -1 & 1 \end{pmatrix} \begin{pmatrix} x_1 \\ x_2 \end{pmatrix} \quad (3.23)$$

Now, the variable $x'_2 = (x_2 - x_1)\gamma_1/(\gamma_1 + \gamma_2)$: just the separation u scaled by a constant factor! However, unlike the case of a completely rigid substrate, where there were no thermal fluctuations in the substrate, we have to deal with thermal fluctuations in the substrate, and on the complex. For a viscous anchor, the full solution for our natural variable u is:

$$u(t) = u_0 e^{-\lambda t} + \frac{f}{\mu} (1 - e^{-\lambda t}) - \sqrt{\frac{2k_B T}{\gamma_1}} \int_0^t e^{-\lambda(t-s)} \xi_1(s) ds + \sqrt{\frac{2k_B T}{\gamma_2}} \int_0^t e^{-\lambda(t-s)} \xi_2(s) ds, \quad (3.24)$$

where $\lambda = \mu(\gamma_1 + \gamma_2)/\gamma_1\gamma_2$. Usefully, we can combine the noise terms, in a version of Pythagoras' theorem. Consider the process

$$Z(t) = X(t) + Y(t), \quad (3.25)$$

where $X(t)$ and $Y(t)$ are independent Gaussian white noise terms, with correlation functions $\langle X(t)X(t') \rangle = \sigma_X^2 \delta(t-t')$, $\langle Y(t)Y(t') \rangle = \sigma_Y^2 \delta(t-t')$, and $\langle X(t)Y(t') \rangle = 0$. The

process $Z(t)$ is another Gaussian white noise, with moments given by [25]:

$$\langle Z(t) \rangle = \langle X(t) \rangle + \langle Y(t) \rangle = 0 \quad (3.26)$$

$$\langle Z(t)Z(t') \rangle = (\sigma_X^2 + \sigma_Y^2)\delta(t - t') = \sigma_Z^2\delta(t - t'), \quad (3.27)$$

As such, we may combine the two white noise terms in Eq. (3.24) as so:

$$\sqrt{\frac{2k_B T}{\gamma_1}}\xi_1(t) + \sqrt{\frac{2k_B T}{\gamma_2}}\xi_2(t) = \sqrt{2k_B T \left(\frac{1}{\gamma_1} + \frac{1}{\gamma_2} \right)}\xi(t) = \sqrt{\frac{2k_B T}{\tilde{\gamma}}}\xi(t), \quad (3.28)$$

where $\tilde{\gamma} = \gamma_1\gamma_2/(\gamma_1 + \gamma_2)$ is the reduced dissipation constant, and we see that the separation u is a one-dimensional Ornstein-Uhlenbeck process with solution

$$u(t) = u_0 e^{-\lambda t} + \frac{f}{\mu} (1 - e^{-\lambda t}) + \sqrt{\frac{2k_B T}{\tilde{\gamma}}} \int_0^t e^{-\lambda(t-s)} \xi(s) ds. \quad (3.29)$$

The relaxation timescale $1/\lambda$ contains a reduced friction coefficient. Now, to use the Ricciardi-Sato formula, we must again shift into coordinates $\tilde{u} = u - f/\mu$, with a starting position $\tilde{u} = -f/\mu$, and boundary $\tilde{S} = u_m - f/\mu$. This is actually just the same formula as for the rigid substrate, with the substitution of the bond dissipation constant with the reduced dissipation constant: $\gamma_2 \rightarrow \tilde{\gamma}$. Therefore, we see that if there is very high dissipation in the viscous anchor, the system behaves as if the substrate is rigid.

The MFPT follows from the Ricciardi-Sato result again, and uses the function $\phi_{\text{visc}}(z)$:

$$\phi_{\text{visc}}(z) = \frac{\tilde{\gamma}}{2\mu} \sum_{n=1}^{\infty} \frac{\Gamma(n/2)}{n!} \left(z \sqrt{\frac{\mu}{2k_B T}} \right)^n, \quad (3.30)$$

so that the MFPT for forces less than the critical force, $f < \mu u_m$, is

$$\tau_{\text{visc}} = \phi_{\text{visc}}(u_m - f/\mu) - \phi_{\text{visc}}(-f/\mu). \quad (3.31)$$

The mean first passage time for a viscous anchor is plotted in Fig. 3.11. The larger the friction coefficient, the longer the unbinding time, as the system takes longer to relax. Note that again, the unbinding time is monotonically decreasing as the force applied increases, in stark contrast to the results from the reaction path approach.

One important thing to note is that if either of the damping coefficients go to zero, then the MFPT $\tau \rightarrow 0$ for both the rigid substrate and the viscous anchor. The reason for this is the fluctuation-dissipation theorem: in the limit of vanishingly small damping, the fluctuations in the system will be massive, and it will be knocked out over the barrier

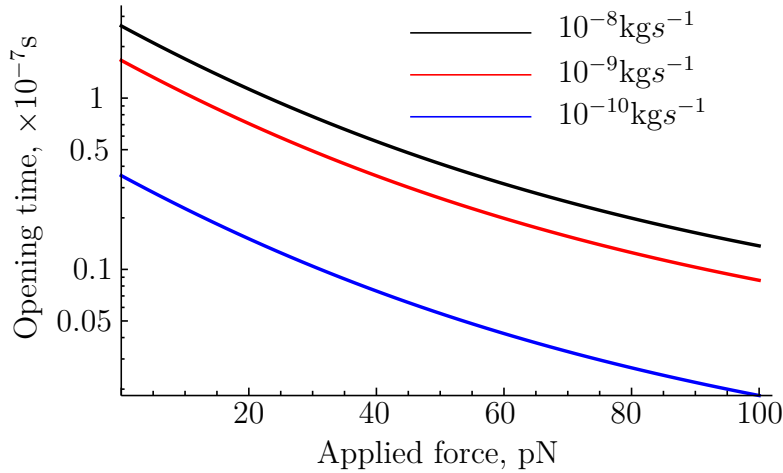


Fig. 3.11 MFPT for a viscous anchor for different values of viscosity γ_1 against applied force. The values of viscosity are chosen to loosely reflect the friction coefficients of polyacrylamide gels. A higher friction coefficient results in a higher first passage time. All other parameters are as given in Section 3.1.1.

almost immediately. Of course, in such a limit, we are no longer free to neglect inertial terms, and so this result is not valid. We will assume here, as in the extra-cellular matrix, that the fluid viscosity is much greater than the friction coefficient of the bond.

3.4 Mean field approach

If we want to consider cases besides the simple limits presented above, then there is no simple transformation of variables to find the separation. In particular, since the separation does not naturally emerge as a normal mode of the system, the formal solution has two exponential terms, and so can't be expressed as a simple Ornstein-Uhlenbeck process. We have to find other ways to isolate the bond separation. The approach explored here integrates out a degree of freedom, and creates a 'mean field' approximation to the probability density, with the bond separation as the independent variable. To do this, we transform into a coordinate system based around the distance from the breaking point. Then we can integrate over lines of fixed distance from the barrier. Now we have a 1D problem, and can use the backward Fokker-Planck formalism to come up with an estimate of the first passage time.

We start at the original diffusion equation in (x_1, x_2) coordinates:

$$\begin{aligned} \frac{\partial p}{\partial t} = & D_1 \frac{\partial^2 p}{\partial x_1^2} + D_2 \frac{\partial^2 p}{\partial x_2^2} - \frac{\partial}{\partial x_1} \left[\left(\frac{\mu}{\gamma_1} (x_2 - x_1) - \frac{\kappa x_1}{\gamma_1} \right) p \right] \\ & - \frac{\partial}{\partial x_2} \left[\left(-\frac{\mu}{\gamma_2} (x_2 - x_1) + \frac{f}{\gamma_2} \right) p \right] \end{aligned} \quad (3.32)$$

This is derived using a standard method from the underlying stochastic differential equations. The coordinate transformation requires a little algebra to derive, but it can be shown that the new coordinates are given by:

$$u = x_2 - x_1, \quad v = x_1 + x_2, \quad (3.33)$$

where it is the v variable that we are to integrate over. Then, by the chain rule, the relevant differential operators are

$$\frac{\partial}{\partial x_1} = \frac{\partial}{\partial v} - \frac{\partial}{\partial u}, \quad \frac{\partial}{\partial x_2} = \frac{\partial}{\partial v} + \frac{\partial}{\partial u}. \quad (3.34)$$

Now, the diffusion equation becomes

$$\begin{aligned} \frac{\partial p}{\partial t} = & (D_1 + D_2) \left(\frac{\partial^2 p}{\partial v^2} + \frac{\partial^2 p}{\partial u^2} \right) + 2(D_2 - D_1) \frac{\partial^2 p}{\partial v \partial u} \\ & - \left(\frac{\partial}{\partial v} - \frac{\partial}{\partial u} \right) \left[\left(\frac{\mu}{\gamma_1} u - \frac{\kappa(v-u)}{2\gamma_1} \right) p \right] - \left(\frac{\partial}{\partial v} + \frac{\partial}{\partial u} \right) \left[\left(-\frac{\mu}{\gamma_2} u + \frac{f}{\gamma_2} \right) p \right] \end{aligned} \quad (3.35)$$

We can now integrate over v , to obtain a new diffusion equation for the effective probability distribution $P = \int dv p(v, u)$. This relies on the behaviour of the full probability distribution and its derivative at $v = \pm\infty$, but since the potential is harmonic, we can say that the probability distribution and its derivative go to zero faster than the potential becomes infinite. We can write this mean-field diffusion equation in u as:

$$\frac{\partial P}{\partial t} = (D_1 + D_2) \frac{\partial^2 P}{\partial u^2} - \frac{\partial}{\partial u} \left[\left(-\left(\frac{\mu}{\tilde{\gamma}} + \frac{\kappa}{2\gamma_1} \right) u + \frac{f}{\gamma_2} \right) P \right] \quad (3.36)$$

We can rewrite the diffusion coefficient using the Stokes-Einstein relation with the effective friction coefficient $\tilde{\gamma}$,

$$D = \frac{k_B T}{\gamma_1} + \frac{k_B T}{\gamma_2} = \frac{k_B T (\gamma_1 + \gamma_2)}{\gamma_1 \gamma_2} = \frac{k_B T}{\tilde{\gamma}} \quad (3.37)$$

Now, we can collect together the potential terms:

$$\frac{\mu}{\tilde{\gamma}} + \frac{\kappa}{2\gamma_1} = \frac{\tilde{\mu}}{\tilde{\gamma}} \quad (3.38)$$

where the effective stiffness of the bond $\tilde{\mu} = \mu + \kappa(\tilde{\gamma}/2\gamma_1)$ is modulated by the characteristics of the viscoelastic substrate, $\tau_1 = \kappa/\gamma_1$. We can use these definitions to rewrite the diffusion equation:

$$\frac{\partial P}{\partial t} = D \frac{\partial^2 P}{\partial u^2} - \frac{\partial}{\partial u} \left[\left(-\frac{\tilde{\mu}u}{\tilde{\gamma}} + \frac{f}{\gamma_2} \right) P \right] \quad (3.39)$$

From this diffusion equation we can write down the effective potential for the separation u :

$$V_{\text{eff}}(u) = \frac{\tilde{\mu}u^2}{2} - \frac{fu\tilde{\gamma}}{\gamma_2}, \quad (3.40)$$

which contains a harmonic term from the bond, and from the restoring force from the substrate, and a term for the work done by the applied force. Note that the force is scaled by the factor $\tilde{\gamma}/\gamma_2$. There will be more discussion on this later, but I claim that this is the effective force felt across the bond at short times. The mean first passage time for constant D as derived in Eq. (1.85) can be adapted for the case when the absorbing boundary is at the upper end of the interval:

$$\tau(u_0) = \frac{1}{D} \int_{u_0}^{u_m} dy e^{\beta V_{\text{eff}}(y)} \int_{-\infty}^y dx e^{-\beta V_{\text{eff}}(x)}. \quad (3.41)$$

It is useful to rewrite the effective potential by completing the square:

$$V_{\text{eff}}(x) = \frac{\tilde{\mu}}{2} \left(x - \frac{f\tilde{\gamma}}{\tilde{\mu}\gamma_2} \right)^2 - \frac{f^2\tilde{\gamma}^2}{2\tilde{\mu}\gamma_2^2}. \quad (3.42)$$

Since the effective potential appears with opposite signs in the integrals in Eq. (3.41), the constant term can be cancelled in the integration. Defining the effective free energy minimum $\bar{u} = f\tilde{\gamma}/\tilde{\mu}\gamma_2$, we are left with

$$\tau(u_0) = \frac{1}{D} \int_{u_0}^{u_m} dy e^{\beta\tilde{\mu}(y-\bar{u})^2/2} \int_{-\infty}^y dx e^{-\beta\tilde{\mu}(x-\bar{u})^2/2} \quad (3.43)$$

The inner integral can be rewritten as the cumulative density of the normal distribution, $\Phi(x)$, scaled by a factor:

$$\tau(u_0) = \tilde{\gamma} \sqrt{\frac{2\pi\beta}{\tilde{\mu}}} \int_{u_0}^{u_m} dy e^{\beta(y-\bar{u})^2/2} \Phi \left(\sqrt{\beta\tilde{\mu}}(y-\bar{u}) \right) \quad (3.44)$$

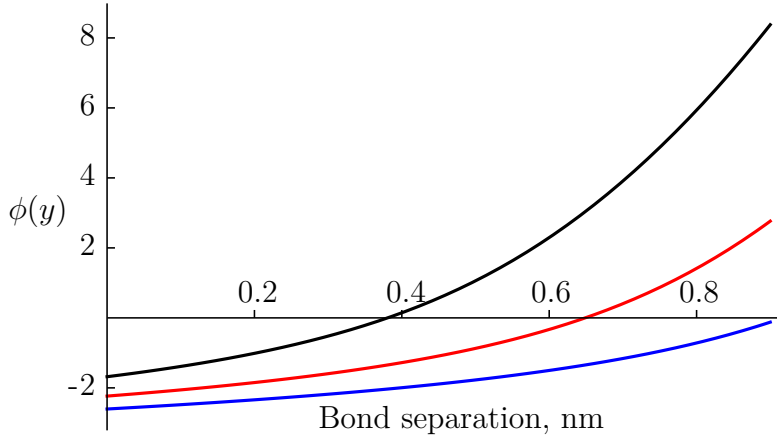


Fig. 3.12 The exponent of the steepest descent $\phi(y)$ plotted as a function of the bond separation u , for a maximal bond length of $u = 0.9\text{nm}$. For low forces, the exponent is very large close to the barrier, and so the integral in Eq. (3.45) will be well approximated by the method of steepest descent around the barrier. However, as the force nears the critical force, at 150pN , this approximation is much less sound.

This integral is not analytically solvable. However, we use the method of steepest descent to make an approximation. In particular, we can write the integrand as an exponential

$$\tau(u_0) = \tilde{\gamma} \sqrt{\frac{2\pi\beta}{\tilde{\mu}}} \int_{-u_m}^{u_0} dy e^{\phi(y)} \quad (3.45)$$

where the function $\phi(y)$ is

$$\phi(y) = \frac{\beta\tilde{\mu}(y - \bar{u})^2}{2} + \ln \Phi \left(\sqrt{\beta\tilde{\mu}}(y - \bar{u}) \right). \quad (3.46)$$

The exponent $\phi(y)$ is plotted in Fig. 3.12, and we can see that it is dominated by the region around the barrier. As such, we can expand the exponent as a Taylor series around the barrier:

$$\phi(y) \approx \phi(u_m) + \phi'(u_m)(y - u_m) \quad (3.47)$$

Using this expansion, the mean first passage time from u_0 can be approximated as

$$\begin{aligned} \tau(u_0) &= \tilde{\gamma} \sqrt{\frac{2\pi\beta}{\tilde{\mu}}} e^{\phi(u_m) - \phi'(u_m)u_m} \int_{u_0}^{u_m} e^{\phi'(u_m)y} dy \\ &= \tilde{\gamma} \sqrt{\frac{2\pi\beta}{\tilde{\mu}}} \frac{e^{\phi(u_m)}}{\phi'(u_m)} \left(1 - e^{\phi'(u_m)(u_0 - u_m)} \right). \end{aligned} \quad (3.48)$$

We are now close to an answer, and all that is left is to average over the initial position distribution. The scenario imagined is one where the force is applied at time $t = 0$, and so the initial position distribution is actually the force-free steady state distribution:

$$p(u_0) = \sqrt{\frac{\beta\tilde{\mu}}{2\pi}} e^{-\beta\tilde{\mu}\frac{u_0^2}{2}}. \quad (3.49)$$

The mean first passage time is

$$\tau = \int_{-\infty}^{u_m} p(u_0)\tau(u_0) \approx \int_{-\infty}^{\infty} p(u_0)\tau(u_0), \quad (3.50)$$

where we are using that the probability decays so fast away from $u_0 = 0$ that we can extend the lower limit past the barrier limit. In this integral, we only have to deal with the integral

$$\sqrt{\frac{\beta\tilde{\mu}}{2\pi}} \int_{-\infty}^{\infty} e^{-\beta\tilde{\mu}u_0^2/2 + \phi'(u_m)u_0} du_0 = e^{\phi'(u_m)^2/2\beta\tilde{\mu}}. \quad (3.51)$$

Finally, we can write down the full mean first passage time:

$$\tau = \tilde{\gamma} \sqrt{\frac{2\pi\beta}{\tilde{\mu}}} \frac{e^{\phi(u_m)}}{\phi'(u_m)} \left(1 - e^{\phi'(u_m)^2/2\beta\tilde{\mu} - \phi'(u_m)u_m}\right) \quad (3.52)$$

Usefully, the function $\Phi(\sqrt{\beta\tilde{\mu}}(y - \bar{u}))$ can be neglected: when the force is below the critical force $f/\tilde{\mu} < u\gamma_2/\tilde{\gamma}$, $f(y)$ is a constant, $\Phi(\sqrt{\beta\tilde{\mu}}(y - \bar{u})) \approx 1$. As such, we can write down the mean first passage time as:

$$\tau = \frac{\tilde{\gamma}}{\tilde{\mu}} \left(\frac{\sqrt{2\pi/\beta\tilde{\mu}}}{u_m - \bar{u}} \right) \exp \left[\frac{\beta\tilde{\mu}}{2} (u_m - \bar{u})^2 \right] \left(1 - \exp \left[\frac{\beta\tilde{\mu}}{2} (\bar{u}^2 - u_m^2) \right] \right) \quad (3.53)$$

The first exponential is the most important factor at forces below the critical force (as the second exponential will only contribute if $\bar{u} \approx u_m$). We can rewrite the mean first passage time in energetic terms:

$$\tau = \frac{\tilde{\gamma}}{\tilde{\mu}} \left(\frac{\sqrt{2\pi k_B T / \tilde{\mu}}}{u - f\tilde{\gamma}/\tilde{\mu}\gamma_2} \right) \exp \left[\beta \left(\Delta G_0 + \frac{\kappa u_m^2 \tilde{\gamma}^2}{8\gamma_1^2} - f u \frac{\tilde{\gamma}}{\gamma_2} + \frac{f^2}{2\tilde{\mu}} \left(\frac{\tilde{\gamma}}{\gamma_2} \right)^2 \right) \right] \times \left(1 - \exp \left[\beta \left(\frac{f^2}{2\tilde{\mu}} \left(\frac{\tilde{\gamma}}{\gamma_2} \right)^2 - \frac{\tilde{\mu} u^2}{2} \right) \right] \right) \quad (3.54)$$

Looking at the exponent, we can see a term coming from the zero-force energy barrier $\Delta G_0 = \mu u_m^2/2$, and an additional harmonic stretching energy of the substrate. At low

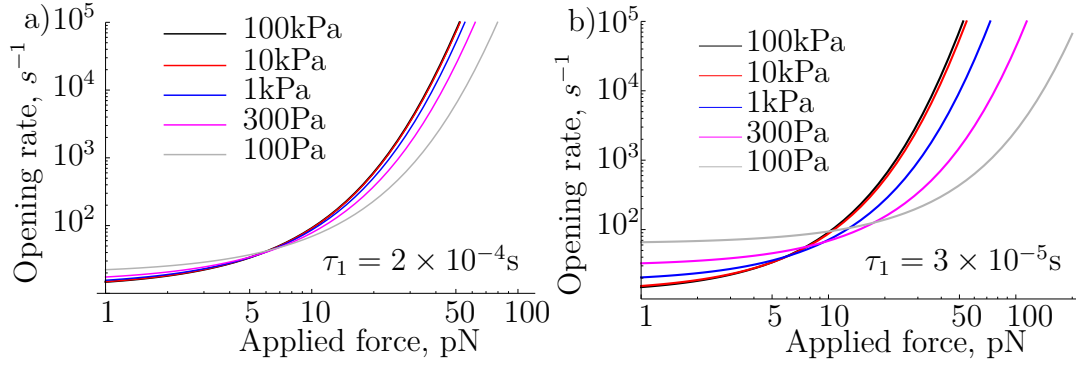


Fig. 3.13 The opening rate k as a function of the applied force for substrates of different stiffness. In a), a longer relaxation time $\tau_1 = 2 \times 10^{-4}$ s reduces the sensitivity of the bond to substrate stiffness compared to the shorter relaxation time in b). In both cases, the applied rate increases more for stiffer substrates up to about 10kPa, before the sensor response stops being stiffness-dependent. This would suggest that the complex is not capable of sensing beyond a certain stiffness threshold. At low forces, the increased fluctuations in softer substrates actually increases the opening rate over stiffer substrates.

forces, these will dominate. The next term we see is proportional to the reduction in the energy barrier due to the applied force, $-fu(\tilde{\gamma}/\gamma_2)$. Finally, the third term is similar to the one seen in the reaction path approach – the change in energy to the free energy minimum from the starting point: $-(f^2/2\tilde{\mu})(\tilde{\gamma}/\gamma_2)^2$. This is simply an Arrhenius activation term. The final bracket in this expression is important for when we surpass the critical force needed to destabilise the bond completely; it prevents the MFPT from diverging to ∞ . However, it seems fair to only consider the regime below the critical force,

$$f < \frac{\tilde{\mu}u\gamma_2}{\tilde{\gamma}} = f_c. \quad (3.55)$$

Then we are free to drop the bracketed term. The rate constant of unfolding is then simply the reciprocal of the MFPT:

$$k \approx \frac{\tilde{\mu}}{\tilde{\gamma}} \left(\frac{u - f\tilde{\gamma}/\tilde{\mu}\gamma_2}{\sqrt{2\pi k_B T/\tilde{\mu}}} \right) \exp \left[-\beta \left(\Delta G_0 + \frac{\kappa u_m^2 \tilde{\gamma}^2}{8\gamma_1^2} - fu \frac{\tilde{\gamma}}{\gamma_2} + \frac{f^2}{2\tilde{\mu}} \left(\frac{\tilde{\gamma}}{\gamma_2} \right)^2 \right) \right] \quad (3.56)$$

This expression is quite intuitive. First of all, it scales with the overall relaxation timescale of the mean field potential, $\tilde{\mu}/\tilde{\gamma}$. Then, it contains a contribution comparing the distance from the free energy minimum to the barrier position $u - \bar{w}$ with the thermal fluctuations within the energy barrier, $\sqrt{k_B T/\tilde{\mu}}$. It is interesting that the rate pre-factor is smaller when the equilibrium fluctuation from the free energy minimum is larger. Finally, we have an Arrhenius-type activation term, as noted above. The opening rate vs applied force is

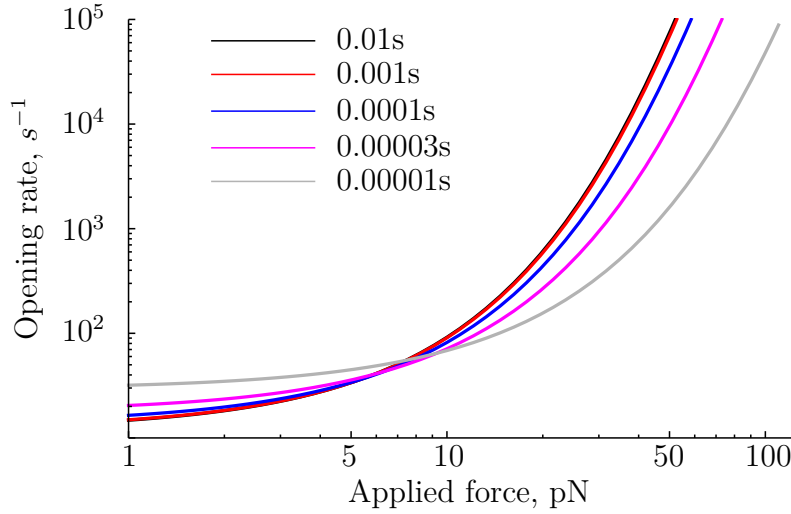


Fig. 3.14 The opening rate k plotted against the applied force for a 1kPa substrate, for different substrate relaxation times $\tau_1 = \gamma_1/\kappa$. Substrates with a shorter relaxation time have a lower rate of opening, and the rate maximum is peaked at higher values of force.

plotted in Fig. 3.13. There is an increase in opening rate on stiffer substrates at higher forces, but the maximum is not within the physiological range of forces (around 100pN). In reality, the rate constant should not decrease – this maximum comes artificially as the steepest descent method loses its validity. In reality, there is no maximum in the rate. In fact, the rate increases to a much higher value than the reaction path results. Secondly, there is a stiffness threshold, above which the complex is incapable of distinguishing substrates of different stiffness. For the parameters plotted here (a mesh size of 10nm and a relaxation time of 2×10^{-4} s), this stiffness threshold is around 10kPa, but depends strongly on the substrate's viscoelastic properties. It happens that this is around the same stiffness that Yeung et al. found a plateau in cell circumference with increasing stiffness [124], and around the stiffness threshold for myofibroblast differentiation [133]. Figure 3.14 shows how the relaxation time of the substrate influences the rate of opening. Longer relaxation times in the mean field approach lead to higher opening rates.

The rate of opening given in Eq. (3.56) shows some interesting features. First of all, the stiffness κ always comes with a scaling factor $\tilde{\gamma}/\gamma_1 = \gamma_2/(\gamma_1 + \gamma_2)$. As such, if $\gamma_2 \gg \gamma_1$, then the scaling factor is zero, and there is no direct dependence of the opening rate on the substrate stiffness (of course, in our study, there is an indirect relationship through the substrate relaxation time, $\tau_1 = \gamma_1/\kappa$). Indeed, for a longer relaxation time, $\tau_1 = 0.01$ s, there is no sensitivity to substrate stiffness at all. This sensitivity is controlled by the balance between the viscous properties of the substrate and those of the bond. When $\gamma_1 \sim \gamma_2$, increasing the substrate stiffness increases the effective stiffness of the

bond in the bond length variable. This has the effect of diminishing the contribution from the f^2 term in the exponent, and increasing the bare rate $\tilde{\mu}/\tilde{\gamma}$.

The qualitative and quantitative differences between the two approaches to the calculation are quite stark, and it is interesting to try and understand the differences between them. First, there is no maximum in the rate for the mean field approach, compared to a very low maximum for the reaction path approach. The reason for this is simple - when we take two reaction paths, the rate is controlled by the time to reach the x_1 minimum, and it is assumed that the system does not reach minimum in u space before it reaches the minimum in x_1 space.

To investigate this, we can plot the deterministic force expected across the bond, without any stochastic forces, using the equations of motion:

$$\begin{aligned}\gamma_1 \dot{x}_1(t) &= -\kappa x_1(t) - \frac{\partial U(x_2(t) - x_1(t))}{\partial x_1} \\ \gamma_2 \dot{x}_2(t) &= -\frac{\partial U(x_2(t) - x_1(t))}{\partial x_2} + f\end{aligned}\quad (3.57)$$

The full solution of this can be found with a harmonic potential $U = \mu u^2/2$. We can solve this set of ordinary differential equations for $x_1(t)$ and $x_2(t)$, and then find the bond separation, $x_2(t) - x_1(t)$ across the bond as a function of time, as plotted in Fig. 3.15. The full expression is unwieldy, but in fact a simple approximation is

$$\begin{aligned}x_2(t) - x_1(t) &= \frac{f}{\mu} \left(\frac{\gamma_1}{\gamma_1 + \gamma_2} \left(1 - e^{-\tilde{\mu}t/\tilde{\gamma}}\right) + \frac{\gamma_2}{\gamma_1 + \gamma_2} \left(1 - e^{-t/\tau_1}\right) \right) \\ &= \frac{f}{\mu} \left(\frac{\tilde{\gamma}}{\gamma_2} \left(1 - e^{-\tilde{\mu}t/\tilde{\gamma}}\right) + \frac{\tilde{\gamma}}{\gamma_1} \left(1 - e^{-t/\tau_1}\right) \right)\end{aligned}\quad (3.58)$$

This gives us a lot of intuition for the final result in the stochastic case. For long substrate relaxation times, the extension rapidly reaches an intermediate free energy minimum $f\tilde{\gamma}/\mu\gamma_2$, extending further as the substrates slowly reaches full extension. Importantly, if the force is larger than the critical force so that the intermediate minimum is past the barrier, $f\tilde{\gamma}/\mu\gamma_2 > u$, then the bond will break in this initial extension phase. There is no reduction in the rate as the force goes to infinity; the deterministic breaking time above the critical force is a monotonically increasing function with force. This interpretation explains the presence of the factor $\tilde{\gamma}/\gamma_2$ in the mean field Arrhenius factor - on the timescale of the MFPT, the relevant value of force is this scaled one. For polyacrylamide gels, this factor is only relevant for soft substrates ($<1\text{kPa}$). The plot of deterministic extension shows that the reaction-path approach does not capture essential parts of the

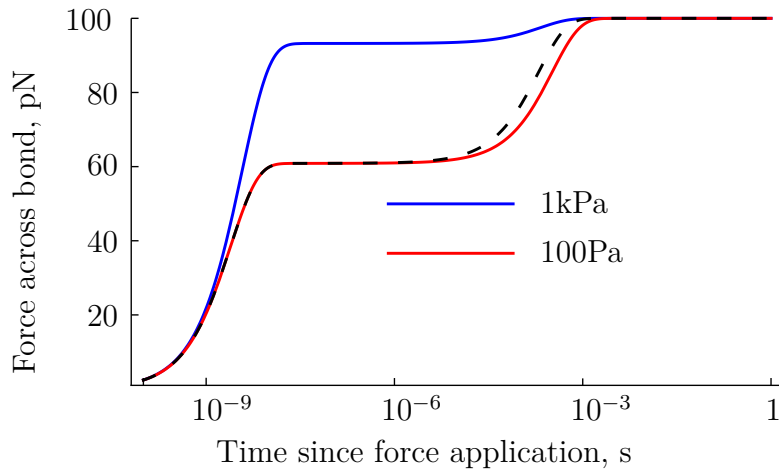


Fig. 3.15 The deterministic force expected over the bond upon application of a subcritical force of 100pN plotted for two different substrate stiffnesses. There is an initial rise in the force to an intermediate threshold, and then a slower increase up to the full value (here, $\tau_{\text{sub}} = 2 * 10^{-4}\text{s}$. This threshold is a balance of the friction coefficients in the bond and in the substrate, and is lower for the softer substrate (this has a lower coefficient of friction). The approximation in Eq. 3.58 is plotted for 100Pa as the dashed black curve. The same approximate expression lies directly on top of the 1kPa curve.

physics at high forces. During the first leg of the movement, there appears to be an assumption that there is no effective force across the bond facilitating the opening event. Figure 3.15 shows this notion to be false; we build up some measure of force across the bond very quickly, and it is this that we should be testing the bond with.

It may well be that the ‘mean field’ approach taken here, to integrate out the fast variable, provides a route to solving the problem for more general viscoelastic substrates. In particular, if the response of the substrate is slow compared to the typical breaking time of the bond, then it may be possible to treat the substrate as quasi-stationary, with an effective force across the bond. Remember that as long as we can find the overall effective friction coefficient on the reaction timescale, and the effective force, then we can use the Ricciardi-Sato formula to obtain the mean first passage time quickly. Again, the reduction in variables might be done by such a ‘mean field’ approach as was taken here.

How could the reaction rates calculated here for the unfolding of molecules such as focal adhesion kinase, or talin, be included in a cellular description of mechanosensing? One prominent description of focal adhesion dynamics is given by the clutch model, which couples an internal mechanosensing molecule (often described as talin), with the on/off rates of integrin binding to the ECM (for a recent survey, see for example [134]). Integrin is a catch-bond: as force is applied to integrins, the integrin-ECM bond strength initially increases, in contrast to the usual trend of biomolecules to become less stable

with increasing force [98, 99]. Above a certain force, the bond strength starts to decrease, in line with ‘conventional’ bond dynamics described by the Bell model [60]. The interplay between the two unbinding/unfolding timescales allow the cell to distinguish between stiff and soft substrates.

In this context, the rate constants calculated here provide more complete expressions for the unfolding rates of the internal mechanosensor, and the dependence upon substrate viscoelasticity, which has not yet been fully addressed in the literature. If we take a rough force of ~ 30 pN across each integrin bond [135], then by Fig. 3.14, we are in the region where greater substrate stress relaxation leads to a higher response from the mechanosensing molecule. This is in accord with experimental results of cells spreading on viscoelastic substrates, where spreading is enhanced on substrates with greater stress relaxation [130]. The same study produces simulation results for such a viscoelastic clutch model.

Finally, it is important to note that such molecules as focal adhesion kinase and talin may not only act as force transmitters (to pass the cytoskeletal pull down to integrin-ECM bond), but also force transducers, initiating signalling pathways throughout the cell. To successfully model these, it is likely that a complex kinetic model is needed, accounting for activation of signalling pathways, turnover of focal adhesion units (and therefore active force transducers), and the feedback mechanisms on e.g. cytoskeletal force changes as a result of downstream signalling events. Such a kinetic model is very sensitive to the rates of its component processes, and the work in this chapter is well placed to inform the activation rates of force transducers in such models.

CHAPTER 4

THE ONSET OF CELL SPREADING AS A STUDY IN POPULATION KINETICS

Matrix stiffness is known to affect cell size and morphology [136, 124, 137]. When cells are plated onto soft substrates, their footprint will not increase as much as on stiff substrates, and their spreading will be more isotropic: resulting cells will be round and dome-like in shape. On stiff substrates, the same cells will spread very strongly, develop concentrated focal adhesion clusters and stress fibers of bundled F-actin, and eventually polarize to initiate migration. This leads to several well-documented biological functions in tissues: variable stem-cell differentiation pathways [136, 138], the fibroblast-myofibroblast transition near scar tissue [139–141], fibrosis in smooth-muscle cells near rigid plaque or scar tissue [142, 143], and the stiffer nature of tumor cells [144, 145]. The definitive review [146] summarizes this topic.

The actual process of spreading, after a planktonic cell is deposited on a substrate, involves several stages. After initial anchoring, which probably occurs due to a non-specific hydrophobic or Van der Waals binding, which could lead to an initial increase of the cell footprint on the surface due to viscoelastic wetting [147, 148]. Once on the surface, the cell must test for the presence of suitable ligands, and then bind to them [149, 150]. This specific adhesion must occur for the cell to spread [151]. Then, the cell tests the elasticity of the extracellular matrix (ECM), and on sufficiently stiff substrates, it continues spreading, approaching its maximal footprint area. Finally, after polarization is triggered on stiff substrates, the cell may start moving in a particular direction.

The dynamics of cells spreading has been studied extensively, and several characteristic universal features have been established [146, 124, 152–154]. In particular, the average cell area has been shown to grow with time as a power law, often with the radius of cell footprint being $R \propto [t - \tau_{\text{lag}}]^{1/2}$, where the ‘lag’ τ_{lag} is referred to as the adhesion time.

[152, 155–157]. It is important to note that the ‘lag time’ is observed in many discussions of the dynamics of spreading, but mostly ignored by subtracting it from the data. Several mechanistic models of how the cell spreading is achieved after the adhesion to ECM is established [152, 157, 155], as well as the spreading and cell orientation response to mechanical deformation of the substrate [158, 159]. A common theme to these studies is the presentation of individual cell trajectories, outlining the time course of a cell response to adhesion (although of course many cells are used to generate statistics). In contrast, here I examine the dynamics of a cell population, by identifying the time at which a cell reaches a specific point early in its spreading sequence (essentially reflecting the ‘decision’ of a cell to start spreading in response to its ECM mechanosensing signal). Frisch and Thoumine [58] have shown that in the early stages of spreading, the cell takes a spherical-cap morphology, and when the increasing adhesion energy becomes similar to the cell cortical tension: the cell contact angle crosses from greater than 90° (representing the partial dewetting) to less than 90° (representing the partial wetting). Such a binary condition, asking if an event has taken place by a certain time, rather than what events are taking place over the course of time, allows the use of stochastic theory to interrogate the cell dynamics, extracting useful information about the underlying kinetics of spreading. In particular, we are able to form a better understanding of the ‘lag time’ and also identify the rate-limiting energy barrier that controls the transition of cells from the initial non-specific binding to the final strongly adhered, and widely spreading regime. This is a useful complementary approach to single cell measurements. I emphasize that here, and in the rest of this chapter, I am discussing isolated cells on a substrate: when cells adhere to each other, their shape transitions are controlled by other mechanisms, based on cadherin and associated pathways [160].

While reporting and discussing the cell area increase on stiffer substrates, Fig. 5(d) of the paper by Yeung et al. [124] and Fig. 2(A) of the paper by Reinhard-King et al. [154] also present data on the time-dependence of cell spreading, which already gives a hint for the central experimental finding: the onset of cell spreading does not depend on the substrate. In this chapter I investigate the time-dependence (kinetics) of the initiation of spreading, asking the question: how long does it take for the cell to recognize the presence of a substrate, and respond by engaging signalling pathways and enacting the required morphological change (spreading on the substrate)? Figure 4.1 illustrates the point: plots (a) and (b) show the same cells: immediately after planting on the substrate, and after some time, when several cells have already responded by engaging their spreading. Two very different cell lines (NIH/3T3 fibroblasts and EA.hy927 endothelial cells) were plated on a variety of substrates that span the range of stiffness from 30 GPa (stiff glass) to

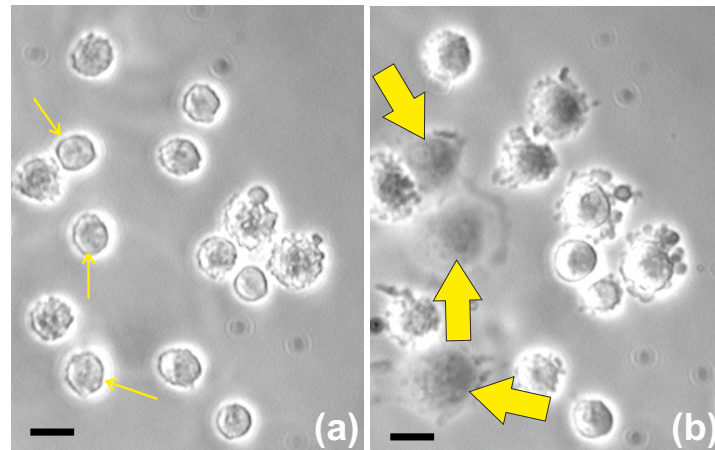


Fig. 4.1 A section of the experimental field of view, illustrating the onset of spreading. Photographs (a) and (b) show the same cells: immediately after planting on the substrate (solid glass with fibronectin), and 15 min later, when several cells have already responded by spreading (labelled by matching arrows). Scale bar = 20 μm .

460 Pa (very soft gel), registering the characteristic time at which the initially deposited planktonic cells start to spread.

We will discover three things: [1] the onset of spreading is completely universal, not depending on the stiffness of substrates (in contrast to the final cell morphology, which strongly depends on it); [2] the rate-limiting process, with the characteristic free energy barrier, is the same in both cell lines; [3] the onset of spreading is controlled by a nucleation event, its universal power-law dependence t^5 suggesting that there are 5 state changes a newly deposited cell must go through before it is able to spread. We will also find that the sum of the free energy changes of these state changes, in contrast to the rate-limiting process, depends on the cell line.

At first, these results on the insensitivity of the onset of spreading to substrate stiffness look counter to much of the literature. It is important to draw a clear line between many existing results on the cell area increase with time on different substrates, and this study that looks at the statistics of a cell population that start spreading. In particular, the criterion observed happens at a very early stage of the overall spreading (see Fig. 4.2), where the cell area has increased only by a factor of 1.26 from its initial settled state.

4.1 Experimental details

In order to assess the analysis presented in this chapter, it is necessary to understand the experimental set-up and choices made. Here, I present a brief overview of the

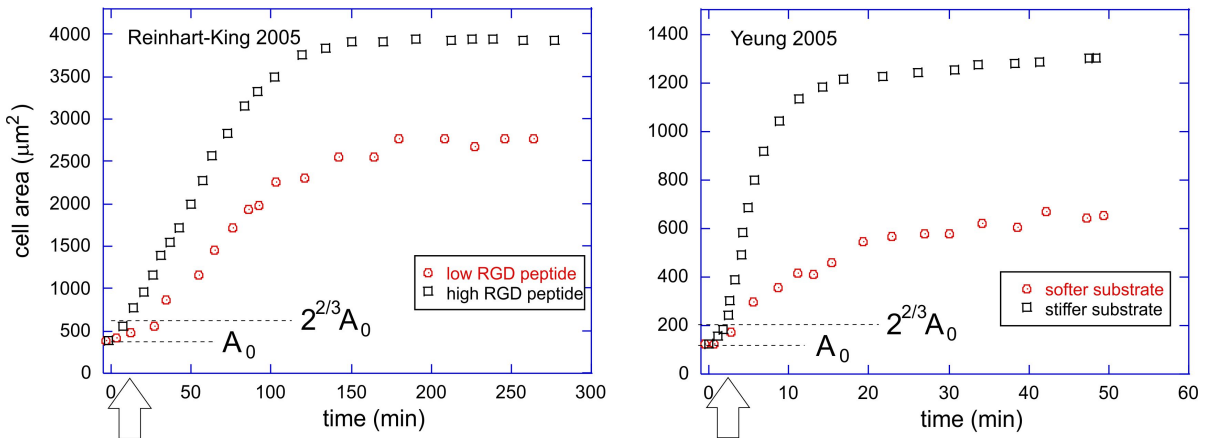


Fig. 4.2 Plotting some digitized data from Reinhart-King 2005 (Fig. 2A), and from Yeung 2005 (Fig. 5(d)) showing the time evolution of spreading cell area: in the first case at varying concentration of ligands for integrin binding, in the second case at varying substrate stiffness. The initial cell area (on first deposition on surface) is A_0 , and the ‘selection criterion’ illustrated in Fig. S2 implies the observed cell area increases by a factor $2^{2/3} \approx 1.6$. This is a very early stage of cell spreading, which I refer to as the onset of spreading response.

experimental procedure undertaken by Anna-Lena Redmann, who collected all of the data used in this chapter.

The cell lines of choice were endothelial cells and fibroblasts, because their adhesion behaviour is important for understanding cardiovascular diseases and tissue engineering. Anna used immortalized cell lines: NIH/3T3 murine fibroblasts (obtained from ATCC) and EA.hy927 endothelial cells. NIH/3T3 fibroblasts are very well characterized, as they have been used in many cell studies since their establishment as cell line; they have also been used in cell adhesion studies, making them a good choice for these experiments [161, 162]. EA.hy927 is a cell line established in 1983 by the fusion of HUVEC with a lung carcinoma line [163]. It has since become a widely used and thus well characterized cell line, popular in studies of cardiovascular diseases. EA.hy927 cells have also been used for adhesion strength assays [164].

Three different substrate stiffnesses were used: standard laboratory glass (elastic modulus 30 GPa), and several versions of siloxane elastomers. The fabricated elastomers were tested on a standard laboratory rheometer (Anton Paar), giving the values of equilibrium modulus $G = 460$ Pa, and 480 kPa, compared to the modulus of 30 GPa for glass. For comparison, the stiffness of typical mammalian tissues is: 100 Pa – 1 kPa in brain tissue; ~ 3 kPa in adipose tissue; 10 – 20 kPa in muscle; 30 – 50 kPa in fibrose tissue; up to a few MPa for bone.

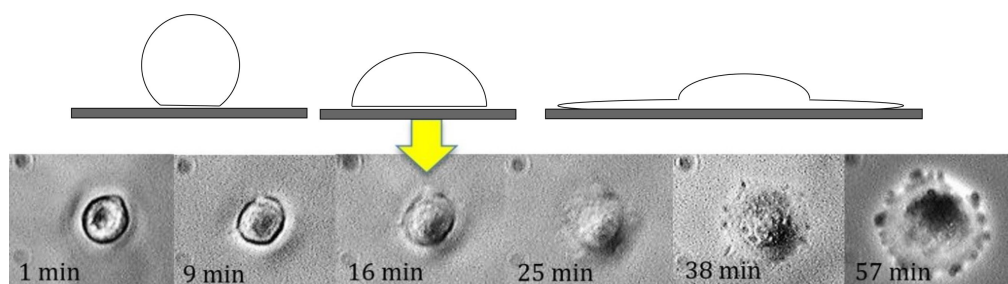


Fig. 4.3 The illustration of the visual criterion used to count the cells as ‘engaged’ in mechanosensing response. We interpreted the loss of the sharp edge in the microscopic image, and the simultaneous loss of the ‘lensing effect’ with the cell shape becoming flatter than semi-sphere. This point in time was associated with the given cell beginning to spread, and therefore counted towards the ‘fraction of cells engaged in spreading’ in the population.

The cell culture was placed over the entire substrate. Cells were left to adhere to the substrate for 2 min, at which point the culture dish containing the substrate is filled slowly with fresh medium to reduce the cell density. This was to prevent new cells depositing, and cell clusters forming on the substrate. Only the cells attached to the substrate at this point were included into the subsequent counting. This initial attachment is certainly purely physical, through van der Waals forces and various non-specific cell adhesion molecule head groups. These physically adhered cells, initially spherical in planktonic culture, maintain the high spherical-cap shape with only a small adhesion footprint, as ordinary inflated bilayer vesicles would do as well. This is readily confirmed by optical interference bands around the cell perimeter when viewed from above, and the lensing effect focusing the light by the short-focal distance near-spherical shape [58].

After a certain time on substrate, the cells finally engage their specific adhesion mechanism, and start spreading, achieving a very widely spread area with highly asymmetric focal adhesions on stiff substrates, or a round dome-like shape on soft substrates. The aim of the study was to determine the time it takes for the cells to engage this active spreading process.

To obtain a population distribution of the onset time of cell spreading, we had to choose a ‘spreading criterion’, which would be clear and easily distinguishable to avoid counting errors. This was chosen to be the transition between the near-spherical cell initially planted (physically attached) on the substrate, and the cell with adhesion processes engaged and its shape developing an inflection zone around the rim. As seen in Fig. 4.3, this morphological transition turns out to be easily identified as the near-spherical cell has a sharp edge, with interference bands in higher magnification, and also

a lensing effect of focusing light, which disappears on the transition to a more flattened shape. It must be emphasized, that in order for the cell count to be meaningful, the cells have to be isolated on the substrate: once the cells come into contact with each other, many other adhesion and mechanosensing mechanisms engage (for example, those based on cadherins), and they spread much more readily and more significantly. As such, initial cell density was chosen such that the initial attachment is in isolation, and the spreading criterion is applied before they spread sufficiently to come in contact (as some cells in Fig. 4.1 have done).

In each individual experiment (given substrate, fixed temperature, and other parameters), once the cells were deposited on the substrate, and the clock started, Anna took broad-field microscopic images at regular time intervals, and counted the fraction of cells that had crossed the threshold defined by the spreading criterion – that is, the cells that have started the active spreading process in response to their mechanosensing cue. This produced a characteristic sigmoidal curve for each experiment (see Fig. 4.4): the fraction of cells engaged in spreading starting from zero at $t = 0$ and saturating at near-100% at very long time (excluding the occasional cell mortality, which was more of a factor at lower temperatures). The typical sample size was 100-120 cells in each experiment (field of view). The main sources of error were: inconsistency of application of the spreading criterion in image analysis, imperfections of fibronectin coverage on substrate, temperature fluctuations, and of course the natural cell variability. All of these are random errors, with no systematic drift. We were satisfied that the results were reproducible, and errors did not dominate the data trends. The plots in Figs. 4.4 and 4.5 do not include error bars only to avoid obscuring distinct data sets.

The experimental results concurred with the results of earlier studies [58, 136, 124, 138]. Cells placed on stiffer substrates spread to larger areas, and were less rounded, for both cell types. There is also a strong dependence on the ECM protein coverage [165], but this was not a variable in the study.

The time of initiation of spreading is presented in Fig. 4.4. These two plots (for 3T3 and EA cells) show the fraction of cells that have started spreading at each given time that has passed after planting on substrate and replacing the medium. The point of steepest gradient in these cumulative curves marks the most probable time for the onset of spreading. We see the timing of cell spreading is completely insensitive to the substrate stiffness: the kinetics of spreading response is exactly the same on each substrate. The work of Sheetz et al. [106] has reported a similar effect (the rate of spreading did not depend on the degree of ECM protein coverage on the surface). Rather than substrate stiffness, the curves in Fig. 4.4 are instead strongly segregated by temperature.

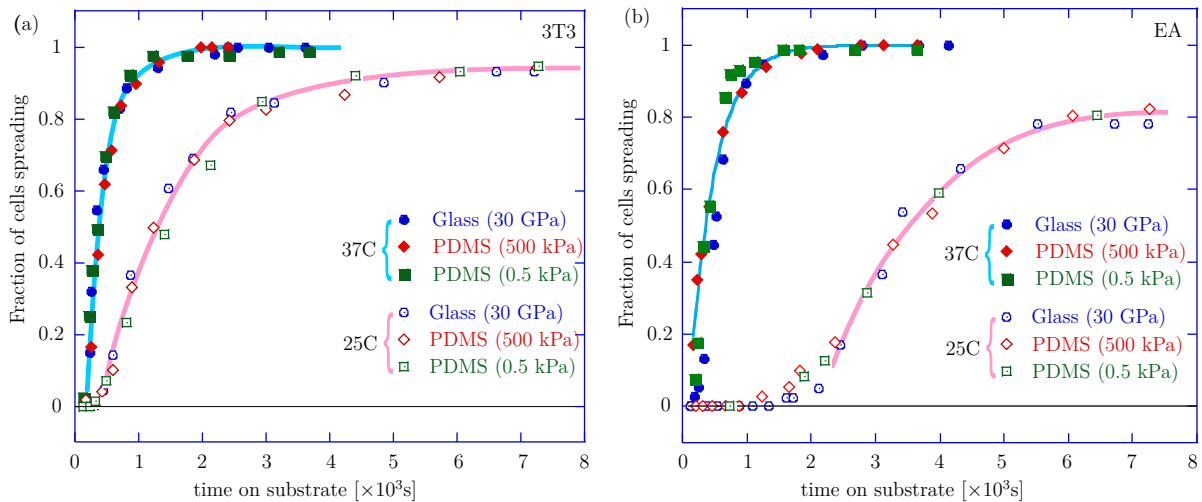


Fig. 4.4 Cumulative population dynamics of cell spreading. Plots (a) and (b) show the growing fraction of cells engaged in spreading on substrates with different stiffness for 3T3 fibroblasts and EA endothelial cells at two different temperatures each. It is clear that the dynamics is not affected by the substrate stiffness, but changes with temperature. In the remainder of this chapter, I analyze in detail the long-time behaviour of these cumulative curves as they approach saturation, and the behaviour at short times when the onset of mechanosensing response occurs.

4.2 Long-time kinetics: a rate-limiting process

To examine the effect of temperature in greater detail, in Fig. 4.5 we can plot the same cumulative spreading fraction curves for the two cell types on glass (as we are now assured that these curves are the same on all substrates). It is noticeable that the initial lag is greater in the EA cells, and that at low temperature the saturation level drops significantly below 100% – presumably because more cells disengage (or die) at low temperature, reducing the saturation fraction. The same effect is much enhanced for the the nutrient-starved cells in the PBS medium, see in Fig. 4.5(a): the onset of spreading is very slow in this case, and a large fraction of cells do not engage at all. But the generic sigmoidal shape of the cumulative curve is universal, and the random spread of data within each individual experiment is not excessive.

The curves of the generic shape seen in Figs. 4.4 and 4.5 are encountered in many areas of science, and their characteristic ‘foot’ at early times, especially obvious at lower temperatures, is usually associated with a ‘lag’ in the corresponding process. I will discuss this early-time regime separately, later in the chapter, but first we can fit exponential relaxation curves to the long-time portion of the data (as the fit lines in Fig. 4.5 indicate): $Q(t) = A \cdot (1 - \exp[-(t - t_{\text{lag}})/\tau])$. It is clear from the plots that the fitting

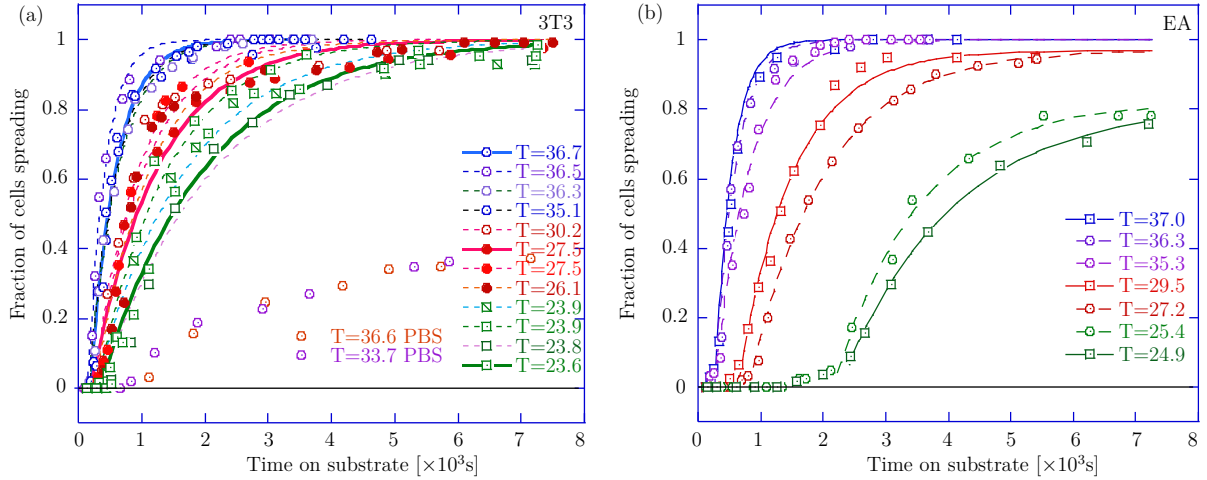


Fig. 4.5 Cumulative population dynamics of cell spreading. Plots (a) and (b) show fraction of spreading cells on glass, at many different temperatures; for 3T3 fibroblasts and EA endothelial cells. Lines in all plots are the fits of the long-time portion of data with the exponential relaxation curves, producing the fitted values of the longest relaxation time τ (see text).

to the single-exponential relaxation law, with just two parameters since A is known for each curve, is very successful. The characteristic relaxation time τ markedly increases at low temperatures. It is interesting that such a characteristic time associated with the ‘spreading of an average cell’ has been discussed in [152], giving the same order of magnitude (of the order of magnitude 50-100s).

To better understand this dependence on temperature, I tested a hypothesis that this relaxation time is determined by the thermally-activated law by producing the characteristic Arrhenius plots of relaxation times, for both cell types, see Fig. 4.6. It is remarkable that both cells show almost exactly the same trend of their relaxation time: the rate limiting process in their spreading pathways is the same: $\tau = \tau_0 e^{\Delta G/k_B T}$, with the activation energy $\Delta G \approx 18.3 \pm 1.5$ kcal/mol, and the thermal rate of attempts $\tau_0^{-1} \approx 4 \times 10^{10} \text{s}^{-1}$. Both values are very sensible: this magnitude of ΔG is typical for the non-covalent bonding energy between protein domains [108], and this rate of thermal collisions is in excellent agreement with the basic Brownian motion values.

4.3 Short-time kinetics: a nucleation process

After discovering that the late-times (rate-limiting) dynamics of the onset of spreading is quite universal across different cells and substrates, it becomes clear that the marked difference between the two cell lines in Fig. 4.5 lies in the early-time behavior: something

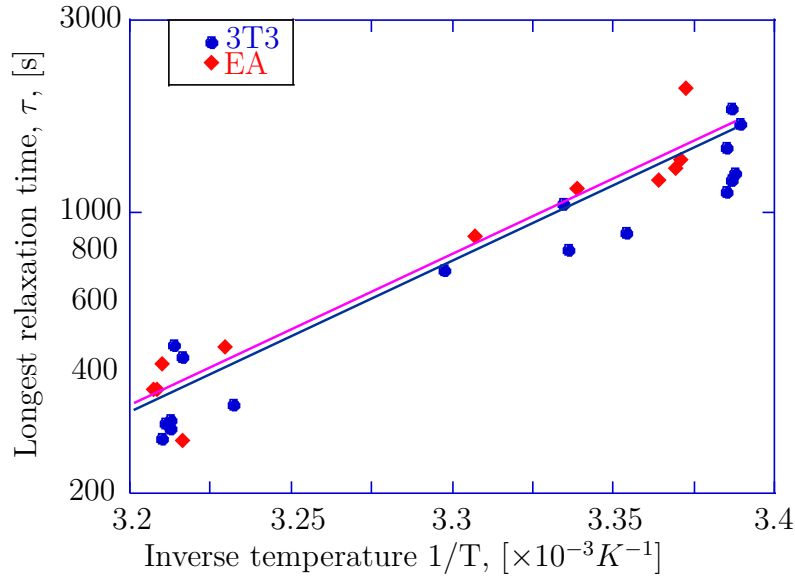


Fig. 4.6 The Arrhenius plot of the longest relaxation time ($\log(\tau)$ vs. inverse absolute temperature) from the exponential fits in Fig. 4.5(a,b), giving almost exactly the same value of binding energy $\Delta G \approx 18$ kcal/mol, for both types of cells.

that I have called a ‘lag’ following many similar situations in protein self-assembly. To examine this early-time regime more carefully, let us re-plot the same time series data on the log-log scale in Fig. 4.7.

This reveals that the process is active from the very beginning ($t = 0$) and the plotted value grows as a power-law of time. The only reason that we appear to see a ‘lag’ is because the experimental technique of counting the cells engaging in spreading did not permit values below 0.01 (1%) to be resolved in this plot; the same certainly applies to other experimental situations reporting similar kinetic data. The trend illustrated in Fig. 4.7 is clear: the early onset of cell spreading follows a universal power law, and the fitting of all the data sets gives $Q(t) = \alpha t^5$ with very good accuracy, where only the prefactor α depends on temperature and the cell type. This result is remarkable: similarly to the universal value of binding energy that controls thermally-activated rate-limiting relaxation time τ , this very specific t^5 power law appears to be the only sensible fit of the early-time data for different cells, temperatures, and substrates.

Again, strong temperature dependence is evident in the subpopulations of cells which start spreading very early: the difference was evident in Figs 4.4 and 4.5, but is very clearly enhanced in Fig. 4.7. What changes between the data sets is the prefactor α of the universal power law αt^5 , which has a systematic temperature dependence. Now expecting the thermally activated behavior, by analogy with the earlier analysis, we plot these prefactors $\alpha(T)$ on the Arrhenius plot in Fig. 4.8. The fitting to $\alpha = \text{const} \cdot e^{-\Delta H/k_B T}$

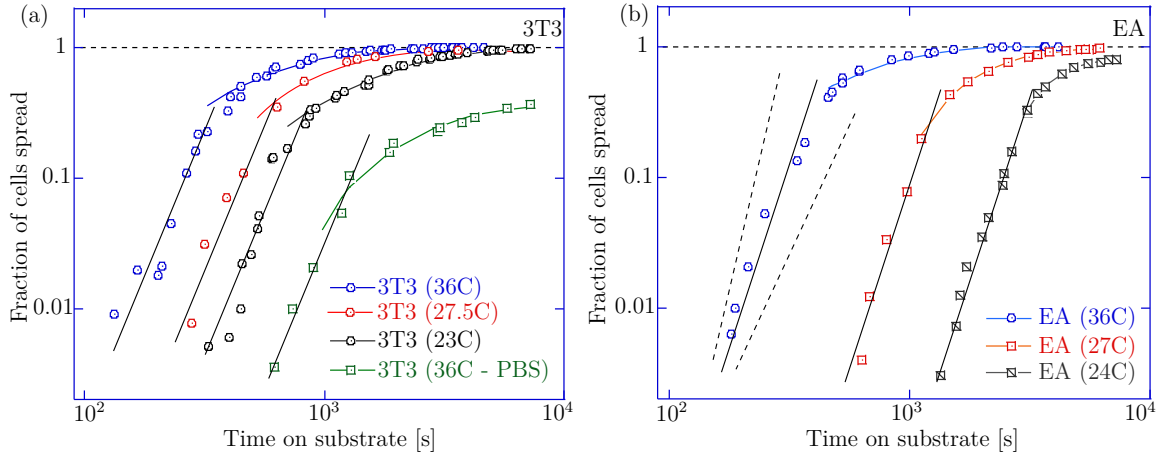


Fig. 4.7 Analysis of the short-time dynamics of cell spreading. Plots (a) and (b) show selected data sets from the Fig. 4.5 (a,b), presented on the log-log scale to enhance the short-time dynamical range. In both plots, the power-law slopes of the short-time data follow the equation: αt^5 , with the coefficient prefactor α depending both on cell type and on temperature. The dashed line illustrate the slopes of t^6 and t^4 to illustrate the strength of fit.

indeed gives a very reasonable trend, with the activation energies $\Delta H = 70$ kcal/mol for 3T3, and 129 kcal/mol for EA. Note that, in contrast to Fig. 4.6, here we have a negative exponent, i.e. the parameter $\alpha(T)$ represents a reaction *rate* rather than a relaxation *time*. In the classical Arrhenius-Kramers thermal activation, the process time is shorter as the temperature increases, while the Fig. 4.8 shows the scaling factor $\alpha(T)$ is decreasing as the temperature decreases instead (which is reflected in the overall observation of longer ‘lag time’ in the cumulative curves).

4.4 Kinetics of adhesome assembly

The time measured is the sum of the adhesion lag time, and the time to reach the binary criterion for the start of spreading. The distribution in the data is due to the statistical distribution of the ‘lag times’. The results show that the stochasticity of lag time has structure. We can use this structure to infer information about the processes underlying adhesion and spreading.

In classical physics, early-time power law kinetics in a cumulative distribution are a hallmark of self-assembly processes such as polymerization or aggregation [166, 29]. As already described in Section 1.6, the first passage time density from a state i to a state j

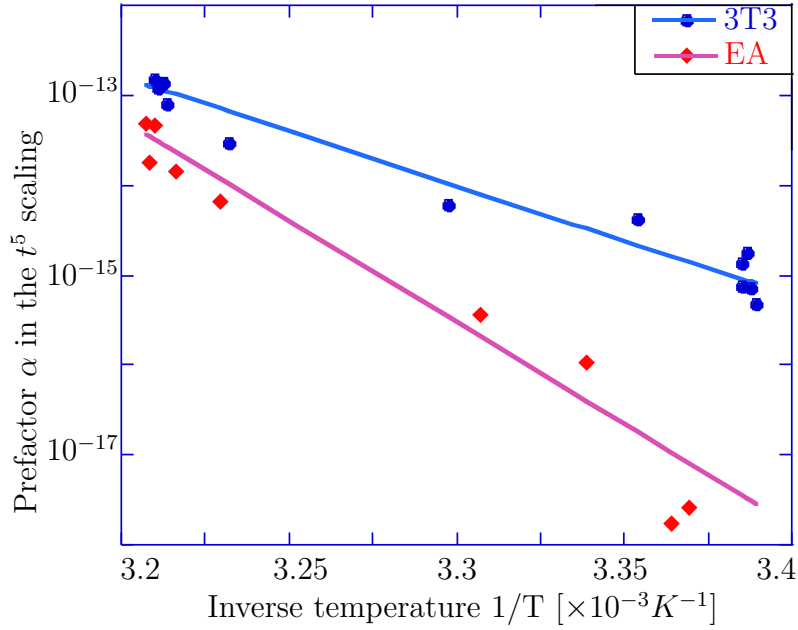


Fig. 4.8 Analysis of the short-time dynamics of cell spreading. The Arrhenius plot of the prefactor $\alpha(T)$, with the fit lines giving the effective activation enthalpy $\Delta H \approx 70$ kcal/mol for 3T3, and 129 kcal/mol for EA. See text, explaining how this value represents the sum of free energy barriers of key proteins assembling into the adhesion complex.

in a reaction network is given by

$$f_{ij}(t) = \left(\frac{k_{iq_1} k_{q_1 q_2} \dots k_{q_m j}}{u_{ij}} \right) \frac{t^m}{m!}, \quad (4.1)$$

where $m + 1$ is the length of the minimum connector between the two states, $i \rightarrow q_1 \rightarrow q_2 \rightarrow \dots \rightarrow q_m \rightarrow j$. The factor u_{ij} is the probability of absorption in state j (this is 1 if j is the only absorbing state). Since the first passage time is related to the survival probability $Q(t)$ (the fraction of cells that have not started spreading), through

$$f(t) = -\frac{\partial Q(t)}{\partial t}, \quad (4.2)$$

and the cumulative probability of having started to spread is merely $P(t) = 1 - Q(t)$, then the short-time behaviour of the cumulative probability $P(t)$ is simply

$$P(t) = \left(\frac{k_{iq_1} k_{q_1 q_2} \dots k_{q_m j}}{u_{ij}} \right) \frac{t^{m+1}}{(m+1)!}, \quad (4.3)$$

i.e. the exponent of the power law gives the length of the minimum connector, $m + 1$. This is simply the number of states you must pass through to reach a final state. In this

case, we must be looking at a process of self-assembly within the cell. The exponent of the power law gives us some idea of how many important assembly steps there are. But, what exactly is being assembled? It seems likely that we are observing the formation of adhesion points and adhesome complexes that allow the cell to bind onto its ECM environment and begin spreading. The idea that the initial assembly of adhesome complexes is responsible for the initial changes in the cell footprint area, e.g. Reinhart-King et al. [154]. Here we are able to infer some quantitative details of this process.

It is well established that disruption of the integrin-fibronectin linkage completely halts cell spreading [151, 167]. Integrins are transmembrane receptors linking the cell to the matrix in focal adhesions [97, 100, 101]. To attach to their ligands, they need to be activated [168, 169]: in isolation, integrin pairs will lie in their inactive state, unable to bind to fibronectin (or other ECM proteins containing the RGD motif). In equilibrium, the level of integrin activation might be dependent on the ECM rigidity [105, 170], however, here we are examining very early stages of cell settling on its substrate, so it is the adhesome assembly and signalling that control the results.

Much of the literature on focal adhesions sees the attachment of the talin head domain to integrin tails as an important activation step [171–173]. Talin is a key protein in mature and nascent adhesions, linking integrins to the actin cytoskeleton, and providing a scaffold for other focal adhesion proteins (see, for example [79]). For the onset of spreading, there is some conflict in the literature: in the study by Zhang et al. [151], where they confirmed that integrin linkage was essential to the onset of spreading, they actually depleted both types of talin, and found that the onset of spreading was not fully inhibited, although spreading was severely limited. This could indicate that talin was not needed for the activation of integrins during the onset of spreading. However, a subsequent knock-out study of talin (among other proteins) [174] found that spreading was actually completely inhibited by the removal of talin (although partial function was restored by the addition of Mn^{2+}). In that work, the authors note that the experimental methods (si-RNA transfection) employed in previous studies left residual amounts of proteins in the cell, and that there may well have been enough talin left in depleted cells to form nascent adhesions. Indeed, in their paper, Zhang et al. say that the decrease in talin2 levels (talin1 was not expressed in their cell lines) was between 40-68%.

In fact, Theodosiou et al. [174] implicate three further players: kindlins, paxillin, and focal adhesion kinase (FAK). This is not a new finding, or point of view: since the early discovery of the key role of FAK in the integrin adhesome [101, 175, 95], it was understood that it is the FAK activation that produces the chemical cue for the subsequent cell mechanosensing pathways via Src, Rho, Rac and Cdc42, as well as Erk [176, 167, 177, 178].

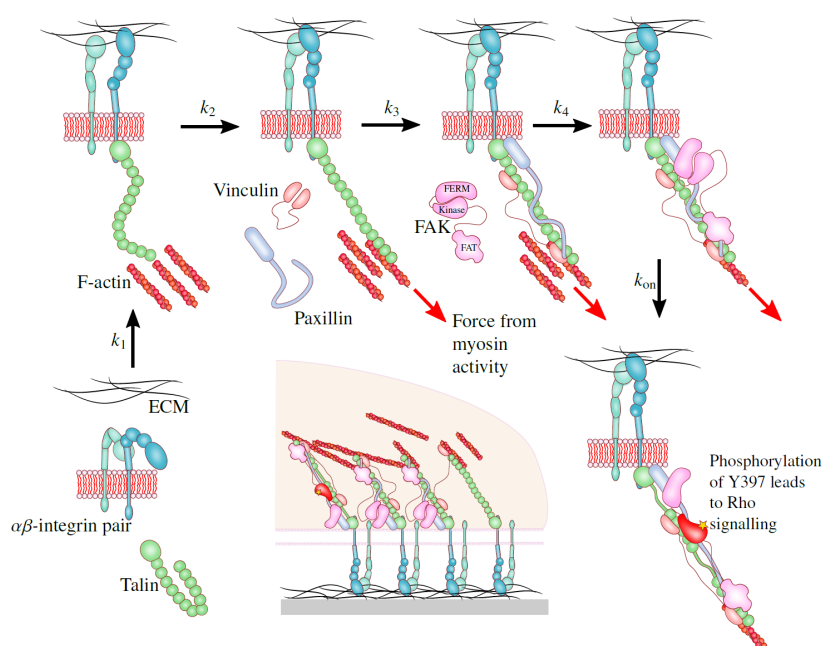


Fig. 4.9 A possible assembly sequence of a mechanosensor complex. Analysis suggests that there are five distinct ‘slow’ stages illustrated in the sequence, with their respective rates k_1 - k_4 and the rate of FAK activation k_{on} (controlled by the free energy barrier $\Delta G \approx 18$ kcal/mol, cf. Fig. 4.6). The product of the five rate constants $\alpha = k_1 k_2 k_3 k_4 k_{on}$ is what we measure in the Arrhenius plot Fig. 4.8. In the center is a sketch of forming focal adhesion cluster, where the individual mechanosensor complexes in various stages of development/turnover are bound by vinculin and actin crosslinking (see text for details).

Theodosiou et al. found that chemical inhibition of FAK reduced lamellopodia formation in cells to the level of kindlin knock-out cells [174]. The formation of these lamellopodia and the initiation of isotropic cell spreading was therefore found to be dependent on FAK activation. The model of FAK as a mechanosensor presented in Chapter 3 shows how the rate of its activation is sensitive to the stiffness of substrate, and the cytoskeletal pulling force. Importantly, when the force is low (as we would expect at early times, before the mechanosensing pathways are activated and the cytoskeletal forces increase), this rate is controlled only by the bonding energy between its FERM and kinase domains, not the stiffness.

FAK clearly sits at the centre of the adhesion signaling network [179]. But the minimal composition of the whole adhesion-mechanosensing complex in the nascent adhesions, as well as the rate of its assembly and turnover, remain a question of active research and debate. Kindlins are known to be a necessary partner for talin in integrin activation [79, 168, 173]. The F3 subdomain of a FERM domain mediates an interaction with β -integrin tails, and ‘cooperates’ with the talin head domain in integrin activation [180]. Paxillin is another player in the adhesion network [79, 174, 179]. In particular, in the nascent adhesions formed at the onset of spreading, kindlin was directly binding paxillin; paxillin was then recruiting FAK to these nascent adhesions. On the other hand, the important role of vinculin in several processes in the integrin-talin-FAK adhesion complex appears to be relevant mostly at the mature focal adhesion stage [181, 106, 182], and I believe its role could be to bind different adhesion complexes into a dense focal adhesion raft.

How does this information tie in with the results in this chapter? A recent molecular-dynamics simulation [108] has explicitly calculated the bonding energy between FERM and Kinase domains of FAK as $\Delta G \approx 17$ kcal/mol. Breaking this bond is the essential step of FAK activation. We can compare this barrier with the longest relaxation time examined in Fig. 4.6, and the agreement of the ΔG values is remarkably close. According to reaction rate theory, this energy barrier is the largest one of the assembly process, as it produces the long-time ‘bottleneck’ in the population dynamics of the onset of spreading.

In a scenario when the spreading response is initiated by the assembly of adhesome complex and engagement of mechanosensors, the cell must undergo 5 changes of state before it can start spreading, with the last being the FAK activation process, as in the previous chapter. This is necessary for the mechanosensing signal to be generated, and the cell morphological response initiated [79]; it also has to be the rate-limiting step, logistically. The possible candidates for the other 4 reaction steps must have a rate slow enough to be counted in the first data points, see Fig. 4.9 for an illustration. Images of cells were taken approximately every minute, and so it is impossible to resolve

fast processes with rates of $k > 1\text{min}^{-1}$ using the experimental data. For instance, the binding of integrins to fibronectin does not fit this criterion: it has been seen that the binding of integrins to an antibody ligand in the presence of different cations has a characteristic binding time of $0.01 - 1\text{ms}$ [183]; this is much faster than could be resolved in the experimental data. In order to form the force-bearing chain from integrin to F-actin of cytoskeleton, I see the following reactions necessary: [a] the binding of talin and kindlin to integrins, [b] the binding of paxillin to kindlin, [c] the binding of talin to F-actin, [d] the binding of FERM domain of FAK to talin, [e] the binding of FAT domain of FAK to paxillin, and [f] the binding of FAK/paxillin to the F-actin. It is difficult to find any estimates of the rates of these processes. One can find evidence for the fast strengthening of focal adhesions under load [184], but this is not the same as the assembly of these complexes at the onset of spreading. The experiments suggest that 4 of these reactions are quite slow (accounting for the need of protein localization on the complex); these can't be identified, but the combined activation energy of these four reactions has been measured (Fig. 4.8) in 3T3 and EA cells. Only once the full force-chain of the integrin adhesome is assembled, the mechanosensor produces the signal for the cell to modify its morphology to the substrate.

Another possible scenario that could account for the 5-step initial kinetics still has to rely on activation and adhesion of integrins, but could include a phase of initial viscoelastic spreading [152] that should be controlled by physical interactions on a more macroscopic scale. In that case we would require fewer slow steps of adhesome assembly. The experimental data cannot rule this out, but it is interesting to note that the universal timescale suggested by Cuvelier et al. (obtained with a much lower ligand density: fibronectin coating ten times less dense than that in this study) was between 5 and 10 minutes. Using their model with parameters they fit for HeLa cells on our fibronectin density estimates a spreading time to our criterion of around 2-3 minutes. As such, this is not inconsistent with our data, with the caveat that we are still seeing the adhesion process before spreading in the early power-law kinetics. It is also unclear whether there should be an Arrhenius activation-type temperature dependence for their spreading timescale (which is prominent in the data presented in this chapter). Certainly, the work of Cuvelier et al. avoids kinetic complications by simply considering the adhesion energy gain per unit area of the cell.

The unusual feature of this work is the use of population dynamics of spreading cells to infer details of the microscopic processes governing the cell response to an external substrate. Linking these results to nucleation theory allows us to cast new light on the onset of cell spreading as a problem of complex assembly.

THE BINDING OF TETHERED LIGANDS TO SURFACE RECEPTORS

Ordered self-assembly requires the ability to organize and bind many molecules into a coherent structure. In biology, most self-assembling structures rely on specific interactions, matching ligands and distinct binding sites. The kinetics of self-assembly is a broad and rich topic, which offers a fundamental understanding of processes being used in the construction of structured and functional aggregates.

One such process is the binding of a tethered ligand to a binding site. This is a fundamental process, involved in many biological settings. The thrombin receptor, a transmembrane protein, activates by cleaving an amino-terminal extension on the extracellular side of the membrane, unmasking a ligand which binds to another part of the receptor nested against the cell membrane [185–187]. Cytoskeletal molecular motors (dynein, kinesin and myosin) all require a periodic binding of their ligand at the end of a flexible ‘arm’ to a site on a substrate (microtubule or F-actin, respectively) a certain distance away [188, 189]. There is also a larger scale process of cell-cell, or cell-surface adhesion. Jeppesen et al. [190, 191] examined this problem for one specific binding site, where ligands tethered to the cell surface by flexible chains could also associate with the matching receptor on an adjacent cell. They found a dependence on the configuration of the polymer tether: in particular, how often the chains entered extended configurations to reach the distant receptors. Their treatment did not extend to an analytical expression of the binding rate. Theoretically solving this problem is one of our main tasks here.

The search for a small target has already been considered in the context of DNA looping [192, 26, 27], where the mean first time for two distant monomers on a polymer chain to meet was calculated. Such loops are observed experimentally in chromatin [193, 194], and in surface-tethered DNA [195, 196]. In fact, my calculation is similar to the work of Szabo et al. [26], although in their problem of forming a loop the distance to the

binding site is zero, and accordingly no activation exponential has been observed. My problem is also similar to the ‘narrow escape problem’ [197, 34, 198, 33]. Here a Brownian particle is confined to a domain whose boundary is entirely reflecting, apart from a small absorbing patch. The ‘narrow escape time’ is the mean first time the particle reaches the absorbing patch and escapes the volume it was diffusing in. The diffusion of a tethered particle (ligand) is different, since it is confined by the polymer chain statistics, rather than hard boundaries.

In the model, this graft to the surface is persistent; we can regard the polymer tether as fixed at the origin. The remaining free chain has a second binding site, subject to thermal motion. The chain has a hard constraint of the wall to which it is grafted to, but its free end (with the binding ligand) also has a soft constraint on how far it can extend from the grafted origin. If the chain end-to-end distance increases, there will be a resulting reduction in its entropy, which leads to an entropic barrier for associated activated processes. Such entropic barriers have been investigated in polymer dynamics [199], and in colloid glassy dynamics [200]. They have an important role to play in cell and molecular biology: entropic barriers show up in polymer translocation through a pore [201, 202], as well as the looping time of a polymer chain [26]. They also play a role in the protein aggregation into amyloids [203], and in more general protein folding funnel problems [30].

In this chapter, I examine a trade-off in the entropic barrier faced by reaching the distant target, which is on the same surface a fixed distance a away, against the reduction in chain confinement. I calculate the mean first time it takes the chain to find the receptor, which is determined by an activation law where the effective potential barrier is purely entropic, $-T\Delta S$. As such, the explicit temperature disappears from the Boltzmann factor and the mean binding time is proportional to $\exp[a^2/R_g^2]$, with R_g the radius of gyration of the tethered chain. If we make the chain very short, there will be a very small chance of it stretching far enough to reach the receptor site, and the time to reach the receptor will be long. If we make the chain very long, there will no longer be such a high entropic penalty for reaching the same receptor; however, the chain will now be able to explore a very large volume, and that reduces the probability that the binding site will hit the target. Once the expression for the average binding time is obtained, we are able to find the optimal chain length for the fastest binding time: this turns out to be exactly when the target separation a is equal to the radius of gyration of the chain. The second aspect of this problem is addressed in the last section of the chapter: I examine binding of the tethered ligand to a receptor on a different surface, across a gap d , in a geometry directly related to cell-cell adhesion of Jeppesen [190]. Again, I find the entropic barrier

defining the activation rate of such a process, and how the rate of such bridging across the gap depends on the distance d .

5.1 Diffusion of a tethered ligand

Consider an ideal polymer chain: N segments of length b , grafted at the origin to a flat surface, where the last (N th) monomer is the binding ligand. To find the equilibrium distribution of the chain configuration, we use the Gaussian chain propagator of an ideal chain $G_N(\mathbf{r}, \mathbf{r}_0)$: the probability that such a chain begins at \mathbf{r}_0 and ends at \mathbf{r} [204]. We need to implement a boundary condition on the substrate plane $z = 0$. This is a question with a very long history [205], culminating with the classical work of Edwards and Freed [206] on the properties of confined chains. Many aspects of this problem, of a chain near a hard wall, were explored over the years, with seminal contributions [207–209] being just a few of many important references, all using and exploiting the ‘exclusion’ condition: $G_N(\mathbf{r}, \mathbf{r}_0)|_{\text{surface}} = 0$. This means that no monomer may rest against the wall. Surprisingly, this restriction is not well covered in the literature, and it is difficult to acquire intuition for it. Exclusion seems drastically different from the reflecting boundary condition one would impose on Brownian particles, if they were not connected on the chain. This is a subtle, yet potent effect of chain configurational entropy – understood first by DiMarzio from the point of view of counting restricted chain configurations [205], and then by Edwards and Freed by looking at the entropic repulsive force arising if we were to push the chain into a wall [206].

When only one planar wall is present, the Gaussian chain propagator can satisfy the boundary condition by adding one negative chain ‘image’. Although we tether the chain at the origin $\mathbf{r} = 0$, it is necessary to insist that the first monomer steps directly away from the surface, so $z_0 = b$, and the image chain starts at $\bar{z}_0 = -b$. The remaining chain is then of length $N - 1$, but since we must assume N is large, we ignore this:

$$G_N(\mathbf{r}) = \left(\frac{3}{2\pi N b^2} \right)^{3/2} \left[e^{-\frac{3(\mathbf{r}-b\hat{z})^2}{2N b^2}} - e^{-\frac{3(\mathbf{r}+b\hat{z})^2}{2N b^2}} \right]. \quad (5.1)$$

The binding ligand (located at \mathbf{r}_N) needs to find a surface receptor placed a distance a from the grafting site, as illustrated in Fig. 5.1. The receptor zone is assumed hemispherical, with a small radius ε . We will now construct an effective radial probability distribution $P_{eq}(\rho)$ for the distance ρ from the binding site \mathbf{r}_N to the target receptor.

In Eq. (5.1), the propagator for the position of the chain end is presented using a Cartesian coordinate system with the origin at the point of grafting. However, since we

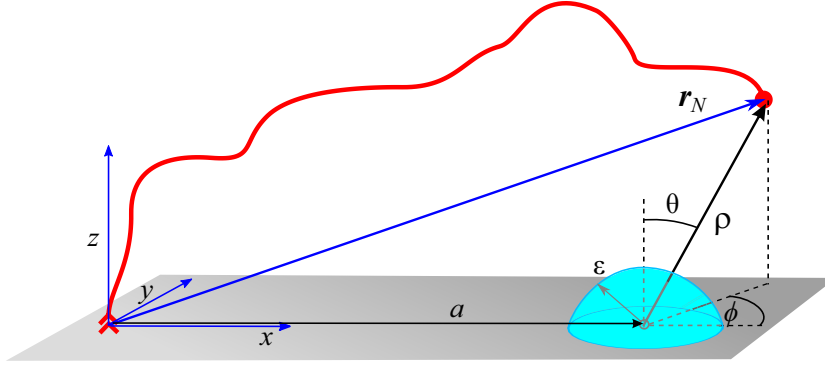


Fig. 5.1 A chain of N monomers is tethered to a hard wall at the origin. A hemispherical absorbing target of radius ε lies on the same surface, a distance a from the tether. We look for the equilibrium radial probability $P_{eq}(\rho)$ for the ligand distance to the target.

are looking for the passage time into a hemisphere centered on the receptor, it is useful to switch to spherical polar coordinates (ρ, θ, ϕ) centered on the target, Fig. 5.1. Then we will need to integrate over the two angles, to finally derive the radial probability density about the target receptor, $P_{eq}(\rho)$, which will be a function of the receptor position a . Let us choose the target to be in the positive x -direction relative to the tethered end. Then the coordinate transformation is

$$x - a = \rho \sin \theta \cos \phi, \quad y = \rho \sin \theta \sin \phi, \quad z = \rho \cos \theta. \quad (5.2)$$

The two scalar products in the combined exponents of Eq.(5.1) become:

$$(\mathbf{r} \pm b\hat{\mathbf{z}})^2 = a^2 + b^2 + \rho^2 + 2a\rho \sin \theta \cos \phi \pm 2b\rho \cos \theta. \quad (5.3)$$

The next step of integration over the solid angle on the unit hemisphere is not easy. We need to evaluate

$$I = \int_0^{\pi/2} d\theta \sin \theta \int_0^{2\pi} d\phi e^{-\alpha \cos \phi \sin \theta \pm \beta \cos \theta}, \quad (5.4)$$

where parameters α and β involve N, b, a and ρ . This is solved by realizing that the integrand has a non-trivial axial symmetry. Exploiting this symmetry, we transform back into Cartesian coordinates about the target: $x' = \cos \phi \sin \theta$, $z' = \cos \theta$, and rotate these new coordinates by an angle $\varphi = \tan^{-1}(\beta/\alpha) = \tan^{-1}(b/a)$ around the y -axis. The direction of this rotation depends on the sign of the z -term in the exponent (i.e. whether we are dealing with the ‘real’ or ‘image’ Gaussian term). The details of this calculation are given in [35], including the full expression for the normalised radial distribution $P_{eq}(\rho)$.

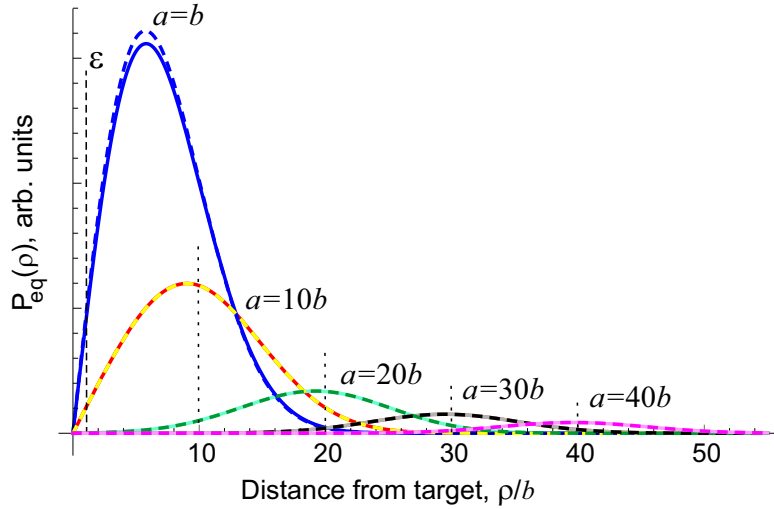


Fig. 5.2 The radial probability density $P_{eq}(\rho)$, given by the Eq. (5.5), for $N = 100$ (so $R_g = 10b$), and for several values of the target position: $a/b = 1, 10, 20, 30$ and 40 . Dashed lines show the exact result of the angular integration (5.4) for comparison: the deviations are only seen at small a .

It turns out that a very good approximation exists to that complicated expression, which is accurate except in the regime $a \leq b$:

$$P_{eq}(\rho) \approx \frac{3}{Nb^2a} e^{-\frac{3(a^2+\rho^2)}{2Nb^2}} I_1\left(\frac{3a\rho}{Nb^2}\right), \quad (5.5)$$

where $I_1(\dots)$ is the 1st rank modified Bessel function of the first kind. Note that the thermodynamic partition function of a grafted Gaussian chain is $\sqrt{6/N\pi}$ here. It is useful to define a length-scale parameter $R_g = \sqrt{Nb}$, closely related to the chain radius of gyration [204].

This distribution is plotted in Fig. 5.2. The probability density goes to zero as $\rho \rightarrow 0$ because of exclusion at the surface, and then peaks before decaying away again due to the chain being over-stretched. This peak of this distribution is going to be close to the target distance: $\rho \approx a$, because the chain is most likely to be found near the tether (which is a distance $\rho = a$ away from the target). The actual peak lies at just less than $\rho = a$, as a result of averaging over the polar angles, but the difference becomes less significant as $a \gg R_g$.

One can identify the radial probability density discussed above with an effective radial potential via the Boltzmann factor: $V_{\text{eff}} = -k_B T \ln[\rho^2 P_{eq}(\rho)]$. The resulting effective potential that the binding ligand on the N^{th} chain segment experiences is a function of distance from the target receptor, and depends on two relevant length scales in the

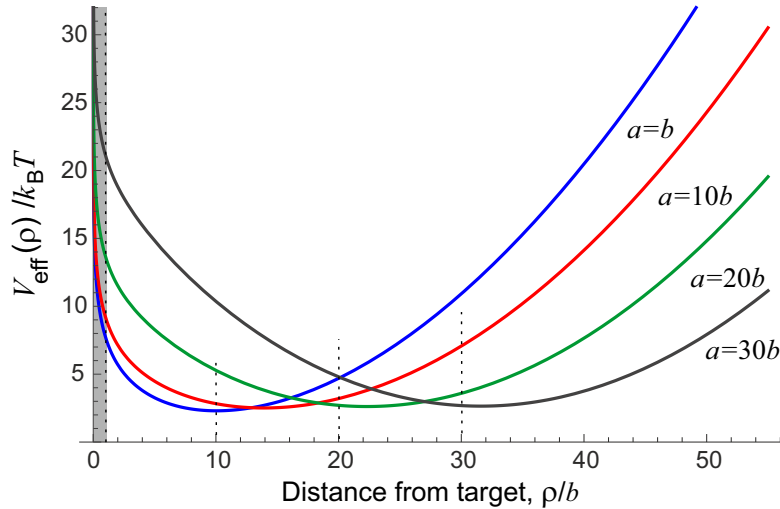


Fig. 5.3 The effective potential $V_{\text{eff}}(\rho)$ of the end of the chain, plotted for $N = 100$, (so $R_g = 10b$ here), and several values of the target position: $a/b = 1, 10, 20$ and 30 . The shaded area around the origin marks the receptor size $\varepsilon = b$.

problem: the chain radius of gyration $R_g = N^{1/2}b$, and the distance to target a . It is plotted in Fig. 5.3 for several values of a : above and below the R_g . The effective potential has a minimum (seen as the peak of the radial probability distribution), but diverges in the close proximity to the target because of the exclusion boundary condition the wall imposes on the chain: this produces an effective (entropic) repulsion that the ligand has to overcome to reach the target at $\rho \rightarrow 0$. We see in Fig. 5.3 that this effective energy barrier (between the minimum of V_{eff} and the value at $\rho = \varepsilon$) is about $4k_B T$ for $a = b$, raising to almost $20k_B T$ for $a = 30b$, for the chain of 100 monomers.

5.2 Mean first passage time to target

To find the reaction rate, we could convert our probability distribution into an effective potential, via the Boltzmann factor: $V = -k_B T \ln P_{\text{eq}}(\rho)$, and then use Kramers theory [23, 210] to derive an expression for the rate. For context, an ideal chain of $N = 100$ monomers has an effective free energy barrier (between the minimum of V_{eff} and the value at $\rho = \varepsilon$) of $\sim 2k_B T$ for $a = 5b$, rising to $\sim 5k_B T$ for $a = 20b$.

However, since we already have the equilibrium probability distribution for the single radial variable ρ (the distance of the dangling ligand from the target receptor), we can instead use a famous relation derived by Szabo et al. [26] to find the mean first passage

time (MFPT) to an absorbing surface at $\rho = \varepsilon$:

$$\tau_{\text{abs}} = \int_{\varepsilon}^{\infty} \frac{d\rho}{D \rho^2 P_{\text{eq}}(\rho)} \left[\int_{\rho}^{\infty} d\rho' \rho'^2 P_{\text{eq}}(\rho') \right]^2, \quad (5.6)$$

where we assume the diffusion coefficient of the free end of the chain, $D = k_B T / \gamma$, is constant and equal to the diffusion coefficient of a single monomer in solution (in the spirit of the Rouse model [204]). In the free particle case, it is necessary to constrain the particle with an upper reflective boundary, but for the polymer chain, the entropic spring effect ensures the integrals converge if we take the upper limit to $\rho = \infty$.

Even for the approximate probability distribution given in Eq. (5.5), the integral in Eq. (5.6) does not have an easy analytical solution. However, it is clear from Eq. (5.6) that the bracketed integral will have a value between 0 and 1 (with the integral equal to 1 for $\rho = 0$, since P_{eq} is normalized). We also notice the probability appearing in the denominator of the final integral. This means that the mean first-passage time will be dominated by any regions where $\rho^2 P_{\text{eq}}(\rho) \rightarrow 0$. For the tethered chain, this does occur as $\rho \rightarrow 0$ (as is obvious from Fig. 5.2), and so the main contribution to the mean first passage time comes from the region of small ρ (where the bracketed integral can be approximated as 1). Expanding the integrand about $\rho = 0$ and retaining only the leading term, we find that Eq. (5.6) reduces to a simple integral

$$\tau_{\text{on}} \approx \frac{2N^2 b^4}{9D} e^{3a^2/2Nb^2} \int_{\varepsilon}^{\infty} \frac{d\rho}{\rho^3} = \frac{N^2 b^4}{9D \varepsilon^2} e^{3a^2/2Nb^2}, \quad (5.7)$$

where, as before, we recognize the characteristic length scale $R_g = N^{1/2}b$: the radius of gyration of an ideal chain. Equation (5.7) is one main result of this chapter. I denote this characteristic time of binding to a receptor on the same surface as τ_{on} .

The comparison between the exact numerical integral and the approximation presented in Eq. (5.7) is shown in Fig. 5.4, where the mean time of the binding ligand reaching the target receptor is plotted against the ‘size’ of the receptor (measured by the radius of the hemisphere ε , see the sketch in Fig. 5.1). The deviations are enhanced in Fig. 5.4 inset by the logarithmic scale, and are evidently very small for sufficiently small targets. Clearly, Eq. (5.7) is a good approximation, offering a compact analytical expression that we can examine.

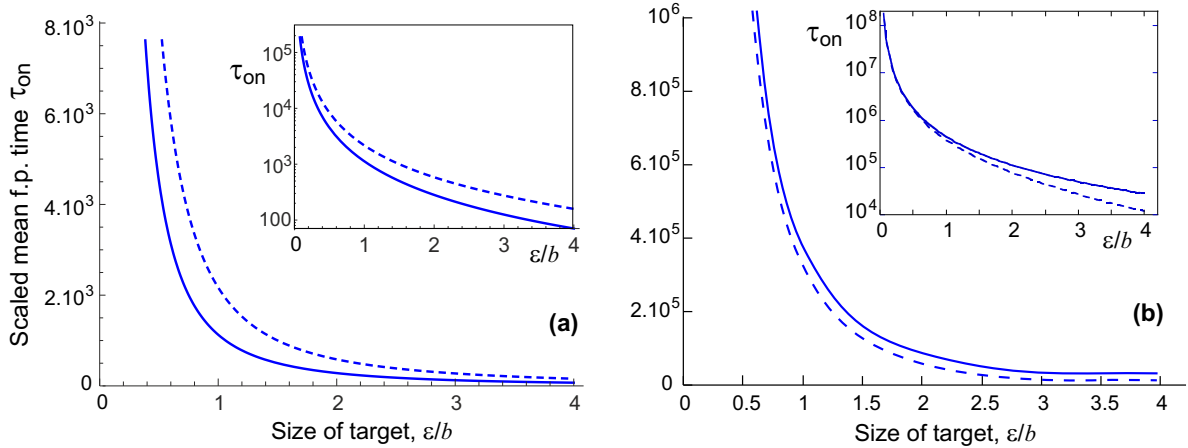


Fig. 5.4 The mean first passage time τ_{on} (in units of b^2/D) calculated numerically from Eq. (5.6) (dashed lines), compared with the approximation of Eq. (5.7) (solid lines). Here, again, $N = 100$ (so $R_g = 10b$; plot (a) is for the close proximity of the receptor, $a = b$, and plot (b) a distant receptor, $a = 20b$). In reality, one might imagine the relevant size of targets for specific binding to be not much greater than b . The insets show the same plots on logarithmic scale, which covers a greater range and also emphasizes the deviations of the approximate expression for τ_{on} .

5.3 Bridging across a gap

During cell-cell adhesion, the two cell membranes come very close to one another. Thus, they can be modelled as two parallel planes a distance d apart, with their actual curvature playing a minor role in the dynamics. As in the single plane case of the previous sections, we must consider the first monomer as stepping directly away from the surface, so the tether in this coordinate system is at $(0,0,b)$. We can then write down the chain propagator in exactly the manner of Edwards and Freed [206], separating the unconstrained chain in the xy -plane from the narrow confining box along z , with one chain end fixed at $z = b$:

$$G_N(x, y, z) = \frac{2}{d} \sum_{n=1}^{\infty} \sin\left(\frac{n\pi z}{d}\right) \sin\left(\frac{n\pi b}{d}\right) e^{-\frac{n^2 \pi^2 N b^2}{6d^2}} \cdot \frac{3}{2\pi N b^2} e^{-\frac{3(x^2+y^2)}{2N b^2}}. \quad (5.8)$$

As before, both planes are monomer excluding due to the chain entropic repulsion. When cells are close to one another, the distance $d^2 \ll N b^2$, we are free to consider only the first term in the sum, as the exponential in the sum suppresses subsequent terms (a regime known as the ground-state dominance in polymer physics).

As in the single-plane case, the key is to derive the radial probability distribution $P_{\text{eq}}(\rho)$ for the ligand a distance ρ away from the binding site, see Fig. 5.5. If the target receptor is placed a perpendicular distance a from the tether, on the opposite plane, then

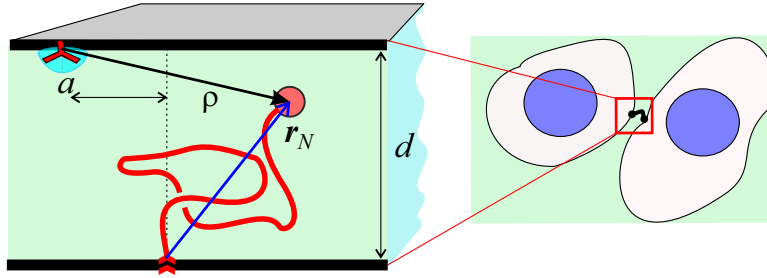


Fig. 5.5 A schematic for the cell-adhesion process, where a flexible linker will bind to a neighbouring cell across a gap d . The inset shows our simplified scenario: assuming the two membranes to be infinite in extent, and parallel to each other, with the receptor displaced by a distance a .

there is no obvious symmetry to exploit. Instead, it is possible to make progress if we use the approximation $a \gg \varepsilon$. The propagator is radial in the xy -plane about the tether. If the receptor is placed in the x -direction, then around the receptor, at small ρ , the gradient of the propagator will have no y -component to first order. Therefore we can assume that $y = 0$ in the propagator without significantly changing its value. This allows us to build our hemispherical shells centered on the target by shifting the coordinate system by $x' = x - a$, then integrating the propagator over semicircles of radius $\sqrt{\rho^2 - x'^2}$, holding x' constant. This eliminates the z -dependence, effectively generating the average $\langle \sin(\pi z/d) \rangle$. The second integration is over the x' -axis from $-\rho$ to $+\rho$, adding these semicircles with an appropriate surface element to recover the radial distribution function about the receptor. This distribution $P_{eq}(\rho)$ can be expanded at small ρ again, exploiting the vanishing denominator as in Eq. (5.7), and in the same way we obtain the result for the mean first passage time:

$$\tau = \frac{2Nb^2d^2}{3\pi^2D\varepsilon^2} e^{3a^2/2Nb^2}. \quad (5.9)$$

One can see the same constrained dependence on the reaction volume ε , due to the difficulty for any chain segment to get that close to the wall. It is possible to consider the $a = 0$ case using a different method, relying on the azimuthal symmetry of the propagator. We recover the non-exponential prefactor in Eq. (5.9), confirming the validity of the analysis. It is also possible to adapt this result for a very small gap, $d < \varepsilon$, where the 2D scaling relation $\tau \sim (Nb^2/D) \ln(\sqrt{Nb^2}/\varepsilon)$ replaces Eq. (5.9). See Schuss et al. [33] for a freely diffusing Brownian particle analogue.

The quadratic dependence of the mean bridging time on the cell gap d in Eq. (5.9) is the novel feature, but it is only valid in the tightly confined case $d \ll R_g$. The general expression for the binding time is complicated, but the calculation in the opposite limit

(short chain or wide gap: $d^2 \gg Nb^2$) is presented in [35]. I found a very accurate interpolation formula for the mean time of bridging between two surfaces, which spans across the whole range between the two limiting cases:

$$\tau_2 = \frac{2R_g^2 d^2}{3\pi^2 D \varepsilon^2} \frac{1}{(1 + 36d^4/\pi^2 R_g^4)} \cdot e^{3(d^2+a^2)/2R_g^2}. \quad (5.10)$$

5.4 Optimising the reaction time

It is interesting to compare the tethered binding time τ_{on} in Eq. (5.7) with the average time for a free polymer chain to make a loop by having the last N th monomer reach a sphere of radius ε around the first monomer [26] (the Szabo problem, corresponding to distance $a = 0$, and no restricting surface):

$$\tau_{\text{loop}} = \sqrt{\frac{\pi}{54}} \frac{(Nb^2)^{3/2}}{D\varepsilon}. \quad (5.11)$$

This involves integrating the free space propagator over the full space in Eq. (5.6), rather than the constrained propagator over the half space in the single plane case. Also instructive is to compare with the average time for a free Brownian particle to escape a closed volume V through a small hole of size ε [33] (the ‘narrow escape problem’ of Holcman et al.), which is estimated as $\tau_{\text{esc}} = V/D\varepsilon$. If the volume is replaced by the average extent of chain spreading, $V = R_g^3$, this matches the Szabo expression in Eq. (5.11). Both have a different scaling with the size of target: $1/\varepsilon$ compared to $1/\varepsilon^2$ in our Eq. (5.7). The chain is inhibited from approaching the wall due to the polymer-specific exclusion boundary condition, and so the average time it takes to reach the target is much longer even without the additional exponential factor reflecting the entropic barrier for binding. The same argument applies to the mean bridging time τ_2 in Eq. (5.10): an entropic repulsion of monomers from the surface causes a stronger, $1/\varepsilon^2$ scaling with the receptor size.

The second factor that distinguishes the mean binding time in Eqs. (5.7) and (5.10) is the exponential factor: $\exp[3a^2/2R_g^2]$ and $\exp[3(a^2 + d^2)/2R_g^2]$, respectively. In both cases this represents thermal activation over an entropic barrier $\Delta G = \frac{3}{2}k_B T(a^2/Nb^2)$, which is essentially the free energy to stretch the chain ends by a distance a . This factor, significantly increasing the time for bridging to a distant target, only arises for the tethered chain (all polymer work on the related narrow escape problems [199, 202, 30] has thus far focused on polymers with no attachment to the boundary of the domain, which fundamentally alters the accessibility of the binding site). One might then, naively

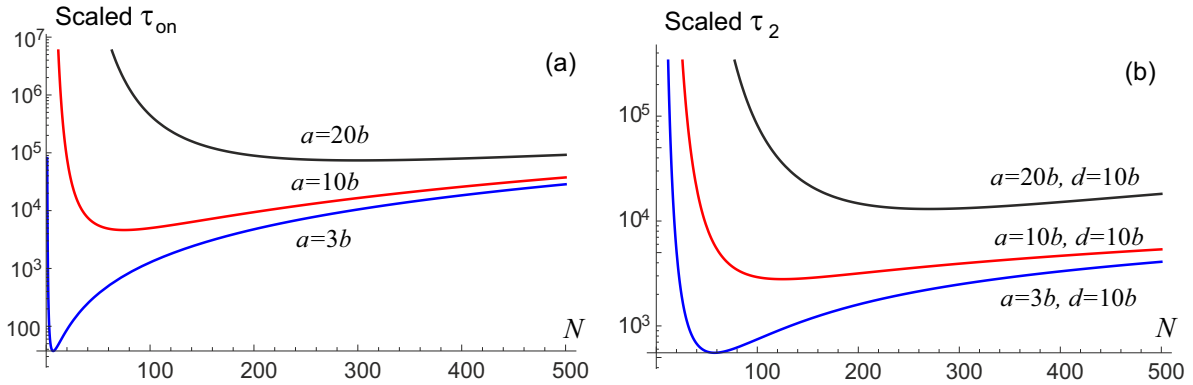


Fig. 5.6 The dependence of scaled mean binding times ($\tau \cdot D\varepsilon^2$) on the chain length via $R_g = \sqrt{Nb}$: (a) for the tethered binding in the same plane, for $a = 3b, 10b, 20b$, and (b) for bridging across the gap, for $a = 3b, 10b, 20b$ with $d = 10b$.

assume that the binding time will decrease monotonically as the length of the chain increases – the entropic penalty will become smaller and smaller.

However, as I find in Eqs. (5.7) and (5.10), there is another competing effect that decreases the rate (or increases the mean first passage time): as the chain gets longer, the effective volume that the site can explore relative to the receptor volume also increases. If we increase the chain to an infinite length, we actually return to a free particle scenario, and there is not enough confinement for the end of the chain to ever hit the receptor. Figure 5.6 illustrates the resulting effect, which predicts a certain optimal (shortest) binding time for any given receptor separation. It is straightforward to find the shortest binding times, and the chain length N^* that achieves this rate in each case:

$$\tau_{\text{on}}^* \approx 0.46 \frac{a^4}{D\varepsilon^2} \quad \text{at} \quad N^* = \frac{3a^2}{4b^2}, \quad (5.12)$$

$$\tau_2^* \approx 0.04 \frac{d^4}{D\varepsilon^2} \quad \text{at} \quad N^* \approx \frac{a^2 + d^2}{2b^2} \quad \text{and} \quad a \rightarrow 0. \quad (5.13)$$

The scaling with the receptor size ε is an interesting feature, especially when compared with the looping or narrow escape problems (which both have the ε^{-1} scaling). Together with the entropic barrier, this effect determines the mean first binding time of a tethered ligand.

I approached this problem in a way completely different to the approach of Holcman et al. in the narrow escape setting [34, 33]. Instead of examining the Smoluchowski problem in an effective potential imposed by the constraints, one can generate the mean-field equilibrium probability density $P_{eq}(\rho)$ by integrating out the angular degrees of freedom. As a result, I was able to utilize the backward Fokker-Planck approach of Szabo et al. [26].

It may well be that this approach generates analytical and numerical solutions more rapidly even for the more complex problems involving potential interaction and non-ideal polymer chain, as well as confined Brownian particles, since you don't have to look at the dynamical effects – only at how these affect the equilibrium effective potential. However, the scope of the method is limited to Markovian processes, using as it does the backward Fokker-Planck operator.

Further, while theoretically clean, the absorbing boundary has only limited biological application as it assumes infinitely fast binding reaction. It is more relevant to consider the case where binding to a surface is slower, and the reaction time becomes a relevant factor slowing down the reaction. For instance, DNA loop formation is much slower than the diffusive end-to-end encounter [211]. In their original work on first passage time, Szabo et al. [26] allowed for this by adopting a radiation condition on the flux at the boundary: $J(\varepsilon, t) = \kappa p(x, t)$. The constant κ is indicative of the reaction rate at the boundary: for $\kappa \rightarrow \infty$ we reach the limit of an ideal absorbing boundary. In our formalism, accounting for κ adds an extra term into the mean process time: $\tau_\kappa = [\kappa\varepsilon^2 P_{eq}(\varepsilon)]^{-1}$. For the laterally displaced receptor, the full form of the mean binding time takes the slightly modified form:

$$\tau_{\text{on}} = \frac{N^2 b^4}{9D\varepsilon^2} e^{\frac{3a^2}{2Nb^2}} \left(1 + \frac{2D}{\kappa\varepsilon} \right). \quad (5.14)$$

A sufficiently small reaction volume (ε) and reaction rate (κ) could significantly slow down the binding process, in addition to the entropic penalty.

5.5 Multiple ligands on a tethered chain

Having considered the problem of a single tethered ligand binding to a receptor, I now consider the more complicated case, where there are multiple ligands spaced along the tether, each attaching to a receptor. This is an interesting problem in ordered self-assembly. The kinetics of ordered self-assembly is a broad and rich topic, which offers insight into the construction of structured and functional aggregates.

Surface adsorption of a polymer is not a new topic; industrial interest in colloid stabilisation and oil extraction led the early theoretical pioneers – Silberberg [212], de Gennes [213, 208] and Alexander [214] – to study the equilibrium properties of polymer chains close to surfaces. As polymer physics matured, there grew a need to understand the kinetics of adsorption. Existing work distinguishes between two regimes, depending on the free energy barrier presented to monomers binding on the surface: chemisorption if the reaction barrier is high, and physisorption if the barrier is low and the characteristic

time to establish a bond on contact is short. In chemisorption, the reaction time of the monomers is larger than the time for the polymer to return to an equilibrated state, so the process becomes quasistatic. Theory [215, 216], experiment [217], and simulations [218–220, 217, 216], have all shown that two mechanisms control chemisorption: the zipping down of sequential monomers, and the formation of extra nucleation points via loop formation. Loop formation lowers the adsorption time relative to a simple sequential zipping mechanism, and so chemisorption is said to take place via the accelerated zipping mechanism.

Physisorption is, on average, a simple zipping mechanism: sequential monomers very quickly attach to the surface, leaving no time for loop formation [220–222, 216]. This forces the chain out of equilibrium, as the remaining unabsorbed segment initially moves more slowly than the chain zipping down. The precise scaling of this adsorption time depends on the strength of the polymer-surface attraction [216]. For irreversible physisorption, the intermediate chain conformation combining a stretched tether at the zipping end, and a coil at the free end, is known as the ‘stem and flower’ model, and was first described by Brochard-Wyart [223] for tethered polymers under strong shear flow.

Many of the systems considered are entirely homogeneous polymer chains with no specificity of binding sites, while others examined copolymers attaching to uniform surfaces [219, 224]. Li et al. have studied stripe-patterned surfaces [225], and copolymers of one attractive and one inert monomer type [226], but many processes in self-assembly are much more specific than this. These processes, such as DNA hairpin formation [227, 228], still show zipper kinetics.

In the rest of the chapter, I do two things: first, using the knowledge acquired about the binding MFPT – see Fig. 5.7(a), I first evaluate the average binding time to a sequence of such receptors, Fig. 5.7(b). This process of chain adsorption may proceed via different pathways, involving purely sequential (zipper) single steps, or multiple-distance looping events. It turns out that, for sufficiently separated binding sites, the simple zipping mechanism becomes the preferred pathway. Secondly, I consider the ‘stem and flower’ effect, and show that for a chain looking to bind its free end to a target a distance a away as fast as possible, non-equilibrium effects associated with a slow drift of the chain towards the receptor targets defines a certain optimal number of intermediate receptors that achieves the fastest mean adsorption time.

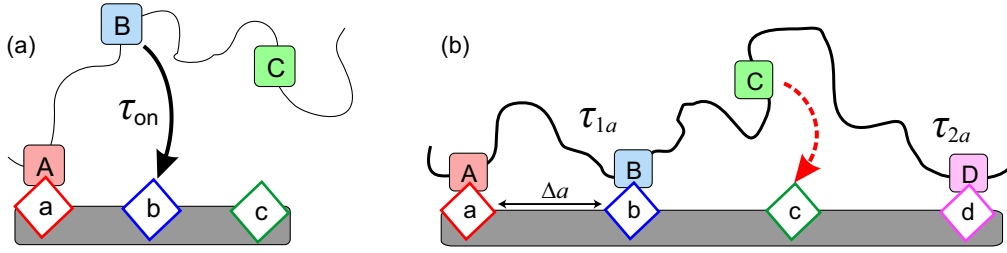


Fig. 5.7 A scheme of ordered self-assembly of a polymer chain binding to a specific sequence of receptors on a substrate. (a) The single binding time τ_{on} is a function of chain length A-B and the receptor separation a-b. (b) Each surface receptor is separated by a distance Δa . In this scenario, the ligand [B] has bound via a single step, with typical time $\tau_{1a} = \tau_{\text{on}}(\Delta a)$, and the ligand [D] has bound with a double step of time τ_{2a} ; the ligand [C] will then bind quickly.

5.6 Accelerated zipper binding

As before, we can consider an ideal polymer chain of N segments of length b , which is grafted at the origin to a flat surface, where the last (N th) monomer is the binding ligand. Its matching receptor is located on the same surface, a distance a away, Fig. 5.7(a). The expected binding time for the ligand to its receptor is given by the familiar expression

$$\tau_{\text{on}} \approx \frac{N^2 b^4}{9D\varepsilon^2} e^{3a^2/2Nb^2}. \quad (5.15)$$

where we assume the receptor zone is hemispherical, with a small radius ε , and the diffusion coefficient of the free end of the chain, $D = k_B T / \gamma$, is a constant equal to the diffusion coefficient of a single monomer in solution.

We can now use Eq. (5.15) for $\tau_{\text{on}}(a, N)$ to examine a simplified version of the multiple-site binding problem. Let us consider M binding sites spaced evenly along a polymer chain of total length N (so that the ligands are $\Delta N = N/M$ monomers apart, along the chain). As in the single-site problem, we must take the first segment of the chain to be already bound (grafted) to the surface, so there are M binding events yet to occur in total. The receptors for these ligands are spaced at equal distances Δa apart in a straight line on a plane reflecting surface, see Fig. 5.7(b). While it should not be difficult to consider arbitrary positioning of chain binding sites and surface receptors, I use this simplified geometry in the hope of finding a clear analytical result for the average binding time.

Assuming that each binding ligand on the chain associates with a specific receptor, the chain may form a loop by binding across several receptors, a distance $q\Delta a$ from the

grafting point, see Fig. 5.7(b) for a $q = 2$ loop. The time to bind to a receptor a distance $q\Delta a$ away is

$$\tau_{qa} = \frac{(qN/M)^2 b^4}{9D\varepsilon^2} e^{\frac{3(q\Delta a)^2 M}{2qNb^2}} = q^2 e^{\frac{3(q-1)M\Delta a^2}{2Nb^2}} \cdot \tau_{1a}, \quad (5.16)$$

where the single-step binding time $\tau_{1a} = \tau_{\text{on}}(\Delta a, N/M)$ from Eq. (5.15). If the chain does not bind sequentially, but with a loop forming (for example, next nearest binding in Fig. 5.7(b)), the subsequent binding of the ‘middle’ ligands is much faster (site [C] between [B] and [D] in Fig. 5.7(b)), and therefore is not a rate-limiting step. The combination of single and multiple steps is the accelerated zipper mechanism.

The kinetics of both single and multiple steps can be understood as a continuous-time Markov chain [229, 230], with $M + 1$ discrete states corresponding to how far along the chain the final binding event has been. This means we can write the rate equations in vector form: $dP/dt = Q \cdot P$, where Q is known as the rate matrix. This is called the backward Kolmogorov equation. The $(M + 1) \times (M + 1)$ rate matrix has the following form:

$$Q = \begin{pmatrix} -\sum_{q=1}^M k_q & k_1 & k_2 & k_3 & \dots & k_M \\ 0 & -\sum_{q=1}^{M-1} k_q & k_1 & k_2 & \dots & k_{M-1} \\ 0 & 0 & \ddots & \ddots & \ddots & \vdots \\ \vdots & \dots & 0 & -\sum_{q=1}^2 k_q & k_1 & k_2 \\ \vdots & 0 & \dots & 0 & -k_1 & k_1 \\ 0 & 0 & 0 & \dots & 0 & 0 \end{pmatrix} \quad (5.17)$$

where $k_q = 1/\tau_{qa}$ are the rates of binding to a receptor a distance $q\Delta a$ away. Instead of explicitly solving the Kolmogorov equation, we can rely on the following fundamental result to derive the recursive relations for mean first passage times $\langle \tau(M + 1 - i) \rangle$ from state i to the final fully bound state (across $M + 1 - i$ receptors, where state $i = 0$ is the tethered chain with no receptors bound, and $i = M + 1$ is when the final M th receptor is bound)[230]:

$$\sum_j Q_{ij} \langle \tau(M + 1 - j) \rangle = -1, \quad (5.18)$$

for all states $1 \leq i < M + 1$. If we start in the final absorbing state, then the mean first passage time is zero by definition, and so $\langle \tau(0) \rangle = 0$. The remaining $\langle \tau(i) \rangle$ can then be constructed recursively.

While Eq. (5.18) is a full solution to the problem of mean binding time, it does not indicate how important loop formation is in the binding process. To make progress, I compared the binding times τ_{qa} . For multiple steps, the rapidly increasing entropic barrier to reach receptors further away means that the expected time for binding gets

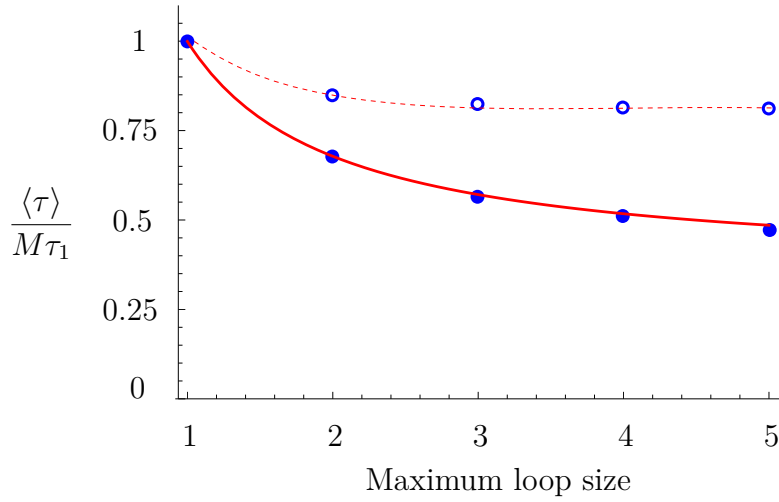


Fig. 5.8 The plot of the (scaled) average adsorption time $\langle \tau(M) \rangle$ for $M = 20$, when the multiple-step jumps (loops) are allowed. The x -axis indicates the largest jump allowed to accelerate the zipper binding. Filled symbols \bullet represent the maximum effect, when the exponential entropic-penalty factor in τ_{1a} is equal to one (i.e. the distance $\Delta a = 0$); the open symbols \circ represent the reduced acceleration effect when $\Delta a^2 = \Delta N b^2$.

longer and longer. Figure 5.8 shows how the mean binding time across $M = 20$ receptors reduces as we include the possibility of longer jumps. It is clear that we are free to neglect steps past $q = 2$ when $\Delta a^2 \geq \Delta N b^2$ (the open symbols in Fig. 5.8, as τ_{qa} rapidly increases with q , and the adsorption time seems to rapidly approach a limiting value. For very closely spaced receptors ($\Delta a^2 \ll (N/M)b^2$) the ratio of $\tau_{qa}/\tau_{1a} = q^2$, and Fig. 5.8 shows that although the largest reduction in binding time comes from increasing the maximum step to $q = 2$, larger size loops do still play an appreciable role. To offer a quantitative idea of how big a role they play, I manually fitted a curve to the closely spaced receptors in Fig. 5.8 (the solid red line), and found that the deviation from a fitted limiting value $\langle \tau_\infty \rangle$ was $\langle \tau_q \rangle - \langle \tau_\infty \rangle \propto 1/q$.

In the regime $\Delta a^2 \geq \Delta N b^2$, I restrict the binding process to either binding at the closest available site, which takes an average time τ_{1a} and follows in a zipper sequence, or at the next nearest site, which takes τ_{2a} , as shown in Fig. 5.7(b); all other binding events across greater distances are neglected ($k_i = 0$ for $i > 2$). Then, Eq. (5.18) defines a recurrence relation for arbitrary M :

$$\begin{aligned} \langle \tau(1) \rangle &= \frac{1}{k_1}, & \langle \tau(2) \rangle &= \frac{2}{k_1 + k_2}, \\ (k_1 + k_2)\langle \tau(M) \rangle &= 1 + k_1\langle \tau(M-1) \rangle + k_2\langle \tau(M-2) \rangle & \text{for } M \geq 2. \end{aligned} \quad (5.19)$$

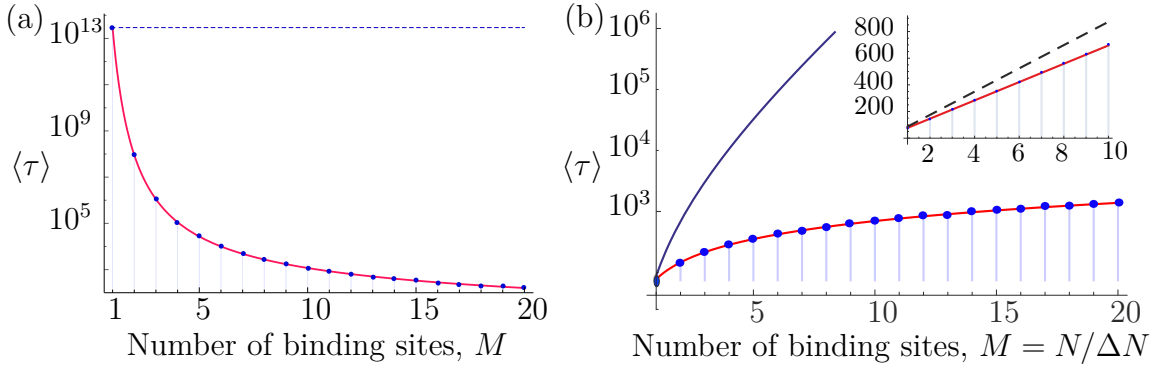


Fig. 5.9 The mean time $\langle \tau \rangle$ (in units of b^2/D , logarithmic scale) to bind the chain to the surface, as a function of the number M of equidistant binding sites. (a) A fixed chain $N = 100$ segments. The dashed blue line marks the case of $M = 1$, when only the N th segment has a binding ligand, reaching for a receptor $a = 40b$ away. As the number of binding sites along the chain increases, the time to bind the final receptor dramatically reduces. (b) A fixed interval between receptors $\Delta N = 20$, so $N = M\Delta N$. The plot compares a chain with single binding site at a distance $a = 3Nb/20$ (solid blue line), and a chain with $M = N/\Delta N$ binding sites every 20 monomers, whose receptors are spaced at $\Delta a = a/M = 3b$. In both cases, the end of the chain binds at the distance a . The inset illustrates that the typical binding time increases almost linearly with chain length or number of sites, in contrast to the exponential increase of this time for the single-site chain. The dashed black line indicates the line $M\tau_{1a}$, which is the strictly single-step zipper binding pathway. The possibility of occasional double steps lowers the binding time of an ‘accelerated zipper’. In both plots, the blue dots represent the exact expression for $\langle \tau \rangle$; the continuous red line is the plot of (5.21), where $\Delta a = a/M$.

Using a standard generating function method to solve the recurrence relation [231], we find that

$$\langle \tau(M) \rangle = \frac{Mk_1^2 + 2(M+1)k_1k_2 + 2k_2^2 \left(1 + \left(-\frac{k_2}{k_1+k_2}\right)^{M-1}\right)}{k_1(k_1 + 2k_2)^2}. \quad (5.20)$$

Since this expression is only valid for sufficient spacing, $k_2 \ll k_1$, and we are free to Taylor expand Eq. (5.20):

$$\langle \tau(1) \rangle \approx M\tau_{1a} - \frac{2(M-1)\tau_{1a}^2}{\tau_{2a}} = \left(M - \frac{M-1}{2} e^{-\frac{3M\Delta a^2}{2Nb^2}}\right) \tau_{1a}. \quad (5.21)$$

This expression is another main result of this chapter. Figure 5.9 shows the comparison of the approximation presented in Eq. (5.21), and the exact sum in Eq. (5.20), the latter plotted as discrete points at integer values of M . Evidently, the approximation (5.21) is virtually indistinguishable from the exact average binding time, when the probability of making a double step is small.

How does adding more binding sites along a chain length influence its time to bind to a surface? Let us consider a chain of fixed length N , as usual grafted at the origin. There is a binding ligand on the end of the chain, and Eq. (5.15) gives the mean time for it to bind at a receptor on the surface a long distance a away: $\tau_{\text{on}}(N, a)$. Let us now add several more binding ligands on the chain, such that they have N/M monomers in between, and the matching sequence of equidistant receptor sites on the surface, such that they are a distance $\Delta a = a/M$ apart. The resulting decrease in binding time is plotted in Fig. 5.9(a). Note that the binding time is plotted on a logarithmic scale, so the effective decrease is quite dramatic when more binding sites are added to the chain. Equation (5.21) gives the scaling $\langle \tau \rangle \propto M^{-1} \exp[\alpha/M]$.

I have also examined the situation where the binding site density is kept constant, i.e binding sites on the chain are equally spaced, and the matching receptors on the surface are always spaced the same distance Δa apart, but vary the total length of the chain. In this case the total chain length $N = M\Delta N$, and the distance to the last receptor is $a = M\Delta a$. The results are plotted in Fig. 5.9(b) for the receptor density $\Delta a = 3\Delta Nb/10 = 6b$. The comparison is made with the mean binding time for the chain with only one binding site at the end, with the chain length and the distance to the single receptor related in the same way: $a = 3Nb/10$ away, to illustrate the role of overall chain length. This time increases almost exponentially, see Eq. (5.15) giving $\tau_{\text{on}} \propto N^2 \exp[\alpha N]$. In contrast, the mean time to bind a sequence of receptors increases only \sim linearly with the chain length, illustrating that multiple sites massively enhance the binding rate. Note that a non-zero probability to make occasional double steps increases the binding rate even further, comparing with the straight zipper sequence, making it an ‘accelerated zipper’ process – this is illustrated by the linear plot in the inset of Fig. 5.9(b).

5.7 Drift of center of mass

When we consider a single binding event, we do not consider the entire chain’s length, but instead just the length between the tether and the binding site. However, in a sequence of binding events, we must consider how the rest of the chain moves around at the time of binding. In a typical monomer-by-monomer physisorption of a chain to a uniform surface, the rapid binding of monomers to the surface moves the effective current grafting point away from the center of mass of the remaining free chain, resulting in the ‘stem and flower’ configuration of Brochard-Wyart [223, 222]. This has an effect on the adsorption kinetics. Is there a similar effect when there is a section of chain between binding sites?

According to equilibrium polymer statistics, at the moment of a binding event, we would expect the remainder of the chain to be centered directly above the new grafting site. This stems from the Markovian treatment of the polymer chain, and is easily derived through Gaussian propagators. However, a study by Guérin et al. [232] found that in reality, non-Markovian effects (i.e. non-Gaussian chain statistics before equilibrium is reached) play a large role in determining the dynamics of polymer configurations for reactions to a target in free space. The delay in reaching the equilibrium is often quite extended, so that the chain leaves the center of mass behind while reaching for a new target. This becomes clear if we consider the Rouse modes of the chain: the typical time for a monomer to fluctuate (travel a distance a) is much smaller than that for the chain center of mass to do the same. As such, the polymer chain is ‘left behind’ when the next binding site finds its receptor, and we will need to consider the subsequent drift of the chain center of mass to the new grafting point. In this case, in contrast to the monomer-by-monomer physisorption, the rare binding steps result in a high stretching of the ‘stem’ and a relatively high force pulling the remaining free chain towards the new equilibrium around the new grafting site. The mean time to diffuse a distance for the center of mass to diffuse the distance a is:

$$\tau_{\text{com}} = \frac{N_f a^2}{D}, \quad (5.22)$$

where N_f is the number of monomers in the remaining free chain, so that $N_f \gamma$ is the effective friction constant for the free chain center of mass. As before, $D = k_B T / \gamma$ is the diffusion constant for a single monomer. In order for the Szabo-based [26] expression for the binding time τ_{1a} to be valid, we should have a chain in equilibrium configuration, which occurs when $\tau_{\text{com}} / \tau_{1a} \ll 1$. This ratio takes the form:

$$\frac{\tau_{\text{com}}}{\tau_{1a}} = 9 \frac{N_f \varepsilon^2 \Delta a^2}{\Delta N^2 b^4} e^{-3\Delta a^2 / 2\Delta N b^2}. \quad (5.23)$$

Assuming only a single-step zipper binding for simplicity, for the m th binding event, the remaining $N_f = (M - m + 1)\Delta N$. Remembering that the total number of monomers, $N = M\Delta N$, and that the M th receptor is placed at a distance $a = M\Delta a$, this condition takes the form:

$$m \gg M + 1 - \frac{MNb^4}{9\varepsilon^2 a^2} e^{3a^2 / 2MNb^2}. \quad (5.24)$$

We can define the crossover point, m_{com}^* , at which the binding time becomes comparable to the characteristic time of the center of mass diffusion by demanding equality in Eq. (5.24). So the equilibrium theory of binding to a distant site is valid at $m \gg m_{\text{com}}^*$, and

in the opposite limit the dynamics is determined by non-equilibrium (non-Markovian) statistics.

How does this affect the zipper action? Let us assume that the polymer chain is initially equilibrated, with its center of mass close to the current point of grafting. After reaching for the next receptor site, the chain binds there, and then the remaining free chain finds its center of mass a distance Δa out of equilibrium. The entropic force due to this stretching of the chain will provide an impetus to move the center of mass of the remaining chain to re-equilibrate above the new grafting position, and we can write down the dynamical equation for the movement of the center of mass:

$$-(N_f \gamma) \dot{x} - \frac{3k_B T}{2N_f b^2} (x - \Delta a) = 0, \quad (5.25)$$

where, again, N_f is the number of monomers in the remaining free chain. It follows that the relaxation time to the new equilibrium of the free chain is given by

$$\tau_{\text{drift}} = \frac{2N_f^2 b^2}{3D}. \quad (5.26)$$

Then, following a similar method to before, we can find a condition on m for the drift time to be dominant, $\tau_{\text{drift}}/\tau_{1a} \gg 1$:

$$m \ll M + 1 - \frac{1}{\sqrt{6}} \frac{b}{\varepsilon} e^{3a^2/4MNb^2}, \quad (5.27)$$

because for early binding events (small m), there is a lot of free chain, and so τ_{drift} is large. For later binding events, the remaining free chain is able to equilibrate fast, and so there is no need to account for the drift of center of remaining mass.

We can define the other crossover point, m_{drift}^* , at which the chain binding changes from being limited by the chain relaxation time, given by Eq. (5.26), to being limited by the time τ_{1a} to reach the next binding site, by setting equality in (5.27). It turns out that, in spite of subtle differences, the crossover expressions are quite close numerically: $m_{\text{com}}^* \approx m_{\text{drift}}^* = m^*$. So when the equilibrium expression for the binding time is valid ($m \gg m_{\text{com}}^*$) it is also the case that the total binding time is dominated by the reaching time. On the other hand, when the chain is not equilibrating fast enough ($m \ll m_{\text{com}}^*$), it is also the case that the binding is limited by the slow drift of the chain center of mass.

Therefore, the first m^* binding events (when the free chain segment is still long) will be relaxation-limited, while the last $(M - m^*)$ events are independent of the chain length.

The effective binding time takes the form:

$$\tau = \sum_{m=1}^{m^*} \tau_{\text{drift}}(m) + (M - m^*)\tau_{1a} \quad (5.28)$$

(neglecting the weaker effect of accelerated zipper, for clarity). If $m^* < 1$, which is always the case at small M , then all binding events are reach-limited, and the expression returns to the simple linear zipper $\tau = M\tau_{1a}$.

Figure 5.10(a) illustrates how increasing the number of intermediary binding sites affects the total time to adsorb a chain, which is essentially the time to bind to the final receptor a fixed distance away. This is analogous to Fig. 5.9(a) obtained in the fully equilibrium-chain setting; in fact, the dashed lines in Fig. 5.10(a) give the lines of Eq. (5.21) as in Fig. 5.9(a). We see that for small M , increasing the number of binding sites along the chain reduces the total binding time, because the process is purely reach-limited ($m^* < 0$). As the number of intermediary sites increases, however, we cross into a regime limited by the relaxation (drift) of the chain center of mass. Here, increasing the number of sites lowers the drift force in the Langevin equation, and so the chain will actually take longer to reach the terminal receptor. Note that all curves saturate on the same line, because the relaxation-limited time does not depend on a : making the summation in Eq. (5.28) for $m^* = M$ gives a linear estimate $\tau \approx M(2Nb^2/9D)$ for this section of the curves in Fig. 5.10(a).

Between these two effects: the zipper time, which becomes shorter when more receptors are added on a fixed interval, and the relaxation (drift) time of the chain center of mass, there is clearly an optimal number of binding sites that achieves the shortest time for the complete chain adhesion. To find this point, one has to solve the derivative of Eq. (5.28): $d\tau(M)/dM = 0$. This is a complicated algebraic task, which simplifies in the limit $a^2 > Nb^2$, that is, when the chain needs to adsorb by stretching over some distance. In this case the minimum of the adhesion time is for the M determined by the equation:

$$16N\varepsilon^3 M^4 - 2\sqrt{6}a^2 b e^{\frac{9a^2}{4MNb^2}} = 0. \quad (5.29)$$

This transcendent equation has a solution in terms of the Lambert W-function, or the product logarithm, but this is too cumbersome to get a clear understanding. However, in the limit $a^2 \gg Nb^2$, the leading contribution to the ‘optimal’ number of receptors for the

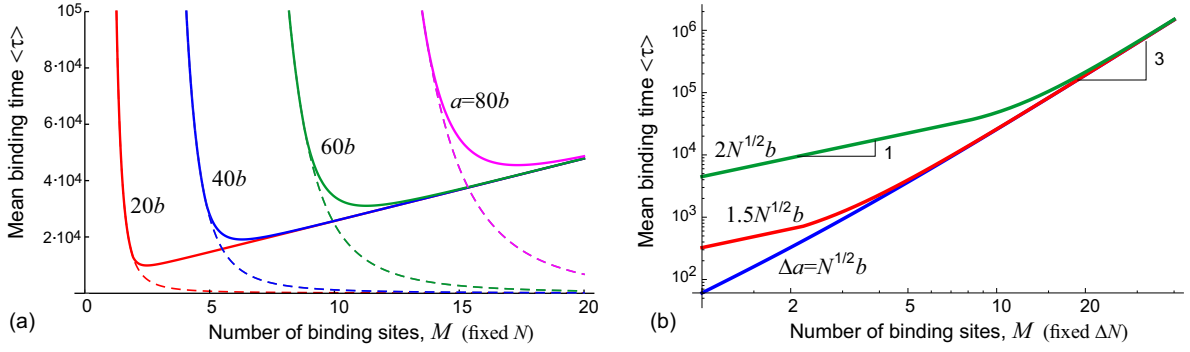


Fig. 5.10 The adhesion time is plotted in units of b^2/D , for $\varepsilon = b$. (a) The linear plot for a fixed $N = 100$. The set-up is M receptors, with the final receptor placed at varying distances a away in different curves (labelled on the plot). The dashed line shows how the reaction-limited time reduces as M increases. (b) The log-log plot, for fixed $\Delta N = N/M = 10$. From top to bottom, the distance between consecutive receptors $\Delta a = \sqrt{\Delta N b^2}$, $1.5\sqrt{\Delta N b^2}$, and $2\sqrt{\Delta N b^2}$. For shorter chains, there is a reach-limited linear ‘zipper’ region (gradient slope of 1 is shown), before switching to the cubic increase of time with length as chains get longer (gradient slope of 3 is shown), see Eq. (5.31). For larger Δa , the linear region is extended.

shortest adhesion time takes the form

$$M_{\text{opt}} \approx \frac{3a^2}{4Nb^2} \left[\ln \left(\frac{9a^2}{16Nb^2} \frac{\varepsilon}{b} \sqrt{\frac{3}{2}} \right) \right]^{-1} = \frac{3a^2/4R_g^2}{\ln(0.69[a^2/R_g^2](\varepsilon/b))}. \quad (5.30)$$

In Figure 5.10(b) I instead fix the distance between receptors, Δa , and the chain length between binding sites, ΔN , as in Fig. 5.9(b). When the total adhesion time is plotted on a log-log scale, one can clearly see the two distinct regimes: the reach-limited at small M (the linear zipper increase), changing to the cubic increase as we go to larger M and the relaxation-limited regime. In this latter regime, Eq. (5.26) with $N_f = [M - m + 1]\Delta N$ dominates the contributions to the total adhesion time (5.28), producing the dominant cubic dependence on the number of receptors, as illustrated in the plot:

$$\tau \approx \sum_{m=1}^M \frac{2(N - [m - 1]\Delta N)^2 b^2}{3D} \rightarrow \frac{2M^3 \Delta N^2 b^2}{9D} + \dots \quad (5.31)$$

The biggest limitation of this model is the specificity of all receptors, and their matching binding ligands on the polymer chain. Non-specific binding of chain segments to the surface has already been covered for uniform surfaces [218–220, 217, 216], and the case of spaced receptors is relevant for applications such as receptor targeting with multivalent polymers [233]. Could this be considered within the framework of this

model? Here, in order to have the dominance of the zipper pathway, we need to be assured that there is no competition for the same receptor by different binding ligands (and therefore a possibility of mis-assembly). This occurs when the second (or higher, number q) ligand along the chain takes a longer time to bind to the nearest receptor. The binding time for forming a loop of (qN/M) monomers, binding a distance Δa , is $\tau_{1a}(q) = q^2 \exp[(1/q - 1)3M\Delta a^2/2Nb^2] \cdot \tau_{1a}$, compare with Eq. (5.16). So the non-specific binding will follow the zipper pathway when $(N/M)b^2 \gg (3(1 - 1/q)/4 \ln q)a^2$, for all q . Since this is a decreasing function with q , we can replace the function with the value for $q = 2$, and get that $Nb^2 \gg 0.54a^2$ (i.e. when receptors are relatively closely spaced). The full model will apply to non-specific binding in this case, but may have to account for larger loop formation to get accurate predictions. I should note that with larger loops, there is a greater chance of binding to the ‘wrong’ receptor, since the fractional change in free chain length between binding sites decreases.

In the problem of chain adhesion to a sequence of binding sites on a surface, I have shown that the addition of intermediary binding sites along a chain length has a ‘zipper effect’, massively decreasing the time for the chain to bind fully along its length. When we examine the main result – the expression for the average binding time in Eq. (5.21), it is important that for large Δa and large M , the dominant binding process is the single-step ‘zipper’ pathway with the mean time approximately equal to $M\tau_{1a}$, as we can see in the inset of Fig. 5.9(b). Only occasionally will a chain bind with a double step, and this correction to the binding time also scales linearly with M , see Fig. 5.9(b). It is not until receptors are very tightly grouped (small Δa) that double-step processes start to become relevant. This is suggestive of reality – if a polymer chain has a specific substrate structure to bind to, then steric effects may well force the polymer to bind in a very conserved and controlled sequence (as in nature), just by virtue of the high entropic penalty for binding ‘out of order’.

The existence of an optimal number of intermediate receptors, M_{opt} for the shortest time of full chain adhesion is the other main result. This is an interesting feature, perhaps contrary to an expectation that by reducing the reaction barrier (and the associated individual binding time) one would increase the overall rate of adsorption. For chains with many intermediate receptors, although there is fast attachment to each individual site, the process of moving the center of mass of the remaining free chain down the line of receptors is slow, because the entropic pulling force causing this drift is weak. Conversely, if there are only a few receptors, even though any attachment event will provide a strong force to move the free chain to its new equilibrium position, the binding time itself is prohibitively slow.

The knowledge of these principles of adsorption kinetics are useful in understanding protein self-assembly, e.g. in β -sheets at the growing end of an amyloid fibril, where the new peptide subunit has to bind to a specific sequence of sites by hydrogen-bonding the β -sheet at the end of the existing filament [234], and the entropic barriers are explicitly reported. In the design of specifically-binding chains, aiming to optimize the rate of self-assembly, this analysis could be used to guide the structural features. The work in this chapter also shows that careful positioning of receptors relative to each other allows tight control of the order of assembly.

DIFFUSION OF MICROSWIMMERS IN OBSTACLE LATTICES

The field of active matter covers the broad spectrum of particles which move by consuming energy from their environment [235]. These range from flocks of birds and insect swarms [236, 237], to cell tissues [238], microswimmers [239], microtubuli [240, 241], and enzymes [242]. Microswimmers such as bacteria and Janus particles self-propel at low Reynolds numbers, the latter being directly powered by an asymmetric chemical reaction on the particle surface, the former by rotating helical filaments. The propulsive mechanisms set up complicated hydrodynamic flows, which determine the characteristics of interactions, both with other microswimmers, and with the boundaries of their environment. These boundary interactions may perform an essential function in nature. Surface-induced accumulation is an important step in the formation of biofilms, which are involved in many chronic diseases and pathogen spread [243, 244]. Blood pathogens are adapted to swimming in crowded environments [245], sperm cells follow the wall of the genital tract to reach the egg cell [246–248], and artificial Janus particles have been guided along microfluidic edges [249] and through obstacle arrays [250–252].

The nature of particle-surface interactions relies on a microswimmer’s propulsion mechanism, including steric and hydrodynamic effects. Microalgae, which are “puller” type swimmers, are scattered off surfaces [253–255], leading to billiard-like motion in polygon structures [256]. In contrast, “pusher” type swimmers, such as bacteria or Janus particles, are trapped by hydrodynamic effects near flat surfaces, where they accumulate [257–259]. When the surface is instead convex, this trapping time can be reduced [260]. In particular, bacteria trace along convex surfaces such as microfluidic pillars before escaping with a small angle [261].

The modelling of these scenarios typically follows one of two approaches: hydrodynamic models, or random walk models. With a full hydrodynamic approach, the particle-surface interactions can be studied by modelling the active particle as a hard

sphere with defined tangential surface velocity [262]. A recent study explored the migration of active particles through a body-centered cubic lattice of spheres of the same size as the particle [263]. Depending on the swimmer type and packing density, the authors found trapped, random walk and straight trajectories. The computational demands of the simulations, however, prevented study of long-time behavior. Random walk models can be used to study the diffusive behavior of active particles. Diffusion in complex media has been studied for several boundary interactions: for model particles that evade obstacles [264], particles that are trapped before being randomly reorientated [265], and particles that interact with obstacles via an excluded volume potential [266]. Hydrodynamic boundary interactions have been shown to play an important role in active systems, e.g. in the control of flow-induced phase separation [267]. Similarly, pusher-type boundary interactions may guide microswimmers through their environment [249, 268], which would facilitate diffusion.

In this chapter, I will look at how different modes of boundary scattering influence the diffusive transport of active particles in ordered arrays of obstacles. We will consider particles specularly reflected from boundaries, as in the Lorentz gas model [31]; particles that scatter by sliding around obstacles, like pushers [260, 261]; and particles that interact with obstacles via a steric, torque-free interaction, which is referred to here as a “slide-off” condition [266]. For these ‘pusher-like’ collisions, simulations and a run-and-tumble particle model predict, counterintuitively, that large diffusive transport is possible even at high obstacle densities. This result contrasts sharply with the expected low diffusivity of Lorentz gas particles at high densities. Further, I will show for the sliding condition, using a simple deterministic model, how this large diffusion at high density is caused by particle guiding by the lattice. Simulations show that the same effect occurs for the slide-off condition, but not for Lorentz gases.

6.1 Equations of motion and boundary conditions

In each simulation, there are N_P non-interacting active particles in a two-dimensional space in which obstacles are placed in a hexagonal lattice. The centres of the obstacles are fixed with distance d , and the obstacle radius R is varied. The equations of motion for the i -th particle are given by

$$\dot{\mathbf{x}}_i = v \mathbf{p}(\varphi_i) \quad (6.1)$$

$$\dot{\varphi}_i = \sqrt{2D_R} \xi_i(t), \quad (6.2)$$

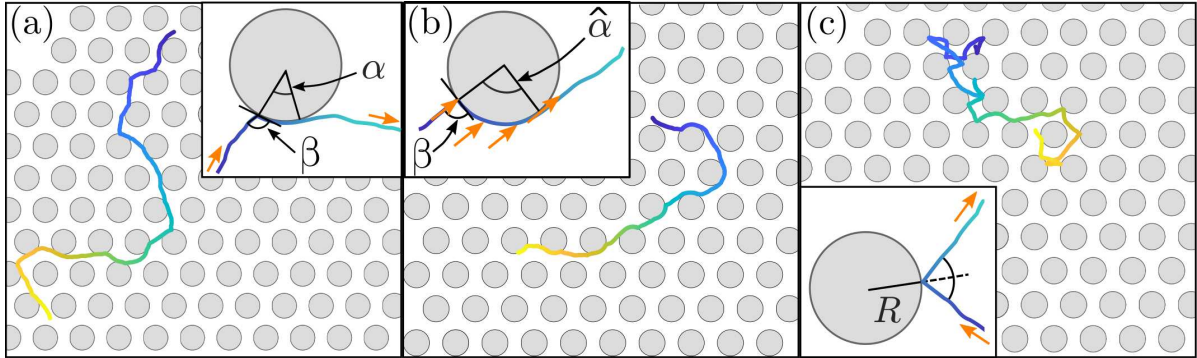


Fig. 6.1 Boundary conditions. Typical trajectory of a particle governed by Eqs. (6.1) and (6.2) with (a) a sliding, (b) a slide-off, or (c) a reflecting boundary condition. For the sliding condition, particle leaves at a tangent to the obstacle after traversing a fixed central angle α . For the slide-off condition, the central angle $\hat{\alpha}$ depends on the incident angle, the obstacle radius, and the magnitude of rotational diffusion on the obstacle.

where dot denotes the time derivative, v is the particle speed, \mathbf{x}_i and φ_i correspond to the position and moving direction of the i -th particle, respectively, and the unit vector $\mathbf{p} = [\cos \varphi, \sin \varphi]$. The white noise in Eq. (6.2) obeys $\langle \xi(t) \rangle = 0$ and $\langle \xi_i(t) \xi_j(t') \rangle = \delta_{ij} \delta(t - t')$. Thus, the moving direction undergoes rotational diffusion with $\langle \varphi(t)^2 \rangle = 2D_R t$. As a result, the particle performs a persistent random walk with persistence length $l_p = v/D_R$ [269].

Recent microfluidic experiments [260] and hydrodynamic models [260, 261] have shown that pillars with radii above a critical threshold strongly trap pushers, which escape at long times by rotational diffusion. Here, I will discuss only pillars with radii below this critical threshold (and so choose parameters motivated by experiment [268, 270]). In this case, swimmers collide with an obstacle at an angle β , defined as the angle between the tangent at the collision point and the orientation \mathbf{p} . If $\beta < \pi/2$, the particle travels clockwise around the obstacle; if $\beta \geq \pi/2$, the particle travels counter-clockwise. After the collision, the angle between it and the obstacle surface tangent decreases until escape [261].

To capture the non-classical particle-surface interaction, we introduce a sliding boundary condition [260]. Consider a collision with an obstacle: β is defined as the angle between the tangent at the collision point and the orientation \mathbf{p} . The particle moves along the obstacle to traverse a central angle α (Fig. 6.1(a) inset). A model of stochastic dynamics could determine, for a given incident β , the resulting distribution of central angles α (leaving times). However, such a model has yet to be developed. We know from modelling and experiments that after collision, the particle quickly rotates, through phoretic and/or hydrodynamic interactions with the surface, to align its orientation vector

with the surface, regardless of the orientation of the particle upon collision [244, 271]. This rotation generally occurs on a much faster timescale than the trapping time of the particle. Therefore, let us choose to neglect the dependence of the sliding angle α on β , i.e., model the probability distribution of α as $P(\alpha)$ instead of as $P(\alpha|\beta)$, with $P(\alpha)$ peaked at some value α^{\max} determined by the competition between rotational diffusion and deterministic alignment with the surface. In this work we will explore the effect of boundary conditions assuming a fixed central angle α and further assume that, when a particle leaves an obstacle, its orientation \mathbf{p} is tangent to the obstacle surface. This is a necessary simplification of the hydrodynamic behaviour of pusher-type particles at convex obstacles. The model also neglects any potential impact of the chemical field surrounding synthetic active particles. The neglect of stochasticity in α can be checked by simulations. Results (not shown) with a fixed (mean) α are qualitatively the same to those obtained with a distribution of α , provided the latter is peaked about its mean (e.g. a Gamma distribution).

As a comparison, let us also consider a slide-off boundary condition, and a reflecting boundary condition. In the slide-off condition, when a particle collides with an obstacle, it retains its orientation vector, and advances around the obstacle depending on the component of its velocity parallel to the obstacle surface (initially β), i.e. $v = v_0 \cos \beta$, as shown in Fig. 1(b). The angle between particle orientation and obstacle tangent decreases as the particle moves around the obstacle's surface. It will leave the obstacle when the orientation vector is parallel to (or pointing away from) the obstacle's surface. In the absence of rotational diffusion, this means that the particle will traverse a central angle of $\hat{\alpha} = \min(\beta, \pi - \beta)$, and so it bears some resemblance to the sliding condition. Here, we consider two different cases: i) when rotational diffusion is fully suppressed while on the obstacle, here called the deterministic slide-off condition, and ii) when rotational diffusion remains the same as in free space while on the obstacle, here called the stochastic slide-off condition. Note that while sliding is motivated by hydrodynamic effects, the slide-off condition is motivated by steric effects, and has been used in various potential-based simulation studies to model Janus particles and active disks [266, 272].

For the reflecting condition, a particle is reflected with an angle equal to the incident angle, as illustrated in Fig. 6.1(c). This interaction type implies time-reversibility, which is an assumption underlying gas kinetic models derived for bacteria transport in porous media [273, 274]. By contrast, both the sliding and slide-off boundary condition are not time-reversible and violate detailed balance [239]. The system of Eqs. (6.1) and (6.2) is solved numerically, and example particle tracks are shown in Fig. 6.1. We derive the diffusion coefficient from N_P simulated particle tracks by fitting the mean square

displacement as

$$\langle \delta x(t)^2 \rangle = 4D_{\text{eff}}t + 4D_{\text{eff}}\eta[\exp(-t/\eta) - 1], \quad (6.3)$$

a result easily derived for self-propelled particles using a standard method (see for example [21]), where the time scale of ballistic motion, η , is the second fitting parameter.

6.2 Diffusion of an active Lorentz gas

First, I will address diffusion of active particles with the classical specular reflection rule on obstacle boundaries. These have already been studied for ballistic particles, both in a physical context [31], and a mathematical context [275]. Ballistic particles undergoing specular reflection are termed a Lorentz gas, and the calculation of the diffusion coefficient can be reduced to the problem of finding the mean free path λ , using the relationship

$$D = \frac{1}{2}\lambda v \quad (6.4)$$

There already exists a well-known result for the mean free path of a Lorentz gas, known as the Santalo formula [275]:

$$\lambda = \pi A/P, \quad (6.5)$$

where A and P are the free area and obstacle perimeter in a unit cell (shown for a hexagonal lattice in Fig. 6.2(a)), respectively. There is an important caveat for this result: it applies only when the space has a finite horizon. This means that it is not possible to place a straight line down onto the space without it intersecting an obstacle. In practice, for our hexagonal lattice, it therefore assume that the rows of the lattice are overlapping, otherwise you would be able to place a straight line down the middle of the channels formed by the lattice. This would limit how small we could make the ratio of obstacle centre separation d to obstacle radius R – simple geometry tells us that for a finite horizon, $R/d > \sqrt{3}/4$.

If the particles in our study were unaffected by rotational diffusion, then we would expect their motion to be ballistic for $R/d < \sqrt{3}/4$. However, since the active particles described by Eqs. (6.1) and (6.2) move diffusively at large time scales, they obviously have a finite effective mean free path in free space (and therefore effectively a finite horizon). This is just the persistence length l_p . To try and capture this, and extend the validity of the Santalo formula to lower obstacle densities, I derived an active version of Santalo's formula, by placing an additional circular boundary of radius l_p into the space, as in Fig. 6.2(b). Now, we can work out the number N of unit cells (with area $\sqrt{3}d^2/2$

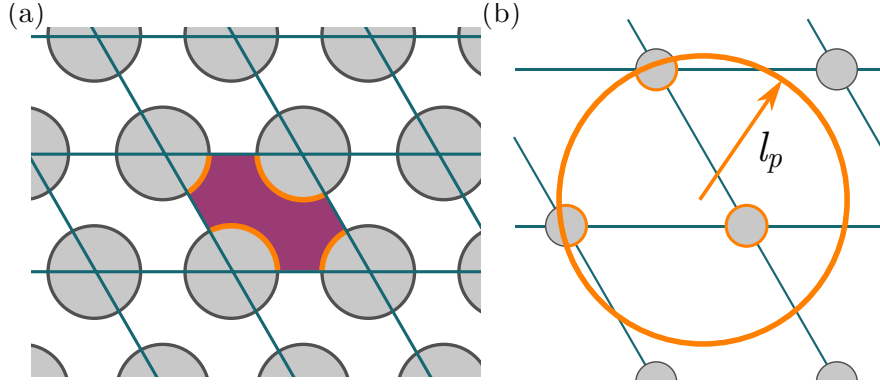


Fig. 6.2 An illustration of the lattice geometry in the reflecting boundary condition calculation. A hexagonal lattice can be patterned by rhombi of side length equation to the lattice spacing, as shown in (a). The shaded area is the area available to particles per unit cell, A , while the orange arcs highlight the obstacle surface per unit cell $P = 2\pi R$. In (b), an extra circular boundary is added, with a radius of the persistence length, to account for reorientation via rotational diffusion, and preventing an infinite mean free path at low densities.

for a hexagonal lattice) held within the persistence circle:

$$N = \frac{\pi l_p^2}{\sqrt{3}d^2/2} = \frac{2\pi l_p^2}{\sqrt{3}d^2} \quad (6.6)$$

The free area per unit cell is, as illustrated in Fig. 6.2(a), given by the area of a parallelogram with sides of the lattice constant d , minus the area of a single circular obstacle:

$$A = \frac{\sqrt{3}d^2}{2} - \pi R^2, \quad (6.7)$$

and the perimeter per unit cell is simply $P = 2\pi R$. Now, the mean free path of an active particle is

$$\tilde{\lambda}_{l_p} = \pi \frac{NA}{NP + 2\pi l_p} = \frac{\pi}{2} \frac{\sqrt{3}d^2 - 2\pi R^2}{2\pi R + \sqrt{3}d^2/l_p} \quad (6.8)$$

In order to obtain the fit seen in Fig. 6.3, we find that this mean free path has to be scaled by $\pi/2$, i.e. $\lambda_{l_p} = 2\tilde{\lambda}_{l_p}/\pi$. We believe that this is due to the choice of averaging conditions made in earlier work [275]. As shown in Fig. 6.3, applying this adjusted mean-free path in $D = \lambda_{l_p} v/2$ matches the simulations.

The inset plots the theoretical prediction and the diffusion coefficient fitted from simulations on a lin-log scale, showing that at large R/d the diffusion coefficient scales as $\ln(1/\rho)$, where obstacle density $\rho = 2\pi/\sqrt{3}(R/d)^2$. If we vary the obstacle separation d instead of the obstacle radius R , we see, as expected, that the diffusion coefficient

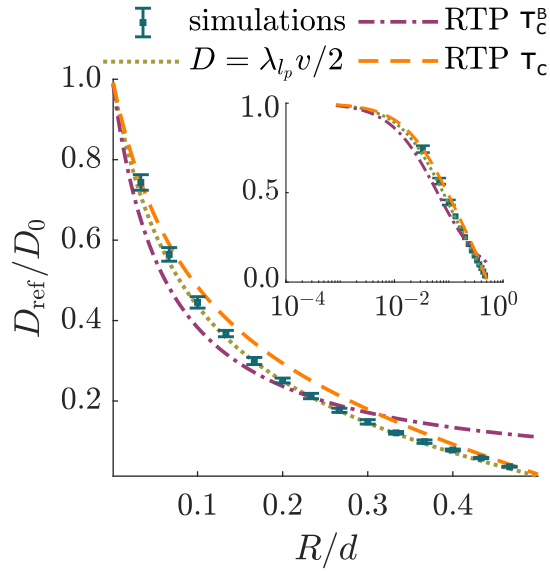


Fig. 6.3 Diffusion with reflecting boundary condition, D_{ref} , is scaled by diffusion coefficient in the absence of any obstacles, $D_0 = v^2/2D_R$. Simulations agree with Santalo's formula that was adjusted for rotational diffusion, λ_{lp} (green dotted curve). The run-and-tumble model in Eq. (6.9) with Santalo mean free path λ in $\tau_c = \lambda/v$ (orange dashed) is compared to RTP model with $\tau_c^B = 1/\rho$ [265] (purple dashed-dotted) and $\langle \cos \psi \rangle = -1/3$. Parameters: $N_P = 1000$, $D_R = 0.1 \text{ s}^{-1}$, $v = 20 \text{ } \mu\text{m s}^{-1}$, $d = 60 \text{ } \mu\text{m}$, unless otherwise stated.

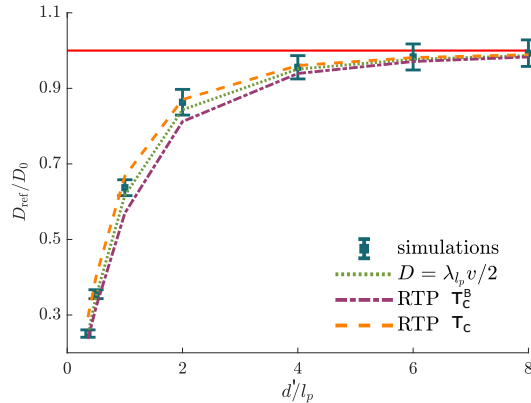


Fig. 6.4 Diffusion with reflecting boundary condition for fixed $R = 12\mu\text{m}$, as the obstacle separation $d' = d - 2R$ is varied. The diffusion coefficient was again scaled by the free space diffusion coefficient D_0 , which is approached as obstacle density gets very small ($d' \gg l_p$).

approaches D_0 when $d \gg l_p$, shown in Fig. 6.4. We can understand the reduction in diffusion coefficient qualitatively: as the obstacle density increases, particles spend most of their time in the wells between triplets of obstacles in the hexagonal lattice, and their motion becomes a jump-diffusion process from well to well, as described by Machta and Zwanzig [31] and illustrated by the particle track in Fig. 6.1(c).

6.3 Run-and-tumble model

While the active Santalo formula matches the reflective simulations well in Fig. 6.3, it cannot account for the persistence introduced by the sliding and slide-off boundary conditions, and a different approach is required. Figure 6.5 shows a sample trajectory at low density, which gives some clue as to how the simulations can be modelled. If we remove the obstacles from the trajectory, the particle appears to follow a series of roughly straight runs (rotational diffusion adds in some variation in direction) of length dictated by the run time τ , followed by sharp tumbles onto a new direction of travel, of angle ψ . These parameters are not necessarily fixed, and may instead obey some sort of probability distribution. This kind of travel is common in bacteria such as *E. coli* [269], and such microswimmers are termed run-and-tumble particles (RTP) [276, 277]. In this case, instead of internal cues forcing a RTP to tumble, these are obstacle-induced reorientations of the particles. The diffusion coefficient for an RTP also undergoing

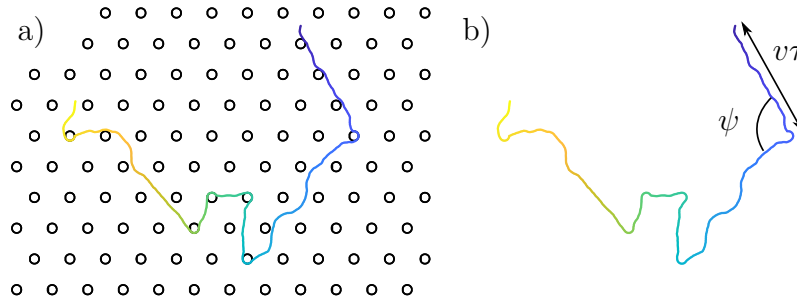


Fig. 6.5 Sample trajectory at low obstacle density. (a) shows a sample trajectory within an obstacle lattice, and (b) shows the same trajectory with the obstacles deleted. It bears resemblance to a particle undergoing roughly straight runs of length $v\tau$, before tumbling through an angle ψ . Both the run time τ and the reorientation angle ψ are sampled from some probability distribution.

rotational diffusion is known to be

$$D = \frac{v^2}{2[D_R + (1 - \langle \cos \psi \rangle)/\tau]}, \quad (6.9)$$

where τ is the mean run time and $\psi = \psi(\alpha, P(\beta))$ is the reorientation angle during a tumble [278, 279]. In the following, I will derive expressions for the parameters in Eq. (6.9): i) the reorientation function $\langle \cos \psi \rangle$, ii) the mean run time τ , and iii) the effective speed v based on the microscopic details of the sliding, the reflecting and the slide-off boundary conditions. We will then apply the RTP model with those parameters to the simulations presented in the previous section.

Sliding boundary condition

Reorientation function

For the sliding BC, the reorientation angle ψ is the combination of alignment upon collision with the obstacle, β , and sliding according to the central angle, α . We can calculate this by considering the geometrical construction in Fig. 6.6. Since we have constructed the line CH to be parallel to the tangent at the collision point BE, and constructed FC to be parallel to OB, angle FCH must be a right angle. Since the particle leaves at a tangent, OCD is also a right angle. By the alternate angle theorem, $\angle OCF = \angle COB = \alpha$, and so $\angle DCF = \pi/2 - \alpha$. Therefore,

$$\psi = \frac{\pi}{2} - \beta - \left(\frac{\pi}{2} - \alpha \right) = \alpha - \beta. \quad (6.10)$$

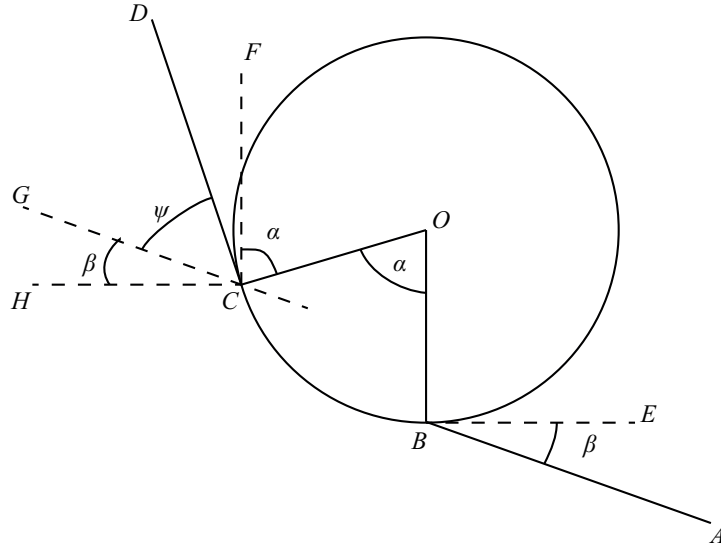


Fig. 6.6 A geometrical construction for determining the reorientation angle, ψ , as a function of collision angle β , and central angle traversed, α . The sliding particle travels along the path $ABCD$. Lines OB and CF are parallel, as are lines AB and CG , and lines EB and CH .

The average $\langle \cos \psi \rangle$ is performed over the collision angle β , with probability distribution $P(\beta)$.

To derive the collision angle distribution, we consider a single circular obstacle of radius R . A particle can start at any distance x from the centre of the obstacle, with its initial direction ϕ uniformly distributed (see Fig. 6.7 for schematic). The particle moves in a straight line, and may or may not collide with the obstacle. Given a uniform distribution of starting directions, what is the observed collision angle distribution $P(\beta)$?

To answer this, we need only consider a truncated distribution

$$P(\phi) = \frac{1}{2 \cos^{-1} \frac{R}{x}} \quad \text{for} \quad -\cos^{-1} \frac{R}{x} \leq \phi \leq \cos^{-1} \frac{R}{x}, \quad (6.11)$$

because beyond this range of angles, the particle will not hit the obstacle (for instance, if $\phi = \pi$, the particle will move away from the obstacle forever and never hit it). From the sine rule, we can see quickly that

$$\frac{x}{\sin(\pi/2 + \beta)} = \frac{R}{\sin \phi}, \quad (6.12)$$

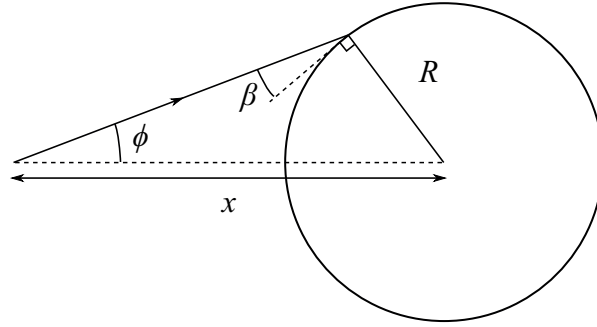


Fig. 6.7 Schematic of the set-up to determine the incoming angle distribution. A particle starts a distance x from the centre of the pillar, and then travels at an orientation ϕ relative to the line joining the centre of the circle to the particle's origin, hitting the circle at an angle β to the tangent of the circle.

and so the relationship between incoming and collision angle at a given distance from the obstacle $\phi(\beta, x)$ is given by

$$\phi(\beta, x) = \sin^{-1} \left(\frac{R}{x} \cos \beta \right). \quad (6.13)$$

The transformation between the uniform initial angle distribution $P(\phi)$ and the collision angle distribution $P_x(\beta)$ is given by $P_x(\beta) = P(\phi) |d\phi/d\beta|$, where

$$\left| \frac{d\phi}{d\beta} \right| = \frac{R \sin(\beta)}{x} \left(1 - \frac{R^2 \cos^2 \beta}{x^2} \right)^{-1/2} \quad (6.14)$$

is the Jacobian of the transformation. We can write the collision angle distribution averaged over all space as

$$P(\beta) = \lim_{L \rightarrow \infty} \frac{\int_R^L dx 2\pi x P_x(\beta)}{\int_0^\pi d\beta \int_R^L dx 2\pi x P_x(\beta)} = \frac{\sin \beta}{2}, \quad (6.15)$$

where L is the system size. Here, the factors of $2\pi x$ arise from summing over annular regions of starting points. The denominator is a normalisation factor, and the lower limit of the x integral comes from the fact that you cannot start less than a distance equal to the radius R from the centre of the obstacle. Despite using deterministic trajectories to calculate this distribution, it fits the observed collision angle distribution for simulations at low densities. Performing the average gives the reorientation function as:

$$\langle \cos \psi \rangle = 2 \int_0^{\pi/2} \cos(\alpha - \beta) P(\beta) d\beta = \frac{1}{4} (2 \cos \alpha + \pi \sin \alpha), \quad (6.16)$$

noting that $\cos \psi$ is even about $\beta = \pi/2$. This framework is general, and so can be adapted for specific boundary conditions, as long as the reorientation function $\langle \cos \psi \rangle$ can be determined. For the reflecting boundary condition, $\psi = 2\beta$, and $\langle \cos \psi \rangle = -1/3$. We will discuss the stochastic slide-off condition in the next section.

Tumble rate

The second parameter in the RTP model (6.9) is the mean run time τ , which corresponds to the time between obstacle collisions. Because the characteristic time between collisions is independent of the details of the random walk and depends purely on confinement [280], we use the mean collision time $\tau_c = \lambda/v$ for all boundary conditions, where λ is the mean free path given by Santalo's formula. Note that this is not the active Lorentz gas formula derived earlier, but the deterministic Santalo formula. In the run-and-tumble model, rotational diffusion is dealt with separately (as in Eq. (6.9)). The reason this is important is more evident at low densities, where the tumble rate will be lower than the rate of reorientation by rotational diffusion. We do not want to artificially enhance the tumble rate at low densities. Of course, there are caveats to the approach: we are applying the Santalo formula beyond the bounds of its applicability (putting it onto an infinite horizon space). However, in my opinion, the results (presented later) justify this approximation.

For the sliding boundary condition, the mean run time is adjusted by the time spent on an obstacle, i.e. $\tau = \tau_c + \tau_R$, with residence time $\tau_R = R\alpha/v$ simply being the arc length traversed divided by the speed on the obstacle.

Effective speed

A final consideration is that travelling on the obstacle causes an effective reduction in velocity. When the particle traces along the pillar, it travels a distance $l < v\tau_R$, which gives $v_{\text{obs}} = l/\tau_R$. By the cosine rule, $l = R\sqrt{2 - 2\cos \alpha}$ for the sliding boundary condition. Using the distance travelled, the effective speed in Eq. (6.9) is then $v_{\text{eff}} = v\tau_c/\tau + v_{\text{obs}}\tau_R/\tau = v\tau_c/\tau + l/\tau$.

Comparison with simulation

As a sanity check, we can first apply the RTP theory to simulations with reflecting boundary condition, using $\langle \cos \psi \rangle = -1/3$ and $\tau_R = 0$. As shown in Fig. 6.3, the RTP model with $\tau = \tau_c$ yields a good approximation of the simulation results. As a comparison, the RTP model with a recently derived mean collision time [265], where

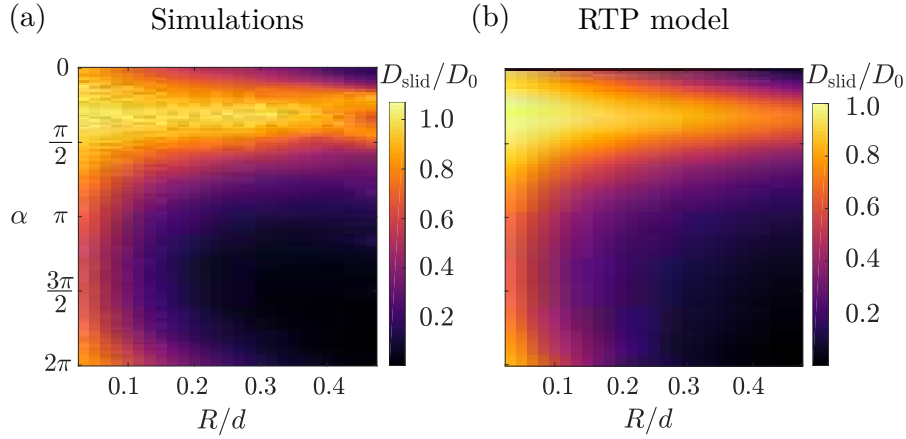


Fig. 6.8 Diffusion with sliding boundary condition. (a) Simulations reveal dependence on both obstacle density and central angle. (b) Theoretical prediction Eq. (6.9) with $\tau_c = \lambda/v$ in $\tau = \tau_c + \tau_R$ and $\langle \cos \psi \rangle$ given by Eq. (6.16). Parameters: $N_P = 1000$, $D_R = 0.1 \text{ s}^{-1}$, $v = 20 \text{ } \mu\text{m s}^{-1}$, $d = 60 \text{ } \mu\text{m}$.

$\tau_c^B = 1/\rho$, approximates the simulations at low densities but diverges in the high density regime.

Numerical solutions of Eqs. (6.1) and (6.2) with a sliding boundary condition reveal that diffusion depends both on the obstacle density ρ and the central angle α [see Fig. 6.8(a)]. A large diffusive transport can be sustained even at large obstacle density ρ for certain values of α . Despite frequent obstacle collisions, the reorientation is small because the sliding boundary condition conserves the major component of the velocity vector for small to intermediate values of α . Large values of α , on the other hand, cause a particle to retrace much of its track. The RTP framework reproduces the main features of these simulations (see Fig. 6.8 for a comparison): it maintains a large diffusion coefficient for small to intermediate α . Since τ_c is independent of the boundary condition, this must stem from the reorientation function $\langle \cos \psi \rangle$ in Eq. (6.16), which has a maximum at $\alpha \approx \pi/3$ and a minimum at $\alpha \approx 4\pi/3$. These extrema coincide with the predicted maximum and minimum of the diffusion coefficient observed for small to intermediate R/d in Fig. 6.8(b). Beyond $\alpha = 4\pi/3$, any increase in the diffusion coefficient due to the reorientation function is suppressed by the increase in residence time τ_R at large R and α . Note that, since the RTP model is oblivious to obstacle arrangement, these results also apply to random lattices at low densities. The discrepancies between the simulation results and the theoretical prediction at high densities is evidence of the geometrical guiding effect, and will be discussed in Section 6.3.1.

6.3.1 Slide-off boundary conditions

The slide-off boundary condition presents a different challenge, especially when rotational diffusion persists on the obstacle.

Reorientation function

For the deterministic slide-off condition, there is by definition no reorientation, and so $\langle \cos \psi \rangle = 1$. For the stochastic slide-off condition, however, the particle can deviate in its orientation while on the obstacle, and so the reorientation function $\langle \cos \psi \rangle \leq 1$. For this condition, the reorientation function depends on the obstacle radius compared to the persistence length, $R/l_p = RD_R/v$. This parameter gives an idea of whether diffusion (D_R) or movement around the pillar (v/R) has a larger effect on the particle's orientation. To see this, consider an extremely large obstacle (large R/l_p). Then, change in the particle's surface angle due to movement around the obstacle will be very small, as the curvature is low. Therefore, diffusion will dominate the reorientation, and $\langle \cos \psi \rangle < 1$. Conversely, a small obstacle will not allow much time for reorientation due to rotational diffusion before the particle leaves again.

To model the dependence of the reorientation function for the stochastic slide-off condition, we must look at the underlying Langevin equation of the angle the particle makes with the obstacle surface, Θ :

$$\dot{\Theta} = -\frac{v}{R} \cos \Theta + \sqrt{2D_R} \xi(t). \quad (6.17)$$

The deterministic drift comes from movement around the surface of the pillar. We want to know the average distance traversed around the pillar for a given incident angle, $\hat{\alpha}(\beta)$. We find this by adding up all the contributions of the particle's movement over the surface during its interaction with the pillar:

$$\hat{\alpha}(\beta) = \left\langle \int_0^T dt \frac{v}{R} \cos \Theta(t) \right\rangle_{\Theta(0)=\beta}, \quad (6.18)$$

where T is the time at which the particle angle Θ first reaches 0 or π and leaves the obstacle. We can substitute using the Langevin equation (6.17):

$$\hat{\alpha}(\beta) = \left\langle \int_0^T dt \left(-\dot{\Theta} + \sqrt{2D_R} \xi(t) \right) \right\rangle_{\Theta(0)=\beta} = \beta - \langle \Theta(T) \rangle_{\Theta(0)=\beta}. \quad (6.19)$$

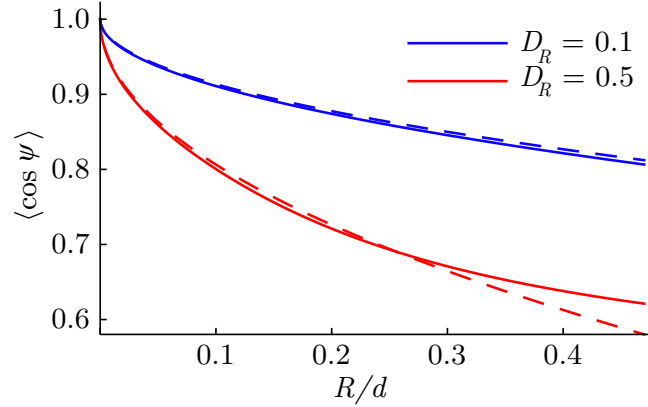


Fig. 6.9 Numerical solution for the reorientation function in Eq. (6.21) (thick curves) vs. the analytical approximation (dashed curves) in Eq. (6.22) for $D_R = 0.1\text{s}^{-1}$ (blue curves) and $D_R = 0.5\text{s}^{-1}$ (red curves). Other parameters are those taken in the simulations.

Here we have made the assumption that the stochastic integral vanishes, which is not obviously true, as we are not averaging over all trajectories at the time T , only those ones that reach the boundaries for the first time. However, this seems reasonable, given the particle may exit the region on both sides.

We are left with needing to calculate the probability of exiting at an angle $x = 0$ or $x = \pi$, $p_{0/\pi}(\beta)$. These probabilities are known as the splitting probabilities, and have the formal solution

$$p_\pi(\beta) = \frac{\int_0^\beta dx \exp\left[\frac{l_p \sin x}{R}\right]}{\int_0^{\pi/2} dx \exp\left[\frac{l_p \sin x}{R}\right]}, \quad (6.20)$$

where again, we consider $\beta \leq \pi/2$ and then use symmetry to deal with $\pi/2 \leq \beta \leq \pi$ (for information on the splitting probability, see for example [281]). Then, $\langle x(T) \rangle = \pi p_\pi + (0)p_0 = \pi p_\pi(\beta)$. To get the reorientation, we integrate over the incident angle:

$$\langle \cos \psi \rangle = 2 \int_0^{\pi/2} \cos(\hat{\alpha}(\beta) - \beta) P(\beta) d\beta = \int_0^{\pi/2} d\beta \sin \beta \cos \langle \Theta(T) \rangle_{x(0)=\beta}. \quad (6.21)$$

This expression can be evaluated numerically, and a very good approximation for small to medium R/l_p (see Fig. 6.9) is given by:

$$\langle \cos \psi \rangle \approx 1 - \frac{1}{2} \sqrt{\frac{R}{l_p}}. \quad (6.22)$$

Tumble rate

To get the residence time for the deterministic slide-off condition, we must take into account speed reduction on the obstacle. Accordingly, we may write the residence time as an integral:

$$\tau_R(\beta) = \int_{\beta}^0 \frac{R d\Theta}{v \cos \Theta} = \frac{R}{v} \ln \left[1 + \frac{2}{\cos(\beta/2) - 1} \right] \quad (6.23)$$

Note that this is not equal to $R\hat{\alpha}/v$, because v is reduced on the obstacle, and so $\tau_R > R\hat{\alpha}/v$. The addition of rotational diffusion also changes the residence time. The residence time averaged over the incident angle distribution is then

$$\tau_R = \int_0^{\pi/2} d\beta \tau_R(\beta) \sin \beta = \frac{\pi R}{2v}. \quad (6.24)$$

Addition of rotational diffusion on the obstacles makes analysis more difficult. Now, the residence time can be characterised by the mean hitting time of the Langevin equation (6.17) on the exiting boundaries. This has a known expression [26]:

$$\tau_R(\beta) = \frac{1}{D_R} \int_0^{\beta} dy e^{l_p \sin y/R} \int_y^{\pi/2} d\Theta e^{-l_p \sin \Theta/R}, \quad (6.25)$$

where there is a reflecting boundary at $\Theta = \pi/2$ and an absorbing boundary at $\Theta = 0$. Again, it is possible to make headway by asymptotics on this integral, but it turns out a more intuitive approximation suffices. For small rotational diffusion $l_p \gg R$, the drift time $\tau_{\text{drift}} = \pi R/2v$ dominates the mean first passage time. However, for large rotational diffusion $l_p \ll R$, we may expect that diffusion time, $\tau_{\text{diff}} = 1/D_R$ – calculated as the mean first passage time out of a flat potential for the incident angle distribution $P(\beta)$ – dominates. It turns out that a very reasonable fit to numerical solutions of the integral is

$$\tau_R = \frac{\tau_{\text{drift}} \tau_{\text{diff}}}{\tau_{\text{drift}} + \tau_{\text{diff}}} = \frac{\pi R}{2v} \frac{1}{1 + \pi R/2l_p}, \quad (6.26)$$

see Fig. 6.10. This expression gives the deterministic time $\tau_R \rightarrow \pi R/2v$ at low rotational diffusion (small R/l_p), and the expected time to exit the free space interval $\{0, \pi\}$ for large rotational diffusion (large R/l_p): $\tau_R \rightarrow 1/D_R$. This latter time assumes that we can neglect the contribution from deterministic drift at large enough rotational diffusion values.

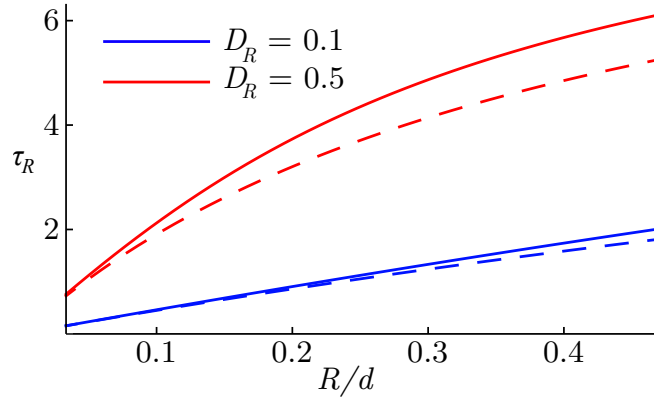


Fig. 6.10 Numerical solution of Eq. (6.24) (thick curves) compared to the analytical approximation in Eq. (6.26) (dashed curves). These are plotted for $D_R = 0.1\text{s}^{-1}$ (blue curves) and $D_R = 0.5\text{s}^{-1}$ (red curves). Other parameters are those taken for the simulations.

Effective speed

It can be quickly shown that for the deterministic slide-off condition, the average angle traversed during a collision is 1 radian. It follows that $l = R\sqrt{2 - 2\cos(1)}$ for the deterministic slide-off condition. For the stochastic slide-off condition, we require the average reorientation angle $\hat{\alpha}$. Using that

$$\hat{\alpha} = \int_0^{\pi/2} d\beta \hat{\alpha}(\beta) \sin \beta, \quad (6.27)$$

and the definition of $\hat{\alpha}(\beta)$ in Eq. (6.19), we can find $\hat{\alpha}$ numerically. It turns out the numerical solution is very close to an analytical approximation:

$$\hat{\alpha} \approx 1 - \sqrt{\frac{\pi R}{2l_p}} + \left(\frac{R}{2l_p}\right)^{3/2}, \quad (6.28)$$

as shown in Fig. 6.11. and then, the average distance travelled for the stochastic slide-off condition is $l = R\sqrt{1 - \cos \hat{\alpha}}$. Using those distances travelled, the effective speed in Eq. (6.9) is then $v_{\text{eff}} = v\tau_c/\tau + v_{\text{obs}}\tau_R/\tau = v\tau_c/\tau + l/\tau$.

Comparison with simulations

For both deterministic and stochastic slide-off conditions, the diffusion coefficient D_{SO} is equal to the free diffusion coefficient D_0 in the limit of small (or very separated) obstacles, as shown in Fig. 6.12. However, at higher obstacle densities, the deterministic slide-off diffusion coefficient increases significantly over the free diffusion coefficient (see the purple

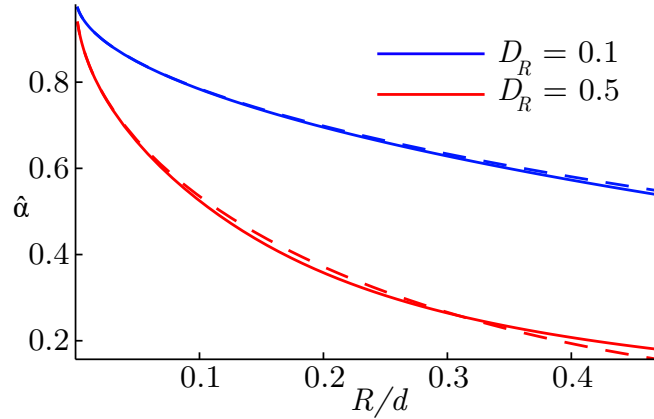


Fig. 6.11 Numerical solution of $\hat{\alpha}$ (thick curves) vs. the analytical approximation in Eq. (6.28) (dashed curves), for $D_R = 0.1\text{s}^{-1}$ (blue curves) and $D_R = 0.5\text{s}^{-1}$ (red curves). Other simulation parameters as in Fig. 6.12.

markers Fig. 6.12). This increase appears despite the decrease in speed on the obstacle: as the speed on the obstacle is given by $v = v_0 \cos \beta$, the particle will propagate very slowly when it is oriented at right angles to the surface. We suspect the suppression of rotational diffusion as cause for this increase, and, thus, use an effective rotational diffusion $D_R^{\text{eff}} = D_R \tau_c / \tau$ in Eq.(6.9). With this correction, the RTP model is a good approximation of the simulation results, see dashed purple line.

Restoring rotational diffusion on the obstacle surface dramatically changes the dependence of D_{SO} on the obstacle density. For the stochastic slide-off condition, the RTP model in Fig. 6.12 reproduces the trends seen in the simulation results: we see a reduction in the diffusion coefficient as the obstacle density increases. This reduction is still much smaller than the Lorentz gas results (compare the green markers in Fig. 6.12 to the markers in Fig. 6.3). The relative decrease in the diffusion coefficient to that of free space is smaller as the persistence length decreases: if the particle is more prone to reorientation in free space, the effect of reorientation due to the obstacles is smaller, as can be seen by comparing the green and orange markers (simulations) and dashed curves (RTP model) in Fig. 6.12. However, the RTP model predicts a much sharper decline in the diffusion coefficient at larger values of R . This gives another strong indication that the obstacle lattice may be playing a large role at high densities for the sliding and slide-off BCs.

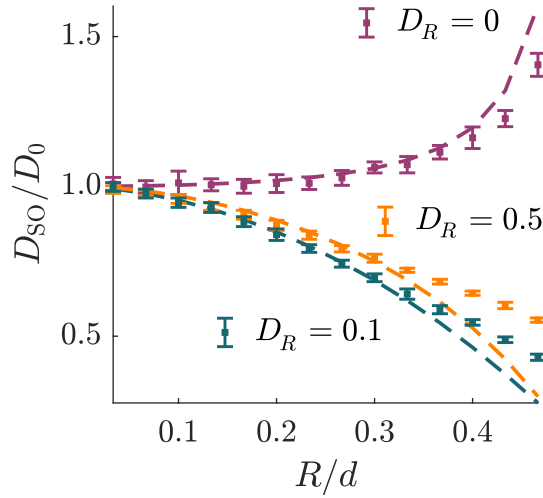


Fig. 6.12 Diffusion with slide-off boundary condition, D_{SO} , is scaled by the free diffusion coefficient. If the particle orientation is fixed on the obstacle (i.e. $D_R = 0$ on obstacle), diffusion is enhanced at large obstacle densities (purple markers). With stochastic slide-off boundary condition (i.e. $D_R \neq 0$), the diffusion coefficient decreases with increasing obstacle density. If D_R is increased (both free space and on obstacle), the relative decrease in diffusion coefficient, D_{SO}/D_0 , due to obstacle collisions is smaller (orange vs. green markers). Note that absolute value of D_{SO} is smaller for larger D_R . The dashed lines are the respective theoretical approximations to the simulations (details given in section 6.3). Parameters: $N_P = 1000$, $D_R = 0.1 \text{ s}^{-1}$, $v = 20 \mu\text{m s}^{-1}$, $d = 60 \mu\text{m}$, unless otherwise stated.

6.4 High-density geometrical effects

I now want to examine the deviations of the RTP model from the simulated diffusion coefficient D_{slid} at high density in more detail. Figure 6.13(a) shows fixed $R/d = 0.47$ (the largest value) cross-sections of the surfaces in Figures 6.8(a) and 6.8(b). At this high density, the diffusion coefficient for the hexagonal lattice simulations has peaks that exceed the RTP model. There are two of these peaks at low α as well as smaller overshoots at higher α . However, if we instead perform the simulations in a square lattice, we get a different peak structure, with a single peak at low α . We will see that this is due to the geometry of the lattice, and its guiding effect on the self-propelled particles.

For the geometry of the lattice to influence the particle paths, there must be a correlation between successive collisions with pillars. This means that the particle must not lose the memory of its orientation between collisions, i.e. the obstacle separation must be much smaller than the persistence length, $d - 2R \ll l_p$. In this case, a purely deterministic model ($D_R = 0$) provides a good approximation to explore correlations between collisions. In such a model, the particle travels in a straight line between

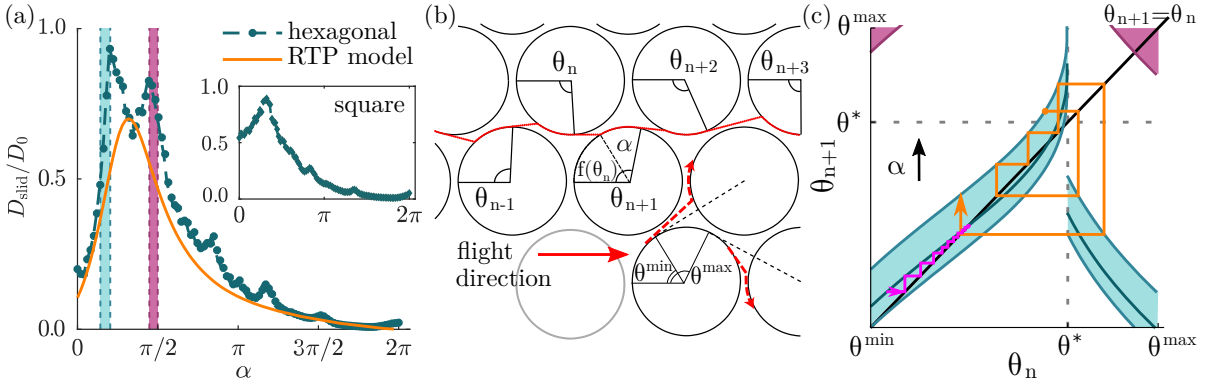


Fig. 6.13 Geometric effects for sliding BC. (a) The discrepancy between the RTP model and the hexagonal lattice simulation results at high density ($R/d = 0.47$) is centred around the deterministic stable regions [shaded as in (c)], revealing influence of geometry. Inset: Diffusion coefficient for a square lattice. (b) Schematic of a 1-D system, considering a flight along one channel in the lattice. The leaving angle at each pillar is given by θ_n . The lower schematic shows possible termination of flights in a horizontal channel. (c) Iterative map of the leaving angle as a function of the previous leaving angle for different central angles α , $\theta_{n+1} = f(\theta_n) + \alpha$. The shaded regions correspond to regions of stable flights. Stable fixed points cross the dashed $\theta_{n+1} = \theta_n$ line with a gradient between -1 and 1 (a mapping with a stable fixed point is shown in the lower shaded region, with an example trajectory in pink). An example of a bounded mapping of leaving angles is shown as orange trajectory.

pillars, and is reoriented by α by sliding scattering. We consider a ‘channel’ defined by two rows of pillars within the lattice (Fig. 6.13(b)). A particle traverses the channel by skirting around pillars, leaving the surface of the n th pillar with a polar angle θ_n . For deterministic (ballistic) dynamics between collisions, we can completely specify a trajectory by the ‘flight’ $\{\theta_n\}_{n=1}^N$, the sequence of leaving angles from successive collisions, as in Fig. 6.13(b). The sequence size N defines the flight length. Successive leaving angles are determined by a recurrence relation:

$$\theta_{n+1} = g_\alpha(\theta_n) = f(\theta_n) + \alpha, \quad (6.29)$$

where, in this deterministic model, $f(\theta_n)$ is a function determined solely by the geometry.

As the particle moves along a channel during a flight, it can transition between pillars on the opposite (e.g. $\theta_{n-1} \rightarrow \theta_n$) or same (e.g. $\theta_{n+2} \rightarrow \theta_{n+3}$) side of the channel, as shown in Fig. 6.13(b). For $R/d > \sqrt{3}/4$ (the close-packed limit of overlapping pillars), a critical angle $\theta_n = \theta^*$ emerges that determines on which side of the channel a particle will next hit. If $\theta_n \leq \theta^*$, the particle will cross over to an obstacle on the other side of

the channel, while if $\theta_n > \theta^*$, it will move to one on the same side. This means the map $g_\alpha(\theta_n)$ is discontinuous at $\theta_n = \theta^*$, as in Fig. 6.13(c).

The flights considered in the deterministic model correspond well to what we observe in our simulations. At high densities, these show particle trajectories made up of long flights along lattice channels, interrupted by ‘tumbles’ into the next long flight. The deterministic model allows to establish if the flights are geometrical in origin. In this model, a flight terminates when the leaving angle θ_n becomes too small ($\theta_n < \theta^{\min}$) or too large ($\theta_n > \theta^{\max}$) as it will be deflected out of the channel on its next collision, illustrated in Fig. 6.13(b). Stable flights are trajectories that remain in the region $\theta^{\min} \leq \theta_n \leq \theta^{\max}$ indefinitely. This can happen in two ways:

1. A stable fixed point may exist (a point θ such that $g_\alpha(\theta) = \theta$, and $|g'_\alpha(\theta)| < 1$), so that long trajectories have a single repeated leaving angle.
2. The map $g_\alpha(\theta_n)$ is bounded within the allowed region of leaving angles: $\theta^{\min} \leq g_\alpha(\theta_n) \leq \theta^{\max}$ for all $\theta^{\min} \leq \theta_n \leq \theta^{\max}$, so that no trajectory may leave the allowed region.

Example trajectories of both types are illustrated in Fig. 6.13(c).

The iterative map $\theta_{n+1} = g_\alpha(\theta_n)$ is plotted for $R/d = 0.47$ in Fig. 6.13(c). Two stable ranges (shaded regions) are seen to emerge corresponding to ranges of α , which controls stability. For $\theta_n < \theta^*$, increasing α causes a stable fixed point to develop. Increasing it further, in the range that defines the lower region (shaded in blue), provides a map bounded in the interval $[\theta_{\min}, \theta_{\max}]$. Flights in this lower shaded region bounce from one side of the channel to the other. If α is increased further, the map again becomes unbounded ($g_\alpha(\theta_n) > \theta^{\max}$) and stability is lost. For $\theta_n > \theta^*$, the upper region (shaded in pink) has a stable fixed point, so that particles perform stable flights by running along only one side of the channel in this region. Stable trajectories from the deterministic model cannot give rise to diffusive behaviour. However, any rotational diffusion, however small, will eventually cause a deviation of trajectory large enough to take the particle out of the stable interval $[\theta^{\min}, \theta^{\max}]$. This will cause flights to terminate, and this is why the observed transport is diffusive, not superdiffusive. In view of the large persistence length of flights for stable values of α , the diffusion coefficient for such flights is expected to be large compared to that corresponding to other values of α . By plotting the stable regions of α predicted by the deterministic model against the simulation results at high density in Fig. 6.13(a), we see that this is indeed the case: the spikes in diffusion coefficient for the simulations correspond well to the stable regions in the deterministic model. It is important to note that the obstacle sizes we are considering here are below the critical

trapping radii typically found [260, 261]. It is possible to reach a high density state where the obstacle separation is larger than the persistence length, where our results wouldn't hold. However, in this regime, the obstacles would be much larger than the trapping radius, and so particles would be trapped for long periods on obstacles [260, 261], making diffusion very slow. Finally, it is not only in the sliding boundary condition that we see significant deviation from the RTP model. The stochastic slide-off collision rule also exhibits an increase over the bare RTP model as R/d gets very large. Although we do not try to model this here, it is clear from particle trajectories in the simulations (see e.g. Fig. 6.1(b)) that in this case there is also a geometrical guiding effect (this is also the case for the deterministic slide-off rule).

6.5 How should we model active particles?

We have seen that non-classical surface interactions significantly impact the active diffusive transport in complex environments, such as ordered obstacle arrays. Compared to a high-density Lorentz gas model, where particles get trapped in the wells of lattices, and the behaviour is jump-diffusive, the sliding and slide-off boundary conditions allow particles to escape these wells and traverse the lattice efficiently. These boundary conditions share certain general features and differences to the classical specular reflection boundary condition. The most striking is that they are not invertible; given an outgoing orientation and leaving point, we cannot infer both the incoming angle and collision point. The sliding condition maps particles with different orientations upon collision to the same leaving point, and so information on the incident angle is lost. Similarly, the deterministic slide-off condition maps particles with the same incident angles but different collision points onto the same leaving point. The stochastic slide-off condition loses both pieces of information. This non-invertibility could provide a stabilising effect on trajectories due to geometrical guiding at high obstacle densities.

The results shown here highlight the importance of choosing realistic microscopic boundary conditions to obtain realistic macroscopic dynamics. In particular, models employing reflective boundary conditions, e.g. those used in [273, 274] to describe bacteria in porous media, should not give realistic results for active particles. While this is generally obvious considering detailed balance [239], the theoretical framework expounded here allows the formulation of particular predictions to be tested experimentally, for instance, using bacteria in microfluidic arrays (in fact, this work is now underway). In particular, it would be interesting to test our prediction of large diffusive transport in dense arrays. The RTP model presented here is general in the sense that it can be

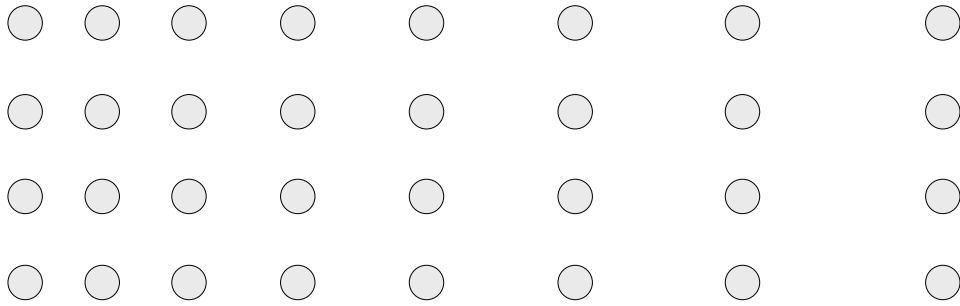


Fig. 6.14 A schematic geometry for determining the stochastic dynamics of microswimmers. A microfluidic device with rows of circular obstacles have these rows separated by a monotonically increasing distance along a microfluidic channel. Therefore, the diffusion coefficient will be given by 6.9. The distribution of these particles can be modelled using a Fokker-Planck equation, and it may be possible to distinguish the appropriate interpretation of the stochastic integral, as discussed in Chapter 1.

applied for different lattices and particles. A different lattice of obstacles requires the re-calculation of $\langle \cos \psi \rangle$ and τ_c . A change in the scattering interaction, on the other hand, requires specification of $\langle \cos \psi \rangle$, τ_R , and potentially v_{obs} , e.g. using experimental measurements. While the description was developed for lattices, the results hold for random environments when the number of obstacle contacts is low.

Finally, the model developed here has a potentially useful application in understanding more completely the underlying stochastic dynamics of microswimmers. Crucially, since the diffusion coefficient of these particles for pillars of fixed radius depends on the obstacle density, we are in a position to probe the underlying Fokker-Planck equation. If a microfluidic device can be constructed with a monotonically changing density, as in Figure 6.14, then we will effectively have an interval with a monotonically changing diffusion coefficient in space. With experimental tests of the boundary interaction for the channel's pillar radius, we should know this function, and thus be able to find the stationary probability distributions expected from the Ito and Stratonovich interpretation.

This is a work in progress, but should be of great interest to those people working in active matter, who routinely write down Fokker-Planck equations for active particles [277, 276].

CONCLUSIONS AND OUTLOOK

Within the field of biophysics, there exists a need to characterise the kinetics of systems. When out of equilibrium, we must find how fast the processes that drive life progress, or we will be unable to understand it. The problems presented in this thesis, I have shown how mean first passage time methods can be used to treat these problems, either for enthalpic barriers of unbinding, or for entropic barriers of assembly. I hope to have shown the utility of the first passage time approach, and how exactly we may use it to approximate the reaction rates in some model systems. Such an approach is not always useful – in problems of protein structure, or reaction pathways, molecular dynamics is king. If we attempt to coarse grain very complex free energy landscapes, we will necessarily lose much of the fine detail of these molecular processes. Nevertheless, for energy landscapes with simple features, the mean field approach to mean first passage problems used in this thesis has its merit. In particular, it allows us to get analytical approximations where saddle-point approximations may fail. With this in mind, I want to show how the problems tackled in this thesis can be built upon, as we seek to understand ever more complex models in cell biology.

The treatment of non-rigid substrates in this thesis lacks generality, although I believe the mean-field approach would be a useful approach for any Markovian substrate (for example, the standard linear solid). However, many materials are not Markovian, and it would be more useful to write the equations of motion using the memory kernel $\gamma_1(t)$

$$\int_0^t \gamma_1(t-t') \dot{x}_1(t') dt' = -\frac{\partial U(x_2 - x_1)}{\partial x_1} + \eta(t) \quad (7.1)$$

$$\gamma_2 \dot{x}_2 = -\frac{\partial U(x_2 - x_1)}{\partial x_2} + f + \xi_2(t). \quad (7.2)$$

The thermal noise terms are now not so easy to deal with; although $\xi_2(t)$ is still a white noise term, the substrate noise term is now coloured, by the fluctuation dissipation

theorem: $\langle \eta(t)\eta(t') \rangle = k_B T \gamma_1(t - t')$. Therefore, the problem is not Markovian and so it is not possible to write down a Smoluchowski equation for these Langevin equations.

It is worth noting that it is not clear what the functions γ and κ written above refer to. In this thesis we talk about the ‘mesh stiffness’ and associated friction coefficient, but meaningful rheological measurements on the nano-scale response of biomaterials are still very difficult to find. As such, we resorted to approximations based on known results in elasticity, and the results of molecular dynamics simulations, but for accurate theoretical modelling, I think there needs to be much more extensive experimental characterisation of substrate behaviour at the force (both magnitude, and area of application) and displacement scales of biological interest.

In this general case, it may be possible to make progress by appealing to a separation of timescales if the substrate relaxes sufficiently slowly. For instance, recall that in Chapter 3 we showed that the deterministic force across the bond was shown to be quasi-static over the reaction timescale (in fact, it remains roughly constant over the reaction timescale). So, for instance, it may have been possible to replace the non-rigid substrate problem in Chapter 3 with a rigid substrate and an effective force, determined by the substrate’s dynamics, reducing the problem to one dimension. This does not deal with the problem of coloured noise in the substrate fluctuations, but may simplify the dynamics enough that a solution becomes more achievable.

Even the equations written above are still linear models of elasticity. For a full treatment of extra-cellular matrices there may have to be an appeal to non-linear viscoelasticity – extra-cellular matrix networks display long-range correlations under stress and have been shown to stiffen under stress from cell contraction [282].

The underlying motivation for understanding the behaviour of focal adhesions is to try and understand the principles underlying cell behaviour and the impact of the mechanical properties of a cell’s environment. One direct application of the work done in this thesis could be to inform a larger-scale model of the transition to cell motility. Typically, on a two dimensional substrate, a cell will adhere and begin to spread (as described in Chapter 4). Some time after that, a cell will become polarised, as stress fibres develop across the cell in some preferred direction, and then start to move. The transition from isotropic to anisotropic, and the subsequent transition from stationary to moving, could be an interesting problem in the dynamics of focal adhesions.

The idea that we have is to consider a polarised cell in equilibrium, before the transition to cell motility. We consider a simple one-dimensional model, where there are N focal contacts in the cell, contained in equal numbers on the left and right cell edge (i.e. $N/2$ on both sides).

We can consider a force f applied from the stress fibres onto the focal contacts. The force f applies equally to each of the focal contacts, and so the overall resultant force applied in the positive x -direction is

$$F(t) = f(n_+(t) - n_-(t)), \quad (7.3)$$

where n_+ and n_- are the numbers of contacts on the positive edge and the negative edge of the cell respectively. Now, we propose that there is some sort of resistive friction force against the cell starting to move, f_{res} . The condition for the transition to mobility is that

$$f|n_+(t) - n_-(t)| > f_{\text{res}}. \quad (7.4)$$

Denoting the activation and release rate of the complexes as k_r , and the rate for assembly of a complex as k_a the kinetic scheme can be written as

$$\frac{\partial \langle n_{\pm}(t) \rangle}{\partial t} = -k_r \langle n_{\pm}(t) \rangle + k_a \left(\frac{N}{2} - \langle n_{\pm}(t) \rangle \right). \quad (7.5)$$

In the steady state $\partial \langle n \rangle / \partial t$, the average number of focal contacts attached to the substrate are equal on the positive and negative edge,

$$\langle n_+(t) \rangle = \langle n_-(t) \rangle = \frac{N}{2(1 + K_{\text{eq}}^{-1})}, \quad (7.6)$$

where the equilibrium constant $K_{\text{eq}} = k_a/k_r$ is the ratio of adhered complexes to released complexes. Clearly, if the reassembly rate is infinite, then $K_{\text{eq}} \rightarrow \infty$, and the number of adhered states is $N/2$, i.e. there are no released states.

The next assumption is that the more focal contacts activated, the stronger the pulling force. This makes sense: concentrated focal contacts are associated with high cellular traction forces. To implement this, it is simplest to assume that the force is proportional to the amount of signal being produced at the focal contacts. The signal is produced when a complex activates and then releases:

$$f = \alpha k_r (n_+(t) + n_-(t)). \quad (7.7)$$

Now, we know that the populations on the negative and positive edge are equal in equilibrium. Therefore, the idea is that the threshold for mobility must only be reached

in a fluctuation. Writing the populations as

$$n_{\pm}(t) = \langle n_{\pm} \rangle + \sigma_{\pm}(t), \quad (7.8)$$

we can write down the condition for mobility to leading order in the small displacements σ :

$$\alpha k_r (\langle n_+ \rangle + \langle n_- \rangle) |\sigma_+(t) - \sigma_-(t)| > f_{\text{res}}, \quad (7.9)$$

or, more compactly,

$$|\sigma_+(t) - \sigma_-(t)| > \frac{f_{\text{res}}}{f_{\text{eq}}}, \quad (7.10)$$

where $f_{\text{eq}} = \alpha k_r (\langle n_+ \rangle + \langle n_- \rangle)$ is the equilibrium overall force on the cell.

This is a first passage problem. To solve it, we will need to work out the magnitude of population fluctuations for given k_a and k_r . First, one can apply the kinetic equations for a small initial displacement from equilibrium:

$$\frac{\partial n(t)}{\partial t} = -k_r n(t) + k_a \left(\frac{N}{2} - n(t) \right) \quad (7.11)$$

$$\implies \frac{\partial \sigma(t)}{\partial t} = -(k_r + k_a) \sigma(t). \quad (7.12)$$

This makes sense: fluctuations are flattened by both the forward and backward processes. To account for fluctuations in the contact populations, we can add a stochastic term:

$$\dot{\sigma}(t) = -(k_r + k_a) \sigma(t) + \eta(t), \quad (7.13)$$

and assume that $\eta(t)$ can be well approximated as a Gaussian white noise term, $\langle \eta(t) \rangle = 0$, and $\langle \eta(t_1) \eta(t_2) \rangle = \Gamma \delta(t_1 - t_2)$. This is reasonable, as I think it is likely that the correlation function of the noise will look roughly like $\langle \eta(t_1) \eta(t_2) \rangle \propto \exp[-(k_r + k_a)|t_1 - t_2|]$, so as long as we are interested in timescales much longer than the reaction times of focal attachments, then it is a reasonable approximation.

All that remains is to calculate the constant Γ is. We can write the solution for $\sigma(t)$:

$$\sigma(t) = \sigma(0) e^{-(k_r + k_a)t} + \int_0^t e^{-(k_r + k_a)(t-t')} \eta(t') dt', \quad (7.14)$$

and, following the usual methods, we can find the mean square deviation of $\sigma(t)$:

$$\langle \sigma^2(t) \rangle = \sigma^2(0) e^{-2(k_r + k_a)t} + \int_0^t \int_0^t e^{-(k_r + k_a)(2t-t'-t'')} \langle \eta(t') \eta(t'') \rangle dt' dt'' \quad (7.15)$$

and so at long times,

$$\langle \sigma^2(t \rightarrow \infty) \rangle = \frac{\Gamma}{2(k_r + k_a)} = \langle \Delta n^2 \rangle. \quad (7.16)$$

The long time variation in σ should be equal to the variation in the equilibrium population of focal contacts. Assuming the distribution of n should be Poisson, in which case, the variance is equal to the mean:

$$\langle \Delta n^2 \rangle = \frac{N}{2(1 + K_{\text{eq}}^{-1})}. \quad (7.17)$$

In this case, we can quickly write down the strength of the fluctuations Γ :

$$\Gamma = 2(k_r + k_a) \frac{N}{2(1 + K_{\text{eq}}^{-1})} = Nk_a. \quad (7.18)$$

Now, the difference between the deviations, $\Delta\sigma(t) = \sigma_+(t) - \sigma_-(t)$, obeys a Langevin equation

$$\dot{\Delta\sigma}(t) = -(k_r + k_a)\Delta\sigma(t) + \eta_+(t) - \eta_-(t) = -(k_r + k_a)\Delta\sigma(t) + \eta(t), \quad (7.19)$$

where the combined noise term has zero mean and a correlation function that is the sum of the two processes in quadrature:

$$\langle \eta(t)\eta(t') \rangle = 2Nk_a\delta(t - t'). \quad (7.20)$$

To ask the question of the mean first passage time out of the interval $\{-f_{\text{res}}/f_{\text{eq}}, f_{\text{res}}/f_{\text{eq}}\}$ is the same as asking the probability of escaping at $\Delta\sigma(t) = -f_{\text{res}}/f_{\text{eq}}$ with a reflecting barrier at zero, because of the symmetry of the process about zero. Thus, we have written down our problem in a way that it can be solved using the backward Fokker-Planck approach.

One important feature that is missing from this treatment is the onset of persistence. Once a cell starts moving, there is a period of persistence before another change of direction. It could be that the rates of attachment and release vary at each side of the cell while it is moving, and it becomes harder to fluctuate out of the new equilibrium position. However, if the population of sensors shifts to this new equilibrium position relatively slowly (i.e. if the rates of the two processes change over a sufficiently slow period of time), there may be a few events that happen before the new equilibrium is reached, effectively keeping the cell in an ‘unstable’ mode of movement, rather than a persistent mode. Accounting for such rich biological behaviour in our models requires

new innovative theoretical approaches - it may well be impossible to describe cells well using a Markov process.

The work on cell mechanosensing and motility has occupied much of my consciousness over the two years, and as such I have several ideas relating to it. However, the other aspects of the work covered in this thesis are not without their own stories. One interesting problem in a similar vein to the problem of multiple receptor binding addressed in Chapter 5 is the problem of flagellar assembly in bacteria. These flagella are made up of individual sub-units, that must be taken from the inside of the cell, to the tip of the growing flagella. One mechanism suggested is that subunits are fed into the flagella, and bind together, being pulled up from the top to the site of sub-unit assembly. The kinetics of how they bind together, given the constraint of a narrow tube, is one in which it might be useful to consider a similar approach to that taken in Chapter 5. Some of the work that I am most excited about in the future is that of the microswimmers in obstacle lattices. As discussed in Chapter 6, there is the potential to try and pinpoint how we should write down the Fokker-Planck equation for these systems, with these spatially-varying microfluidic lattices. Indeed, there is experimental work being done now by Theresa Jakuszeit, with the hope of having some results later this year. Particularly in these active matter systems, there is still a relative scarcity of experimental results, and so it will be a pleasure to work on the project, and see if the theory works out in practice. These methods could also be applied to cells (perhaps in a temperature gradient), to see if they observe similar Fokker-Planck equations.

The experimental test of theory is a cornerstone of science, and worked now as a theoretician through the course of the last three years, it has become clear to me that biophysics needs a good alloying of both experimental and theoretical methods. It is exciting that many of the problems I have tackled in this thesis can be directly compared against experiment. However, from what I have experienced so far, there is a feeling among some that such theoretical methods may often be too reductionist for messy biological systems. My own view is that where biophysics exists as a tool to try and tackle specific questions, such as the roots of certain pathologies in biology, this is to an extent true – we can not have that much to say about the mis-expression of a gene, for example. However, where we seek to try and understand biology more generally, and look for the principles underlying form and function, we should try and retain the eye for a simple and intuitive picture, or risk missing the essential physics of life. It is a theoretical biophysicist's mission then, to not only seek to do this, but to speak with experimentalists, and convince them that such an approach is not futile.

REFERENCES

- [1] Brown R 1828 *Phil. Mag.* **4** 161–173
- [2] Van der Pas P W 1971 *Scientarium Historia* **13** 27–35
- [3] Perrin J 1910 *J. Phys. Theor. Appl.* **9** 5–39
- [4] Gouy M 1888 *J. Phys. Theor. Appl.* **7** 561–564
- [5] Einstein A 1905 *Ann. d. Phys.* **322** 549–560
- [6] Einstein A 1907 *Z. Elektrochem. Angew. P.* **13** 41–42
- [7] Von Smoluchowski M 1906 *Ann. d. Phys.* **326** 756–780
- [8] Langevin P 1908 *C. R. Acad. Sci. (Paris)* **146** 530–533
- [9] Lemons D S and Gythiel A 1997 *Am. J. Phys.* **65** 1079–1081
- [10] Ornstein L S 1919 On the brownian motion *Proc. Amst.* vol 21 pp 96–108
- [11] Burger H C and Ornstein L S 1919 *P. K. Ned. Akad. B: Phys.* **21** 922–931
- [12] Kubo R 1966 *Rep. Prog. Phys.* **29** 255–284
- [13] Nyquist H 1928 *Phys. Rev.* **32** 110–113
- [14] Jardine A P, Alexandrowicz G, Hedgeland H, Allison W and Ellis J 2009 *Phys. Chem. Chem. Phys.* **11** 3355–3374
- [15] Richter D, Butera R, Fetters L J, Huang J S, Farago B and Ewen B 1992 *Macromolecules* **25** 6156–6164
- [16] Jardine A P, Hedgeland H, Alexandrowicz G, Allison W and Ellis J 2009 *Prog. Surf. Sci.* **84** 323–379
- [17] Fokker A D 1914 *Ann. d. Phys.* **348** 810–820
- [18] Planck M 1917 *Über einen Satz der statistischen Dynamik und seine Erweiterung in der Quantentheorie* vol 24 (Reimer)
- [19] Smoluchowski M V 1916 *Ann. d. Phys.* **353** 1103–1112
- [20] Wang M C and Uhlenbeck G E 1945 *Rev. Mod. Phys.* **17** 323

-
- [21] Risken H 1984 *The Fokker-Planck equation: methods of solution and applications* (Springer)
- [22] Wong E and Zakai M 1965 *Ann. Math. Stat.* **36** 1560–1564
- [23] Kramers H A 1940 *Physica* **7** 284–304
- [24] Brinkman H C 1956 *Physica* **XXII** 149–155
- [25] Gardiner C W 1985 *Handbook of Stochastic Methods* 2nd ed (Springer Verlag, Berlin)
- [26] Szabo A, Schulten K and Schulten Z 1980 *J. Chem. Phys.* **72** 4350–4357
- [27] Pastor R W, Zwanzig R and Szabo A 1996 *J. Chem. Phys.* **105** 3878–3882
- [28] Zwanzig R 2001 *Nonequilibrium Statistical Mechanics* (Oxford University Press, New York)
- [29] Valleriani A, Li X and Kolomeisky A B 2014 *J. Chem. Phys.* **140** 064101
- [30] Bicout D J and Szabo A 2000 *Prot. Sci.* **9** 452–465
- [31] Machta J and Zwanzig R 1983 *Phys. Rev. Lett.* **50** 1959
- [32] Lubensky D K and Nelson D R 1999 *Biophys. J.* **77** 1824–1838
- [33] Schuss Z, Singer A and Holcman D 2007 *Proc. Natl. Acad. Sci. USA* **104** 16098–16103
- [34] Holcman D and Schuss Z 2014 *SIAM Review* **56** 213–257
- [35] Bell S and Terentjev E M 2017 *Macromolecules* 8810–8815
- [36] Litshits I M, Grosberg A Y and Khokhlov A R 1978 *Rev. Mod. Phys.* **50** 683–713
- [37] Muthukumar M 1987 *J. Chem. Phys.* **86** 7230–7237
- [38] Kumar S and Li M S 2010 *Phys. Rep.* **486** 1–74
- [39] Engel A, Gaub H and Müller D 1999 *Curr. Biol.* **9** R133–R136
- [40] Fisher T E, Oberhauser A F, Carrion-Vazquez M, Marszalek P E and Fernandez J M 1999 *Trends Biochem. Sci.* **24** 379–384
- [41] Bustamante C, Bryant Z and Smith S B 2003 *Nature* **421** 423–7
- [42] Rief M 1997 *Science* **276** 1109–1112
- [43] Fowler S B, Best R B, Toca Herrera J L, Rutherford T J, Steward A, Paci E, Karplus M and Clarke J 2002 *J. Mol. Biol.* **322** 841–849
- [44] Garcia-Manyes S, Brujić J, Badilla C L and Fernández J M 2007 *Biophys. J.* **93** 2436–46

- [45] Oberhauser A F, Hansma P K, Carrion-Vazquez M and Fernandez J M 2001 *Proc. Natl. Acad. Sci. USA* **98** 468–472
- [46] Fixman M and Kovac J 1973 *J. Chem. Phys.* **58** 1564–1570
- [47] Marko J and Siggia E 1995 *Macromolecules* **28** 8759–8770
- [48] Ha B Y and Thirumalai D 1997 *J. Chem. Phys.* **106** 4243–4247
- [49] Blundell J R and Terentjev E M 2009 *Macromolecules* **42** 5388–5394
- [50] Halperin A and Zhulina E B 1991 *Europhys. Lett.* **15** 417–421
- [51] Craig A and Terentjev E M 2005 *J. Chem. Phys.* **122** 194901
- [52] Polotsky A A, Smolyakova E E and Birshtein T M 2011 *Macromolecules* **44** 8270–8283
- [53] Polotsky A A, Smolyakova E E, Borisov O V and Birshtein T M 2010 *Macromol. Symp.* **296** 639–646
- [54] Dill K A 1999 *Protein Sci.* **8** 1166–1180
- [55] Hummer G and Szabo A 2003 *Biophys. J.* **85** 5–15
- [56] Dudko O K, Hummer G and Szabo A 2008 *Proc. Natl. Acad. Sci. USA* **105** 15755–60
- [57] Dudko O K, Filippov A E, Klafter J and Urbakh M 2003 *Proc. Natl. Acad. Sci. USA* **100** 11378–81
- [58] Frisch T and Verga A 2002 *Phys. Rev. E* **65**(4) 041801
- [59] Lam P M and Zhen Y 2010 *J. Stat. Mech.: Theory and Exp.* **2010** P05011
- [60] Bell G I 1978 *Science* **200** 618–627
- [61] Brujic J, Hermans Z R I, Walther K A and Fernandez J M 2006 *Nat. Phys.* **2** 282–286
- [62] Lannon H, Vanden-Eijnden E and Brujic J 2012 *Biophys. J.* **103** 2215–2222
- [63] Saven J G, Wang J and Wolynes P G 1994 *J. Chem. Phys.* **101** 11037–11042
- [64] Hagen S J and Eaton W A 1996 *J. Chem. Phys.* **104** 3395–3398
- [65] Zwanzig R 1990 *Acc. Chem. Res.* **23** 148–152
- [66] Kuo T L, Garcia-Manyes S, Li J, Barel I, Lu H, Berne B J, Urbakh M, Klafter J and Fernández J M 2010 *Proc. Natl. Acad. Sci. USA* **107** 11336–11340
- [67] Hyeon C, Hinczewski M and Thirumalai D 2014 *Phys. Rev. Lett.* **112**(13) 138101
- [68] Zheng Y, Bian Y, Zhao N and Hou Z 2014 *J. Chem. Phys.* **140** 125102

- [69] Geissler P L and Shakhnovich E I 2002 *Macromolecules* **35** 4429–4436
- [70] Bell S and Terentjev E M 2015 *J. Chem. Phys.* **143** 184902
- [71] Abraham F F 1974 *Homogeneous nucleation theory* (Academic Press, New York)
- [72] Korn G A and Korn T M 2013 *Mathematical Handbook for Scientists and Engineers* 2nd ed (Dover Publications, Mineola, NY)
- [73] Raines R T and Hansen D E 1988 *J. Chem. Educ.* **65** 757–759
- [74] Vijay-Kumar S, Bugg C E and Cook W J 1987 *J. Mol. Biol.* **194** 531–544
- [75] Stacklies W, Vega M C, Wilmanns M and Gräter F 2009 *PLoS Comp. Biol.* **5** e1000306
- [76] Costescu B I, Sturm S and Gräter F 2017 *J. Struct. Biol.* **197** 43–49
- [77] Lazaridis T and Karplus M 1997 *Science* **278** 1928–1931
- [78] Bershadsky A D, Kozlov M and Geiger B 2006 *Curr. Opin. Cell Biol.* **18** 472–481
- [79] Geiger B, Spatz J P and Bershadsky A D 2009 *Nat. Rev. Mol. Cell Biol.* **10** 21–33
- [80] Opsahl L R and Webb W W 1994 *Biophys. J.* **66** 71–74
- [81] Sachs F 2010 *Physiology* **25** 50–56
- [82] Haswell E S, Phillips R and Rees D C 2011 *Structure* **19** 1356–1369
- [83] Evans E and Ritchie K 1997 *Biophys. J.* **72** 1541–1555
- [84] Bruinsma R 2005 *Biophys. J.* **89** 87–94
- [85] Hanggi P 1986 *J. Stat. Phys.* **42** 105–148
- [86] Tilghman R W and Parsons J T 2008 *Seminars Cancer Biol.* **18** 45–52
- [87] Brancaccio M, Hirsch E, Notte A, Selvetella G, Lembo G and Tarone G 2006 *Cardiovasc. Res.* **70** 422–433
- [88] Giannone M P S 2006 *Trends Cell Biol.* **11** 213–223
- [89] Frame M C, Patel H, Serrels B, Lietha D and Eck M J 2010 *Nat. Rev. Mol. Cell Biol.* **11** 802–814
- [90] Hytönen V P and Wehrle-Haller B 2016 *Exp. Cell Res.* **343** 35–41
- [91] Cai X, Lietha D, Ceccarelli D F, Karginov A V, Rajfur Z, Jacobson K, Hahn K M, Eck M J and Schaller M D 2008 *Mol. Cell Biol.* **28** 201–214
- [92] Zhao J and Guan J L 2009 *Cancer Metastasis Rev.* **28** 35–49
- [93] Dunty J M, Gabarra-Niecko V, King M L, Ceccarelli D F J, Eck M J and Schaller M D 2004 *Mol. Cell Biol.* **24** 5353–5368

- [94] Zaidel-Bar R, Ballestrem C, Kam Z and Geiger B 2003 *J. Cell. Sci.* **116** 4605–4613
- [95] Parsons J T 2003 *J. Cell Sci.* **116** 1409–1416
- [96] Hynes R O 1992 *Cell* **69** 11–25
- [97] Hynes R O 2002 *Cell* **110** 673–687
- [98] Novikova E A and Storm C 2013 *Biophys. J.* **105** 1336–1345
- [99] Kong F, Garcia A J, Mould A P, Humphries M J and Zhu C 2009 *J. Cell Biol.* **185** 1275–1284
- [100] Giancotti F G 2000 *Nat. Cell Biol.* **2** E13–E14
- [101] Guan J L, Trevithick J E and Hynes R O 1991 *Cell Reg.* **2** 951–964
- [102] Guan J L and Shalloway D 1992 *Nature* **358** 690–692
- [103] Schaller M D, Borgman C A, Cobb B S, Vines R R, Reynolds A B and Parsons J T 1992 *Proc. Natl. Acad. Sci. USA* **89** 5192–5196
- [104] Erdmann T and Schwarz U S 2004 *J. Chem. Phys.* **121** 8997–9017
- [105] Schwarz U S, Erdmann T and Bischofs I B 2006 *BioSystems* **83** 225–232
- [106] Margadant F, Chew L L, Hu X, Yu H, Bate N, Zhang X and Sheetz M 2011 *PLoS Biol.* **9** e1001223
- [107] Yao M, Goult B T, Klapholz B, Hu X, Toseland C P, Guo Y, Cong P, Sheetz M P and Yan J 2016 *Nat. Comms.* **7** 11966
- [108] Zhou J, Aponte-Santamaría C, Sturm S, Bullerjahn J T, Bronowska A and Gräter F 2015 *PLoS Comp. Biol.* **11** e1004593
- [109] Provenzano P P and Keely P J 2011 *J. Cell Sci.* **124** 1195–1205
- [110] Duke T A J and Bray D 1999 *Proc. Natl. Acad. Sci. USA* **96** 10104–10108
- [111] Duke T A J, Novère N L and Bray D 2001 *J. Mol. Biol.* **308** 541–553
- [112] Bhaskara R M and Srinivasan N 2011 *Sci. Rep.* **1** 40
- [113] Brenner M D, Zhou R and T H 2011 *Biopolymers* **95** 332–344
- [114] Lecuit T, Lenne P F and Munro E 2011 *Annu. Rev. Cell Dev. Biol.* **27** 157–184
- [115] Finer J T, Simmons R M and Spudich J A 1994 *Nature* **368** 113–119
- [116] Bershadsky A D, Balaban N Q and Geiger B 2003 *Annu. Rev. Cell Dev. Biol.* **19** 677–695
- [117] Pollock C M and Shadwick R E 1994 *Am. J. Physiol.* **266** R1016–R1021

- [118] Gosline J M, Lillie M A, Carrington E, Guerette P, Ortlepp C and Savage K 2002 *Philos. Trans. R. Soc. Lond. B Biol. Sci.* **357** 121–132
- [119] Bellingham C M, Lillie M A, Gosline J M, Wright G M, Starcher B C, Bailey A J, Woodhouse K A and Keeley F W 2003 *Biopolymers* **70** 445–455
- [120] Mithieux S M, Rasko J E J and Weiss A S 2004 *Biomaterials* **25** 4921–4927
- [121] Kolahi K S, Donjacour A, Liu X, Lin W, Simbulan R K, Bloise E, Maltepe E and Rinaudo P 2012 *PloS One* **7** e41717
- [122] Handorf A M, Zhou Y, Halanski M A and Li W J 2015 *Organogenesis* **11** 1–15
- [123] Landau L D and Lifshitz I M 1986 *Theory of Elasticity* 3rd ed (Butterworth-Heinemann, Oxford)
- [124] Yeung T, Georges P, Flanagan L A, Marg B, Ortiz M, Funaki M, Zahir N, Ming W, Weaver V and Janmey P 2005 *Cell Motil. Cytoskeleton* **60** 24–34
- [125] Mayor U, Johnson C M, Daggett V and Fersht A R 2000 *Proc. Natl. Acad. Sci. USA* **97** 13518–13522
- [126] Abidine Y, Laurent V M, Michel R, Duperray A, Palade L I and Verdier C 2015 *EPL* **109** 38003
- [127] Dudko O K, Hummer G and Szabo A 2006 *Phys. Rev. Lett.* **96** 108101
- [128] Langer J S 1969 *Ann. Phys. (N.Y.)* **54** 258–275
- [129] Yohichi S and Dudko O K 2009 *Phys. Rev. Lett.* **104** 048101
- [130] Chaudhuri O, Gu L, Darnell M, Klumpers D, Bencherif S A, Weaver J C, Huebsch N and Mooney D J 2015 *Nat. Comms.* **6** 6364
- [131] Escudé M, Rigozzi M K and Terentjev E M 2014 *Biophys. J.* **106** 124–133
- [132] Ricciardi L M and Sato S 1988 *J. Appl. Prob.* **25** 43–57
- [133] Wipff P, Rifkin D, Meister J J and Hinz B 2007 *J. Cell Biol.* **179** 1311–1323
- [134] Elosegui-Artola A, Trepas X and Roca-Cusachs P 2018 *Trends Cell. Biol.* **28** 356–367
- [135] Moore S W, Roca-Cusachs P and Sheetz M P 2010 *Dev. Cell* **19** 194–206
- [136] Discher D E, Janmey P and Wang Y L 2005 *Science* **310** 1139–1143
- [137] Nisenholz N, Rajendran K, Dang Q, Chen H, Kemkemer R, Krishnan R and Zemel A 2014 *Soft Matter* **10** 7234–7246
- [138] Engler A J, Sen S, Sweeney H L and Discher D E 2006 *Cell* **126** 677–689
- [139] Hinz B 2007 *J. Inv. Dermatol.* **127** 526–537

- [140] Tomasek J J, Gabbiani G, Hinz B, Chaponnier C and Brown R A 2002 *Nat. Rev. Mol. Cell Biol.* **3** 349–363
- [141] Solon J, Levental I, Sengupta K, Georges P C and Janmey P A 2007 *Biophys. J.* **93** 4453–4461
- [142] Sinha S, Hoofnagle M H, Kingston P A, McCanna M E and Owens G K 2004 *Am. J. Physiol. Cell Physiol.* **287** C1560–C1568
- [143] Cheung C, Bernardo A S, Trotter M W B, Pedersen R A and Sinha S 2012 *Nat. Biotechnol.* **30** 165–173
- [144] Alliston T, Choy L, Ducy P, Karsenty G and Derynck R 2001 *EMBO J.* **20** 2254–2272
- [145] Butcher D T, Alliston T and Weaver V M 2009 *Nat. Rev. Cancer* **9** 108–122
- [146] Schwarz U S and Safran S A 2013 *Rev. Mod. Phys.* **45** 1327–1381
- [147] Bruinsma R and Sackmann E 2001 *C. R. Acad. Sci. Paris* **2** 801–815
- [148] Sackmann E and Bruinsma R F 2002 *Chem. Phys. Chem.* **3** 262–169
- [149] Döbereiner H G, Dubin-Thaler B J, Giannone G and Sheetz M P 2005 *J. Appl. Physiol.* **98** 1542–1546
- [150] Cohen M, Joester D, Geiger B and Addadi L 2004 *Chembiochem* **5** 1393–1399
- [151] Zhang X, Jiang G, Cai Y, Monkley S J, Critchley D R and Sheetz M P 2008 *Nat. Cell Biol.* **10** 1062–1068
- [152] Cuvelier D, Théry M, Chu Y S, Dufour S, Thiéry J P, Bornens M, Nassoy P and Mahadevan L 2007 *Curr. Biol.* **17** 694–699
- [153] Brill-Karniely Y, Nisenholz N, Rajendran K, Dang Q, Krishnan R and Zemel A 2014 *Biophys. J.* **107** L37–L40
- [154] Reinhart-King C A, Dembo M and Hammer D A 2005 *Biophys. J.* **89** 676–689
- [155] Li J, Han D and Zhao Y P 2013 *Sci. Rep.* **4** 3910
- [156] Döbereiner H G, Dubin-Thaler B, Giannone G, Xenias H S and Sheetz M P 2004 *Phys. Rev. Lett.* **93** 108105
- [157] Xiong Y, Rangamani P, Fardin M A, Lipshtat A, Dubin-Thaler B, Rossier O, Sheetz M P and R I 2010 *Biophys. J.* **98** 2136–2146
- [158] Xu G K, Li B, Feng X Q and Gao H 2016 *Biophys. J.* **111** 1478–1486
- [159] Xu G K, Feng X Q and Gao H 2018 *Biophys. J.* **114** 701–710
- [160] Buckley C D, Tan J, Anderson K L, Hanein D, Volkmann N, Weis W I, Nelson W J and Dunn A R 2014 *Science* **346** 1254211

- [161] Todaro G J and Green H 1963 *J. Cell Biol.* **17** 299–313
- [162] Rocha A, Hahn M and Liang H 2010 *J. Mater. Sci.* **45** 811–817
- [163] Edgell C J, McDonald C C and Graham J B 1983 *Proc. Natl. Acad. Sci. USA* **80** 3734–3737
- [164] Han Y L, Xu Q, Lu Z and Wang J Y 2013 *Coll. Surf. B: Biointerfaces* **111** 479–485
- [165] Dubin-Thaler B J, Giannone G, Döbereiner H G and Sheetz M P 2004 *Biophys. J.* **86** 1794–1806
- [166] Hofrichter J, Ross P D and Eaton W A 1974 *Proc. Natl. Acad. Sci. USA* **71** 4864–4868
- [167] Price L S, Leng J, Schwartz M A and Bokoch G M 1998 *Mol. Biol. Cell* **9** 1863–1871
- [168] Kim C, Ye F and Ginsberg M H 2011 *Annu. Rev. Cell Dev. Biol.* **27** 321–345
- [169] Shattil S J, Kim C and Ginsberg M H 2010 *Nat. Rev. Mol. Cell Biol.* **11** 288
- [170] Xu G K, Yang C, Du J and Feng X Q 2014 *J. Biomech.* **47** 1479–1484
- [171] Tadokoro S, Shattil S J, Eto K, Tai V, Liddington R C, de Pereda J M, Ginsberg M H and Calderwood D A 2003 *Science* **302** 103–106
- [172] Wegener K L, Partridge A W, Han J, Pickford A R, Liddington R C, Ginsberg M H and Campbell I D 2007 *Cell* **128** 171–182
- [173] Moser M, Legate K R, Zent R and Fässler R 2009 *Science* **324** 895–899
- [174] Theodosiou M, Widmaier M, Böttcher R T, Rognoni E, Veelders M, Bharadwaj M, Lambacher A, Austen K, Müller D J, Zent R and Fässler R 2016 *Elife* **5** e10130
- [175] Sieg D J, Hauck C R, Ilic D, Klingbeil C K, Schaefer E, Damsky C H and Schlaepfer D D 2000 *Nat. Cell Biol.* **2** 249–256
- [176] Huvneers S and Danen E H J 2009 *J. Cell Sci.* **122** 1059–1069
- [177] Schwartz M A and Shattil S J 2000 *Trends Biochem. Sci.* **25** 388–391
- [178] Pajic M, Herrmann D, Vennin C, Conway J R W, Chin V T, Johnsson A K E, Welch H C E and Timpson P 2015 *Small GTPases* **6** 123–133
- [179] Zaidel-Bar R, Itzkovitz S, Ma'ayan A, Iyengar R and Geiger B 2007 *Nat. Cell Biol.* **9** 858–867
- [180] Moser M, Nieswandt B, Ussar S, Pozgajova M and Fässler R 2008 *Nat. Med* **14** 325–330
- [181] Hemmings L, Rees D J, Ohanian V, Bolton S J, Gilmore A P, Patel B, Priddle H, Trevithick J E, Hynes R O and Critchley D R 1996 *J. Cell Sci.* **109** 2715–2726
- [182] Yao M, Goult B T, Chen H, Cong P, Sheetz M P and Yan J 2014 *Sci. Rep.* **4** 4610

- [183] Hu D D, Barbas C F and Smith J W 1996 *J. Biol. Chem.* **271** 21745–21751
- [184] Strohmeyer N, Bharadwaj M, Costell M, Fässler R and Müller D J 2017 *Nat. Mater.* **16** 1262–1270
- [185] Vu T K H, Hung D T, Wheaton V I and Coughlin S R 1991 *Cell* **64** 1057–1068
- [186] Chen J, Ishii M, Wang L, Ishii K and Coughlin S R 1994 *J. Biol. Chem.* **269** 16041–16045
- [187] Coughlin S R 2000 *Nature* **407** 258–264
- [188] Howard J 2001 *Mechanics of Motor Proteins and the Cytoskeleton* (Sinauer Associates, Inc.)
- [189] Fletcher D A and Mullins R D 2010 *Nature* **463** 485–492
- [190] Jeppesen C, Wong J Y, Kuhl T L, Israelachvili J N, Mullah N, Zalipsky S and Marques C M 2001 *Science* **293** 465–468
- [191] Wong J Y, Kuhl T L, Israelachvili J N, Mullah N and Zalipsky S 1997 *Science* **275** 820–822
- [192] Wilemski G and Fixman M 1974 *J. Chem. Phys.* **60** 866–877
- [193] Göndör A and Ohlsson R 2009 *Nature* **461** 212–217
- [194] Deng W, Lee J, Wang H, Miller J, Reik A, Gregory P D, Dean A and Blobel G A 2012 *Cell* **149** 1233–1244
- [195] Vafabakhsh R and Ha T 2012 *Science* **337** 1097–1101
- [196] Waters J T and Kim H D 2013 *Macromolecules* **46** 6659–6666
- [197] Bressloff P C and Newby J M 2013 *Rev. Mod. Phys.* **85** 135–196
- [198] Singer A, Schuss Z, Holcman D and Eisenberg R S 2006 *J. Stat. Phys.* **122** 437–463
- [199] Muthukumar M and Baumgärtner A 1989 *Macromolecules* **22** 1937–1941
- [200] Schweizer K S and Saltzman E J 2003 *J. Chem. Phys.* **119** 1181–1196
- [201] Sung W and Park P J 1996 *Phys. Rev. Lett.* **77** 783–786
- [202] Muthukumar M 1999 *J. Chem. Phys.* **111** 10371–10374
- [203] Knowles T P J, Shu W, Devlin G L, Meehan S, Auer S, Dobson C M and Welland M E 2007 *Proc. Natl. Acad. Sci. USA* **104** 10016–10021
- [204] Doi M and Edwards S F 1988 *The Theory of Polymer Dynamics* (Oxford University Press)
- [205] DiMarzio E A 1965 *J. Chem. Phys.* **42** 2101–2106

- [206] Edwards S F and Freed K F 1969 *J. Phys. A.* **2** 145–150
- [207] Joanny J F, Leibler L and De Gennes P G 1979 *J. Polym. Sci. Polym. Phys.* **17** 1073–1084
- [208] de Gennes P G 1980 *Macromolecules* **13** 1069–1075
- [209] Bickel T, Jeppesen C and Marques C M 2001 *Eur. Phys. J. E* **4** 33–43
- [210] Chandrasekhar S 1943 *Rev. Mod. Phys.* **15** 1–89
- [211] Vologodskii A and Frank-Kamenetskii M D 2013 *Nucleic Acids Res.* **14** 6785–6792
- [212] Silberberg A 1962 *J. Phys. Chem.* **66** 1872–1883
- [213] de Gennes P G 1976 *J. de Phys.* **37** 1445–1452
- [214] Alexander S 1977 *J. Phys. (Paris)* **38** 983–987
- [215] O’Shaughnessy B and Vavylonis D 2003 *Phys. Rev. Lett.* **90** 056103
- [216] Panja D, Barkema G T and Kolomeisky A B 2009 *J. Phys.: Condens. Matter* **21** 242101
- [217] O’Shaughnessy B and Vavylonis D 2005 *J. Phys.: Condens. Matter* **17** R63–R99
- [218] Shaffer J S and Chakraborty A K 1993 *Macromolecules* **26** 1120–1136
- [219] Shaffer J S 1994 *Macromolecules* **27** 2987–2995
- [220] Ponomarev A L, Sewell T D and Durning C J 2000 *Macromolecules* **33** 2662–2669
- [221] Descas R, Sommer J U and Blumen A 2006 *J. Chem. Phys.* **124** 094701
- [222] Bhattacharya S, Milchev A, Rostiashvili V G, Grosberg A Y and Vilgis T A 2008 *Phys. Rev. E* **77** 061603
- [223] Brochard-Wyart F 1995 *EPL* **30** 387
- [224] Milchev A, Rostiashvili V, Bhattacharya S and Vilgis T 2011 Polymer chain adsorption on a solid surface: scaling arguments and computer simulations *Nanophenomena at Surfaces* (Springer) pp 185–204
- [225] Li H, Gong B, Qian C J and Luo M B 2015 *Soft Matter* **11** 3222–3231
- [226] Li H, Qian C J and Luo M B 2016 *J. Chem. Phys.* **144** 164901
- [227] Bonnet G, Krichevsky O and Libchaber A 1998 *Proc. Natl. Acad. Sci. USA* **95** 8602–8606
- [228] Dudko O K, Mathé J, Szabo A, Meller A and Hummer G 2007 *Biophys. J.* **92** 4188–4195
- [229] Medhi J 1994 *Stochastic processes* (New Age International, Delhi)

- [230] Norris J R 1998 *Markov chains* (Cambridge University Press, Cambridge)
- [231] Wilf H S 1990 *Generatingfunctionology* (Academic Press, New York) ISBN 0127519556
- [232] Guérin T, Bénichou O and Voituriez R 2012 *Nat. Chem.* **4** 568–573
- [233] Dubacheva G V, Curk T, Mognetti B M, Auzély-Velty R, Frenkel D and Richter R P 2014 *J. Am. Chem. Soc.* **136** 1722–1725
- [234] Buell A K, Dhulesia A, White D A, Knowles T P, Dobson C M and Welland M E 2012 *Angew. Chem.* **51** 5247–5251
- [235] Bechinger C, Di Leonardo R, Löwen H, Reichhardt C, Volpe G and Volpe G 2016 *Rev. Mod. Phys.* **88** 045006
- [236] Puckett J G, Ni R and Ouellette N T 2015 *Phys. Rev. Lett.* **114** 258103
- [237] Sinhuber M and Ouellette N T 2017 *Phys. Rev. Lett.* **119** 178003
- [238] Giavazzi F, Paoluzzi M, Macchi M, Bi D, Scita G, Manning M L, Cerbino R and Marchetti M C 2018 *Soft Matter* **14** 3471–3477
- [239] Cates M E 2012 *Rep. Prog. Phys.* **75** 042601
- [240] Sanchez T, Chen D T, DeCamp S J, Heymann M and Dogic Z 2012 *Nature* **491** 431
- [241] Keber F C, Loiseau E, Sanchez T, DeCamp S J, Giomi L, Bowick M J, Marchetti M C, Dogic Z and Bausch A R 2014 *Science* **345** 1135–1139
- [242] Jee A Y, Dutta S, Cho Y K, Tlusty T and Granick S 2018 *Proc. Natl. Acad. Sci. USA* **115** 14–18
- [243] Costerton J W, Stewart P S and Greenberg E P 1999 *Science* **284** 1318–1322
- [244] Drescher K, Dunkel J, Cisneros L H, Ganguly S and Goldstein R E 2011 *Proc. Natl. Acad. Sci. USA* **108** 10940–10945
- [245] Heddergott N, Krüger T, Babu S B, Wei A, Stellamanns E, Uppaluri S, Pfohl T, Stark H and Engstler M 2012 *PLoS Pathog.* **8** e1003023
- [246] Eisenbach M and Giojalas L C 2006 *Nat. Rev. Mol. Cell Biol.* **7** 276
- [247] Guidobaldi A, Jeyaram Y, Berdakin I, Moshchalkov V V, Condat C A, Marconi V I, Giojalas L and Silhanek A V 2014 *Phys. Rev. E* **89** 032720
- [248] Denissenko P, Kantsler V, Smith D J and Kirkman-Brown J 2012 *Proc. Natl. Acad. Sci. USA* **109** 8007–8010
- [249] Simmchen J, Katuri J, Uspal W E, Popescu M N, Tasinkevych M and Sánchez S 2016 *Nat. Comms.* **7** 10598

- [250] Volpe G, Buttinoni I, Vogt D, Kümmerer H J and Bechinger C 2011 *Soft Matter* **7** 8810–8815
- [251] Brown A T, Vladescu I D, Dawson A, Vissers T, Schwarz-Linek J, Lintuvuori J S and Poon W C K 2016 *Soft Matter* **12** 131–140
- [252] Wykes M S D, Zhong X, Tong J, Adachi T, Liu Y, Ristroph L, Ward M D, Shelley M J and Zhang J 2017 *Soft Matter* **13** 4681–4688
- [253] Kantsler V, Dunkel J, Polin M and Goldstein R E 2013 *Proc. Natl. Acad. Sci. USA* **110** 1187–1192
- [254] Contino M, Lushi E, Tuval I, Kantsler V and Polin M 2015 *Phys. Rev. Lett.* **115** 258102
- [255] Lushi E, Kantsler V and Goldstein R E 2017 *Phys. Rev. E* **96** 023102
- [256] Spagnolie S E, Wahl C, Lukasik J and Thiffeault J L 2017 *Physica D* **341** 33–44
- [257] Berke A P, Turner L, Berg H C and Lauga E 2008 *Phys. Rev. Lett.* **101** 038102
- [258] Li G and Tang J X 2009 *Phys. Rev. Lett.* **103** 078101
- [259] Elgeti J, Kaupp U B and Gompper G 2010 *Biophys. J.* **99** 1018–1026
- [260] Sipos O, Nagy K, Di Leonardo R and Galajda P 2015 *Phys. Rev. Lett.* **114** 258104
- [261] Spagnolie S E, Moreno-Flores G R, Bartolo D and Lauga E 2015 *Soft Matter* **11** 3396–3411
- [262] Elgeti J, Winkler R G and Gompper G 2015 *Rep. Prog. Phys.* **78** 056601
- [263] Chamolly A, Ishikawa T and Lauga E 2017 *New J. Phys.* **19** 115001
- [264] Chepizhko O and Peruani F 2013 *Phys. Rev. Lett.* **111** 160604
- [265] Bertrand T, Zhao Y, Bénichou O, Tailleur J and Voituriez R 2018 *Phys. Rev. Lett.* **120** 198103
- [266] Zeitz M, Wolff K and Stark H 2017 *Eur. Phys. J. E* **40** 23
- [267] Thutupalli S, Geyer D, Singh R, Adhikari R and Stone H A 2018 *Proc. Natl. Acad. Sci. USA* **115** 5403–5408
- [268] Raatz M, Hintsche M, Bahrs M, Theves M and Beta C 2015 *Eur. Phys. J. Spec. Top.* **224** 1185–1198
- [269] Berg H C 1993 *Random walks in biology* (Princeton University Press)
- [270] Tavaddod S, Charsooghi M, Abdi F, Khalesifard H and Golestanian R 2011 *Eur. Phys. J. E* **34** 16
- [271] Das S, Garg A, Campbell A I, Howse J, Sen A, Velegol D, Golestanian R and Ebbens S J 2015 *Nat. Comms.* **6** 8999

-
- [272] Reichhardt C and Reichhardt C O 2018 *Phys. Rev. E* **97** 052613
- [273] Barton J W and Ford R M 1997 *Biotechnol. Bioeng.* **53** 487–496
- [274] Ford R M and Harvey R W 2007 *Adv. Water Resour.* **30** 1608–1617
- [275] Chernov N 1997 *J. Stat. Phys.* **88** 1–29
- [276] Tailleur J and Cates M E 2008 *Phys. Rev. Lett.* **100** 218103
- [277] Schnitzer M J 1993 *Phys. Rev. E* **48** 2553
- [278] Taktikos J, Stark H and Zaburdaev V 2013 *PloS One* **8** e81936
- [279] Lovely P S and Dahlquist F W 1975 *J. Theor. Biol.* **50** 477–496
- [280] Blanco S and Fournier R 2003 *EPL* **61** 168
- [281] Werner E and Lutz S G 2003 *Stochastic dynamics of reacting biomolecules* (World Scientific)
- [282] Han Y L, Ronceray P, Xu G, Malandrino A, Kamm R D, Lenz M, Broedersz C P and Guo M 2018 *Proc. Natl. Acad. Sci. USA* **115** 4075–4080